East European Journal of Physics. **2.** 302-318 (2026)
DOI:10.26565/2312-4334-2026-2-32 ISSN 2312-4334

ANALYSIS OF THERMO-MAGNETIC CASSON HYBRID NANOFLUID FLOW OVER A POROUS STRETCHING SHEET CONSIDERING CHEMICAL REACTION USING RSM

Esara Sivasankar[1], **M. Sreedhar Babu**[1]*, **S. Vijaya Kumar Varma**[2]
[1]Department of Applied Mathematics, Yogi Vemana University, Kadapa, Andhra Pradesh, 516005, India
[2]Department of Mathematics, School of Applied Sciences, REVA Research Center, REVA University, Bengaluru, Karnataka, 560064, India
**Corresponding Author email:* *msreedharyvu@gmail.com*
E-mail: [1]*sivaesara1234@gmail.com*,[2]*vijayakumar.varma@reva.edu.in*

Received February 4, 2026; revised March 31, 2026; accepted April 2, 2026

Thermophysical analysis of heat and mass transmission has many potential uses in solar collectors, chemical reactors, medicinal devices, and sophisticated cooling systems, among other applications. Owing to this incentive, the present work often employs response surface methodology for heat and mass transfer analysis of a Casson hybrid nanofluid over a permeable stretching sheet with convective and radiative effects. The control system of the PDEs defining the developed model is transformed into a coupled set of nonlinear ODEs by applying appropriate similarity transformations. The shooting method, implemented with MATLAB's BVP4c solver, is used to numerically integrate these simplified equations. Using tabulated data and graphical representations, the effects of relevant physical parameters on the distributions of velocity, temperature, and concentration are systematically examined. Additionally, Response Surface Methodology is used to statistically evaluate key response variables across a broad range of governing parameters, such as the skin-friction coefficient, heat, and mass-transfer rates. The findings show that increasing the Casson parameter reduces the temperature profile because the fluid's effective yield stress decreases. Furthermore, due to increased Lorentz forces, a higher magnetic field considerably reduces fluid velocity. Additionally, it has been observed that an increased solid volume fraction raises the nanofluid's temperature due to enhanced thermal conductivity. The statistical analysis indicates that the mass-transfer accuracy for the derived mathematical model in kerosene is 99.85%.

Keywords: *Casson Hybrid nanofluid; MHD; Porous stretching sheet; Chemical Reaction; Response Surface Method (RSM)*
PACS: 44.30 +v, 44.05 +e, 44.20.+b, 45.65.cb

INTRODUCTION

A stretching sheet is a theoretical and practical concept in fluid mechanics where a flexible sheet is continuously stretched in a particular direction, typically in an unbounded fluid medium. Also, stretching sheets are studied to improve heat transfer efficiency in cooling systems, in energy-efficient coatings, and smart materials. Furthermore, to boost the heat transfer, the researchers added the nanoparticles to the conventional fluids, such as nanofluid, first coined. The dispersion of a single type of nanoparticle in a base fluid is often insufficient to attain the enhanced thermal performance required in advanced heat transfer applications. To overcome this limitation, a mixture of two distinct nanoparticles suspended in a base fluid referred to as a hnf has been introduced to improve thermophysical properties. The influence of magnetohydrodynamics (MHD) on nanofluid flow plays a crucial role in controlling fluid motion and heat transfer behavior, and its significance has been demonstrated across numerous practical engineering and industrial applications. In this area of research, Crane [1] was the first to present the fundamental two-dimensional boundary layer solution for flow induced by a stretching surface. Subsequently, Khashi'ie et al. [2] conducted a numerical study on the heat transfer behavior of an MHD hybrid nanofluid (Al_2O_3/H_2O) over a stretching sheet. Shoaib et al. [3] analyzed the influence of system rotation on magnetized hybrid nanofluid flow past an extending surface, while more recently, Sreedevi et al. [4] explored the transient magnetohydrodynamic heat and mass transfer characteristics of hybrid nanofluid flow over a stretching sheet. The impact of thermal radiation on magnetohydrodynamic hybrid nanofluid flow over a stretched wedge was investigated by Waini et al. [5], underscoring the growing significance of radiative effects in hybrid nanofluid transport. The behavior of unstable magnetohydrodynamic hybrid nanofluid flow over a stretching surface was examined by Santhi et al. [6].

The function of velocity slip in both steady and unsteady flow regimes across a stretching sheet. Dinarvand et al. [7] conducted a detailed study on the flow and thermal characteristics near the stagnation region of a shrinking porous surface. Haq et al. [8] explored the heat transfer performance of a Newtonian hybrid nanofluid containing Cu and Al_2O_3 nanoparticles over a stretching sheet. Shah et al. [9] assessed the thermal efficiency of magnetohydrodynamic hybrid nanofluid flow along a stretching surface. Elattar et al. [10] analyzed the flow behavior of an electrically conducting hybrid nanofluid over a thin, non-porous stretching sheet. Farooq et al. [11] investigated the coupled influence of surface permeability, internal heat source or sink, and thermal radiation on magnetohydrodynamic nanofluid flow over an inclined stretching surface. Non-Newtonian fluids such as Casson fluids are characterized by the presence of a yield stress, exhibiting solid-like behavior until a critical stress limit is exceeded. These fluids are widely employed to represent practical materials including blood, printing inks, and food products such as tomato paste. Consequently, considerable research attention has been devoted to Casson nanofluid flow over stretching surfaces. In this sense, under constant

---

Cite as: E. Sivasankar, M.S. Babu, S.V.K. Varma, East Eur. J. Phys. 2, 302 (2026), https://doi.org/10.26565/2312-4334-2026-2-32

boundary layer conditions, Bhattacharyya [12] investigated the velocity and thermal properties of Casson fluid flow toward a stretching sheet. The effects of slip velocity and viscous dissipation were taken into account when Aly et al. [13] theoretically and statistically investigated magnetohydrodynamic stagnation point flow of a hybrid nanofluid across a stretching surface.

Jamaludin et al. [14] studied the magnetohydrodynamic stagnation-point flow of a hybrid nanofluid over a permeable stretched sheet. Nandi et al. [15] analyzed unsteady magnetohydrodynamic mixed convection stagnation-point flow of a hybrid nanofluid within a homogeneous porous medium over an exponentially stretching surface. Rashid et al. [16] studied the flow characteristics of a hybrid nanofluid containing alumina and silver nanoparticles past a stretching sheet. Khan et al. [17] examined boundary-layer flow and heat transfer behavior of a water-based hybrid nanofluid over a stretching surface. Ghasemi et al. [18] explored the simultaneous influence of thermal radiation and an applied magnetic field on nanofluid flow along a stretching sheet. While Zainal et al. [19] examined the continuous flow of an Al2O3–Cu/water hybrid nanofluid under a magnetic influence over stretching and shrinking surfaces, Ali et al. [20] examined the flow dynamics of a magnetically driven hybrid nanofluid over a stretching sheet. Magnetohydrodynamic nanofluid flow over a porous stretched surface was investigated by Neethu et al. [21]. The impact of a chemical reaction on the flow behavior of a Casson nanofluid was investigated by Nadeem et al. [22]. Magnetohydrodynamic Casson nanofluid flow across a permeable stretching surface was assessed by Qing et al. [23]. Khan et al. [24] examined the behavior of unsteady mass and heat transfer while accounting for chemical processes. Dahab et al. [25] investigated how Casson nanofluid flow over a stretched sheet was affected by wall suction and injection. A nonlinear, surface-induced, two-dimensional Casson hybrid nanofluid flow was investigated by Hameed et al. [26]. Meenakumari et al. [27] investigated the mass and heat transfer properties of a Casson nanofluid flow over an inclined, permeable stretched sheet.

The coupled effects of a Casson hybrid nanofluid moving over a permeable stretching surface, while accounting for magnetic field effects, internal heat generation, viscosity dissipation, and chemical reactions, have not yet been described, according to a careful review of previous research. The present work investigates the influence of governing parameters on the flow of a thermally magnetized Casson hybrid nanofluid over a porous stretching sheet, while incorporating the effects of viscous dissipation and chemical reactions to address the identified research gap. The hybrid nanofluid is formulated by dispersing alumina (Al_2O_3) and cobalt (Co) nanoparticles into a kerosene–water base fluid. Because of its improved thermal conductivity, magnetic responsiveness, and reactive-transport properties, this combination has garnered increasing attention and is appropriate for advanced engineering and industrial heat and mass-transfer applications. Al_2O_3 and Co nanoparticles combined with a water hybrid nanofluid base fluid are used in biomedical cooling systems, microchannel heat sinks for quick heat dissipation, and to enhance solar energy absorption and thermal transfer, particularly in the presence of varying sun intensities. Al_2O_3 and Co nanoparticles are combined with kerosene as the base fluid. Al_2O_3 enhances thermal stability, while Co could assist with combustion that is magnetically appropriate. This mixed nanofluid can be applied to cloaking or cooling jackets to lessen infrared signatures. The BVP4c package's shooting technique produced the solution. The RSM is also used to analyze mass transfer, shear stress, and heat rate.

MATHEMATICAL FORMULATION

The present study considers a two-dimensional, steady, incompressible flow of an Al_2O_3–cobalt hybrid nanofluid over a porous stretching surface, as illustrated schematically in Figure 1. The composition of the hybrid nanofluid, formed by dispersing two different types of nanoparticles into the base fluids water and kerosene, is summarized in Table 1.

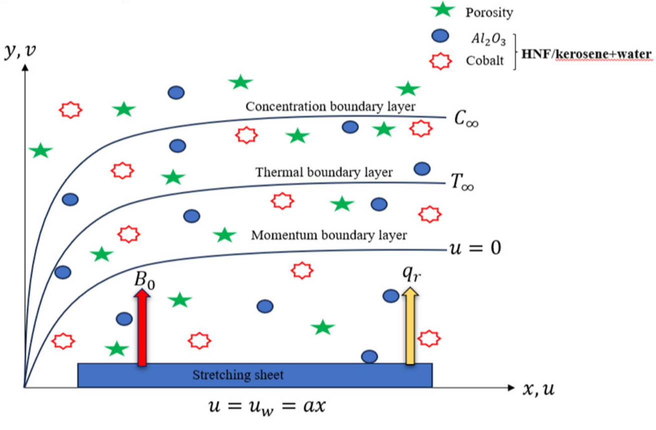

Figure 1. Geometry of the problem

The velocity components in the Cartesian coordinate system are denoted by u and v along the x- and y-directions, respectively. The stretching velocity of the sheet is prescribed as $u_w = ax$, while a uniform transverse magnetic field of strength B_0 is applied. The surface temperature and ambient fluid temperature are represented by T_w, T_∞ respectively, whereas the surface and ambient concentrations are denoted by C_w, C_∞. To describe the flow behavior, the rheological constitutive relation for an isotropic, incompressible Casson fluid is employed and is expressed as follows.

$$\tau_{ij} = \begin{cases} 2(\mu_D + \dfrac{p_y}{\sqrt{2\pi}})e_{ij},\ \pi > \pi_c, \\ 2(\mu_D + \dfrac{p_y}{\sqrt{2\pi}})e_{ij},\ \pi < \pi_c, \end{cases}$$

where μ_D represents the fluid's plastic dynamic viscosity, p_y represents the fluid's yield stress, $\pi = e_{ij}e_{ij}$ is the product of the deformation component's rate with itself, and π_c indicates a crucial value of this product using the fluid model as a basis. In this instance, the Casson parameter is $\beta = \mu_D\sqrt{2\pi_c}/p_y$. Furthermore, it provides the formula for the kinematic viscosity of the Casson fluids, which is $\upsilon = \dfrac{\mu_D}{\rho}\left(1+\dfrac{1}{\beta}\right)$.

Table 1. Nanofluid and hybrid nanofluid thermophysical characteristics (Tanuja et al. [29])

Properties	**Nanofluid**	**Hybrid nanofluid**
Viscosity (μ)	$\mu_{nf} = \dfrac{1}{(1-\phi_1)^{2.5}}$	$\mu_{hnf} = \dfrac{\mu_f}{(1-\phi_1)^{2.5}(1-\phi_2)^{2.5}}$
Density (ρ)	$\rho_{nf} = (1-\phi_1)\rho_f + \phi_1\rho_{S1}$	$\rho_{hnf} = (1-\phi_2)\left((1-\phi_1)\rho_f + \phi_1\rho_{S1}\right) + \phi_2\rho_{S2}$
Kinematic viscosity (υ)	$\upsilon_{nf} = \dfrac{\mu_{nf}}{\rho_{nf}}$	$\upsilon_{hnf} = \dfrac{\mu_{hnf}}{\rho_{hnf}}$
Heat capacity (ρc_p)	$(\rho c_p)_{nf} = (1-\phi_1)(\rho c_p)_f + \phi_1(\rho c_p)_{S1}$	$(\rho c_p)_{hnf} = (1-\phi_2)(1-\phi_1)(\rho c_p)_f$ $+\phi_1(\rho c_p)_{S1}(1-\phi_2) + \phi_2(\rho c_p)_{S2}$
Thermal conductivity (κ)	$\kappa_{nf} = \kappa_f\left[\dfrac{(s-1)\kappa_f + \kappa_{S1} - (s-1)\phi_1(\kappa_f - \kappa_{S1})}{(s-1)\kappa_f + \kappa_{S1} + \phi_1(\kappa_f - \kappa_{S1})}\right]$	$\kappa_{hnf} = \kappa_{nf}\left[\dfrac{(s-1)\kappa_{nf} + \kappa_{S2} - (s-1)\phi_2(\kappa_{nf} - \kappa_{S2})}{(s-1)\kappa_{nf} + \kappa_{S2} + \phi_2(\kappa_{nf} - \kappa_{S2})}\right]$
Electrical conductivity (σ)	$\sigma_{nf} = \sigma_f\left[\dfrac{(s-1)\sigma_f + \sigma_{S1} - (s-1)\phi_1(\sigma_f - \sigma_{S1})}{(s-1)\sigma_f + \sigma_{S1} + \phi_1(\sigma_f - \sigma_{S1})}\right]$	$\sigma_{hnf} = \sigma_{nf}\left[\dfrac{(s-1)\sigma_{nf} + \sigma_{S2} - (s-1)\phi_2(\sigma_{nf} - \sigma_{S2})}{(s-1)\sigma_{nf} + \sigma_{S2} + \phi_2(\sigma_{nf} - \sigma_{S2})}\right]$
Thermal expansion coefficient (β)	$\beta_{nf} = (1-\phi_1)\beta_f + \phi_1\beta_{S1}$	$\beta_{hnf} = (1-\phi_2)\left((1-\phi_1)\beta_f + \phi_1\beta_{S1}\right) + \phi_2\beta_{S2}$

The governing flow equations are stated as follows (Chandra and Ramasekhar, [28])

$$\frac{\partial u}{\partial x} + \frac{\partial v}{\partial y} = 0 \tag{1}$$

$$u\frac{\partial u}{\partial x} + v\frac{\partial u}{\partial y} = \frac{\mu_{hnf}}{\rho_{hnf}}\left(1+\frac{1}{\beta}\right)\frac{\partial^2 u}{\partial y^2} + g(\beta_c)_{hnf}(C - C_\infty) + g(\beta_t)_{hnf}(T - T_\infty) - \frac{\sigma_{hnf}}{\rho_{hnf}}B_0^2 u - \frac{\mu_{hnf}}{k^*\rho_{hnf}}u \tag{2}$$

$$u\frac{\partial T}{\partial x} + v\frac{\partial T}{\partial y} = \left[\begin{array}{l} \dfrac{k_{hnf}}{(\rho c_p)_{hnf}}\dfrac{\partial^2 T}{\partial y^2} - \dfrac{1}{(\rho c_p)_{hnf}}\dfrac{\partial q_r}{\partial y} + \dfrac{\sigma_{hnf}}{(\rho c_p)_{hnf}}B_0^2 u^2 + \dfrac{\mu_{hnf}}{k^*(\rho c_p)_{hnf}}u^2 \\ + \dfrac{\mu_{hnf}}{(\rho c_p)_{hnf}}\left(1+\dfrac{1}{\beta}\right)\left(\dfrac{\partial u}{\partial y}\right)^2 + \dfrac{Q_1}{(\rho c_p)_{hnf}}(T - T_\infty) \end{array}\right] \tag{3}$$

$$u\frac{\partial C}{\partial x} + v\frac{\partial C}{\partial y} = -k_1(C - C_\infty) + D\frac{\partial^2 C}{\partial y^2} \tag{4}$$

By Rosseland approach, the thermal radiation is considered as follows:

$$q_r = -\frac{4\sigma^* T_\infty^3}{3k^*}\frac{\partial T^4}{\partial y}, \tag{5}$$

From the Taylor's series extension of approximately and T^4 about T_∞ eliminating higher order terms, the following equation is obtained and considered for the study:

$$T^4 = 4T_\infty^3 T - 3T_\infty^4 \tag{6}$$

Putting Eq. (6) in Eq. (3), we get

$$u\frac{\partial T}{\partial x}+v\frac{\partial T}{\partial y}=\left.\begin{bmatrix}\dfrac{k_{hnf}}{(\rho c_p)_{hnf}}\dfrac{\partial^2 T}{\partial y^2}-\left(\dfrac{16\sigma^* T_\infty^3}{3k^*}\dfrac{\partial^2 T}{\partial y^2}\right)\dfrac{1}{(\rho c_p)_{hnf}}+\dfrac{\sigma_{hnf}}{(\rho c_p)_{hnf}}B_0^2u^2\\ +\dfrac{\mu_{hnf}}{k^*(\rho c_p)_{hnf}}u^2+\dfrac{\mu_{hnf}}{(\rho c_p)_{hnf}}\left(1+\dfrac{1}{\beta}\right)\left(\dfrac{\partial u}{\partial y}\right)^2+\dfrac{Q_1}{(\rho c_p)_{hnf}}(T-T_\infty)\end{bmatrix}\right\} \tag{7}$$

The relevant boundary restrictions are:

$$\left.\begin{array}{l} u=u_w(x)=ax, v=0, \dfrac{\partial C}{\partial y}=\dfrac{q_m}{D}\left(C_f-C\right), \dfrac{\partial T}{\partial y}=\dfrac{q}{k_f}\left(T_f-T\right), as, y\to 0\\ T=T_f, C=C_f, u\to 0, T\to T_\infty, C\to C_\infty, as, y\to\infty \end{array}\right\} \tag{8}$$

The similarity transformations are defined as:

$$u=axf'(\eta), v=\sqrt{a\upsilon_f}\,f(\eta),\ \theta(\eta)=\frac{T-T_\infty}{T_f-T_\infty},\ \phi(\eta)=\frac{C-C_\infty}{C_f-C_\infty},\ \eta=y\sqrt{\frac{a}{\upsilon_f}} \tag{9}$$

Eqs. (2) to (7) are transformed to dimensional ODEs by using Eq. (9).

$$\left(1+\frac{1}{\beta}\right)f'''-\left(f'\right)^2+ff''+K_6\left(\frac{Gr}{\mathrm{Re}^2}\right)\theta+K_7\left(\frac{Gm}{\mathrm{Re}^2}\right)\phi-\frac{1}{K_2}\left(K_5M+K_1K\right)f'=0 \tag{10}$$

$$\left.\frac{1}{\mathrm{Pr}}\left(\frac{K_4}{K_3}+\frac{4Rd}{3}\frac{1}{K_3}\right)\theta''+f\theta'+\frac{Q}{\mathrm{Pr}\,K_3}\theta+\frac{Ec}{K_3}\left(K_5M+K_1K\right)\left(f'\right)^2+\left(1+\frac{1}{\beta}\right)\frac{K_1}{K_3}Ec\left(f''\right)^2=0\right\} \tag{11}$$

$$\frac{1}{Sc}\phi''+f\phi'-Kr\phi=0\,, \tag{12}$$

where

$$K_1=\frac{\mu_{hnf}}{\mu_f},\ K_2=\frac{\rho_{hnf}}{\rho_f},\ K_3=\frac{\left(\rho c_p\right)_{hnf}}{\left(\rho c_p\right)_f},\ K_4=\frac{k_{hnf}}{k_f},\ K_5=\frac{\sigma_{hnf}}{\sigma_f},\ K_6=\frac{\left(\beta_t\right)_{hnf}}{\left(\beta_t\right)_f},\ K_7=\frac{\left(\beta_c\right)_{hnf}}{\left(\beta_c\right)_f} \tag{13}$$

The reduced boundary conditions are described as:

$$\left.\begin{array}{l} f(0)=0, f'(0)=1,\ \theta'(0)=-B_{i1}(1-\theta(0)),\ \phi'(0)=-B_{i2}(1-\phi(0)),\ at,\ \eta=0\\ f'(\infty)=0,\ \theta(\infty)=0,\ \phi(\infty)=0,\ at,\ \eta=\infty \end{array}\right\} \tag{14}$$

Table 2. Thermophysical properties of water and Kerosene, Al_2O_3 and Co hybrid nanofluid (Divya *et. al.* [30])

Property	Kerosene	Water	Al_2O_3	Cobalt
Density $\rho\left(kgm^{-3}\right)$	783	997.1	3970	8900
Specific heat $C_p\left(Jkg^{-1}K^{-1}\right)$	2090	4179	765	420
Heat conductivity $k_f\left(Wm^{-1}K^{-1}\right)$	0.145	0.613	40	100
Electrical conductivity $\sigma(\Omega m)^{-1}$	21×10^{-6}	0.05	1×10^{-10}	1.602×10^{7}
Thermal expansion coefficient $\beta\left(K^{-1}\right)$	9.9×10^{-4}	21×10^{-5}	0.00000850	1.3×10^{-5}
Pr (Prandtl number)	21	6.8		

Dimensionless parameters

$$M=\frac{\sigma_f B_0^2}{\rho_f a},\quad \mathrm{Pr}=\frac{\mu_f(c_p)_f}{k_f},\quad Rd=\frac{4\sigma^* T_\infty^3}{k^* k_f},\quad Ec=\frac{a^2x^2}{(c_p)_f(T_f-T_\infty)},\quad K=\frac{\upsilon_f}{ak^*},\quad Q=\frac{Q_1\upsilon_f}{k_f}, Sc=\frac{\upsilon_f}{D},\quad B_{i1}=\frac{q}{k_f}\sqrt{\frac{\upsilon_f}{a}},$$

$$B_{i2}=\frac{q_m}{D}\sqrt{\frac{\upsilon_f}{a}},\ Kr=\frac{k_1}{a},\ Gr=\frac{g(\beta_t)(T_f-T_\infty)x^3}{\upsilon_f^{\,2}},\ Gm=\frac{g(\beta_c)(C_f-C_\infty)x^3}{\upsilon_f^{\,2}},\ \mathrm{Re}=\frac{ax^2}{\upsilon_f}$$

Derived quantities

The skin friction coefficient (Cf), Nusselt number (Nu) and Sherwood number (Sh) transferred in their dimensional form are written as

$$Cf = \frac{\tau_w}{\rho_f u_w^2} \tag{15}$$

Where, shear stress τ_w is $\tau_w = \mu_{hnf} \left.\frac{\partial u}{\partial y}\right|_{y=o}$

$$Nu = \frac{x q_w}{k_f \left(T_w - T_\infty\right)} \tag{16}$$

Where, the heat flux q_w is $q_w = -k_{hnf} \left.\frac{\partial T}{\partial y}\right|_{y=o}$

$$Sh = \frac{x q_m}{D_B \left(C_w - C_\infty\right)} \tag{17}$$

Where, mass flux q_m is $q_m = -D_B \left.\frac{\partial C}{\partial y}\right|_{y=o}$

The non-dimensional form of equations (15-17) is converted to

$$\left.\begin{array}{l} \mathrm{Re}_r^{1/2} C_f = Cf = K_1 f''(0) \\ \mathrm{Re}_r^{-1/2} Nu_r = Nu = -K_4 \theta'(0) \\ \mathrm{Re}_r^{-1/2} Sh_m = Sh = -\phi'(0) \end{array}\right\} \tag{18}$$

where, Re_r is the local Reynold number.

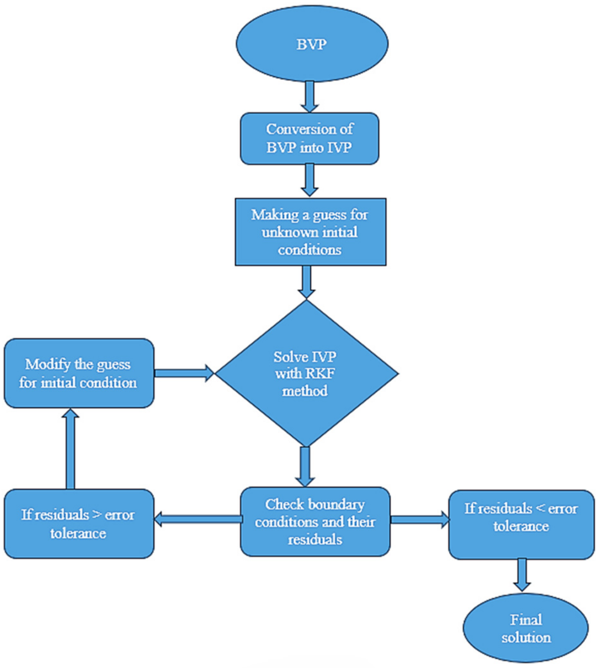

Figure 2. Flow chat for BVP4C

Numerical Technique

The nonlinear ODEs (10–12), subject to the boundary conditions (14), are solved using MATLAB's built-in function of the BVP4C package. This solver for boundary value problems is based on the shooting technique. Due to the highly nonlinear nature of this modified non-dimensional coupled system of equations, finding an accurate solution can be challenging. For equations (10–12), we utilize numerical methods. Introducing new variables into ordinary differential equations (10–12) transforms the highly nonlinear third- and second-order coupled system into a first-order system. Let's proceed with this process by defining the new variables as

$$\left. f = f(1),\ f' = f(2),\ f'' = f(3),\ \theta = f(4),\ \theta' = f(5), \phi = f(6),\ \phi' = f(7) \right\} \tag{19}$$

The first-order ODEs system is now obtained by substituting these variables into equations (10–12). (Manjunatha et al. [31])

$$\frac{d}{d\eta}\begin{pmatrix} f(1)\\ f(2)\\ f(3)\\ f(4)\\ f(5)\\ f(6)\\ f(7)\end{pmatrix}=\begin{pmatrix} f(2)\\ f(3)\\ \dfrac{\left(f(2)\right)^2-f(1)f(3)-K_6\left(\dfrac{Gr}{\mathrm{Re}^2}\right)f(4)+K_7\left(\dfrac{Gm}{\mathrm{Re}^2}\right)f(6)-\dfrac{1}{K_2}\left(K_5M+K_1K\right)f(2)}{\left(1+\dfrac{1}{\beta}\right)}\\ f(5)\\ \dfrac{-f(1)f(5)+\dfrac{Q}{\Pr K_3}f(4)-\dfrac{Ec}{K_3}\left(K_5M+K_1K\right)\left(f(2)\right)^2-\left(1+\dfrac{1}{\beta}\right)\dfrac{K_1}{K_3}Ec\left(f(3)\right)^2}{\dfrac{1}{\Pr}\left(\dfrac{K_4}{K_3}+\dfrac{4Rd}{3}\dfrac{1}{K_3}\right)}\\ f(7)\\ Sc\left(-f(1)\phi(7)+Krf(6)\right)\end{pmatrix} \tag{20}$$

RESULTS AND DISCUSSION

The reduced ordinary differential equations from (10-12) ate solved numerically using shooting package through BVP4C package. The numerical results were compared with previous findings and showed good agreement. This section analyzes the impact of relevant parameters using graphs, as illustrated in Figures 3-22. The non-dimensional parameter values chosen for numerical calculations are $M=1, Gr=2, Gm=4, \beta=1.4, Rd=0.1, Ec=0.1, Q=0.1, \mathrm{Re}=4,$ $Kr=1.8, Sc=0.6, K=1.2, \Pr=21$ (kerosene) and $\Pr=6.8$ (water), and they remain fixed during the present simulation.

The $f'(\eta)$ and $\theta(\eta)$ distributions are influenced by magnetic field parameters, as seen in Figure 3 and 4. The $f'(\eta)$ is influenced by the M, which lowers velocity in both water and kerosene by producing a Lorentz force that opposes the fluid motion as shown in Figure 3. As the M upsurges, the fluid flow slows down due to the resistive force that effect on fluid velocity. Kerosene increases viscosity causes this effect to be more apparent, as it amplifies the viscous force with the magnetic field and damping effects. Figure 4 illustrates that the M impacts the temperature profile $(\theta(\eta))$ for kerosene and water. Heat buildup and a rise in $\theta(\eta)$ result from this decrease in velocity, which limits convective heat transport. Its higher viscosity helps with the impact, which is evident in water because it enhances flow in damping.

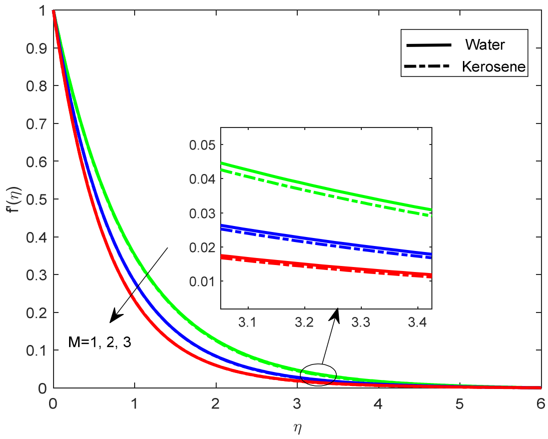

Figure 3. Influence of magnetic field parameter on $f'(\eta)$

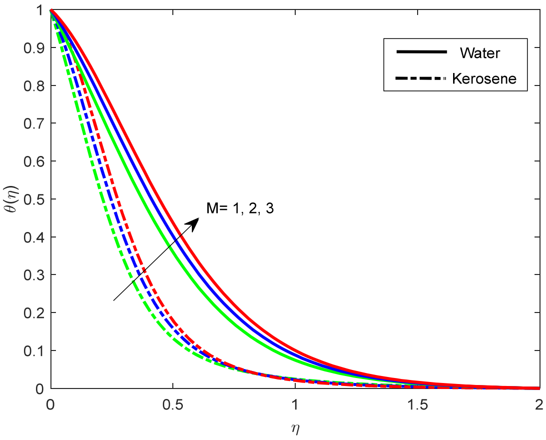

Figure 4. Influence of magnetic field parameter on $\theta(\eta)$

The impact of the on the $\theta(\eta)$ and $f'(\eta)$ is depicted in Figures 5 and 6. The $f'(\eta)$ declines as K increases. As a result, Figure 5 shows that using water as the base fluid causes the velocity boundary layer to decay more rapidly, whereas using kerosene yields a thicker velocity boundary layer. The impact of the porosity parameter on the $\theta(\eta)$ for the base fluids is shown in Figure 6. This figure shows that, when water is used as the base fluid, increasing the porosity parameter K increases the thermal boundary-layer thickness.

Based on Figure 7, the Casson parameter (β) upsurges the flow resistance due to yield stress, which lowers the $f'(\eta)$ in both water and kerosene. This effect is more significant for kerosene than water because of its higher viscosity and apparent non-Newtonian behavior. The Casson parameter influences the temperature profile $\theta(\eta)$, which controls the fluid's yield stress as depicted in Figure 8. When Casson parameter decreases the heat transfer is enhanced then the temperature profile for both kerosene and water as a base fluid increase. This effect is evident because water has less viscosity and better thermal conductivity.

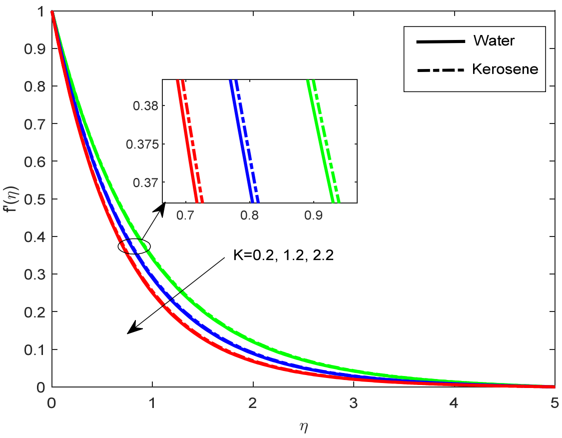

Figure 5. Influence of porosity parameter on $f'(\eta)$

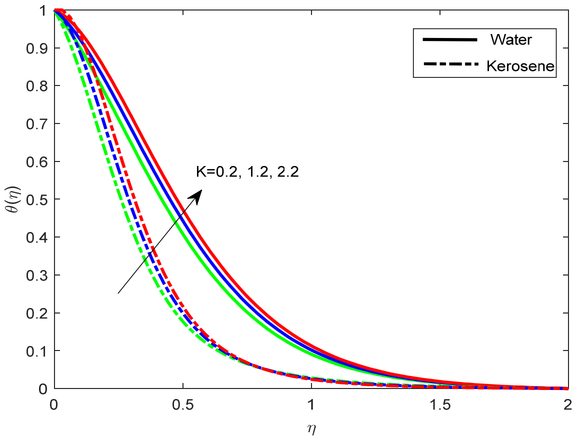

Figure 6. Influence of porosity parameter on $\theta(\eta)$

The effect of the thermal Grashof number (Gr) is shown in Figure 9. The Gr signifies the proportion of buoyant force to viscous force on velocity. For both kerosene and water, as increase in Gr and $f'(\eta)$ increases. Generally, a rise in thermal Grashof causes a surge in buoyancy forces, which raises velocity. In Figure 10, the least value of the solutal Grashof number (Gm = 2) has the least effect on the primary flow of water based Casson hybrid nanofluid as compared to kerosene based Casson hybrid nanofluid and gradually rises for a higher value of Gm. These phenomena occurred due to the fact that the buoyancy force driven by solutal differences leads to increases in fluid flow.

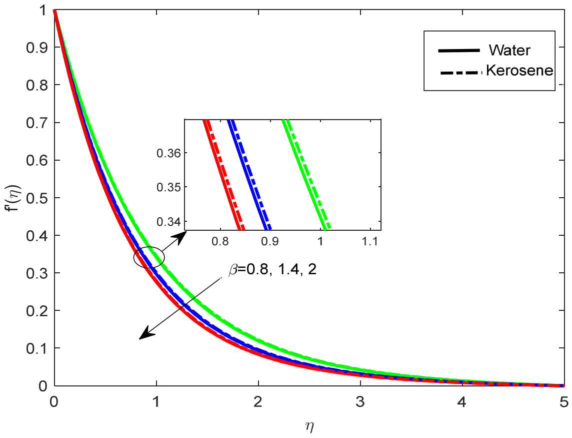

Figure 7. Influence of the Casson parameter on the $f'(\eta)$

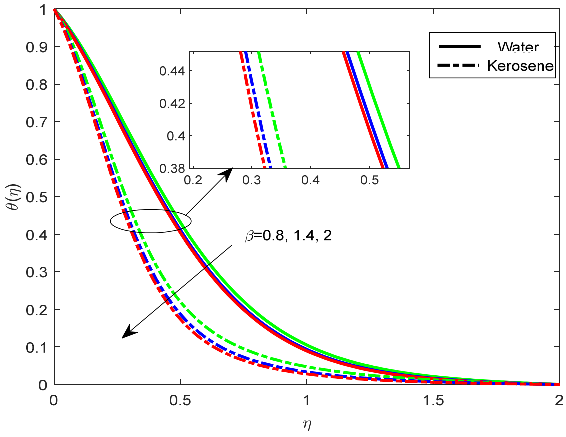

Figure 8. Influence of Casson parameter on $\theta(\eta)$

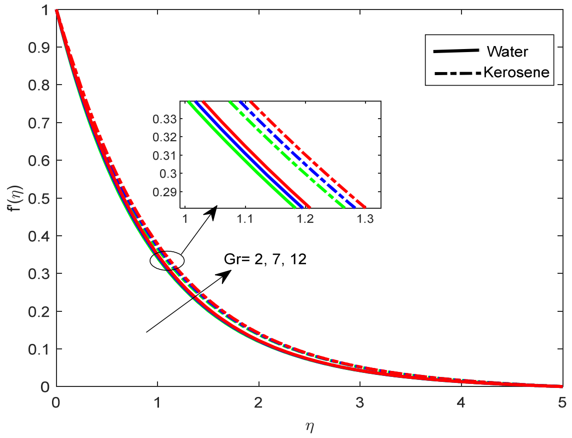

Figure 9. Influence of thermal Grashof number on $f'(\eta)$

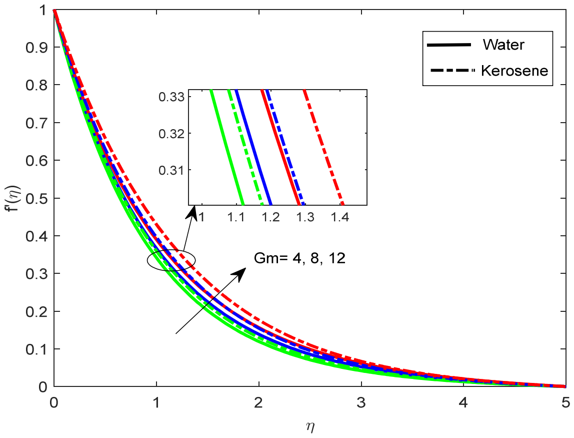

Figure 10. Influence of mass Grashof number on the $f'(\eta)$

Figure 11 shows how the Reynolds number impacts the velocity distribution. For the non-Newtonian fluid (Casson fluid), this figure demonstrates that increasing the Reynolds number causes a drop in velocity over a stretching sheet in both water and kerosene. Figure 12 shows that the radiation parameter (Rd) impacts $\theta(\eta)$.

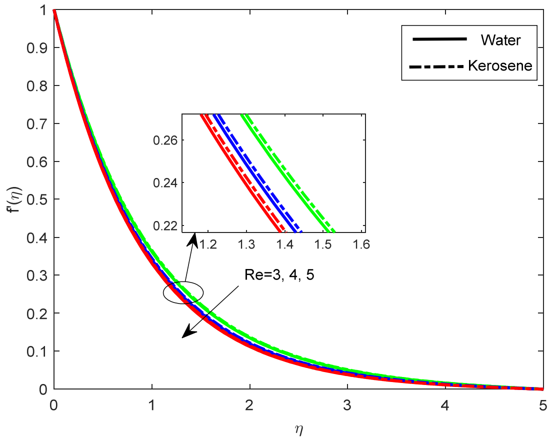

Figure 11. Influence of Reynolds number on $f'(\eta)$

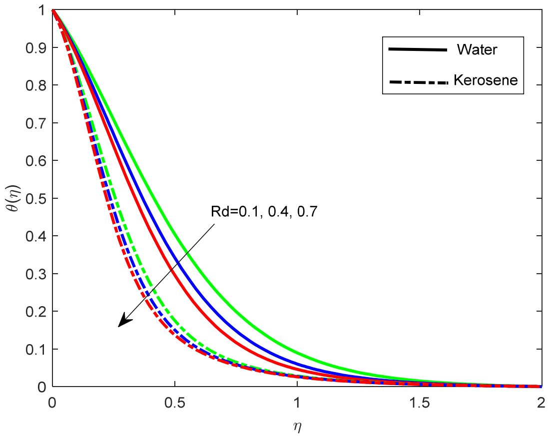

Figure 12. Influence of radiation parameter on $\theta(\eta)$

For a more significant value of Rd the viscosity of the boundary layer declines as the $\theta(\eta)$ increases. For the $Co + Al_2O_3$ /water+kerosene hybrid nanofluid, Rd addresses thermal conduction heat transfer, radiation parameters from a physical point, and its relative immersion of Rd . Thus, warmth is added to the regime for values of the Rd , which enhances $\theta(\eta)$, and Rd enhances the thermal diffusivity of nanofluids. Here, we analyze heat transport in the presence of radiation and talk about forced flow over a stretching sheet. Radiation enhances the effect of heat conductivity. Heat transport is linearly enhanced by radiation.

According to Figure 13, the constant heat source parameter (Q) produces heat in the hybrid nanofluid. By increasing the Q, the $\theta(\eta)$ of the system upsurges in both kerosene and water. As Q rises, the fluid's temperature increases, water heats up more quickly due to its lower specific heat capacity. Kerosene shows a slower rate of temperature increase because of its greater specific heat capacity. The higher heat produces a more prominent thermal boundary layer in both fluids, resulting in a significant temperature difference near the wall. Figure 14 represents the effects of Eckert number on $\theta(\eta)$. When the number of Eckert increases, the viscous dissipation increases, which changes the kinetic energy into thermal energy. The process increases the fluid temperature in water-based and kerosene-based hybrid nanofluids. The temperature at the boundary layer increases as Ec rises due to the conversion of greater velocity-related to energy into heat. Water heat reduces viscosity, making it possible for the temperature to rise more quickly, making the effect more apparent. Kerosene's greater viscosity causes $\theta(\eta)$ to rise while reducing the temperature increase.

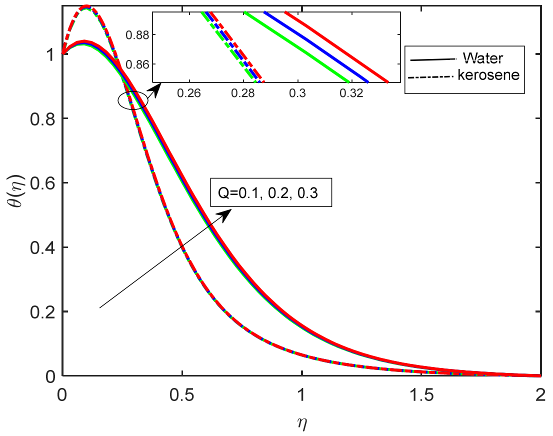

Figure 13. Influence of heat source parameter on $\theta(\eta)$

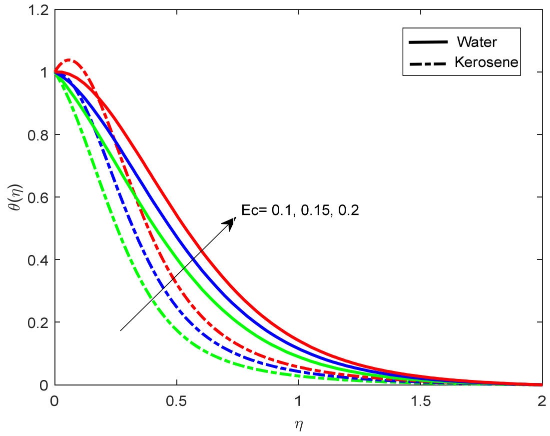

Figure 14. Influence of the Eckert number on $\theta(\eta)$

The effect of Sc on $\phi(\eta)$ is depicted in Figure 15. A rise in the Sc leads to slower mass diffusion, which causes a more uniform concentration distribution. The impact of kerosene base fluid is greater due to the higher viscosity. An increased Schmidt number results in a more steady and less noticeable concentration gradient in both fluids. As shown in Figure 16, the chemical reaction parameter (Kr) suppresses the concentration profile $\phi(\eta)$ in both water and kerosene by enhancing solute absorption. The concentration of the fluid declines significantly as Kr increases due to increase in reaction rates. Although each fluid's concentration diminishes at varying rates due to its unique transport properties, this phenomenon occurs in both fluids. An elevated Kr yields a more uniform and reduced concentration distribution in both cases.

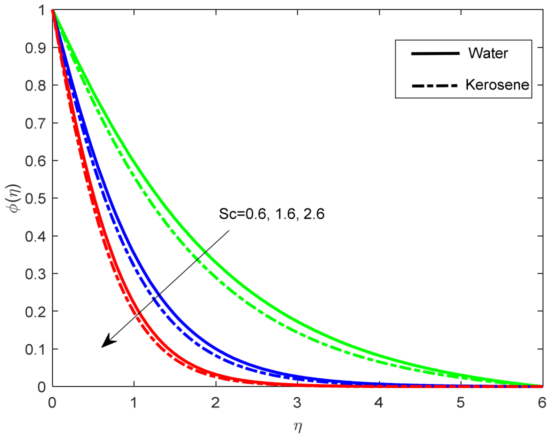

Figure 15. Influence of Schmidt number on $\phi(\eta)$

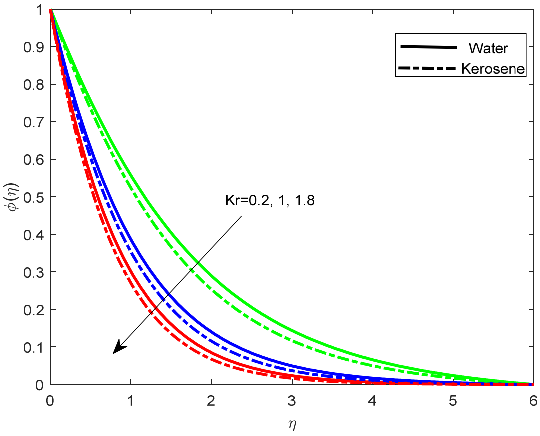

Figure 16. Influence of chemical reaction parameter on $\phi(\eta)$

Response Surface Methodology

The RSM is a valuable technique for creating empirical relationships between a wide range of relevant characteristics. It allows one to look at the input elements with the least and most significant influence on the outputs. RSM aims to maximise replies; this study ascertains how selected input parameters, specifically M, β, and Gm, affect Cf, Q, Ec, and Rd affect Nu, and Kr, Sc affect Sh. Table 3-5 displays the three levels and a specified range of input parameter adjustments. (Manaswini et al. [32])

Table 3: The effects of various parameter values

Parameter	Symbol	Level		
		-1	0	1
$1 \le M \le 3$	W1	1	2	3
$0.8 \le \beta \le 2$	W2	0.8	1.4	2
$4 \le Gm \le 12$	W3	4	8	12

Table 4: The effects of various parameter values

Parameter	Symbol	Level		
		-1	0	1
$0.1 \le Q \le 0.3$	W1	0.1	0.2	0.3
$0.1 \le Ec \le 0.2$	W2	0.1	0.15	0.2
$0.1 \le Rd \le 0.7$	W3	0.1	0.4	0.7

Table 5: The effects of various parameter values

Parameter	Symbol	Level		
		-1	0	1
$0.2 \le Kr \le 1.8$	W1	0.2	1	1.8
$0.6 \le Sc \le 2.6$	W2	0.6	1.6	2.6

In the subsequent stage, a numerical framework comprising 20 simulation runs is developed using the selected input parameters to evaluate the Cf, and Nu as reported in Tables 6 and 7. Additionally, 13 numerical runs are conducted for the chosen parameters, and the corresponding Sh results are presented in Table 8. A second-order polynomial model is employed to represent the relationship between the input variables and the responses. This approach effectively captures the interaction effects among the governing parameters.

Table 6. A CCD-based investigative approach

Run	Code values			Real values			Response	
	W1	W2	W3	M	β	Gm	Cf / Kerosene	Cf / water
1	1	-1	-1	3	0.8	4	1.469513	1.5254
2	0	0	0	2	1.4	8	1.441879	1.502736
3	1	0	0	3	1.4	8	1.613828	1.668639
4	0	0	0	2	1.4	8	1.441879	1.502736
5	-1	1	1	1	2	12	1.256014	1.331229
6	0	1	0	2	2	8	1.533192	1.590474

Run	Code values			Real values			Response	
	W1	W2	W3	M	β	Gm	Cf / Kerosene	Cf / water
7	0	0	-1	2	1.4	4	1.503529	1.556749
8	1	1	1	3	2	12	1.654406	1.713686
9	1	1	-1	3	2	4	1.783811	1.828922
10	0	0	1	2	1.4	12	1.380485	1.448841
11	0	0	0	2	1.4	8	1.441879	1.502736
12	0	-1	0	2	0.8	8	1.275628	1.345393
13	0	0	0	2	1.4	8	1.441879	1.502736
14	1	-1	1	3	0.8	12	1.374032	1.441922
15	0	0	0	2	1.4	8	1.441879	1.502736
16	-1	-1	-1	1	0.8	4	1.168365	1.24209
17	-1	0	0	1	1.4	8	1.441879	1.32327
18	0	0	0	2	1.4	8	1.441879	1.502736
19	-1	1	-1	1	2	4	1.39995	1.456847
20	-1	-1	1	1	0.8	12	1.06423	1.152761

Table 7. A CCD-based investigative approach

Run	Code values			Real values			Response	
	W1	W2	W3	Ec	Q	Rd	Nu /Kerosene	Nu /Water
1	1	1	-1	0.2	0.3	0.1	1.902361	1.379571
2	0	-1	0	0.15	0.1	0.4	0.813153	1.383466
3	0	0	1	0.15	0.2	0.7	1.284033	1.383972
4	0	0	0	0.15	0.2	0.4	0.849009	1.383268
5	0	0	0	0.15	0.2	0.4	0.849009	1.383268
6	0	1	0	0.15	0.3	0.4	0.885069	1.383066
7	-1	1	1	0.1	0.3	0.7	1.902361	1.386893
8	0	0	0	0.15	0.2	0.4	0.849009	1.383268
9	0	0	0	0.15	0.2	0.4	0.849009	1.383268
10	0	0	-1	0.15	0.2	0.1	0.416939	1.382287
11	-1	-1	-1	0.1	0.1	0.1	1.063311	1.384939
12	1	-1	-1	0.2	0.1	0.1	1.834498	1.38002
13	-1	-1	1	0.1	0.1	0.7	0.907105	1.387217
14	0	0	0	0.15	0.2	0.4	0.849009	1.383268
15	1	-1	1	0.2	0.1	0.7	3.383973	1.381126
16	1	0	0	0.2	0.2	0.4	2.66211	1.380437
17	1	1	-1	0.2	0.3	0.1	1.882659	1.379571
18	-1	0	0	0.1	0.2	0.4	0.969722	1.3861
19	-1	1	-1	0.1	0.3	0.1	1.013761	1.384609
20	0	0	0	0.15	0.2	0.4	0.849009	1.383268

Table 8. A CCD-based investigative approach

Run	Code values		Real values		Response	
	W1	W2	Kr	Sc	Sh /Kerosene	Sh /Water
1	-1	-1	0.2	0.6	0.689451	1.502736
2	1	0	1.8	1.6	1.871837	1.530168
3	1	1	1.8	2.6	2.397922	1.540488
4	0	0	1	1.6	1.489013	1.522568
5	0	1	1	2.6	1.909637	1.532369
6	1	-1	1.8	0.6	1.156877	1.513357
7	0	0	1	1.6	1.489013	1.522568
8	0	0	1	1.6	1.489013	1.522568
9	-1	1	0.2	2.6	1.248423	1.51955
10	-1	0	0.2	1.6	0.983639	1.511771
11	0	0	1	1.6	1.489013	1.522568
12	0	0	1	1.6	1.489013	1.522568
13	0	-1	1	0.6	0.943398	1.508495

The created model's practical applications and consequences are validated through the use of Analysis of Variance (ANOVA). For all derived quantities, Table 9-11 indicates that the parameter is significant if the p value is less than 0.05. Conversely, it is not significant otherwise. The interactions M^2, β^2, $M\beta$, $M\,Gm$, and βGm for kerosene, along with Gm^2, $M\,Gm$, for water, are considered non-significant. The R^2 values are 96.67% kerosene and 99.98% water for Cf. Conversely, Q^2, Rd^2, $Q\,Ec$ for kerosene and Q^2, Ec^2, $Q\,Rd$ for water are non-significant. The R^2 values are 98.96%

kerosene and 100.00% water for Nu. The R^2 values are 99.85% kerosene and 99.72% water for Sh, and the relationship with input values (Kr, Sc) demonstrates the model's accuracy.

Table 9. ANOVA of Cf for kerosene and water

Source	DF	Adj SS		Adj MS		F-Value		P-Value		Coeff	
		case-1	case-2	case-1	case-2	case-1	case-2	case-1	case-2	case-1	case-2
Model	9	0.474391	0.466478	0.052710	0.051831	32.28	5864.55	0.000	0.000		
Linear	3	0.443209	0.454167	0.147736	0.151389	90.46	17129.32	0.000	0.000	1.4556	1.50268
M	1	0.244970	0.279683	0.244970	0.279683	150.0	31645.48	0.000	0.000	0.1565	0.167237
β	1	0.162717	0.147281	0.162717	0.147281	99.64	16664.47	0.000	0.000	0.1276	0.121359
Gm	1	0.035522	0.027203	0.035522	0.027203	21.75	3078.01	0.001	0.000	-0.0596	-0.052157
Square	3	0.026768	0.007556	0.008923	0.002519	5.46	285.00	0.017	0.000		
M^2	1	0.007354	0.000121	0.007354	0.000121	4.50	13.71	**0.060**	0.004	0.0517	-0.00664
β^2	1	0.014150	0.003303	0.014150	0.003303	8.66	373.76	0.015	0.000	-0.0717	-0.03466
Gm^2	1	0.003204	0.000000	0.003204	0.000000	1.96	0.01	**0.192**	**0.912**	-0.0341	0.00020
2-Way Interaction	3	0.004415	0.004755	0.001472	0.001585	0.90	179.34	0.474	0.000		
$(M)(\beta)$	1	0.003668	0.004143	0.003668	0.004143	2.25	468.80	**0.165**	0.000	0.0214	0.02276
$(M)(Gm)$	1	0.000067	0.000033	0.000067	0.000033	0.04	3.73	**0.843**	**0.082**	0.0029	0.00203
$(\beta)(Gm)$	1	0.000679	0.000579	0.000679	0.000579	0.42	65.49	**0.533**	0.000	-0.0092	-0.00851
Error	10	0.016331	0.000088	0.001633	0.000009						
Lack-of-Fit	5	0.016331	0.000088	0.003266	0.000018						
Pure Error	5	0.000000	0.000000	0.000000	0.000000						
Total	19	0.490722	0.466567								

Model Summary

S		**R-sq**		**R-sq(adj)**		**R-sq(pred)**	
Case-1	Case-2	Case-1	Case-2	Case-1	Case-2	Case-1	Case-2
0.0404119	0.002972	**96.67%**	**99.98%**	**93.68%**	**99.96%**	76.98%	99.84%

$$Cf = E_0 + E_1 M + E_2\beta + E_3 Gm + E_{11}M^2 + E_{22}\beta^2 + E_{33}Gm^2 + E_{12}(M)(\beta) + E_{13}(M)(Gm) + E_{23}(\beta)(Gm) \tag{21}$$

$$Cf\,/\,Kerosene = 1.4556 + 0.1565M + 0.1276\beta - 0.0596Gm - 0.0717\beta^2 \tag{22}$$

$$Cf\,/\,water = \left.\begin{matrix} 1.50268 + 0.167237M + 0.121359\beta - 0.052157Gm \\ -0.00664M^2 - 0.03466\beta^2 + +0.02276(M)(\beta) - 0.00851(\beta)(Gm) \end{matrix}\right\} \tag{23}$$

$$\left.\begin{matrix} Cf\,/\,Kerosene = 0.0517M^2 - 0.0341Gm^2 + 0.0214(M)(\beta) + 0.0029(M)(Gm) - 0.0092(\beta)(Gm) \\ Cf\,/\,Water = 0.00020Gm^2 + 0.00203(M)(Gm) \end{matrix}\right\} \tag{24}$$

Table 10. ANOVA of Nu for Kerosene and Water

Source	DF	Adj SS		Adj MS		F-Value		P-Value		Coeff	
		case-1	case-2	case-1	case-2	case-1	case-2	case-1	case-2	case-1	case-2
Model	9	10.2410	0.000093	1.13788	0.000010	95.47	30461.68	0.000	0.000		
Linear	3	5.1592	0.000086	1.71972	0.000029	144.29	84657.48	0.000	0.000	0.8209	1.38327
Q	1	0.2319	0.000057	0.23192	0.000057	19.46	168346.27	0.001	0.000	0.1782	-0.002797
Ec	1	4.6835	0.000000	4.68350	0.000000	392.97	855.21	0.000	0.000	0.8007	-0.000199
Rd	1	1.8982	0.000005	1.89818	0.000005	159.27	14169.19	0.000	0.000	0.5277	0.000840
Square	3	5.3207	0.000000	1.77358	0.000000	148.81	82.73	0.000	0.000		
Q^2	1	0.0134	0.000000	0.01337	0.000000	1.12	0.00	**0.314**	**0.992**	0.0704	-0.000000
Ec^2	1	2.8980	0.000000	2.89798	0.000000	243.16	0.05	0.000	**0.821**	1.0373	-0.000003
Rd^2	1	0.0139	0.000000	0.01390	0.000000	1.17	153.56	**0.306**	0.000	0.0718	-0.000139
2-Way Interaction	3	1.0014	0.000001	0.33380	0.000000	28.01	537.03	0.000	0.000		
$(Q)(Ec)$	1	0.0028	0.000000	0.00282	0.000000	0.24	20.53	**0.637**	0.001	-0.0227	-0.000036

Source	DF	Adj SS		Adj MS		F-Value		P-Value		Coeff	
		case-1	case-2	case-1	case-2	case-1	case-2	case-1	case-2	case-1	case-2
$(EC)(Rd)$	1	0.2080	0.000000	0.20801	0.000000	17.45	1349.18	0.002	0.000	0.2029	-0.000301
$(Q)(Rd)$	1	0.6846	0.000000	0.68459	0.000000	57.44	0.65	0.000	**0.439**	0.3681	-0.000007
Error	10	0.1192	0.000000	0.01192	0.000000						
Lack-of-Fit	4	0.1190	0.000000	0.02975	0.000000	919.61		0.000			
Pure Error	6	0.0002	0.000000	0.00003	0.000000						
Total	19	10.3601	0.000093								

Model Summary

S		**R-sq**		**R-sq(adj)**		**R-sq(pred)**	
Case-1	Case-2	Case-1	Case-2	Case-1	Case-2	Case-1	Case-2
0.109171	0.0000184	**98.85%**	**100.00%**	**97.81%**	**99.99%**	76.07%	99.95%

$$Nu = E_0 + E_1 Q + E_2 Ec + E_3 Rd + E_{11} Q^2 + E_{22} Ec^2 + E_{33} Rd^2 + E_{12}(Q)(Ec) + E_{13}(Q)(Rd) + E_{23}(Ec)(Rd) \tag{25}$$

$$Nu\,/\,Kerosene = \left.\begin{array}{l} 0.8209 + 0.1782Q + 0.8007Ec + 0.5277Rd \\ +1.0373Ec^2 + 0.2029(Q)(Rd) + 0.3681(Ec)(Rd) \end{array}\right\} \tag{26}$$

$$Nu\ /\text{Water} = \left.\begin{array}{l} 1.38327 - 0.002797Q - 0.000199Ec + 0.000840Rd \\ -0.000139Rd^2 - 0.0000036(Q)(Ec) - 0.000301(Ec)(Rd) \end{array}\right\} \tag{27}$$

$$\left.\begin{array}{l} Nu\,/\,kerosene = 0.0704Q^2 + 0.07018Rd^2 - 0.0227(Q)(Ec) \\ Nu\,/\,Water = -0.00000Q^2 - 0.000139Ec^2 - 0.000007(Q)(Rd) \end{array}\right\} \tag{28}$$

Table 11. ANOVA of Sh for kerosene and water

Source	**DF**	**Adj SS**		**Adj MS**		**F-Value**		**P-Value**		**Coeff**	
		case-1	case-2	case-1	case-2	case-1	case-2	case-1	case-2	case-1	case-2
Model	5	2.46769	0.001237	0.49354	0.000247	953.11	492.65	0.000	0.000		
Linear	2	2.32130	0.001183	1.16065	0.000591	2241.4	1176.99	0.000	0.000	1.48792	1.52254
Kr	1	1.04594	0.000416	1.04594	0.000416	2019.9	827.99	0.000	0.000	0.41752	0.008326
Sc	1	1.27536	0.000767	1.27536	0.000767	2462.9	1526.00	0.000	0.000	0.46104	0.011303
Square	2	0.03008	0.000028	0.01504	0.000014	29.04	28.15	0.000	0.000		
Kr^2	1	0.00912	0.000006	0.00912	0.000006	17.60	12.41	0.004	0.010	-0.0574	-0.001502
Sc^2	1	0.00951	0.000011	0.00951	0.000011	18.36	22.88	0.004	0.002	-0.0587	-0.002040
2-Way Interaction	1	0.11631	0.000027	0.11631	0.000027	224.61	52.97	0.000	0.000		
$(Kr)(Sc)$	1	0.11631	0.000027	0.11631	0.000027	224.61	52.97	0.000	0.000	0.1705	0.002579
Error	7	0.00362	0.000004	0.00052	0.000001						
Lack-of-Fit	3	0.00362	0.000004	0.00121	0.000001						
Pure Error	4	0.00000	0.000000	0.00000	0.000000						
Total	12	2.47131	0.001241								

Model Summary

S		**R-sq**		**R-sq(adj)**		**R-sq(pred)**	
Case-1	Case-2	Case-1	Case-2	Case-1	Case-2	Case-1	Case-2
0.0227556	0.0007088	**99.85%**	**99.72%**	**99.75%**	**99.51%**	98.51%	97.12%

$$Sh = E_0 + E_1 Kr + E_2 Sc + E_{11} Kr^2 + E_{22} Sc^2 + E_{12}(Kr)(Sc) \tag{29}$$

$$Sh\ /\text{kerosene} = \left.\begin{array}{l} 1.48792 + 0.41752Kr + 0.46104Sc - 0.0574Kr^2 \\ -0.0587\,Sc^2 + 0.1705(Kr)(Sc) \end{array}\right\} \tag{30}$$

$$Sh\ /\text{water} = \left.\begin{array}{l} 1.52254 + 0.008326Kr + 0.011303Sc - 0.001502Kr^2 \\ -0.002040Sc^2 + 0.002579(Kr)(Sc) \end{array}\right\} \tag{31}$$

Table 12. Comparative table for the current study's different Prandtl numbers.

Pr	Present Study	Ali et al. [21].
0.7	0.45601	0.4560
2.0	0.91332	0.9133

The Shooting method with the bVp4c package is used to solve the non-dimensional equations. Published study validates the current numerical finding for various Prandtl numbers. As the table illustrates, the numerical results are in good accord with the published study.

Figures 17-22 display and provide reference to the residual charts. The mean possibility plots of the residuals indicate exceptional conditions. The observed and fitted values show a significant correlation, as evidenced by the residual diagrams. Kerosene and water as base fluids have the most considerable residuals for the Cf, Nu and Sh.

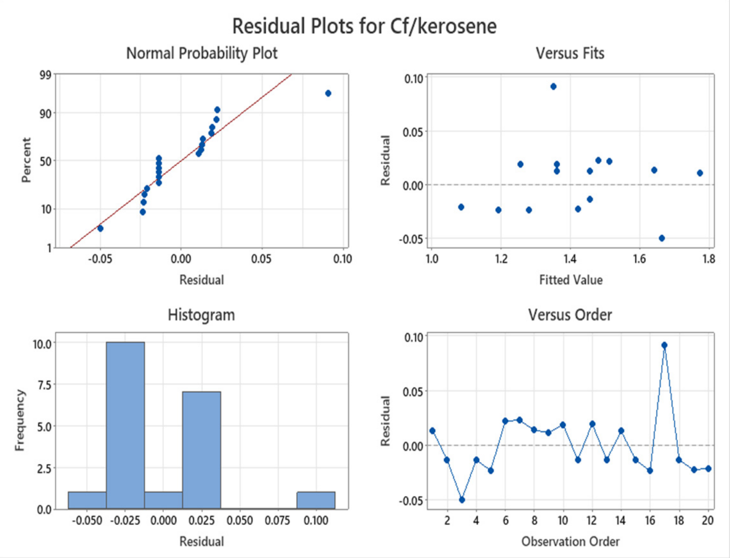

Figure 17. The skin friction coefficient residual plots for the kerosene as a base fluid

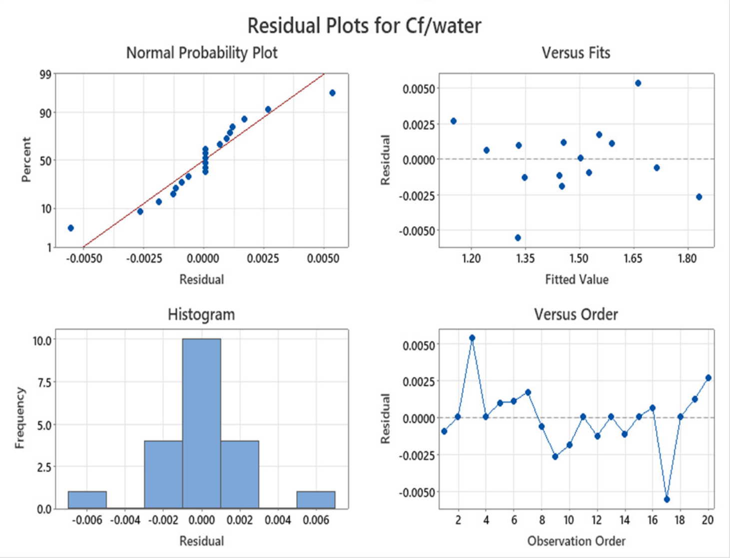

Figure 18. The skin friction coefficient residual plots for water as a base fluid.

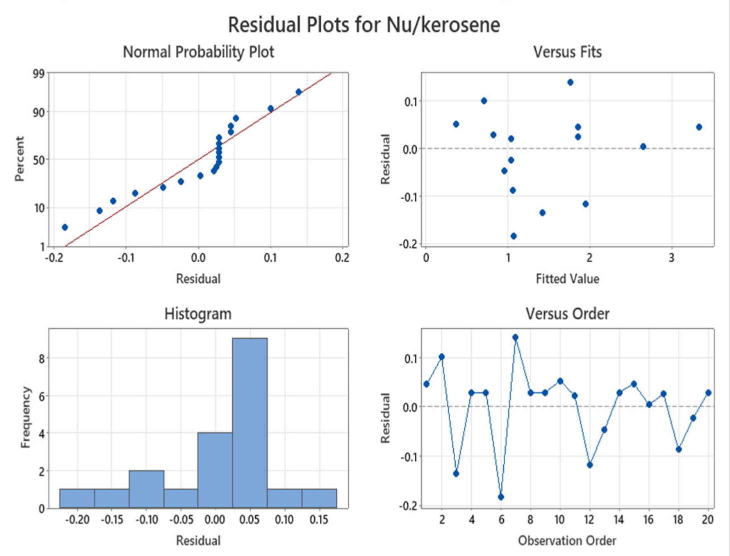

Figure 19. The Nusselt number residual plots for the kerosene as a base fluid.

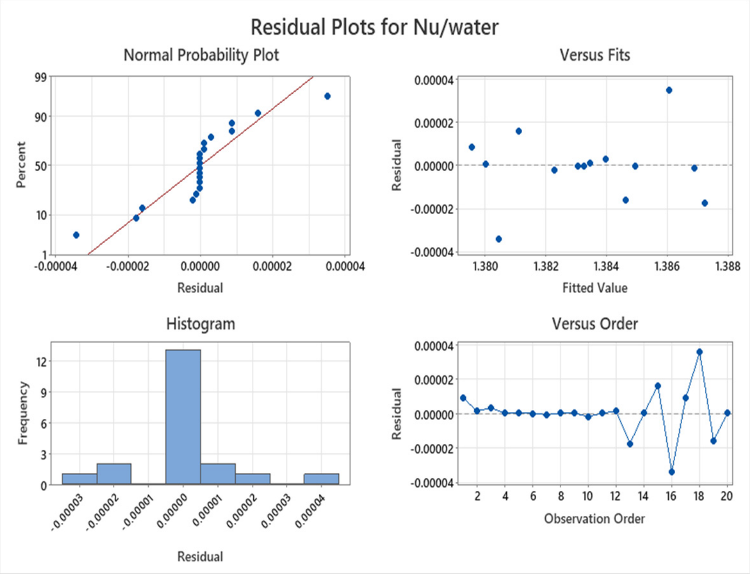

Figure 20. The Nusselt number residual plots for the water as a base fluid.

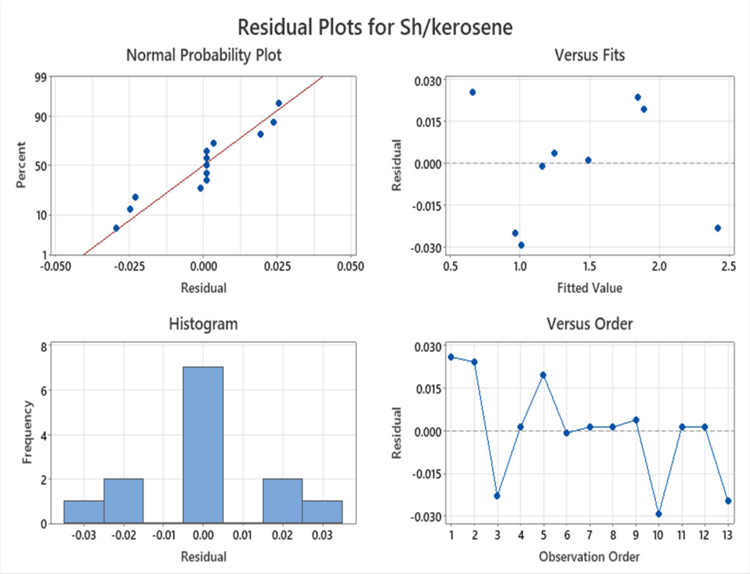

Figure 21. The Sherwood number residual plots for the kerosene as a base fluid

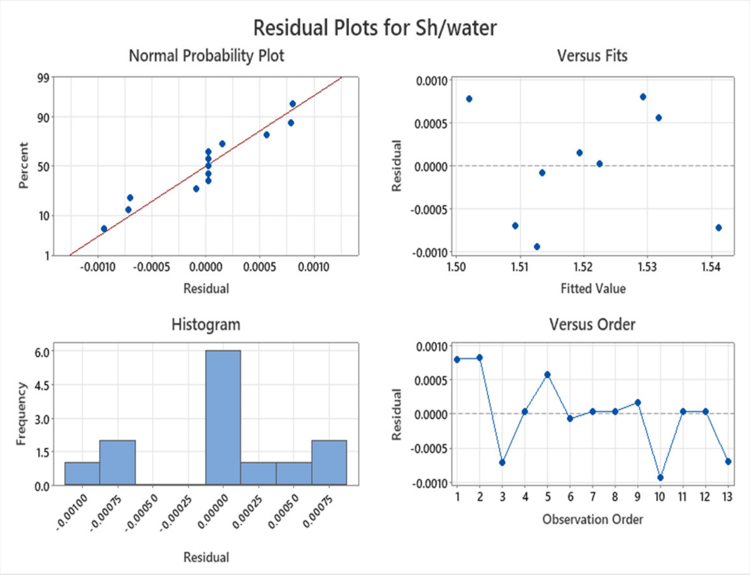

Figure 22. The Sherwood number residual plots for water as a base fluid

The constructed regression models for each response are represented by Equations (21), (25), and (29) in Response Surface Methodology (RSM). Equations (23) and (24) reflect the skin friction regression model, Equations (26) and (27) the Nusselt number model, and Equations (30) and (31) the Sherwood number model. When a word has a statistically significant impact on the answer and its p-value is less than 0.05, it is deemed significant. On the other hand, if a term's p-value is higher than 0.05, it is considered inconsequential and may be the result of random fluctuation. According to the study, several variables in Equations (24) and (28), which represent the skin friction and the Nusselt number, are deemed inconsequential since their p-values are more than 0.05. All factors in the Sherwood number regression model, however, are statistically significant because all p-values are less than 0.05.

Grid Convergence Analysis

To assess the numerical accuracy of this approach, a mesh sensitivity analysis was performed. Figure 23(a) and (b) show the results, with supporting data in **Tables 13a and 13b** for water- and kerosene-based fluids. The computational domain was divided using different grid sizes, and the skin-friction coefficient, Nusselt number, and Sherwood number were calculated. Increasing the number of grid points has very little effect on the calculated values. Changes in Cf, Nu, and Sh are almost unnoticeable once the grid size reaches a moderate level, indicating that making the grid even finer does not change the results. The small differences between grids are confined to the higher decimal places, indicating strong numerical consistency. The graphs in Figure 23(a) and (b) support this finding, as all profiles look almost unchanged with finer grids. This shows that the chosen numerical method yields stable, reliable results for both base fluids. Therefore, a grid size of N = 100 is sufficient to capture the main physics of the problem while keeping the calculations efficient.

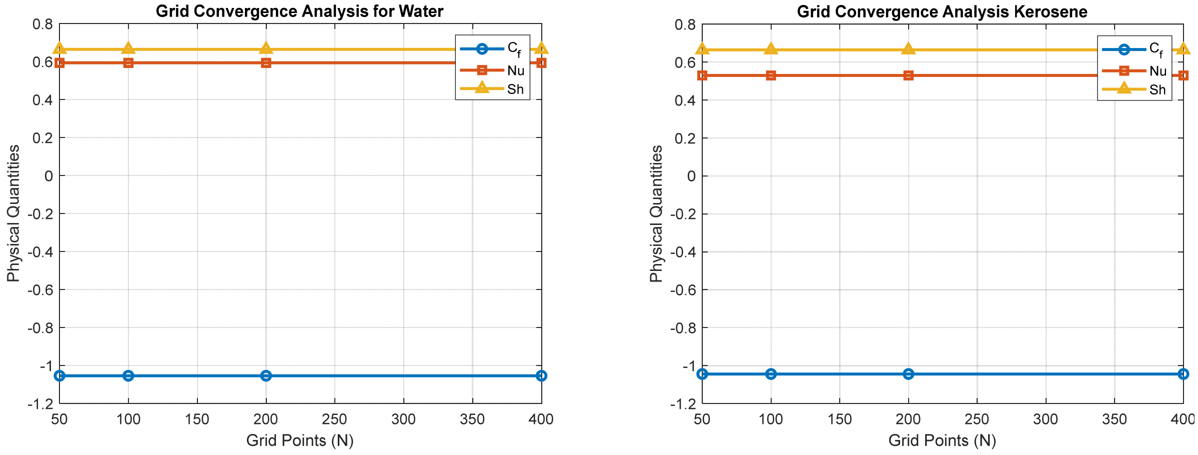

(a) (b)

Figure 23. Grid convergence of Cf, Nu, and Sh for (a) water and (b) kerosene base fluids

Table 13a. Grid convergence results for water-based fluid.

N	*Cf*	*Nu*	*Sh*
50	-1.05421	0.59247	0.66336
100	-1.05421	0.59247	0.66336
200	-1.05421	0.59247	0.66336
400	-1.05421	0.59247	0.66336

Table 13b. Grid convergence results for kerosene base fluid.

N	*Cf*	*Nu*	*Sh*
50	-1.05421	0.59247	0.66336
100	-1.05421	0.59247	0.66336
200	-1.05421	0.59247	0.66336
400	-1.05421	0.59247	0.66336

CONCLUSIONS

This study delves into the numerical analysis of the interaction between hybrid flow ($Al_2O_3 + Co$ /kerosene+water) over a two-dimensional stretching in an imposed magnetic field with the non-Newtonian fluid. This research holds great consequences in hybrid nanofluids, such as kerosene and water, as base fluids. This investigation yields the following noteworthy findings:

- A rise in the M parameter reduces the corresponding $f'(\eta)$ due to the resistance force.
- The Casson fluid parameter decelerates the velocity of the HNF very fast in water compared to kerosene as a base fluid over a stretching sheet.

- The thermal Grashof number (Gr) enhances the $f'(\eta)$ of the fluid in kerosene.
- The heat source and Eckert number escalate water's thermal boundary layer thickness as a base fluid due to the hybrid nano fluid thermal conductivity.
- In the $Al_2O_3 + Co$ /water boosts the radiation parameter, speeds up heat transfer by convection, and raises the suction value, enhancing fluid flow.
- The Casson parameter increases the friction factor rate in a hybrid nanofluid.
- The $\phi(\eta)$ decline significantly as Kr increases due to increased reaction rate.

List of symbols

B_0	Magnetic field strength (A/m)	B_{i1}	Thermal Biot number
Ec	Eckert number	B_{i2}	Concentration Biot-number
Rd	thermal radiation	Gr	Thermal Grashof number
q_r	radiation heat flux	Gm	Mass Grashof number
K	Porosity/permeability	u_w	surface velocity(m/s)
M	magnetic parameter	f	base fluids
Re	Reynold number	nf	nanofluids
Nu_x	Nusselt number	hnf	hybrid nanofluids
x	stream-wise coordinate	k^*	Rosseland approximation
Cf_x	Skin friction coefficient	T_∞	ambient temperature (K)
Sh_x	Sherwood number	$f(\eta)$	dimensionless stream function $f(\eta)$
y	transverse coordinate	$f'(\eta)$	velocity
Q	constant heat generation	η	Dimensionless similarity variable
Sc	Schmidt number	w	surface conditions (near wall)
Kr	Chemical reaction parameter	∞	free stream conditions(ambient)

Data availability

The research reported in the paper did not use any data.

Acknowledgement

I sincerely thank Prof. S. Vijay Kumar Varma for their valuable guidance and constant support throughout this research work.

ORCID

Esara Sivasankar, https://orcid.org/0009-0004-7463-4708; **S. Vijaya Kumar Varma,** https://orcid.org/0000-0002-9757-9316; **M. Sreedhar Babu,** https://orcid.org/0000-0001-9880-6253

REFERENCES

[1] L.J. Crane, Z. Angew. Math. Phys. **21**, 645 (1970). https://doi.org/10.1007/BF01587695

[2] N.S. Khashi'ie, N.M. Arifin, R. Nazar, E.H. Hafidzuddin, N. Wahi, and I. Pop, Chin. J. Phys. **64**, 251 (2020). https://doi.org/10.1016/j.cjph.2019.11.008

[3] M. Shoaib, M.A.Z. Raja, M.T. Sabir, S. Islam, Z. Shah, P. Kumam, and H. Alrabaiah, Sci. Rep. **10**, 18533 (2020). https://doi.org/10.1038/s41598-020-75254-8

[4] P. Sreedevi, P. Sudarsana Reddy, and A. Chamkha, SN Appl. Sci. **2**, 1222 (2020). https://doi.org/10.1007/s42452-020-3017-7

[5] I. Waini, A. Ishak, and I. Pop, Appl. Math. Mech. **41**, 507 (2020). https://doi.org/10.1007/s10483-020-2584-7

[6] M. Santhi, K.V.S. Rao, P.S. Reddy, and P. Sreedevi, Heat Transfer **50**, 2929 (2021). https://doi.org/10.1002/htj.22047

[7] S. Dinarvand, M. Yousefi, and A. Chamkha, J. Appl. Comput. Mech. **8**, 11 (2022). https://doi.org/10.22055/JACM.2021.37057.2938

[8] I. Haq, M.F. Yassen, M.E. Ghoneim, M. Bilal, A. Ali, and W. Weera, Symmetry **14**, 1759 (2022). https://doi.org/10.3390/sym14091759

[9] S.A.A. Shah, N.A. Ahammad, E.M.T.E. Din, F. Gamaoun, A.U. Awan, and B. Ali, Nanomaterials **12**, 2174 (2022). https://doi.org/10.3390/nano12132174

[10] S. Elattar, M.M. Helmi, M.A. Elkotb, M.A. El-Shorbagy, A. Abdelrahman, M. Bilal, and A. Ali, Alexandria Eng. J. **61**, 10319 (2023). https://doi.org/10.1016/j.aej.2022.12.013

[11] U. Farooq, A. Jan, and M. Hussain, ZAMM, **104**, e202300306 (2024). https://doi.org/10.1002/zamm.202300306

[12] K. Bhattacharyya, Front. Heat Mass Transf. **4**, 023003 (2013). https://doi.org/10.5098/hmt.v4.2.3003

[13] E. H. Aly and I. Pop, Powder Technol. **367**, 192 (2020). https://doi.org/10.1016/j.powtec.2020.03.026

[14] A. Jamaludin, K. Naganthran, R. Nazar, and I. Pop, Eur. J. Mech. B Fluids **84**, 71 (2020). https://doi.org/10.1016/j.euromechflu.2020.07.003

[15] S. Nandi, B. Kumbhakar, and G. S. Seth, Chin. J. Phys. **77**, 2090 (2022). https://doi.org/10.1016/j.cjph.2022.03.004

[16] A. Rashid, M. Ayaz, S. Islam, A. Saeed, P. Kumam, and P. Suttiarporn, S. Afr. J. Chem. Eng. **42**, 255 (2022). https://doi.org/10.1016/j.sajce.2022.07.009

[17] U. Khan, A. Zaib, A. Ishak, N. C. Roy, S. A. Bakar, T. Muhammad, A. H. Abdel-Aty, and I. S. Yahia, Eur. Phys. J. Spec. Top. **231**, 1195 (2022). https://doi.org/10.1140/epjs/s11734-022-00482-3
[18] S.E. Ghasemi, S. Mohsenian, S. Gouran, and A. Zolfagharian, Results Phys. **32**, 105141 (2022). https://doi.org/10.1016/j.rinp.2021.105141
[19] K. Ali, S. Ahmad, K.S. Nisar, A.A. Faridi, and M. Ashraf, Int. J. Energy Res. **45**, 1 (2021). https://doi.org/10.1002/er.6572
[20] N. A. Zainal, R. Nazar, K. Naganthran, and I. Pop, Neural Comput. Appl. **33**, 11285 (2021). https://doi.org/10.1007/s00521-020-05613-z
[21] T.S. Neethu, A.S. Sabu, A. Mathew, A. Wakif, and S. Areekara, Int. Commun. Heat Mass Transf. **135**, 106115 (2022). https://doi.org/10.1016/j.icheatmasstransfer.2022.106115
[22] S. Nadeem, R.U. Haq, and N.S. Akbar, IEEE Trans. Nanotechnol. **13**, 109 (2014). https://doi.org/10.1109/TNANO.2013.2293735
[23] J. Qing, M.M. Bhatti, M.A. Abbas, M.M. Rashidi, and M.S. Ali, Entropy **18**,123 (2016). https://doi.org/10.3390/e18040123
[24] K.A. Khan, A.R. Butt, and N. Raza, Results Phys. **8**, 610 (2018). https://doi.org/10.1016/j.rinp.2017.12.024
[25] S.M. Abo-Dahab, M.A. Abdelhafez, F. Mebarek-Oudina, and S.M. Bilal, Indian J. Phys. **95**, 2703 (2021). https://doi.org/10.1007/s12648-020-01961-7
[26] N. Hameed, S. Noeiaghdam, W. Khan, B. Pimpunchat, U. Fernandez-Gamiz, M.S. Khan, and A. Rehman, Results Eng. **16**, 100601 (2022). https://doi.org/10.1016/j.rineng.2022.100601
[27] R. Meenakumari, P. Lakshminarayana, K. Vajravelu, and G. Sucharitha, Numer. Heat Transf. A, **83**, 1 (2023). https://doi.org/10.1080/10407782.2023.2175289
[28] R.C.S. Reddy and G. Ramasekhar, East Eur. J. Phys. (4), 286 (2023). https://doi.org/10.26565/2312-4334-2023-4-29
[29] T.N. Tanuja, L. Kavitha, K.U. Rehman, S.V.K. Varma, G.V. Kumar, and Z. Asghar, Int. J. Thermofluids **26**, 101089 (2025). https://doi.org/10.1016/j.ijft.2024.101089
[30] A. Divya, and P.B.A. Reddy, Proc. IMechE Part E, **237**, 196 (2023). https://doi.org/10.1177/09544089221143566
[31] S. Manjunatha, J.S. Kumar, K.U. Rehman, W. Shatanawi, and S.V.K. Varma, Int. J. Thermofluids **26**, 101130 (2025). https://doi.org/10.1016/j.ijft.2024.101130
[32] R. Manaswini, B.N. Hanumagowda, T.N. Tanuja, L. Kavitha, A. Abdulrahman, R.J. Punith Gowda, and S.V.K. Varma, Mod. Phys. Lett. B, **39**(07), 2450420 (2025). https://doi.org/10.1142/S0217984924504207

АНАЛІЗ ТЕРМОМАГНІТНОГО ПОТОКУ ГІБРИДНОЇ НАНОРІДИНИ КАССОНА ЧЕРЕЗ ПОРИСТИЙ ЛИСТ ЩО РОЗТЯГУЄТЬСЯ З ВРАХУВАННЯМ ХІМІЧНОЇ РЕАКЦІЇ З ВИКОРИСТАННЯМ RSM

Есара Сівасанкар[1], М. Срідхар Бабу[1], С. Віджая Кумар Варма[2]
[1]Кафедра прикладної математики, Університет Йогі Вемана, Кадапа, Андхра-Прадеш, 516005, Індія
[2]Кафедра математики, Школа прикладних наук, Дослідницький центр REVA, Університет REVA,
Бенгалуру, Карнатака, 560064, Індія

Термофізичний аналіз тепло- та масопередачі має багато потенційних застосувань у сонячних колекторах, хімічних реакторах, медичних пристроях та складних системах охолодження, серед інших застосувань. Завдяки цьому стимулу, у цій роботі часто використовується методологія поверхні відгуку для аналізу тепло- та масопередачі гібридної нанорідини Кассона над проникним розтягуваним листом з конвективними та радіаційними ефектами. Система керування диференціальними рівняннями в похідних похідних, що визначають розроблену модель, перетворюється на зв'язаний набір нелінійних диференціальних рівнянь шляхом застосування відповідних перетворень подібності. Метод стрільби, реалізований за допомогою розв'язувача BVP4c у MATLAB, використовується для чисельного інтегрування цих спрощених рівнянь. Використовуючи табличні дані та графічні представлення, систематично досліджується вплив відповідних фізичних параметрів на розподіли швидкості, температури та концентрації. Крім того, методологія поверхні відгуку використовується для статистичної оцінки ключових змінних відгуку в широкому діапазоні визначальних параметрів, таких як коефіцієнт поверхневого тертя, тепло- та масопередачі. Результати показують, що збільшення параметра Кассона зменшує температурний профіль, оскільки ефективна границя текучості рідини зменшується. Крім того, через збільшення сил Лоренца, сильніше магнітне поле значно зменшує швидкість рідини. Крім того, було помічено, що збільшення об'ємної частки твердої речовини підвищує температуру нанорідини через підвищену теплопровідність. Статистичний аналіз показує, що точність масопередачі для отриманої математичної моделі в гасі становить 99,85%.

Ключові слова: *гібридна нанорідина Кассона; МГД; пористий розтягуваний лист; хімічна реакція; метод відгуку поверхні (RSM)*

EAST EUROPEAN JOURNAL OF PHYSICS. **2.** 319-331 (2026)
DOI:10.26565/2312-4334-2026-2-33 ISSN 2312-4334

MHD DUCT FLOW OF NANOFLUID INFLUENCED BY A DUAL HEAT SOURCE IN THE PRESENCE OF AN ELECTRIC FIELD (E_o) AND A MAGNETIC FIELD (B_o)

Bishnu Ram Das[1], Hirak Jyoti Dehingia[2], Kaushik Dehingia[3,4], Rupjyoti Borah[5], Utpal Saikia[6]
[1]Department of Mathematics, BCM College, Kamrup-781102, Assam, India
[2]Department of Basic Science and Humanities, DUIET, Dibrugarh University, Dibrugarh, Assam, India, 786004
[3]Department of Mathematics, Sonari College, Charaideo, Assam, India, 785690
[4]Research Center of Applied Mathematics, Khazar University, Baku, Azerbaijan, AZ1096
[5]Department of Mathematics, Tingkhong College, Tingkhong-786612, Dibrugarh, Assam, India
[6]Department of Mathematics, Golaghat Polytechnic, 785610, Furkating, Golaghat, Assam, India
Corresponding Author email: hirakjyotidehingia11@gmail.com

Received February 11, 2026; revised April 26, 2026; accepted May 8, 2026

The flow of copper (Cu), silver (Ag), titanium oxide (TiO_2), copper oxide (CuO) nanoparticles with water as a base fluid in the presence of a high magnetic field in a vertical rectangular duct are examined in this research. The duct's left and right walls are kept at various steady temperatures and concentrations. The temperature, velocity, and nanoparticle concentration fields are all described by the transport equations. The second-order upwind method, an explicit finite-difference method (EFDM), is used to discretize the coupled nonlinear Navier-Stokes equations. To examine the heat transfer efficiency of this nanofluid, we nondimensionalized the governing equations and obtained solutions using an explicit numerical scheme. MATLAB code is used to perform computational steps. We have plotted the velocity, temperature, and concentration fields for different values of the magnetohydrodynamic (MHD) flow parameters, including the thermal Grashof number (G_r), solutal Grashof number (G_c), Hartmann number (H_a), electrical field load parameter (E), Brinkman number (B_r), and nanoparticle volume fraction (ϕ).

Keywords: *Electrical field; Magnetic field; Nanofluids; Nonlinear; Explicit finite difference technique (EFDT); Rectangular vertical duct; MHD flow; Buoyancy force; Viscous flow*
PACS: 44.20.+b, 44.40.+a, 44.30.+v, 47.11.-j, 47.11.Bc

1. INTRODUCTION

Smooth restraint of convective transport phenomena is a significant challenge across diverse fields of engineering, and biomedical devices that absorb magneto-hydrodynamics (MHD) coupled with Multiphysics. MHD convective transport has broad applications in industry and engineering and is advancing rapidly in medical sciences. Thermal aspects are closely connected to bio-heat and thermal treatment in various tumors. Targeted drug delivery, imaging, and the use of nanoparticles during chemotherapy are well-established. MHD convection is widely used in biomedical technology for magnetic endoscopy, cell separation, tumor treatment and cancer therapy, targeted drug delivery in the body, blood flow control during medical surgery, control of gastrointestinal disorders, transport of complex bio-waste fluids, etc. Adding nanoparticles into the base fluid is an innovative way to enhance heat transfer. The resulting mixture of base fluid and nanoparticles, which has unique physical and chemical properties, is referred to as a nanofluid. Nanofluids exhibit better suspension stability, Newtonian behavior, and enhanced thermal conductivity, and the chaotic motion of nanoparticles is responsible for the enhancement of heat transfer. In natural convection studies, the base fluid has low thermal conductivity, limiting heat transfer enhancement. Researchers applied the innovative technique using nanofluids with higher conductivities to enhance heat transfer. Firstly, Choi studied nanoparticles in 1995 and the base fluid [1, 2] at the Argonne National Laboratory in the U.S.A. After that, the idea has been extended [3] to incorporate an additive nanoparticle into a base fluid to increase the thermal conductivity of the interruption. Many authors [4-6] have reported that thermal conductivity can be enhanced by about 20% at very low volume fractions (1-5%). Thermal conductivity of copper-water nanofluid up to 7.5% of nanoparticle volume fraction empirically determined by Xuan *et al.* [6]. Many authors [7-12] have studied the increase in heat transfer with nanofluids. Tavman *et al.* [13] reported in 2010 a considerable increase in the viscosity of a nanofluid containing aluminum oxide, titanium oxide, and silicon oxide nanoparticles in water. As in the Einstein representation [14], they also show that the traditional verifiable hypothesis, that intellectual investigation of specific heats is minimal for nanofluids, is also true. Namburu [15] in 2009 studied that ethylene glycol-based nanofluids demonstrated lower specific heat than their individual base fluids. Likewise, Bergman [16] confirmed that a water-based aluminum oxide nanofluid exhibited increased thermal conductivity, but only when the specific heat was lower than that of the base fluid. Magnetohydrodynamics (MHD) plays a significant role in nanofluid flow, owing to its expanding industrial applications and use in reactor cooling analysis. Younsi [17] has studied double heat-source magnetohydrodynamics (MHD), which is essential for the material-freezing process. Sharma and Singh [18] and Vadher et al. [19] investigated electrically conducting fluid oiling, the concept of coating synthesis, the salvation of liquefied metals, and active, etc.

Several authors have studied magnetohydrodynamic (MHD) flows and heat transfer in rectangular ducts. In an earlier numerical study [20], the characteristics of different metallic nanofluids with cooling provided by a constant-

---

Cite as: B.R. Das, H.J. Dehingia, K. Dehingia, R. Borah, U. Saikia, East Eur. J. Phys. 2, 319 (2026), https://doi.org/10.26565/2312-4334-2026-2-33

temperature wall were studied. In another study, Ellahi *et al.* [21] considered a water-based nanofluid with Al_2O_3. To study the aggregation effect on such a nanofluid, Hamad [22] investigated the analytical solution for natural convection flow of a nanofluid over a similar drawing out in the presence of a magnetic field. Mixed convection of Casson nanofluid over a stretching sheet with convectively heated heat source/sink and chemical reaction observed by Hayat *et al.* [23]. Kameswaran *et al.* [24] studied hydromagnetic nanofluid flow owing to a stretching or shrinking sheet. Boundary layer flow of a nanofluid past a stretching sheet with a convective boundary condition studied by Makinde and Aziz [25]. Beg *et al.* [26] investigated the calculation of thermo-solutal convection with Soret-Dufour cross-diffusion in a vertical duct filled with metallic/carbon nanofluids. Nadeem *et al.* [27] studied the magnetohydrodynamic (MHD) three-dimensional layer flow of a Casson nanofluid past a linearly stretching sheet with convective boundary conditions. Abu-Nada and Oztop [28] have numerically investigated free convection in a partially heated rectangular duct saturated with nanofluids. Rashidi *et al.* [29] studied the buoyancy effect on magnetohydrodynamic (MHD) flow of a nanofluid over a stretching sheet in the presence of thermal radiation. Simulation of magnetohydrodynamics (MHD) convective heat transfer and copper-oxide/water nanofluid flow considering Lorentz forces discussed by Sheikholeslami *et al.* [30]. Turkyilmanzoglu [31] has examined the natural convection flow past an impulsive, radiative vertical plate. Very recently [32], Rao and Deka studied the transport phenomena in a nanofluid under the action of a transverse magnetic field. In a vertical square rectangular duct, Das *et al.* [33] numerically investigated the magnetohydrodynamics (MHD) miscellaneous displacement flow of $\mathrm{Al_2O_3}-$ water nanofluids. Many authors who have recently studied the heat transfer nanofluid boundary-layer problem are listed in the reference [34-36].

The goal of our present work is to investigate the flow of copper (Cu), Silver (Ag), Titanium oxide (TiO_2), and Copper oxide (CuO) nanoparticles with water (H_2O) in a rectangular vertical duct, the non-dimensional conservation equations are strongly nonlinear and are solved numerically. Appropriate values of the flow parameters are considered for investigation. The numerical results are presented graphically, including velocity, temperature, concentration, and flow parameters. Utilize the MATLAB code estimation procedure to implement.

Table 1. Thermo-physical numerical values of water (H_2O) and nanoparticles copper (Cu), silver (Ag), titanium oxide (TiO_2), and copper oxide (CuO)

Nanoparticle/base fluid	Density (ρ)	Specific heat capacity (C_p)	Thermal conductivity (k)	Electrical conductivity (σ)
H_2O	997.1	4179	0.613	5.5×10^{-6}
Cu	8933	385	401	59.6×10^{6}
Ag	10490	235	429	6.30×10^{7}
TiO_2	4250	686.2	8.9528	2.58×10^{-7}
CuO	6310	530	20	10^{-5}

2. MATHEMATICAL FORMULATION

In this model, we have considered a laminar steady flow of incompressible fluid through a duct which is vertically positioned, and the $Z-$axis of the reference frame is along the duct $Y-$axis, taken along the magnetic field B_0, is sufficiently strong and acting normally on the surface of the duct, and the $X-$axis taken along the electrical field E_o. The model of the present problem is shown in Fig. 1. $\vec{g}$ is the gravitational acceleration, acting downward. The heat source for the flow is taken to be the left duct wall, which is maintained at a constant temperature T_1 with concentration C_1. Similarly, the other heat source is taken as the right duct wall, which is kept at a constant temperature, T_2 on C_2. The right fence is hotter than the left wall, so in this case, $C_2 > C_1$. Here, we have considered prime a to be the length and prime b to be the breadth of the vertical rectangular duct. The well-known Boussinesq approximation is adopted. To get convergent solutions, the Successive-Over-Relaxation (SOR) method, along with the Gauss-Seidel method, was implemented to solve the reduced difference equations.

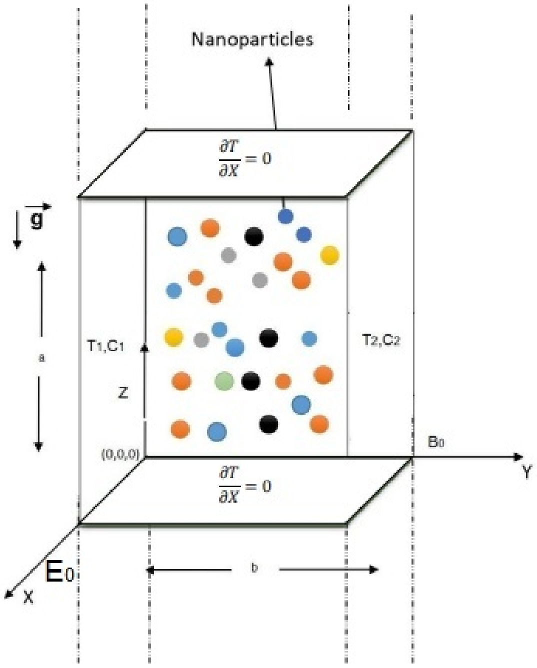

Figure 1. Schematic diagram of the problem

The following assumptions are made in this study:

- Laminar steady flow of incompressible fluid through a duct.
- The flow field is exhibited through the Velocity profile in the mesh (x, y, v); Temperature profile in mesh (x, y, T) and the concentration profile in the mesh (x, y, c) for copper nanoparticles.

Governing equations

Equation of continuity:

$$\nabla \cdot \vec{V} = 0. \tag{1}$$

MHD momentum equation:

$$\rho_{nf}\left[\left(\vec{V}\cdot\nabla\right)\vec{V}\right] = \mu_{nf}\nabla^2\vec{V} + \vec{g}(\rho\beta)_{nf}(T - T_o) + \vec{g}(\rho\beta)_{nf}(C - C_o) + \left(\vec{J}\times\vec{B}\right) + \sigma_{nf}B_o^2E_o. \tag{2}$$

Energy equation:

$$\left(\rho C_p\right)_{nf}\left[\left(\vec{V}\cdot\nabla\right)T\right] = k_{nf}\nabla^2T + \mu_{nf}\phi + \left(\frac{D_mK_T}{C_sC_p}\right)\nabla^2T + \sigma_{nf}B_o^2E_o^2 - \sigma_{nf}B_o^2\vec{V} + 2\sigma_{nf}B_o^2E_o\,\vec{V}. \tag{3}$$

Concentration equation:

$$\left(\vec{V}\cdot\nabla\right)C = \mathrm{D_m}\nabla^2C + \frac{K_T}{T_m}\nabla^2T. \tag{4}$$

We know that the body force term corresponding to a magnetohydrodynamics (MHD) flow is the Lorentz force $\left(\vec{J}\times\vec{B}\right)$, and this Lorentz force by Hussanan *et al.* [37] becomes

$$\left(\vec{J}\times\vec{B}\right) = -\sigma_{nf}B_o^2\,\vec{V}. \tag{5}$$

Here σ_{nf} is the nanofluid electrical conductivity, B_o is the assessed magnetic field, and the velocity vector V. We know that the dynamic viscosity of nanofluid, effective density of nanofluid, thermal expansion coefficient of nanofluid, heat capacity of nanofluid, thermal diffusivity, and thermal conductivity of nanofluid are:

$$\mu_{nf} = \frac{\mu_f}{(1-\phi)^{2.5}}, \tag{6}$$

$$\rho_{nf} = (1-\phi)\rho_f + \phi\rho_s = \left(1 - \phi + \phi\,\frac{\rho_s}{\rho_f}\right)\rho_f, \tag{7}$$

$$(\rho\beta)_{nf} = (1-\phi)(\rho\beta)_f + \phi(\rho\beta)_s = \left(1 - \phi + \phi\frac{(\rho\beta)_s}{(\rho\beta)_f}\right)(\rho\beta)_f, \tag{8}$$

$$\sigma_{nf} = (1-\phi)\sigma_f + \phi\sigma_s = \left(1 - \phi + \phi\frac{\sigma_s}{\sigma_f}\right)\sigma_f \tag{9}$$

$$\left(\rho C_p\right)_{nf} = (1-\phi)\left(\rho C_p\right)_f + \phi\left(\rho C_p\right)_s = \left(1 - \phi + \phi\frac{\left(\rho C_p\right)_s}{\left(\rho C_p\right)_f}\right)\left(\rho C_p\right)_f, \tag{10}$$

$$\alpha_{nf} = \frac{K_{nf}}{\left(\rho C_p\right)_{nf}}, \tag{11}$$

$$k_{nf} = \left[\frac{k_s + 2k_f - 2\phi(k_f - k_s)}{k_s + 2k_f + \phi(k_f - k_s)}\right]k_f. \tag{12}$$

Now, according to Newton's law of viscosity, according to Fourier's law of heat conduction, and also according to Fick's law of species diffusion, can be reduced as [2]

$$\frac{1}{(1-\phi)^{2.5}}\,\mu_f\left[\frac{\partial^2V}{\partial X^2} + \frac{\partial^2V}{\partial Y^2}\right] + \left[1 - \phi + \phi\frac{(\rho\beta)_s}{(\rho\beta)_f}\right]g\rho_f\,\beta_f(T - T_o) + \left[1 - \phi + \phi\frac{(\rho\beta)_s}{(\rho\beta)_f}\right]g\rho_f\,\beta_f(C - C_o) - \left[1 - \phi + \phi\frac{\sigma_s}{\sigma_f}\right]\sigma_fB_o^2V + \left[1 - \phi + \phi\frac{\sigma_s}{\sigma_f}\right]\sigma_fB_o^2E_o = 0, \tag{13}$$

$$\left[\frac{k_s + 2k_f - 2\phi(k_f - k_s)}{k_s + 2k_f + \phi(k_f - k_s)}\right]k_f\left[\frac{\partial^2T}{\partial X^2} + \frac{\partial^2T}{\partial Y^2}\right] + \frac{1}{(1-\phi)^{2.5}}\,\mu_f\left[\left(\frac{\partial V}{\partial X}\right)^2 + \left(\frac{\partial V}{\partial Y}\right)^2\right] + \frac{D_mK_T}{C_SC_P}\left[\frac{\partial^2C}{\partial X^2} + \frac{\partial^2C}{\partial Y^2}\right] + \left[1 - \phi + \phi\frac{\sigma_s}{\sigma_f}\right]\sigma_fB_o^2E_o^2 + \left[1 - \phi + \phi\frac{\sigma_s}{\sigma_f}\right]\sigma_fB_o^2V^2 - 2\left[1 - \phi + \phi\frac{\sigma_s}{\sigma_f}\right]\sigma_fB_o^2E_oV = 0, \tag{14}$$

$$D_m\left[\frac{\partial^2C}{\partial X^2} + \frac{\partial^2C}{\partial Y^2}\right] + \frac{K_T}{T_m}\left[\frac{\partial^2T}{\partial X^2} + \frac{\partial^2T}{\partial Y^2}\right] = 0. \tag{15}$$

Equations (13), (14), and (15) are solved employing the following boundary conditions:

$$V = 0, T = T_1, C = C_1 \; at \; Y = 0 \; for \; 0 \le X \le b,$$

$$V = 0, T = T_2, C = C_2 \; at \; Y = a \; for \; 0 \le X \le b,$$

$$V = 0, \frac{\partial T}{\partial X} = 0, \frac{\partial C}{\partial X} = 0 \; at \; X = 0 \; for \; 0 \leq Y \leq a,$$

$$V = 0, \frac{\partial T}{\partial X} = 0, \frac{\partial C}{\partial X} = 0 \; at \; X = b \; for \; 0 \leq Y \leq a. \tag{16}$$

The dimensionless variables are given below:

$$x = \frac{X}{a}, y = \frac{Y}{a}, v = \frac{V\rho_f a}{\mu_f}, \theta = \frac{T - T_o}{T_2 - T_1}, c = \frac{C - C_o}{C_2 - C_1}, T_o = \frac{T_1 + T_2}{2}, C_o = \frac{C_1 + C_2}{2}, A = \frac{b}{a}. \tag{17}$$

Now given in equation (17), employed in the governing equations (13), (14), and (15), and after solving, we have

$$\left[\frac{\partial^2 v}{\partial x^2} + \frac{\partial^2 v}{\partial y^2}\right] + A_1\theta + A_2 c - A_3 v + A_4 = 0, \tag{18}$$

$$\left[\frac{\partial^2 \theta}{\partial x^2} + \frac{\partial^2 \theta}{\partial y^2}\right] + A_5\left[\left(\frac{\partial v}{\partial x}\right)^2 + \left(\frac{\partial v}{\partial y}\right)^2\right] + A_6\left[\frac{\partial^2 c}{\partial x^2} + \frac{\partial^2 c}{\partial y^2}\right] + A_7(E - v)^2 = 0, \tag{19}$$

$$\left[\frac{\partial^2 c}{\partial x^2} + \frac{\partial^2 c}{\partial y^2}\right] + A_8\left(\frac{\partial^2 \theta}{\partial x^2} + \frac{\partial^2 \theta}{\partial y^2}\right) = 0. \tag{20}$$

where $G_r = \frac{g\rho_f^2\beta_f(T_2 - T_1)a^3}{\mu_f^2}$ is the thermal Grashof number, which is the ratio of thermal buoyancy force to viscous force, $G_c = \frac{g\rho_f^2\beta_f(C_2 - C_1)a^3}{\mu_f^2}$ is the solutal Grashof number, which is the ratio of species buoyancy force to the viscous hydrodynamic force, $H_a = B_o a\sqrt{\frac{\sigma_f}{\mu_f}}$ is the Hartmann number, which is the proportion of electromagnetic force to viscous force, $E = E_o\frac{\rho_f a}{\mu_f}$ is the electrical field load parameter, $B_r = \frac{\mu_f^3}{k_f\rho_f^2(T_2 - T_1)a^2}$ is the Brinkman number, and $D_f = \frac{D_m K_T(C_2 - C_1)}{\nu_f C_s C_p(T_2 - T_1)}$ is the Dufour number, which is the ratio of the concentration difference to the temperature difference. Also, $P_r = \frac{\nu_f}{k_f}$ is the Prandtl number, which is the ratio of kinematic viscosity to the thermal conductivity, $S_r = \frac{K_T(T_2 - T_1)}{\nu_f T_m(C_2 - C_1)}$ is the Soret number, which is the ratio of the temperature difference to the concentration, $S_c = \frac{\nu_f}{D_m}$ is the Schmidt number, the ratio of the momentum diffusivity (kinematic viscosity) to the mass diffusivity.

The corresponding boundary conditions after introducing equation (16) give

$$v = 0, \theta = -0.5, c = -0.5 \; at \; y = 0 \; for \; 0 \leq x \leq A,$$

$$v = 0, \theta = 0.5, c = 0.5 \; at \; y = 1 \; for \; 0 \leq x \leq A,$$

$$v = 0, \frac{\partial \theta}{\partial x} = 0, \frac{\partial c}{\partial x} = 0 \; at \; x = 0 \; and \; x = A \; for \; 0 \leq y \leq 1. \tag{21}$$

Let

$$E_1 = (1 - \phi)^{2.5}, E_2 = \left(1 - \phi + \phi\frac{\rho_s}{\rho_f}\right), E_3 = \left(1 - \phi + \phi\frac{(\rho\beta)_s}{(\rho\beta)_f}\right),$$

$$E_4 = \left(1 - \phi + \phi\frac{\sigma_s}{\sigma_f}\right), E_5 = \left(1 - \phi + \phi\frac{(\rho C_p)_s}{(\rho C_p)_f}\right), E_6 = \left[\frac{k_s + 2k_f - 2\phi(k_f - k_s)}{k_s + 2k_f + \phi(k_f - k_s)}\right].$$

3. NUMERICAL TECHNIQUE AND GRID INDEPENDENCE STUDY

The system of governing equations from (18) to (20), in conjunction with the boundary conditions as defined in equations (21), is solved through the application of a finite difference method. Uniform grids (Fig. 2) are generated for the computational domain. The domain of definition is portioned uniformly into M_x and M_y divisions along the x and y axes respectively. Central differencing of second-order accuracy is employed for the first and second-order derivatives. The equations (18), (19), and (20), along with the boundary conditions given in equation (21), were discretized using the finite-difference method. We know that the finite difference is second order $\partial^2 v/\partial x^2$ and first order $\partial v/\partial x$, were discretized as $\frac{\partial^2 v}{\partial x^2} = \frac{v_{i+1,j} - 2v_{i,j} + v_{i-1,j}}{\Delta x^2} + O(\Delta x^2)$ and $\frac{\partial v}{\partial x} = \frac{v_{i+1,j} - v_{i-1,j}}{2\Delta x} + O(\Delta x^2)$, respectively. Therefore, the resultant difference equations give

$$v_{i,j} = A_9(v_{i+1,j} + v_{i-1,j}) + A_{10}\left(v_{i,j+1} + v_{i,j-1}\right) + A_{11}(T_{i,j}) + A_{12}(c_{i,j}) + A_{13}. \tag{22}$$

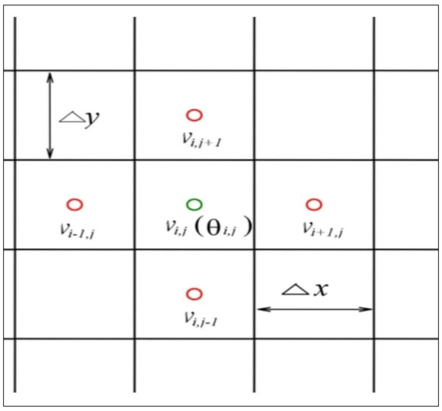

Figure 2. Uniform grid system

$$T_{i,j} = A_{14}\left(T_{i+1,j}+T_{i-1,j}\right) + A_{15}\left(T_{i,j_{+1}}+T_{i,j_{-1}}\right) + A_{16}\left(v_{i+1,j}-v_{i-1,j}\right)^2 + A_{17}\left(v_{i,j_{+1}}-v_{i,j_{-1}}\right)^2 + A_{18}\left(c_{i+1,j}-2c_{i,j}+c_{i_{-1},j}\right) + A_{19}\left(c_{i,j_{+1}}-2c_{i,j}+c_{i,j_{-1}}\right) + A_{20}\left(E - v_{i,j}\right)^2. \tag{23}$$

$$c_{i,j} = A_{14}\left(c_{i+1,j}+c_{i-1,j}\right) + A_{15}\left(c_{i,j_{+1}}+c_{i,j_{-1}}\right) + A_{21}\left(\theta_{i_{+1},j}-2\theta_{i,j}+\theta_{i-1,j}\right) + A_{22}\left(\theta_{i,j_{+1}}-2\theta_{i,j}+\theta_{i,j_{-1}}\right). \tag{24}$$

where:

$A_1 = \frac{E_3}{E_1}Gr, A_2 = \frac{E_3}{E_1}Gc, A_3 = \frac{E_4}{E_1}Ha^2, A_4 = \frac{E_4}{E_1}Ha^2E, A_5 = \frac{E_1}{E_6}Br, A_6 = \frac{1}{E_6}D_f Pr, A_7 = \frac{E_4}{E_6}BrHa^2, A_8 = SrSc, A_9 = \frac{k^2}{2(k^2+h^2+A_3h^2k^2)}, A_{10} = \frac{h^2}{2(k^2+h^2+A_3h^2k^2)}, A_{11} = \frac{A_1h^2k^2}{(k^2+h^2+A_3h^2k^2)}, A_{12} = \frac{A_2h^2k^2}{(k^2+h^2+A_3h^2k^2)}, A_{13} = \frac{A_4h^2k^2}{(k^2+h^2+A_3h^2k^2)}, A_{14} = \frac{k^2}{2(k^2+h^2)}, A_{15} = \frac{h^2}{2(k^2+h^2)}, A_{16} = A_5.\frac{k^2}{4(k^2+h^2)}, A_{17} = A_5.\frac{h^2}{4(k^2+h^2)}, A_{18} = A_6A_{14}, A_{19} = A_6A_{15}, A_{20} = \frac{A_7h^2k^2}{(k^2+h^2)}, A_{21} = A_8A_{14}, A_{22} = A_8A_{15}$ are constants. $\Delta x = h \, and \, \Delta y = k$.

Finally, we get the discretized boundary conditions:

$$v_{i,0} = -v_{i,1}, \theta_{i,0} = -1 - \theta_{i,1}, c_{i,0} = -1 - c_{i,1}$$
$$v_{i,My_{+1}} = -v_{i,My}, \theta_{i,My_{+1}} = 1 - \theta_{i,My}, c_{i,My_{+1}} = 1 - c_{i,My}$$
$$v_{0,j} = -v_{1,j}, \theta_{0,j} = \theta_{1,j}, c_{0,j} = c_{1,j}$$
$$v_{Mx_{+1},j} = -v_{Mx,j}, \theta_{Mx_{+1},j} = \theta_{Mx,j}, c_{Mx_{+1},j} = c_{Mx,j}. \tag{25}$$

Here i goes from 1 to M_x and j 1 to M_y.

4. RESULTS AND DISCUSSION

The flow of copper (Cu), silver (Ag), titanium oxide (TiO_2), and copper oxide (CuO) nanoparticles with water (H_2O) as base fluid in a vertical rectangular duct has been studied in this work. The influence of parameters like the thermal Grashof number G_r, solutal Grashof number G_c, Hartmann number H_a, nanoparticle volume fraction ϕ, electrical field load parameter E and the Brinkmann parameter B_r in a vertical rectangular duct, the velocity, temperature, and nanoparticle concentration profiles are presented graphically. In this plotting, we have employed an explicit finite-difference scheme in MATLAB. The outcomes of this work are presented in terms of the effects of different copper nanoparticles (Cu), silver (Ag), titanium oxide (TiO_2), and copper oxide (CuO), the thermal Grashof number ($0.5 \leq G_r \leq 20$), solutal Grashof number ($0.5 \leq G_c \leq 15$), electric field load parameter ($-2 \leq E \leq 2$), Brinkmann parameter ($0 \leq B_r \leq 2.5$), solid volume fraction ($0 \leq \phi \leq 0.06$) are shown in the velocity, temperature, and nanoparticle concentration profiles.

Verification of the result:

Since no directly analogous literature is accessible for this specific configuration, endorsement of the result is accomplished through physical reasoning and consistency with established magnetohydrodynamic (MHD) theory. The effects of Hartmann number, which is responsible for the application of a magnetic field on the velocity profile, are reported in Fig. 7. From this figure, it is perceived that the velocity distribution of the fluid has been diminished with the increasing values of Hartmann number (Ha). Physically, an increase in the Hartmann number intensifies the Lorentz force, which acts as a resistive drag on the fluid motion. Consequently, the fluid velocity decreases, which is consistent with classical MHD flow behavior.

We have taken $H_a = 2, A = 2.5, P_r = 6.93, R_m = 1, Ec = 0.001, h = k = 0.001, m = n = 200, \phi = 0.02, k_f = 0.613, k_s = 429, \theta = \pi/2$. We have plotted (Fig. 3, Fig. 4, and Fig. 5) the velocity profile, temperature profile, and concentration profile for various values of G_r and water-based floodplain copper nanoparticles. In these plots, we have observed that the velocity of the Cu-water nanofluid increases with the increase of G_r. With these significant values of thermal Grashof number G_r, buoyancy force control, and on the other hand, due to small values of thermal Grashof number G_r, viscosity control, i.e., profile velocity stimulated by the buoyancy force. Due to thermal buoyancy, an increase in G_r tends to produce stronger flow in the boundary layer. However, in the temperature and concentration profiles, we have noticed that they are invariant, which is mainly due to the neglect of viscous dissipation in the energy equation. We have plotted the velocity profile (Fig. 6) for different values of G_c and a water-based nanofluid employing copper nanoparticles.

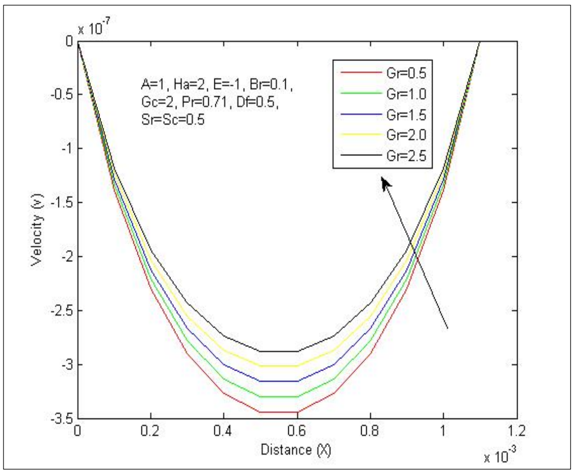

Figure 3. Variation in (v) with G_r

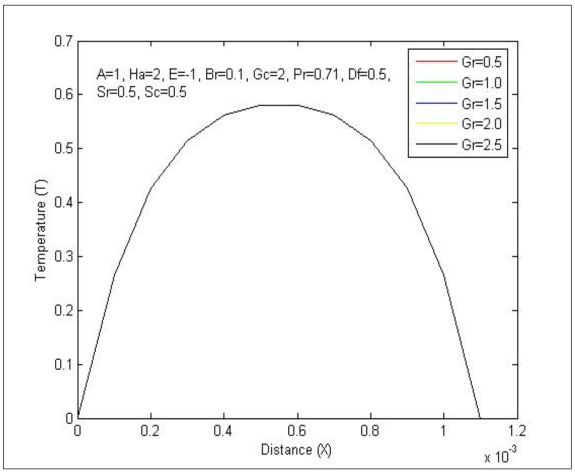

Figure 4. Variation in (T) with G_r

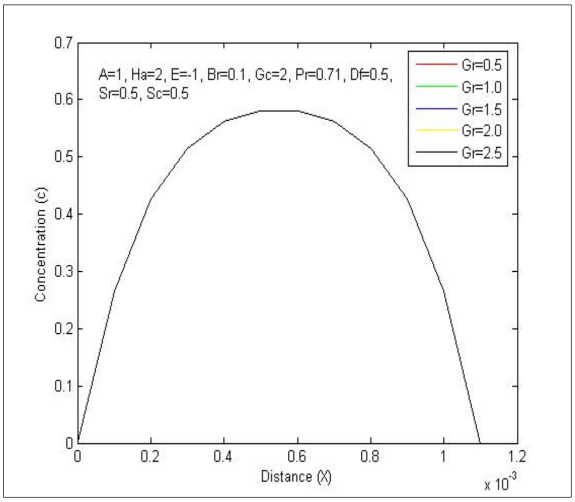

Figure 5. Variation in (c) with G_r

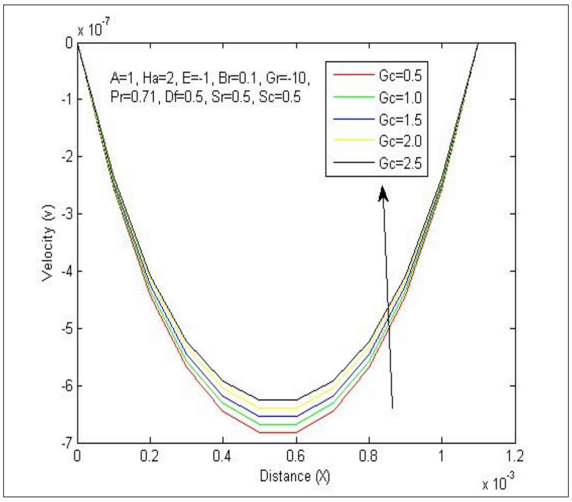

Figure 6. Variation in (v) with G_c

In these plots, we have observed that the profile velocity with copper-water nanofluid enhances due to the increase in G_c, with the most significant values of solutal Grashof number cap G_c, species hydrodynamic buoyancy force control, and on the other hand, due to small values of solutal Grashof number G_c, viscosity control. Due to the effect of thermal buoyancy, an increase in the values of G_c tends to produce a large amount of flow in the boundary layer. The temperature and concentration profiles are not displayed graphically because they exhibit topologies similar to those of the thermal Grashof number G_r. We have plotted (Fig. 7) the velocity profile in the boundary layer for distinct values of the Hartmann number H_a, and for a water-based nanofluid employing copper nanoparticles. In these plots (Fig. 7), we observe that the flow rate decreases with increasing Hartmann number H_a when copper nanoparticles are present, due to the enhanced H_a. The magnetic field introduced into the electrically conducting nanofluid, acting normal to the boundary, generates a resistive pressure force in the duct, which is part of the Lorentz force. The temperature and concentration profiles are not displayed graphically because they exhibit topologies similar to those of the thermal Grashof number G_r. We have plotted (Fig. 8) the velocity in the boundary layer for different values of nanoparticle volume fraction ϕ, using water as the base fluid and employing copper nanoparticles. In these plots, we observe that the flow rate of the nanoparticle volume fraction phi with copper nanoparticles increases as ϕ increases. The temperature and concentration profiles are not displayed graphically, as they exhibit topologies similar to those of the temperature and concentration profiles for the thermal Grashof number G_r.

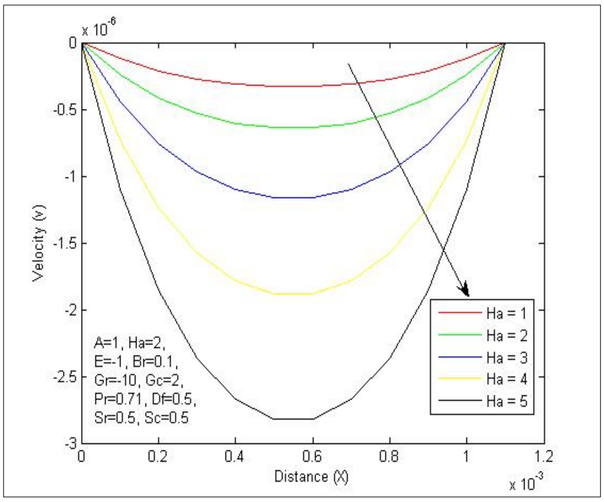

Figure 7. Variation in (v) with H_a

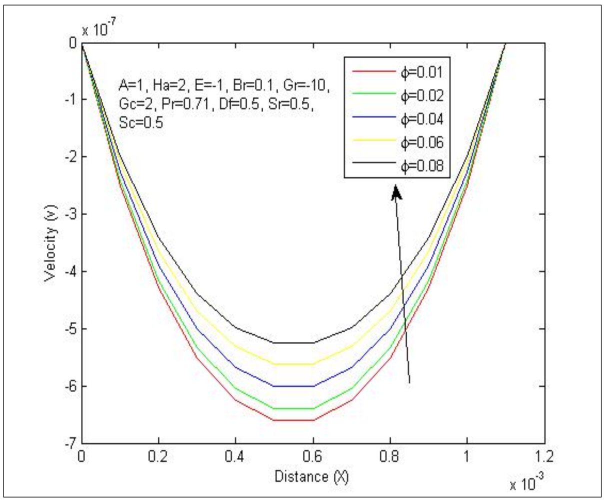

Figure 8. Variation in (v) with ϕ

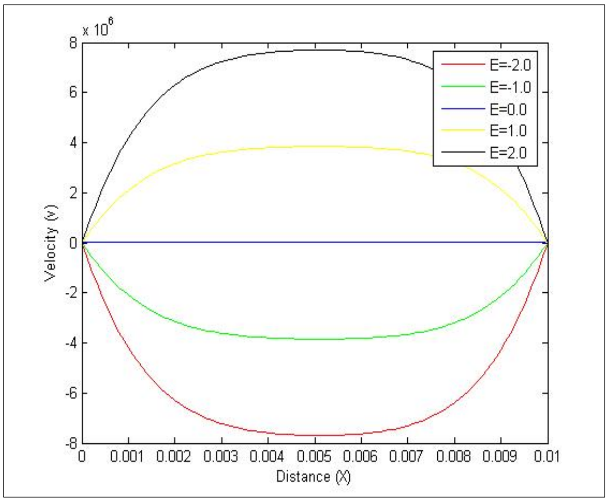

Figure 9. Variation in (v) with E

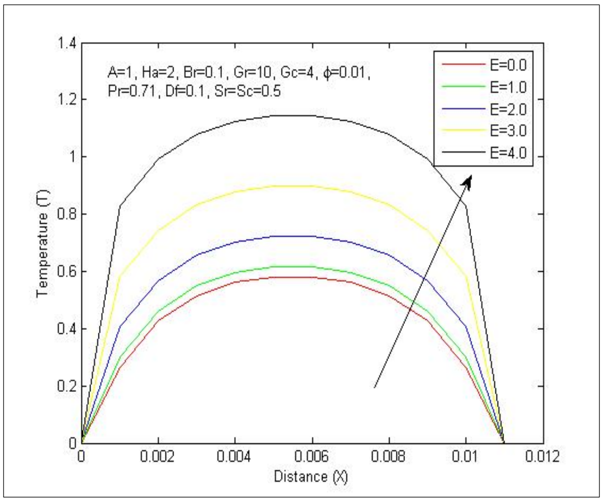

Figure 10. Variation in (T) with E

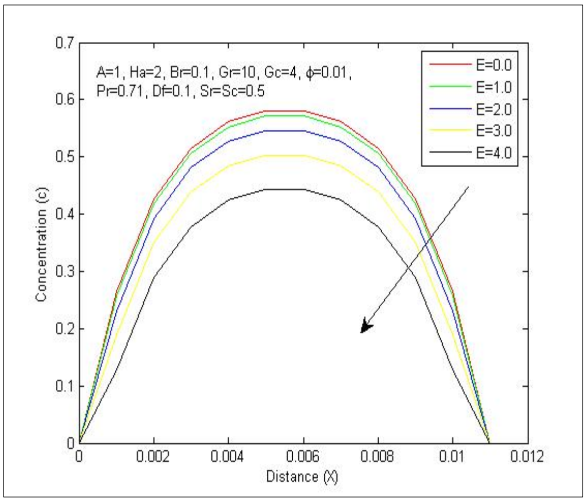

Figure 11. Variation in (c) with E

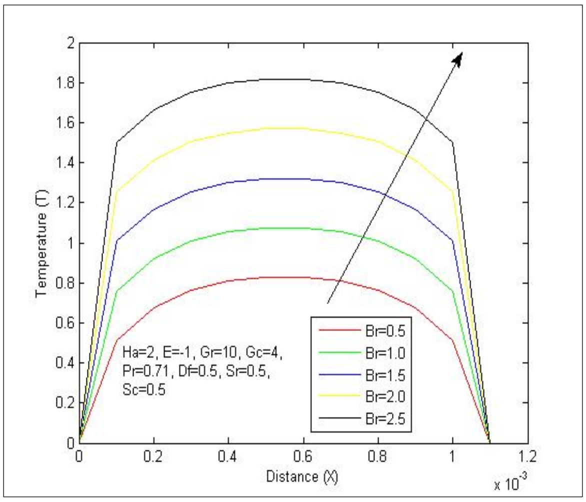

Figure 12. Variation in (T) with B_r

We have plotted (Fig. 9, Fig. 10, and Fig. 11) for velocity, temperature, and concentration profiles in the boundary layer for different values of electrical field load parameter E, base fluid water employing copper nanoparticles. In these plottings, we have noticed that the velocity of Cu −water nanofluid enhances due to the enhancement of electrical field load parameter E. i.e, flow is accelerated due to the enhancement in electrical field load parameter E. Similarly, in the temperature profile of Cu −water nanofluid we have observed that this profile is also enhance due to the enhancement of electrical field load parameter E. However, in the concentration profile of the Cu −water nanofluid, we observed a decrease in concentration with increasing electrical field load parameter E. We have plotted (Fig. 12) the temperature and concentration profiles in the boundary layer for different values of the Brinkmann number B_r, for a base fluid of water containing copper nanoparticles. On the contrary, in the temperature profile, we have observed that it increases with increasing Brinkman number B_r. However, it was observed that, with an increase in the Brinkman number B_r, the boundary-layer thickness decreased at all points. The velocity profile is not displayed graphically because it exhibits a topology similar to that of the thermal Grashof number G_r.

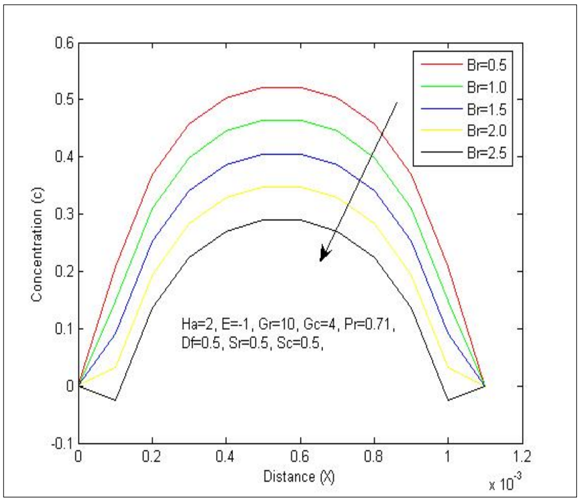

Figure 13. Variation in (c) with B_r

Case I for copper/water nanofluid:

Sl. No.	G_c	Leading value of velocity	Rate of increase of the leading value of velocity for different Solutal Grashof number G_c
	G_i	L_i	$R_i = \frac{L_{i+1} - L_i}{L_i}$
1	$G_1 = 0.10$	$L_1 = -6.10$	$R_1 = -0.0163934426$
2	$G_2 = 0.20$	$L_2 = -6.20$	$R_2 = -0.0161290323$
3	$G_3 = 0.30$	$L_3 = -6.30$	$R_3 = -0.0158730159$
4	$G_4 = 0.40$	$L_4 = -6.40$	$R_4 = -0.0156250000$
5	$G_5 = 0.50$	$L_5 = -6.50$	$R_5 = -0.0153846154$
6	$G_6 = 0.60$	$L_6 = -6.60$	$R_6 = -0.0151515152$
7	$G_7 = 0.70$	$L_7 = -6.70$	$R_7 = -0.0149253731$
8	$G_8 = 0.80$	$L_8 = -6.80$	$R_8 = -0.0147058824$
9	$G_9 = 0.90$	$L_9 = -6.90$	$R_9 = -0.0144927536$
10	$G_{10} = 1.00$	$L_{10} = -7.00$	

Case II: For silver/water nanofluid:

Sl. No.	G_c	Leading value of velocity	Rate of increase of the leading value of velocity for different Solutal G_c
	G_i	L_i	$R_i = \frac{L_{i+1} - L_i}{L_i}$
1	$G_1 = 0.10$	$L_1 = -8.10$	$R_1 = -0.0123456790$
2	$G_2 = 0.20$	$L_2 = -8.20$	$R_2 = -0.0121951220$
3	$G_3 = 0.30$	$L_3 = -8.30$	$R_3 = -0.0120481928$
4	$G_4 = 0.40$	$L_4 = -8.40$	$R_4 = -0.0119047619$
5	$G_5 = 0.50$	$L_5 = -8.50$	$R_5 = -0.0117647059$
6	$G_6 = 0.60$	$L_6 = -8.60$	$R_6 = -0.0116279070$
7	$G_7 = 0.70$	$L_7 = -8.70$	$R_7 = -0.0114942529$
8	$G_8 = 0.80$	$L_8 = -8.80$	$R_8 = -0.0113636364$
9	$G_9 = 0.90$	$L_9 = -8.90$	$R_9 = -0.0112359551$
10	$G_{10} = 1.00$	$L_{10} = -9.00$	

Case III For titanium oxide/water nanofluid:

Sl. No.	G_c	Leading value of velocity	Rate of increase of the leading value of velocity for different Solutal G_c
	G_i	L_i	$R_i = \frac{L_{i+1} - L_i}{L_i}$
1	$G_1 = 0.10$	$L_1 = -2.70$	$R_1 = -0.0370370370$
2	$G_2 = 0.20$	$L_2 = -2.80$	$R_2 = -0.0357142857$
3	$G_3 = 0.30$	$L_3 = -2.90$	$R_3 = -0.0344827586$
4	$G_4 = 0.40$	$L_4 = -3.00$	$R_4 = -0.0333333333$
5	$G_5 = 0.50$	$L_5 = -3.10$	$R_5 = -0.0322580645$
6	$G_6 = 0.60$	$L_6 = -3.20$	$R_6 = -0.0312500000$
7	$G_7 = 0.70$	$L_7 = -3.30$	$R_7 = -0.0303030303$
8	$G_8 = 0.80$	$L_8 = -3.40$	$R_8 = -0.0294117647$
9	$G_9 = 0.90$	$L_9 = -3.50$	$R_9 = -0.0285714286$
10	$G_{10} = 1.00$	$L_{10} = -3.60$	

Case IV For copper oxide/water nanofluid:

Sl. No.	G_c	Leading value of velocity	Rate of increase of the leading value of velocity for different Solutal G_c
	G_i	L_i	$R_i = \frac{L_{i+1} - L_i}{L_i}$
1	$G_1 = 0.10$	$L_1 = -2.80$	$R_1 = -0.0357142857$
2	$G_2 = 0.20$	$L_2 = -2.90$	$R_2 = -0.0344827586$
3	$G_3 = 0.30$	$L_3 = -3.00$	$R_3 = -0.0333333333$
4	$G_4 = 0.40$	$L_4 = -3.10$	$R_4 = -0.0322580645$
5	$G_5 = 0.50$	$L_5 = -3.20$	$R_5 = -0.0312500000$
6	$G_6 = 0.60$	$L_6 = -3.30$	$R_6 = -0.0303030303$
7	$G_7 = 0.70$	$L_7 = -3.40$	$R_7 = -0.0294117647$
8	$G_8 = 0.80$	$L_8 = -3.50$	$R_8 = -0.0285714286$
9	$G_9 = 0.90$	$L_9 = -3.60$	$R_9 = -0.0277777778$
10	$G_{10} = 1.00$	$L_{10} = -3.70$	

We have plotted (Fig. 14) the rate-of-rise leading velocity for different nanofluids against the corresponding solutal Grashof number G_c, in the duct under the same configuration. We have plotted the graphs for the following nanofluids: copper (Cu) and silver (Ag), titanium oxide (TiO_2) and copper oxide (CuO). These plots provide a comparative advantage in mass transfer for different nanofluids at a given temperature. From the plots (Fig. 14), we see that as the solute Grashof number G_c increases, the difference in flow rate between the nanofluids decreases. For a low value of the solutal Grashof number G_c, gives the high flow rate, and titanium oxide (TiO_2) gives a low flow rate. For high solutal G_c, all the nanofluids considered show no significant difference in volumetric flow rate.

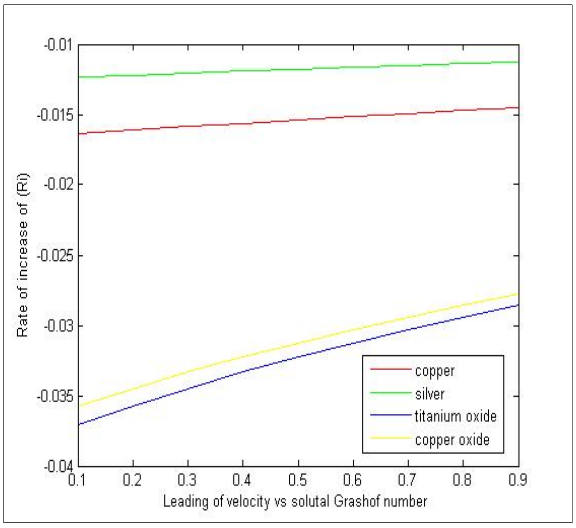

Figure 14. Rate of increase of solutal Grashof number G_c for different nanoparticles, copper (Cu), silver (Ag), titanium oxide (TiO_2) and copper oxide (CuO)

The 3D temperature distribution shows that the disk occupies the convex region, and the copper contours are more nonlinear than those of aluminum and titanium oxide. The concentration distribution and the topology are in a concave position, and the contours are much less disturbed for all the nanoparticles. For the flow concerning copper nanofluids, we have plotted the graphs in (x, y, v) mesh, (x, y, T) mesh and (x, y, c) mesh in Fig. 10. Similarly, graphs are plotted for other nanofluids of silver, aluminum, and titanium oxide in Fig. 12, Fig. 14, and Fig. 17. Further, in Fig. 11, Fig. 13, Fig. 15, and Fig. 17, we have employed 100×100 grid size for the velocity profile at $x = 1$ when $y = 0$ and we have employed 20×20 grid size for temperature and concentration profiles at $x = 1$ when $y = 1$. We have plotted velocity, temperature, and concentration profiles in the duct for Cu-water, Ag-water, and TiO_2-water nanofluids. We can get a regular profile of velocity, temperature, and concentration about the center section of the duct $(at\ x = \frac{1}{2})$.

Copper (Cu) nanoparticles

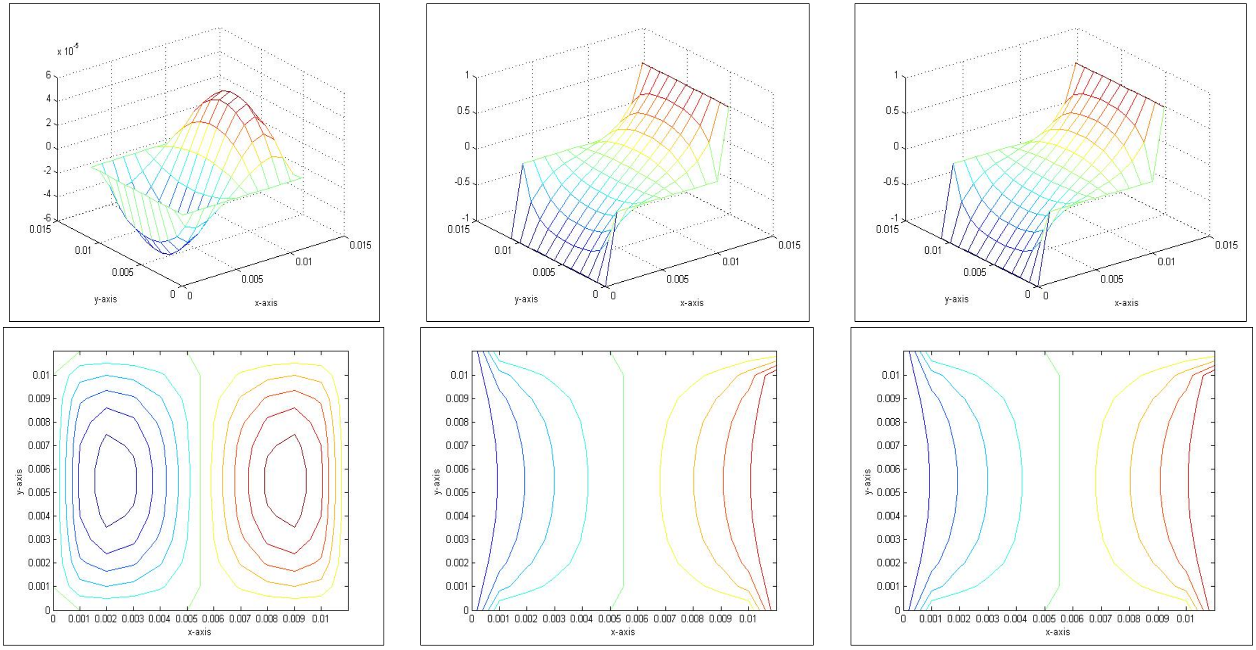

Velocity (v) Temperature (T) Concentration (c)

Figure 15. Velocity profile in mesh (x, y, v); Temperature profile in mesh (x, y, T) and Concentration profile in mesh (x, y, c) for copper nanoparticles

Silver (Ag) nanoparticles

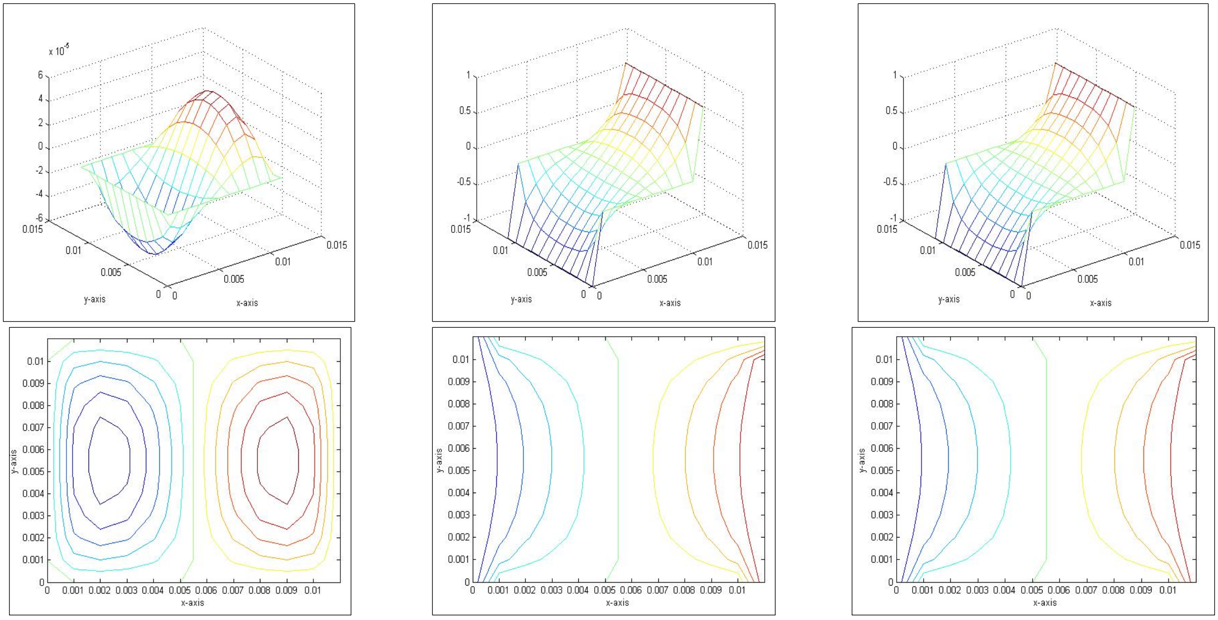

Velocity (v) Temperature (T) Concentration (c)

Figure 16. Velocity profile in mesh (x, y, v); Temperature profile in mesh (x, y, T) and Concentration profile in mesh (x, y, c) for silver nanoparticles

Titanium oxide (TiO_2) nanoparticles

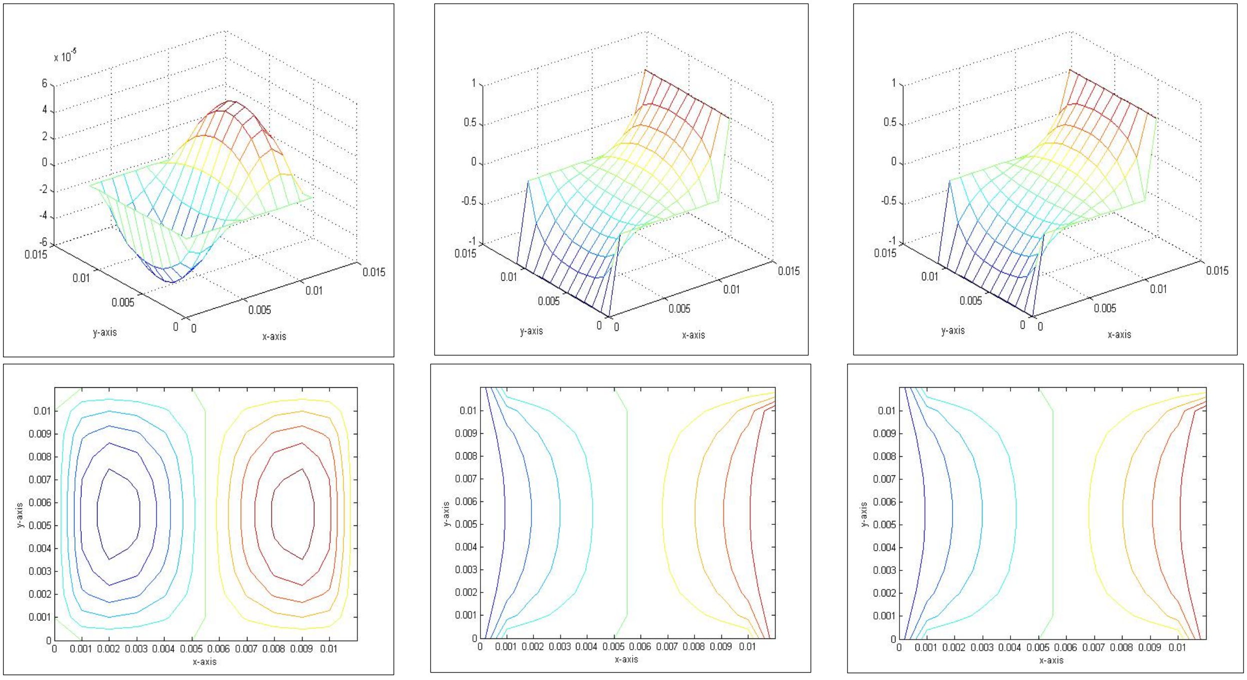

Velocity (v) Temperature (T) Concentration (c)

Figure 17. Velocity profile in mesh (x, y, v); Temperature profile in mesh (x, y, T) and Concentration profile in mesh (x, y, c) for titanium oxide nanoparticles

Copper oxide (CuO) nanoparticles

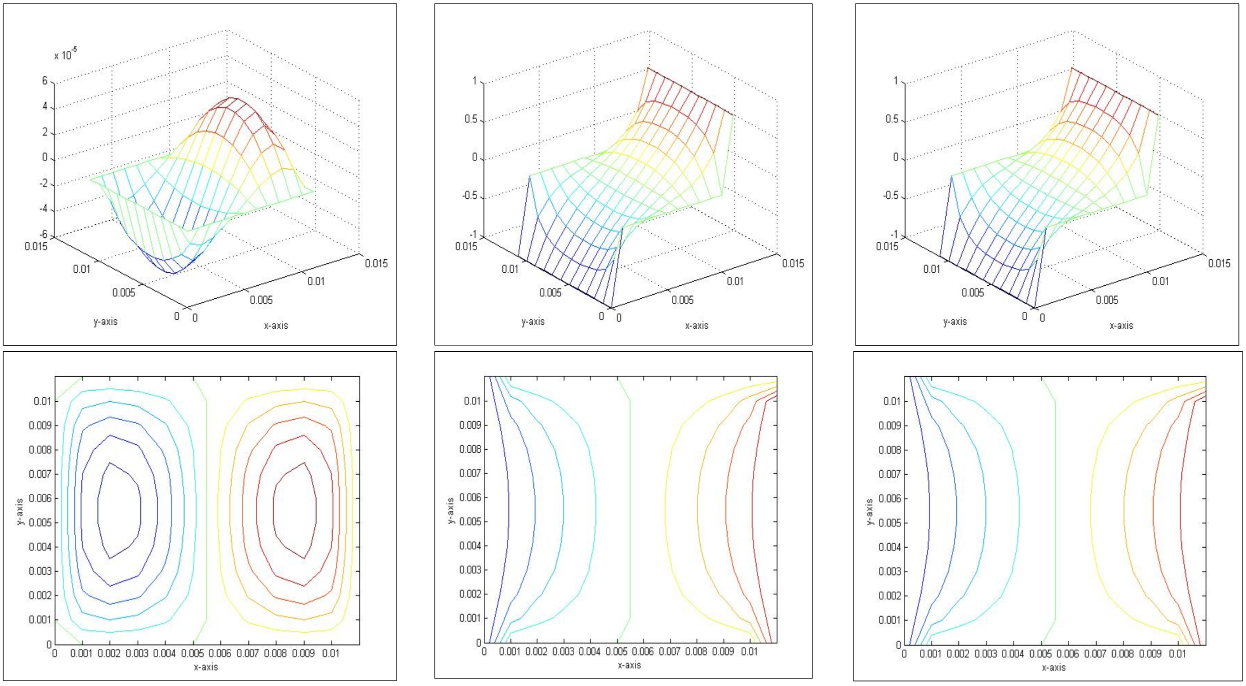

Velocity (v) Temperature (T) Concentration (c)

Figure 18. Velocity profile in mesh (x, y, v); Temperature profile in mesh (x, y, T) and Concentration profile in mesh (x, y, c) for copper oxide nanoparticles

5. CONCLUSIONS

In this work, we have studied a vertical rectangular duct in the presence of a strong transverse magnetic field, with velocity, temperature, and concentration profiles of different copper-based nanofluids (Cu) , silver (Ag), titanium oxide (TiO_2), and copper oxide (CuO) nanoparticles with water as a base fluid. The governing equations are solved using the explicit finite difference method (EFDM), also known as the second-order upwind method. The results are shown graphically for different parameter values. The computational process is carried out using MATLAB code. The following conclusions we have found from the present investigations:

1. From the plotting of (Fig. 5), we have seen that with increasing solutal Grashof number G_c. The difference in flow rate for different nanofluids is decreasing. For a low value of the solutal Grashof number G_c, titanium oxide (TiO_2) gives a high flow rate and silver (A_g) gives a low flow rate. For high solutal Grashof number G_c, all the nanofluids considered show no significant difference in volumetric flow rate.
2. For increasing values of thermal Grashof number G_r, solutal Grashof number G_c, electrical field load parameter E and the nanoparticle volume fraction ϕ. The fluid velocity also increases. But with the increasing values of the Hartmann number H_a, the velocity decreases in copper-water nanofluids.
3. With the increasing values of the electrical field load parameter E and the Brinkmann number B_r, the temperature and concentration profiles are found to increase due to an increase in the values of the electrical field load parameter E and Brinkmann number B_r, but the boundary layer reduces the concentration; its thickness decreases.

ORCID

Hirak Jyoti Dehingia, https://orcid.org/0000-0002-3119-0842; **Kaushik Dehingia,** https://orcid.org/0000-0002-8042-4166
Rupjyoti Borah, https://orcid.org/0000-0001-7765-7877; **Utpal Saikia,** https://orcid.org/0000-0003-0235-6871

REFERENCES

[1] S.U.S. Choi, "Enhancing thermal conductivity of fluids with nanoparticles, in developments and applications of non-Newtonian flows," ASME FED 231/MD, **66**, 99-103 (1995). https://doi.org/10.1115/imece1995-0926
[2] L. Godson, B. Raja, D.M. Lal, and S. Wongwises, "Enhancement of heat transfer using nanofluids-An overview," Renewable and Sustainable Energy Reviews, **14**, 629-641 (2010). https://doi.org/10.1016/j.rser.2009.10.004
[3] J.C. Maxwell, *A Treatise on Electricity and Magnetism*, (Clarendon Press, Oxford, UK, 1881).
[4] S. Lee, S.U.S.S. Choi, S. Li, and J.A. Eastman, "Measuring thermal conductivity of fluids containing oxide nanoparticles," ASME. J. Heat Transfer, **121**, 280-289 (1999). https://doi.org/10.1115/1.2825978
[5] J.A. Eastman, S.U.S. Choi. and S. Li, and W.L. Thompson, "Anomalously increased effective thermal conductivities of ethylene glycol-based nanofluids containing copper nanoparticles," Appl. Phys. Lett. **78**, 718-720 (2001). https://doi.org/10.1063/1.1341218
[6] Y. Xuan, and Q. Li, "Heat transfer enhancement of nanofluids," Int. J. Heat Fluid Flow, **21**, 58-64 (2000). https://doi.org/10.1016/s0142-727x(99)00067-3
[7] S.K. Das, S.U.S. Choi, W. Yu, and T. Pradet, *Nanofluids: Science and Technology*, (Wiley, New Jersey, 2007).
[8] W. Daungthongsuk, and S. Wongwises, "A critical review of convective heat transfer nanofluids," Renewable Sustainable Energy Rev. **11**, 797-817 (2007). https://doi.org/10.1016/j.rser.2005.06.005
[9] X.Q. Wang, and A.S. Mujumdar, "A review on nanofluids-part I: Theoretical and numerical investigations," Braz. J. Chem. Eng. **25**, 613-630 (2008). https://doi.org/10.1590/s0104-66322008000400001
[10] X.Q. Wang, and A.S. Mujumdar, "A review on nanofluids-part II: Experimental and application investigations," Braz. J. Chem. Eng. **25**, 631-648 (2008). https://doi.org/10.1590/s0104-66322008000400002
[11] S. Kakaç, and A. Parmuanjaroenkij, "Review of Convective Heat Transfer Enhancement with Nanofluids," International Journal of Heat Mass Transfer, **52**, 3187-3196 (2009). https://doi.org/10.1016/j.ijheatmasstransfer.2009.02.006
[12] Y. Ding. H. Chen, I. Wang, C.Y. Yang. Y. Hel W. Yang W.P. Lee, *et al.*, "Heat transfer intensification using nanofluids," Kona, **25**, 3187-3196 (2007). https://doi.org/10.14356/kona.2007006
[13] I. Tavman, A. Turgut, M. Chirtoc, K. Hadjov, O. Fudym, and S. Tavman, "Experimental Study on Thermal Conductivity and Viscosity of Water-Based Nanofluids," Heat Transfer Res. **41**(3), 339-351 (2010). https://doi.org/10.1615/heattransres.v41.i3.100
[14] A. Einstein, "Correction of My Work: A New Determination of the Molecular Dimensions", Ann. Phys. **34**(3), 591-592 (1911).
[15] P.K. Namburu, D.K. Das, K.M. Tanguturi, and R.S. Vajjha, "Numerical Study of Turbulent Flow and Heat Transfer Characteristics of Nanofluids Considering Variable Properties," Int. J. Therm. Sci., **48**(2), 290-302 (2009). https://doi.org/10.1016/j.ijthermalsci.2008.01.001
[16] T. Bergman, "Effect of Reduced Specific Heats of Nanofluids on Single Phase, Laminar Internal Forced Convection," Int. J. Heat Mass Transfer, **52**(5-6), 1240-1244 (2009). https://doi.org/10.1016/j.ijheatmasstransfer.2008.08.019
[17] R. Younsi, "Computational analysis of MHD flow, heat and mass transfer in trapezoidal porous cavity," Thermal Science, **13**, 13-22 (2009). https://doi.org/10.2298/tsci0901013y
[18] P.R. Sharma, and G. Singh, "Effects of Ohmic heating and viscous dissipation on steady MHD flow near a stagnation point on an isothermal stretching sheet," Thermal Science, **13**, 5-12 (2009). https://doi.org/10.2298/tsci0901005s
[19] P.A. Vadher, G.M. Deheri, and R.M. Patel, "Performance of hydromagnetic squeeze films between conducting porous rough conical plates," Meccanica, **45**, 767-783 (2010). https://doi.org/10.1007/s11012-010-9279-y
[20] J.C. Umavathi, I.C. Liu, and M.A. Sheremet, "Convective heat transfer in a vertical rectangular duct filled with a nanofluid," Heat Transfer Asian Research, **45**, 661-679 (2016). https://doi.org/10.1002/htj.21182
[21] R. Ellahi, M. Hassan, and A. Zeeshan, "Aggregation Effects on Water-Based Al_2O_3- Nanofluid over Permeable Wedge in Mixed Convection," Asia-Pacific Journal of Chemical Engineering, **11**, 179-186 (2015). https://doi.org/10.1002/apj.1954
[22] M.A.A. Hamad, "Analytical Solution of Natural Convection Flow of a Nanofluid over a Linearly Stretching Sheet in the Presence of Magnetic Field," International Communications in Heat and Mass Transfer, **38**, 487-492 (2011). https://doi.org/10.1016/j.icheatmasstransfer.2010.12.042
[23] T. Hayat, M.B. Ashraf, S.A. Shehzad, and A. Alsaedi, "Mixed Convection Flow of Casson Nanofluid over a Stretching Sheet with Convectively Heated Chemical Reaction and Heat Source/Sink," J. Appl Fluid Mechanics, **8**, 803-813 (2015). https://doi.org/10.18869/acadpub.jafm.67.223.22995

[24] P.K. Kameswaran, M. Narayana, P. Sibanda, and P.V.S.N. Murthy, "Hydromagnetic Nanofluid Flow Due to a Stretching or Shrinking Sheet with Viscous Dissipation and Chemical Reaction Effect," International Journal of Heat and Mass Transfer, **55**, 7587-7595 (2012). https://doi.org/10.1016/j.ijheatmasstransfer.2012.07.065
[25] O.D. Makinde, and A. Aziz, "Boundary Layer Flow of a Nanofluid Past a Stretching Sheet with a Convective Boundary Condition," Int. J. Therm. Sci. **50**, 1326-1332 (2011). https://doi.org/10.1016/j.ijthermalsci.2011.02.019
[26] J.C. Umavathi, and O.A. Beg, "Computation of thermo-solutal convection with Soret-Dufour cross diffusion in a vertical duct containing carbon/metallic nanofluids," Journal of Mechanical Engineering Science, **236**(13), (2022). https://doi.org/10.1177/09544062211072693
[27] S. Nadeem, R.U. Haq, and N.S. Akbar, "MHD Three-Dimensional Boundary Layer Flow of Casson Nanofluid Past a Linearly Stretching Sheet with Convective Boundary Condition," IEEE Transactions on Nanotechnology, **13**, 109-115 (2014). https://doi.org/10.1109/tnano.2013.2293735
[28] H.F. Oztop and E. Abu-Nada "Numerical Study of Natural Convection in Partially Heated Rectangular Enclosures Filled with Nanofluids," Int. J. Heat. Mass Transf. **29**, 1326-1336 (2008). https://doi.org/10.1016/j.ijheatfluidflow.2008.04.009
[29] M.M. Rashidi, N. Vishnu Ganesh, A.K. Abdul Hakeem, and B. Ganga, "Buoyancy Effect on MHD Flow of Nanofluid Over a Stretching Sheet in the Presence of Thermal Radiation," Journal of Molecular Liquids, **198**, 234-238 (2014). https://doi.org/10.1016/j.molliq.2014.06.037
[30] M. Sheikholeslami, M.G. Bandpy, R. Ellahi, and A. Zeeshan, "Simulation of MHD CuO-Water Nanofluid Flow and Convective Heat Transfer Considering Lorentz Forces," Journal of Magnetism and Magnetic Materials, **369**, 69-80 (2014). https://doi.org/10.1016/j.jmmm.2014.06.017
[31] M. Turkyilmanzoglu, "Natural Convective Flow of Fluids Past a Radiative and Impulsive Vertical Plate," J. Aerosp. Eng. **29**, 1-8 (2016). https://doi.org/10.1061/(asce)as.1943-5525.0000643
[32] S. Rao, and P.A. Deka, "Numerical investigation on transport phenomena in a nanofluid under the transverse magnetic field over a stretching plate associated with solar radiation," in: *Nonlinear Dynamics and Applications. Springer Proceedings in Complexity*, edited by S. Banerjee and A. Saha (Springer, Cham. 2022), pp. 473-492. https://doi.org/10.1007/978-3-030-99792-2_39
[33] B.R. Das, P.N. Deka, and S. Rao, "Numerical analysis on MHD mixed convection flow of aluminum-oxide/water nanofluids in a vertical square duct," East European Journal of Physics, (2), 51-62 (2023). https://doi.org/10.26565/2312-4334-2023-2-02
[34] A. Majeed, A. Zeesham, M. Jawad, and M.S. Alhodaly, "Influence of melting heat transfer and chemical reaction on the flow of non-Newtonian nanofluid with Brownian motion: Advancement in mechanical engineering," in: *Proceedings of the Institution of Mechanical Engineers, Part E: Journal of Process Mechanical Engineering*, **238**(1), (2022). https://doi.org/10.1177/09544089221145527
[35] M. Jawad, M.K. Hameed, K.S. Nisar, and A.H. Majeed, "Darcy-Forchheimer flow of Maxwell nanofluid flow over a porous stretching sheet with Arrhenius activation energy and Nield boundary conditions," Case Studies in Thermal Engineering, **44**, 102830 (2023). https://doi.org/10.1016/j.csite.2023.102830
[36] M. Jawad, and K.S. Nisar, "Upper-convected flow of Maxwell fluid near stagnation points through porous surface using Cattaneo-Chrisov heat flux model," Case Studies in Thermal Engineering," **48**, 103155 (2023). https://doi.org/10.1016/j.csite.2023.103155
[37] A. Hussanan, Z. Ismail, I. Khan, A.G. Hussein, and S. Shafie, "Unsteady boundary layer MHD free convection flow in a porous medium with constant mass diffusion and Newtonian heating," Eur. Phys. J. Plus, **129**(3), 46 (2014). https://doi.org/10.1140/epjp/i2014-14046-x

МГД КАНАЛЬНИЙ ПОТІК НАНОРІДИНИ ПІД ВПЛИВОМ ПОДВІЙНОГО ДЖЕРЕЛА ТЕПЛА ЗА НАЯВНОСТІ ЕЛЕКТРИЧНОГО (E_o) ТА МАГНІТНОГО (B_o) ПОЛІВ

Бішну Рам Дас[1], Хірак Джйоті Дехінгія[2], Каушік Дехінгія[3,4], Рунджйоті Бора[5], Утпал Саікія[6]
[1]*Департамент математики, коледж BCM, Камруп-781102, Ассам, Індія*
[2]*Відділ фундаментальних і гуманітарних наук, DUIET, Університет Дібругарх, Дібругарх, Ассам, Індія, 786004*
[3]*Департамент математики, коледж Сонарі, Чарайдео, Ассам, Індія, 785690*
[4]*Дослідницький центр прикладної математики, Хазарський університет, Баку, Азербайджан, AZ1096*
[5]*Департамент математики, коледж Тінгхонг, Тінгхонг-786612, Дібругарх, Ассам, Індія*
[6]*Департамент математики, Політехнічний університет Ґолагхат, 785610, Фуркатінг, Ґолагхат, Ассам, Індія*

У цьому дослідженні розглядається потік наночастинок міді (Cu), срібла (Ag), оксиду титану (TiO_2), оксиду міді (CuO) з водою як основною рідиною в присутності сильного магнітного поля у вертикальному прямокутному каналі. Ліва та права стінки каналу підтримуються при різних стаціонарних температурах та концентраціях. Поля температури, швидкості та концентрації наночастинок описуються рівняннями переносу. Для дискретизації зв'язаних нелінійних рівнянь Нав'є-Стокса використовується метод проти вітру другого порядку, явний метод скінченних різниць (EFDM). Щоб дослідити ефективність теплопередачі цієї нанорідини, ми знерозміриили визначальні рівняння та отримали рішення за допомогою явної числової схеми. Для виконання обчислювальних кроків використовується код MATLAB. Ми побудували графіки полів швидкості, температури та концентрації для різних значень магнітогідродинамічних (МГД) параметрів потоку, включаючи теплове число Грасгофа (G_r), розчинне число Грасгофа (G_c), число Гартмана (H_a), параметр навантаження електричного поля (E), число Брінкмана (B_r) та об'ємну частку наночастинок (ϕ).

Ключові слова: *електричне поле; магнітне поле; нанорідини; нелінійність; явний метод скінченних різниць (EFDT); прямокутний вертикальний канал; МГД-потік; сила плавучості; в'язкий потік*

East European Journal of Physics. **2.** 332-340 (2026)
DOI:10.26565/2312-4334-2026-2-34 ISSN 2312-4334

COMPUTATIONAL MODELING OF THE STRUCTURAL STABILITY OF METAL NANOCLUSTERS BASED ON THE MOLECULAR DYNAMICS METHOD

Akbarali M. Rasulov, Nodirbek I. Ibrokhimov, Azamat G. Tukhtasinov, Jakhongir M. Khodjimatov*
Fergana State Technical University, Fergana, Uzbekistan
**Corresponding Author e-mail: johnhojimatov@gmail.com*

Received February 14, 2026; revised April 20, 2026; accepted May 7, 2026

The paper examines the results of molecular dynamics modeling of metallic clusters of copper (Cu), silver (Ag) and cobalt (Co). The focus was on how the geometric properties and energetic stability of nanoclusters vary with size. Numerical calculations were performed using the Lammps software suite. This software package is widely used for atomistic modeling tasks and has proven itself in the study of systems with a large number of particles. The interatomic interactions were described using EAM and MEAM potentials, and the simulations were performed in a high-performance computing environment with MPI/OpenMP support. The work was conducted in two sequential stages. In the first stage, the clusters were relaxed at a temperature of 0K to obtain configurations corresponding to the minimum energy state. The systems were then gradually heated to 300K, which made it possible to trace changes in their stability and assess possible structural rearrangements during thermal evolution. The computational results showed that as the number of atoms increases, the overall geometry of the clusters approaches a spherical shape, and the system's energetic stability is enhanced due to the increase in the volume of the inner atoms. We present a systematic MD simulation study of structural evolution and energetic stability in Cu, Ag, and Co nanoclusters comprising 13 to 55 atoms. By identifying magic-number clusters and comparing compositional behavior from 0K to 300K, we reveal distinct size-dependent stability trends across the three metals. These findings offer quantitative insight into nanocluster formation mechanisms relevant to catalysis and nanomaterial engineering.

Keywords: *Molecular dynamics simulation; Interatomic interactions; Thermostatization; Barostatization; External pressure; Model NVE, NVT, and NPT; Atomic configurations; Geometric structures; Binding energy; Magic numbers; Structural stability*
PACS: 61.46.Bc, 36.40.Ei, 02.70.Ns

INTRODUCTION

Due to the small sizes of nanoclusters, their investigation is a complex process. As a result, in recent years, great importance has been placed on studying such systems in materials science through computer modeling at the atomic level [1].

Due to the physical limitations on the operating speed of traditional single-core Central Processing Units (CPUs) common in personal computers, today's computer architecture for modeling such nanoscale systems is multi-processor, the need for multiprocessor, multi-core, and many-core systems is growing. In order to fully utilize the capabilities of new architectures, computer modeling methods are actively used, in particular molecular dynamics and the Monte Carlo (MC) method. These approaches allow us to study the structural features and thermodynamic properties of nanomaterials at the atomistic level. In a number of studies, phase transitions and surface effects in nanoclusters were examined using modeling, after which the obtained results were compared with similar processes characteristic of large single crystals. Molecular dynamics simulations show that copper (Cu) nanoclusters become liquid at temperatures significantly lower than bulk crystals of the same metal. Such behavior is generally associated with a large reduction in their thermodynamic stability [2,3]. A similar trend is observed for silver (Ag) nanoclusters. The simulation results indicate that as the cluster size decreases, its melting temperature also decreases [4]. In such studies, the melting process is typically initiated at the surface of the cluster, after which the resulting structural changes gradually spread to its internal regions, without affecting the entire structure at once. This is why, when modeling metal nanoclusters, the potentials of the embedded atom method (EAM) or its modified version, the modified embedded atom method (MEAM), are most often used. This approach allows for a more accurate consideration of the characteristics of interatomic interactions in metallic systems. In a number of studies, specially parameterized EAM potentials for silver were used to describe the processes of bond formation and structural evolution in bimetallic nanoclusters, including in Ag-Pd and Ag-Cu systems [5,6].

In recent years, interest in computer modeling of copper nanoclusters has increased significantly. Early studies using molecular dynamics showed that their melting temperature depends significantly on cluster size [7]. Over time, the research focus expanded. Beginning around 2020, attention shifted from melting processes to phase transitions from amorphous to crystalline states in copper nanoclusters. In a number of fundamental works, the behavior of copper nanoparticles during heating was first analyzed using classical molecular dynamics calculations [8]. Analysis of the obtained data showed that as particle size decreases, their melting temperature decreases. Moreover, both the structural and dynamic characteristics of the system are largely determined not only by cluster size but also by temperature conditions. In addition, a number of studies have noted that the formation of a silver shell on the surface of a copper nanocluster is accompanied by a noticeable increase in its crystallization temperature [2]. These results provide grounds to assume that the heterogeneous coating can influence the mechanisms of phase transitions in nanoclusters and likely contributes to increased their thermal and structural stability.

Cite as: A.M. Rasulov, N.I. Ibrokhimov, A.G. Tukhtasinov, J.M. Khodjimatov, East Eur. J. Phys. 2, 332 (2026), https://doi.org/10.26565/2312-4334-2026-2-34

In [6], the processes of aggregation and dissolution of bimetallic Ag-Cu nanoclusters were examined in detail using molecular dynamics simulations. It was shown that both the initial mutual arrangement of clusters and the degree of their structural ordering significantly affect the rate of aggregation. The obtained results allowed us to conclude that the features of melting and solidification.

In recent years, molecular dynamics-based studies have significantly expanded the possibilities for modeling cobalt nanoclusters. The application of the MEAM (Modified Embedded Atom Method) potential in MD calculations made it possible to describe with sufficient accuracy the behavior of cobalt nanoclusters in a crystal structure with hexagonal close packing (HCP). In the course of these studies, it was established that the processes of melting and solidification in bimetallic nanoclusters are determined not only by their size, but also by the features of their structural organization. The configuration of a system has as significant an impact as its scale. Moreover, the use of the MEAM potential provides a fairly correct description of both hexagonal close-packed (HCP) and face-centered cubic (FCC) crystal structures. This approach also allows one to estimate the surface energies and relative stability of cobalt-based nanoclusters with acceptable accuracy.

As a classical, physically motivated model, this potential demonstrates numerically stable behavior in molecular dynamics calculations and provides good convergence in long-time simulations of clusters containing thousands of atoms. Molecular dynamics calculations based on the MEAM potential have shown that in cobalt nanoclusters, the melting temperature approaches values characteristic of large monocrystals as the cluster size increases [9–13].

The literature review above shows that the field of computational modeling of Co, Cu, and Ag nanoclusters has been developing rapidly since 2020. Modern atomistic simulations make it possible to determine the spatial properties of nanoclusters as a function of size and to analyze the differences between clusters and monocrystals. While the MD method allows for observing the system's evolution in different ensembles (microcanonical ensemble-NVE or isothermal-isobaric ensemble-NPT conditions), Monte Carlo methods are aimed at determining the structural configurations corresponding to the smallest states of the clusters. [14] presents experimental results for small Ag clusters using the EAM potential to examine several different isomers to identify the most stable structure and then to determine their energetic states by DFT (Density Functional Theory). Using this approach, the size-dependent odd-even electron effect was identified in silver clusters up to 2-3 nm, and this phenomenon was confirmed by the corresponding trends observed in EAM and DFT calculations. As noted in the literature, the intrinsic energetic stability (binding energy per atom) of nanoclusters increases with cluster size [15]. In the present study, copper (Cu), silver (Ag), and cobalt (Co) were selected as model systems for the following reasons. Cu and Ag are archetypal face-centered cubic (FCC) metals that have been extensively characterized both experimentally and computationally, and well-validated EAM interatomic potentials are available for both, making them ideal reference systems for benchmarking MD simulations of nanoclusters [3, 4, 6, 14]. Cobalt, with its hexagonal close-packed (HCP) crystal structure and distinctly higher cohesive energy, provides a structurally contrasting case, allowing the influence of crystal symmetry on nanocluster stability to be assessed [9–13]. Together, these three metals span a wide range of lattice parameters, surface energies, and interatomic interaction strengths, enabling a broad and systematic comparative analysis of size-dependent nanocluster behavior.

In this article, we computationally investigate the structural stability and geometric evolution of Cu, Ag, and Co nanoclusters as a function of cluster size ($n = 13, 19, 23, 38$, and 55 atoms) using molecular dynamics simulations. The equilibrium configurations at 0 K are determined, and the size-dependent binding energy is analyzed to identify energetically favorable "magic number" structures. Geometric parameters — including cluster radius and volume — are evaluated and compared across all three metals. Additionally, structural rearrangements upon heating from 0K to 300K are systematically traced. The obtained results are presented and discussed in the following sections.

COMPUTATIONAL METHODS

Currently, several modern computer modeling methods are used to investigate processes at the atomic level.

Molecular Dynamics Method.

In the molecular dynamics method, all atoms in the system are treated as classical particles whose trajectories are determined by numerically solving Newton's equations of motion. The method was first proposed by Alder and Wainwright (1957) [16] and developed by Rahman [17] and Verlet [18] using the Lennard–Jones potential. Since the 1990s, MD has been successfully applied to study cluster–surface interactions [19–21], and today it is a standard tool for investigating the structural and thermodynamic properties of nanoscale systems with time resolution from femtoseconds to nanoseconds.

As the computational power of computers has increased, it has become possible to model larger and more complex systems using MD simulations. M. Moseler and his colleagues modeled the sequential deposition of cluster ions (sequential irradiation) process, demonstrating that the simulation system is rapidly approaching real experimental conditions and that the nonlinear effects of cluster impacts can be analyzed more accurately through computer modeling [21].

Embedded Atom Method potential.

In computational modeling, methods based on interatomic potentials are widely used. By knowing these potentials, the system’s structure and properties can be calculated much more accurately. Potentials can be calculated theoretically, i.e., based on “first principles”, or they can be determined by fitting to experimentally known properties. Subsequently, calculations are performed under the assumption that these potentials also apply over a broader range of pressures and temperatures. As mentioned earlier, the force fields are determined from the system's potential energy, and to realistically model elements with a crystalline structure, it is crucial to account for the influence of nearby atoms.

Currently, one of the most effective methods widely used in the computational modeling of metal systems is the use of a many-body interaction potential based on the Embedded Atom Method (EAM). The EAM was originally proposed by Daw and Baskes in 1984 [25] and subsequently formalized by Foiles, Baskes, and Daw in 1986 [26].

Previously, in the study (modeling) of metallic systems, mainly pair potentials, particularly the Lennard–Jones potential, were used [20,21]. However, such potentials cannot describe metallic systems with sufficiently high accuracy. Therefore, it is necessary to use a multiparticle interaction potential (EAM) that is more suitable for metal systems. The EAM-based description of interatomic interactions does not require a separate quantum mechanical calculation of the electrons in the metal structure, since the effect of the electrons is already accounted for within the EAM potential itself. In the EAM potential, the interaction of the atomic nuclei with the electrons is expressed through a single function (the embedding functional) that depends on the total electron density. In this approach, the total electron density within the metal is treated as a linear sum of the individual atoms, and the electron density generated by each atom is assumed to be spherically symmetric. In the EAM model, the total energy of the system is the sum of the pair interaction energy between atoms and the interaction energies of each atom with the electronic density created by the surrounding atoms:

$$E_{tot} = \sum_i F_i\left(\rho_{h,i}\right) + \frac{1}{2}\sum_{i\neq j}^{N} i,j\ \phi_{ij}(R_{ij}), \tag{1}$$

where ϕ_{ij} is the short-range pair interatomic potential, R_{ij} is the distance between atoms i and j, $F_i(\rho_i)$ is the embedding function reflecting the influence of surrounding atoms on the interaction energy, ρ_i is the electron density at the location of atom i, defined as the sum of the contributions of the electron density of all neighboring atoms [25,26].

$$\rho_{h,i} = \sum_{j\neq i} \rho_j^{(a)}(R_{ij}). \tag{2}$$

This approach has proven to be an effective tool for modeling face-centered cubic (FCC) metals. In this study, the potential of the modified embedded atom method (MEAM) was used.

The modified embedded atom method is a development of the classical EAM approach that additionally accounts for directional interactions between atoms. The MEAM was originally proposed by Baskes in 1987 [27] and has subsequently been widely used in modeling metals, semiconductors, and diatomic gases. The method has also been successfully applied in the study of silicon, germanium, and their alloys. Due to good agreement with experimental data, practical applicability and relative ease of implementation, the MEAM approach is considered as an effective tool for atomistic modeling of metallic systems.

SIMULATION PARAMETERS

In molecular dynamics simulations, the processes of thermostatization and barostatization are of significant physical importance. Thermostatization controls the temperature of the particles, while barostatization regulates the system's pressure. Since pressure includes a kinetic component, both processes are directly related to temperature determination. In modeling processes, the target values for temperature (T) and pressure (P) are typically specified in advance, and the thermostat and barostat are responsible for bringing the system to these values and maintaining it in equilibrium.

Interatomic potentials. For Cu and Ag clusters, the EAM potential by Foiles, Baskes, and Daw (1986) [26] was used, which provides well-established parametrizations for FCC metals that have been extensively validated against bulk properties, surface energies, and defect formation energies. For Co clusters, the MEAM potential by J. Lee, M. I. Baskes, H. Kim, and Y. Koo Cho was employed, as it correctly reproduces the HCP ground-state structure and surface properties of cobalt. These potential choices ensure that the fundamental bonding characteristics of each metal are captured with sufficient accuracy for the cluster sizes studied.

In [28], it was proposed to include external pressure as a total force in the equation of motion. Based on this, the Andersen, Berendsen, and Nosé–Hoover barostats were used in MD simulations. The effect of pressure on the crystallization of bimetallic nanoparticles was first considered in [29], but accurately determining the system's volume remains a complex issue. Despite the existing challenges, the MD method is considered the most effective and sufficiently accurate approach for studying micro- and nano-objects. Using modern stochastic thermostats, the MD method can reliably model NVE, NVT, and NPT ensembles. Although maintaining a constant temperature is a complex issue, in practice the Berendsen, Andersen, and Nosé–Hoover thermostats are widely used [30].

The initial 0 K ground-state geometric coordinates for each cluster were derived from preliminary geometric relaxations of ideal spherical cuts. To evaluate thermal stability at finite temperatures, these relaxed 0 K configurations were loaded into the simulation box. Initial atomic velocities were assigned stochastically according to a Gaussian distribution corresponding to the target simulation temperature (300 K). To prevent artificial cluster interactions, a large bounding box was employed rather than periodic boundary constraints on the cluster itself. The subsequent calculations were carried out under the isothermal-isochoric (NVT) thermodynamic ensemble. The Verlet algorithm was chosen for the numerical integration of the equations of motion, with a time step set to 0.002 ps. Molecular dynamics simulations were conducted at room temperature (300 K) over 100 ps, governed by the Berendsen thermostat. Thermal equilibrium was strictly verified by continuously monitoring the temporal evolution of the system's kinetic energy, potential energy, and temperature over the NVT trajectory. The thermodynamic state was considered fully equilibrated when the fluctuations of these energy parameters stabilized within standard statistical deviations, ensuring the prevention of non-physical structural deformations.

RESULTS AND DISCUSSION

The atomistic behavior of copper, silver, and cobalt metal clusters was analyzed using molecular dynamics simulations implemented in the LAMMPS software package [32]. EAM and MEAM potentials were used to calculate the interatomic interactions in the metal clusters. JMol [33] was used for the visual analysis of the obtained atomic configurations and structural changes, and for creating computer models of the stable structures and configurations of the metal clusters.

Initially, computer experiments were conducted to determine the geometric structures and equilibrium (stable) configurations of the Cu, Ag, and Co metal clusters at 0K, after which the gradual heating of the clusters up to 300K was modeled.

To address the temperature dependence and verify the thermodynamic stability of the initial configurations, comparative finite-temperature molecular dynamics simulations were conducted at 300K. Table 1 summarizes the average binding energies calculated for the sequence of structural "magic numbers" (n = 13, 19, 23, 38, 55) for all three metals after reaching thermal equilibrium.

Table 1. Average binding energies of Ag, Cu, and Co clusters at 300K.

Number of atoms (N)	Metal	Binding Energy at 300 K (eV/atom)
N = 13	Ag	-2.207
N = 19	Ag	-2.261
N = 23	Ag	-2.275
N = 38	Ag	-2.370
N = 55	Ag	-2.447
N = 13	Cu	-2.614
N = 19	Cu	-2.675
N = 23	Cu	-2.728
N = 38	Cu	-2.852
N = 55	Cu	-2.951
N = 13	Co	-2.923
N = 19	Co	-3.081
N = 23	Co	-3.118
N = 38	Co	-3.344
N = 55	Co	-3.497

Comparing these results with the 0 K energetic trends reveals that the transition to 300 K leads to an expected reduction in the absolute magnitude of the binding energies. This is primarily attributed to the kinetic contribution of thermal atomic vibrations and a minor degree of thermal expansion, which slightly weakens the effective interatomic bond strengths. However, rigorous trajectory analysis over the 100ps NVT interval thermally confirmed that none of the studied clusters underwent bulk melting or structural collapse at 300K. Consequently, although the absolute binding energy values deviate slightly from the 0K minimum states, the primary size-dependent configurations strictly conserved their stabilities at room temperature.

Figure 1 shows a plot of the average binding energy versus the number of atoms for the Cu, Ag, and Co metal clusters. The graph shows that as the cluster size increases, their binding energy also increases steadily. This phenomenon is explained by the fact that as the cluster size increases, the proportion of surface atoms decreases, and the degree of interatomic bonding among the interior atoms increases. Furthermore, the peaks and troughs observed in the graphs at certain atom counts indicate that clusters possess energetically more stable states at specific sizes (These stable configurations are called “magic numbers” [31], and they typically arise when fully closed-shell structural layers - such as icosahedral, decahedral, and cuboctahedral - form). In the graph, a sharp increase in the binding energy was observed for clusters with 13, 19, and 55 atoms, as they formed a complete geometric shell. The addition of a subsequent atom to the cluster led to a temporary decrease in energy due to symmetry breaking and structural rearrangement. The results of the study revealed that cobalt clusters possess a higher binding energy and a more stable structural configuration compared to copper and silver clusters. It was determined that this stability is associated with strong interactions between cobalt atoms and a high surface energy.

These findings are in good agreement with previously reported MD simulation results. In particular, the observed decrease in binding energy with decreasing cluster size is consistent with results reported for copper nanoclusters by Wang et al. [3] and Canan and Celtek [8], who also demonstrated a pronounced size-dependent reduction in thermal stability associated with the increasing proportion of undercoordinated surface atoms. The higher binding energy of Co nanoclusters compared to Cu and Ag is consistent with the bulk cohesive energy trend (Co: 4.39 eV, Cu: 3.49 eV, Ag: 2.95 eV), suggesting that the relative stability ranking observed at the nanoscale reflects the intrinsic bonding characteristics of the bulk metals. Furthermore, the identification of "magic number" clusters at n = 13, 19, and 55 atoms is consistent with the results reported by Garg et al. [14] for silver clusters, where closed-shell icosahedral configurations were found to exhibit significantly enhanced stability.

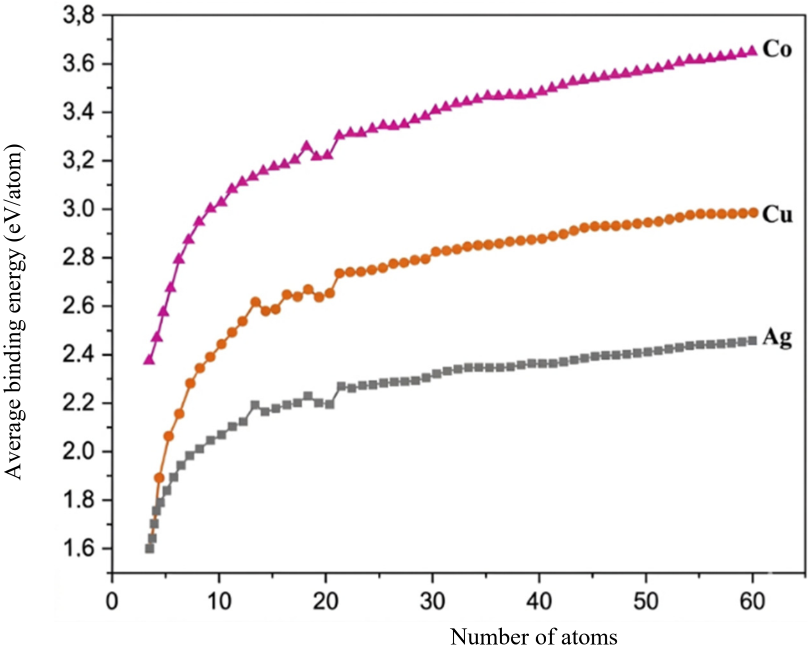

Figure 1. Dependence of the cluster average binding energy on the number of atoms in the cluster

Table 2 presents the effective physical volumes of Ag_n, Cu_n, and Co_n metal clusters (n = 13, 19, 23, 38, and 55). Since the modeled clusters, especially those containing fewer atoms, deviate from perfect spherical symmetry due to surface reconstructions, describing their size using a single scalar radius or diameter is physically ambiguous. Therefore, the spatial extent of the clusters is more accurately characterized by their effective volume. The volume of each cluster was calculated by summing the effective atomic volumes, based on the bulk Wigner-Seitz atomic radii for each metal, accounting for relaxed, non-spherical geometric configurations. The table shows that, for a given number of atoms, silver clusters occupy the largest geometric volume, which is explained by their relatively large lattice constant. Cobalt clusters, on the other hand, exhibit the most compact dimensions due to the dense packing and short interatomic distances of their hexagonal close-packed (HCP) structure. Copper clusters possess intermediate geometric properties. A consistent, linear increase in effective volume with an increasing number of atoms is clearly observed for all three metals.

Table 2. Effective volumes of Cu, Ag, and Co metal clusters as a function of size.

Cluster	**Volume V (Å³)**
Ag_{13}	221.7065
Ag_{19}	324.0326
Ag_{23}	392.2500
Ag_{38}	648.0652
Ag_{55}	937.9891
Cu_{13}	153.5353
Cu_{19}	224.3978
Cu_{23}	271.6394
Cu_{38}	448.7955
Cu_{55}	649.5725
Co_{13}	143.9595
Co_{19}	210.4024
Co_{23}	254.6976
Co_{38}	420.8047
Co_{55}	609.0594

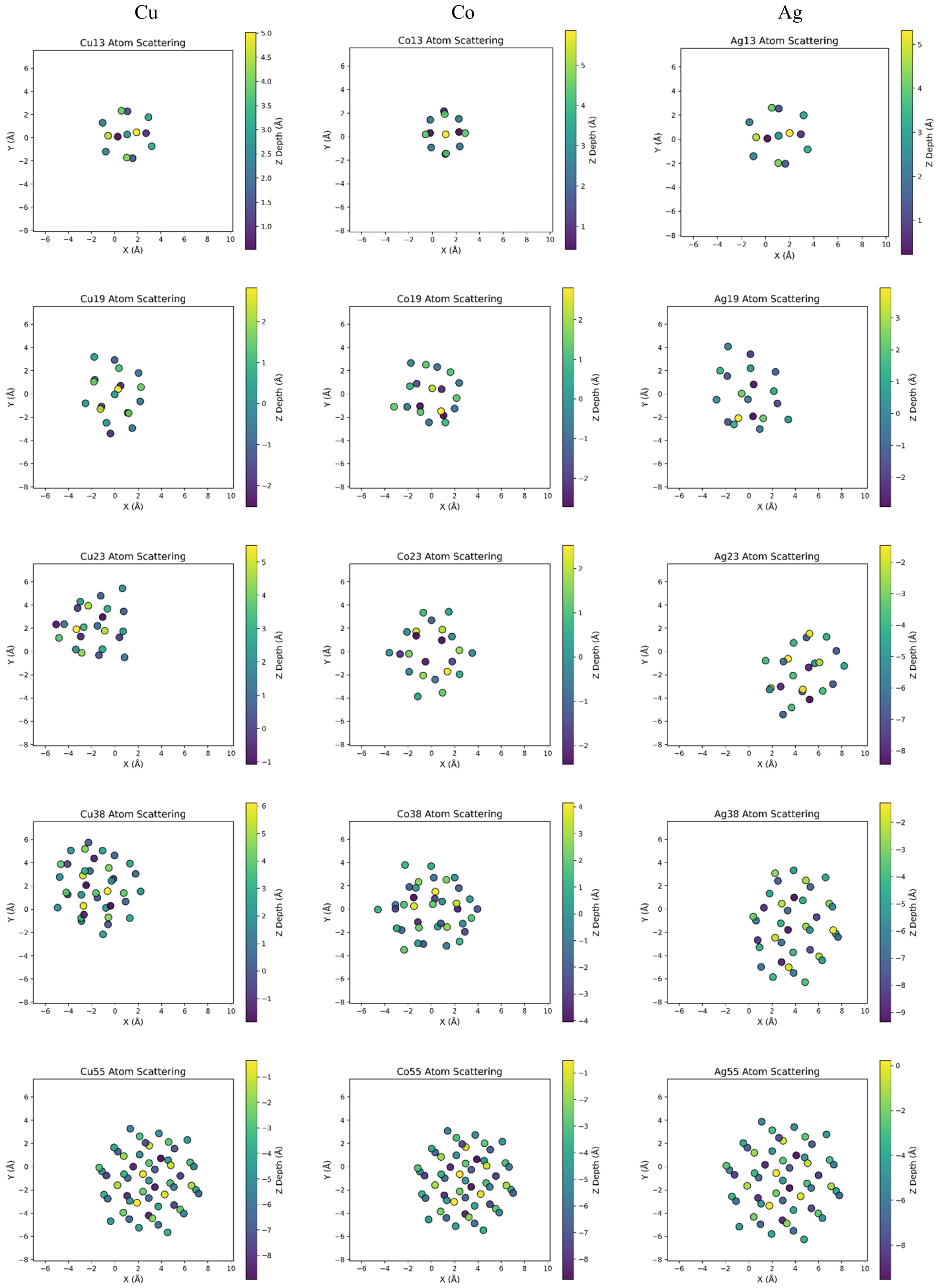

Figure 3. Distribution of atoms in a two-dimensional projection of metal clusters Ag_n, Cu_n, Co_n.

Figure 3 shows the spatial distribution of atoms in Ag, Cu, and Co metal clusters of different sizes, modeled with cluster configurations containing 13, 19, 23, 38, and 55 atoms. The graphical projections show the position of each atom in X-Y coordinates, as well as a color representation of the depth in the Z direction, clearly reflecting the spatial (3D) structure of the cluster.

Small clusters ($n \leq 23$) predominantly have central symmetry and relatively uniform atomic density. As the cluster size increases ($n = 38$-55), the spatial arrangement of atoms becomes more layered and elements of the crystalline structure are formed.

The differences in the direction of the Z-axis of the atoms, indicated by the colors, namely the predominance of dark violet in the lower layers and light yellow in the upper layers, indicate that the upper and lower parts of the cluster are not the same – there is a clear vertical difference between them. It can be seen that with increasing size in Figure 1, they are completely consistent with the geometric parameters, radius, diameter and volume, given in Table 1, and with increasing size of the cluster, a three-dimensional arrangement of the structure and the formation of crystalline layers were observed.

To quantitatively complement the visual geometric analysis, the average coordination number (CN) and the fraction of surface atoms ($\mathrm{f_{surf}} = \mathrm{N_{surf}}/\mathrm{N_{total}}$) were mathematically computed for the relaxed configurations. A surface atom was structurally defined by a coordination limit systematically lower than the bulk atomic phase. For the prototypical closed-shell $n = 13$ clusters (such as Cu and Ag), the surface fraction is exactly 92.3% ($\mathrm{N_{surf}} = 12$,$\mathrm{N_{core}} = 1$) with an average CN of 6.46, computationally confirming the precise formation of a single-layer icosahedron. As the cluster size expands, the proportion of undercoordinated surface atoms monotonically decreases, inducing denser internal atomic packing. Ultimately, at the definitive "magic number" size of $n = 55$, all three transition metals (Cu, Ag, Co) rigidly converge to an average coordination number of 8.51 and a surface fraction of 76.4% ($\mathrm{N_{surf}} = 42$,$\mathrm{N_{core}} = 13$). This quantitative descriptor distribution distinctly verifies the assembly of a complete two-shell Mackay icosahedron, thus rigorously corroborating the visual structural layering observed in Figure 3 and dictating the abrupt spikes in binding energies.

Crucially, while the general geometric evolution (e.g., reaching icosahedral magic numbers) is similar across the transition metals studied, their distinct chemical compositions heavily govern their structural and thermodynamic distinctions at equivalent sizes. Comparing clusters of identical size (for instance, $n = 55$), Cobalt exhibits the highest structural compactness and the strongest energetic stability (cohesive energy of -3.497 eV/atom at 300K). This robust cohesion correlates with its bulk hexagonal close-packed (HCP) nature and the active involvement of unfilled 3d-orbitals in metallic bonding. Conversely, Silver clusters represent the most loosely bound structures (-2.447 eV/atom) with the largest effective spatial volumes, which is directly attributable to its fully occupied 4d-shell and naturally softer, highly polarizable electron cloud (large bulk lattice constant of 4.09 Å). Copper exhibits intermediate characteristics (-2.951 eV/atom), maintaining highly symmetric icosahedral forms characterized by shorter bond lengths than Ag but weaker cohesion than Co. Thus, at any uniform physical size scale, the intrinsic chemical bonding capabilities of the specific transition metal distinctly predetermine the cluster's cohesive depth, volumetric density, and susceptibility to thermal surface deformations.

To quantify the subtle structural deviations from ideal icosahedral symmetry highlighted visually, a generalized mathematical variance metric was applied by computing the standard deviation (σ) of the radial distances of the outermost surface atoms relative to the cluster's center of mass. For a perfectly symmetric, unrelaxed icosahedron, the surface atoms form exactly equidistant sub-shells. The computational geometric analyses of the fully relaxed states (for instance at $n=55$) demonstrate that Ag clusters incur the largest absolute radial standard deviation ($\sigma \approx 0.33$ Å). This mathematical deviation definitively quantifies a higher propensity toward deformed icosahedral structures, driven by its larger atomic radius and softer electron cloud. In contrast, the icosahedral symmetry in Cu clusters is relatively well-preserved, exhibiting a smaller radial deviation ($\sigma \approx 0.29$ Å). Meanwhile, in Co clusters, the strong short-range interatomic interactions and high cohesive surface energy yield a highly compact, dense, and symmetrically tight core structure, reflected by the lowest absolute radial deviation for closed shells ($\sigma \approx 0.26$ Å).

CONCLUSION

The paper examined the structural stability and geometric features of Cu, Ag and Co metal clusters, and analyzed the dependence of the average binding energy on their size. The atomic characteristics of the systems were assessed using molecular dynamics simulations with the LAMMPS software package. Interatomic interactions were described using EAM and MEAM potentials. Analysis of the results suggests a close relationship between the energy state of clusters and their internal geometry, the proportion of surface atoms, and the degree of structural symmetry. In addition, it was found that as cluster size increases, binding energy naturally increases. In particular, clusters with “magic numbers” such as 13, 19, 38, and 55 exhibited higher binding energies. This phenomenon was explained by the formation of fully or partially icosahedral, cuboctahedral, or decahedral shells. It was determined that the temporary decrease in energy resulting from symmetry breaking upon adding an additional atom to the cluster is associated with structural reorganization processes.

Our geometric analyses established that Ag clusters tend to adopt more deformed icosahedral structures due to softer electron clouds, while Cu clusters better preserve their icosahedral symmetry. Conversely, the high surface energy and intrinsic interatomic properties of Co clusters drive them toward highly compact, symmetrically tight, and dense core configurations.

The main scientific novelty of the study is the determination of the structural evolution, stability, and energetic properties of silver, copper, and cobalt metal clusters under conditions from 0K to 300K through detailed MD modeling, and, compared to previous work, the internal reorganization mechanisms of the clusters are described in greater detail.

Furthermore, this work provides a comparative analysis of the stable configurations of Cu, Ag, and Co clusters at "magic numbers" based on a consistent methodology.

In summary, molecular dynamics simulations reveal a consistent picture of size-dependent structural evolution in Cu, Ag, and Co nanoclusters across the range of 13–55 atoms. Energetic stability is governed by the decreasing surface-to-volume ratio with increasing cluster size, while magic-number configurations corresponding to closed-shell geometries emerge as thermodynamically preferred states. The pronounced compositional dependence of cluster dimensions and binding energies – with Co being the most stable and Ag the least stable – reflects the underlying differences in cohesive energy among these metals. These results provide a systematic comparative framework for understanding transition metal nanocluster behavior and offer a foundation for targeted synthesis strategies in catalysis and nanophotonic.

ORCID

Jakhongir M. Khodjimatov, https://orcid.org/0009-0008-9108-9018

REFERENCE

[1] M.M. Komilov, R. Aliev, A.A. Mirzaalimov, S.R. Aliev, M.K. Abduvohidov, N.A. Mirzaalimov, J. Ziyoitdinov, *et al.*, "Enhancing and Optimizing Optical Properties of Bifacial Solar Cells by Incorporating Metal Nanoparticles," East European Journal of Physics, (4), 291–297 (2025). https://doi.org/10.26565/2312-4334-2025-4-27

[2] G.M. Poletaev, Yu.A. Gafner, S.L. Gafner, Yu.V. Bebikhov, and A.A. Semenov, "Molecular Dynamics Study of the Devitrification of Amorphous Copper Nanoparticles in Vacuum and in a Silver Shell," Metals, **13**(10), 1664 (2023). https://doi.org/10.3390/met13101664

[3] L. Wang, Y. Zhang, X. Bian, and Y. Chen, "Melting of Cu nanoclusters by molecular dynamics simulation," Physics Letters A, **310**(2–3), 197–202 (2003). https://doi.org/10.1016/S0375-9601(03)00263-9

[4] T. Kuruganti, P.K. Joshi, and M. Goswami, "Simulation of two nanoparticle melting to understand the conductivity drop of 3D-printed silver nanowires," Materials and Design, **236**, 112502 (2023). https://doi.org/10.1016/j.matdes.2023.112502

[5] F. Sánchez-Pérez, F. Sánchez-Pérez, O. Borrell-Grueiro, A. Casasnovas-Melián, D.J. Ramos-Ramos, A. Guerrero-Martínez, L. Bañares, A. Prada, *et al.*, "Formation of hollow silver nanoparticles under irradiation with ultrashort laser pulses," Nanophotonics. **13**(7), 1149-1157 (2024). https://doi.org/10.1515/nanoph-2023-0881

[6] H. Guo, L. Zhang, Q. Zhu, C. Wang, G. Chen, and P. Zhang, "Molecular Dynamics Simulation of the Coalescence and Melting Process of Cu and Ag Nanoparticles,' Advances in Condensed Matter Physics, **2021**, Article 9945723 (2021). https://doi.org/10.1155/2021/9945723

[7] L. Wang, Y. Zhang, X. Bian, and Y. Chen, "Melting of Cu nanoclusters by molecular dynamics simulation," Physics Letters A, **310**(2–3), 197–202 (2003). https://doi.org/10.1016/S0375-9601(03)00263-9

[8] C. Canan, and M. Celtek, "Size dependence on melting of copper nanoparticles via molecular dynamics simulation," in: *Proceedings of the 25th International Scientific Conference UNITECH*, (Gabrovo, Bulgaria, 2025).

[9] S.-H. Oh, J.-S. Kim, C.S. Park, and B.-J. Lee, "Second nearest-neighbor modified embedded-atom method interatomic potentials for the Mo–M (M = Al, Co, Cr, Fe, Ni, Ti) binary alloy systems," Computational Materials Science, **194**, 110473 (2021). https://doi.org/10.1016/j.commatsci.2021.110473

[10] A. Mahata, T. Mukhopadhyay, and M.A. Zaeem, "Modified embedded-atom method interatomic potentials for Al–Cu, Al–Fe and Al–Ni binary alloys: From room temperature to melting point," Computational Materials Science, **201**, 110902 (2022). https://doi.org/10.1016/j.commatsci.2021.110902

[11] M. Muralles, J.T. Oh, and Z. Chen, "Modified embedded atom method interatomic potentials for the Fe–Al, Fe–Cu, Fe–Nb, Fe–W, and Co–Nb binary alloys," Computational Materials Science, **230**, 112488 (2023). https://doi.org/10.1016/j.commatsci.2023.112488

[12] M.S. Nitol, M.J. Echeverria, K. Dang, M.I. Baskes, and S.J. Fensin, "New modified embedded-atom method interatomic potential to understand deformation behavior in VNbTaTiZr refractory high entropy alloy," Computational Materials Science, **237**, 112886 (2024). https://doi.org/10.1016/j.commatsci.2024.112886

[13] A.O. Moghaddam, R. Fereidonnejad, M. Moaddeli, D. Mikhailov, A. Vasenko, and E. Trofimov, "Second nearest-neighbor modified embedded-atom method interatomic potentials for the Zr–X (X = Co, Fe, Ni) binary alloys," Computational Materials Science, **247**, 113534 (2025). https://doi.org/10.1016/j.commatsci.2024.113534

[14] S. Garg, N. Kaur, N. Goel, M. Molayem, V.G. Grigoryan, and M. Springborg, "Properties of Naked Silver Clusters with Up to 100 Atoms as Found with Embedded-Atom and Density-Functional Calculations," Molecules, **28**(7), 3266 (2023). https://doi.org/10.3390/molecules28073266

[15] S. Garg, N. Kaur, N. Goel, M. Molayem, V.G. Grigoryan, and M. Springborg, "Properties of Naked Silver Clusters with Up to 100 Atoms as Found with Embedded-Atom and Density-Functional Calculations," Molecules, **28**(7), 266 (2023). https://doi.org/10.3390/molecules28073266

[16] B.J. Alder, and T.E. Wainwright, "Phase Transition for a Hard Sphere System," The Journal of Chemical Physics, **27**(5), 1208-1209 (1957).

[17] A. Rahman, "Correlations in the Motion of Atoms in Liquid Argon," Physical Review, **136**(2A), A405–411 (1964). https://doi.org/10.1103/PhysRev.136.A405

[18] L. Verlet, "Computer "Experiments" on Classical Fluids. I. Thermodynamical Properties of Lennard-Jones Molecules," Physical Review, **159**(1), 98–103 (1967). https://doi.org/10.1103/PhysRev.159.98

[19] R.S. Averback, and T. Diaz de la Rubia, H. Hsieh, and R. Benedek, "Interactions of energetic particles and clusters with solids," Nuclear Instruments and Methods in Physics Research Section B: Beam Interactions with Materials and Atoms, **59-60**, 709–717 (1990). https://doi.org/10.1016/0168-583X(91)95688-A

[20] Z. Insepov, and B. Kabdiev, "Film Deposition with Cluster Beams: An Alternate Path to Epitaxial, Crystalline Films," Proc. of Intern. Conf. on Phys. and Chem. of Finite Systems: from Clusters to Crystals, NATO ASI Series B, **2**, 429 (1992).

[21] M. Moseler, J. Nordiek, O. Rattunde, and H. Haberland, "Energetic impact of Cu-clusters on Cu-surfaces," Radiation Effects and Defects in Solids, **142**(1-4), 27-38 (1997). https://doi.org/10.1080/10420159708211594
[22] N. Boumerdassi, Molecular dynamics simulations of multiple Ag nanoclusters deposition on a substrate: Master's Thesis. The University of Texas at Austin, May 2014.
[23] M. Turdimatov, F. Mukhtarov, N. Ibrokhimov, Sh. Umarov, J. Mirzayev, and R. Rakhmatov, "Mathematical approximator based on basic spline approximation," E3S Web of Conferences. **508**, 04010 (2024). https://doi.org/10.1051/e3sconf/202450804010
[24] O.V. Bachurina, Nonlinear Spatially Localized Vibrational Modes in Metals, Ph.D. thesis (Ufa State Petroleum Technological University, Ufa, 2019).
[25] M.S. Daw, and M.I. Baskes, "Embedded-atom method: Derivation and application to impurities, surfaces, and other defects in metals," Physical Review B, **29**(12), 6443–6453 (1984). https://doi.org/10.1103/PhysRevB.29.6443
[26] S.M. Foiles, M.I. Baskes, and M.S. Daw, "Embedded-atom-method functions for the fcc metals Cu, Ag, Au, Ni, Pd, Pt, and their alloys," Physical Review B, **33**(12), 7983–7991 (1986). https://doi.org/10.1103/PhysRevB.33.7983
[27] M.I. Baskes, "Application of the embedded-atom method to covalent materials: A semiempirical potential for silicon," Physical Review Letters, **59**(23), 2666–2669 (1987). https://doi.org/10.1103/PhysRevLett.59.2666
[28] H.J.C. Berendsen, J.P.M. Postma, W.F. van Gunsteren, A. DiNola, and J.R. Haak, "Molecular dynamics with coupling to an external bath," The Journal of Chemical Physics, **81**(8), 3684-3690 (1984). https://doi.org/10.1063/1.448118
[29] H.C. Andersen, "Molecular dynamics at constant pressure and/or temperature," The Journal of Chemical Physics, **72**(4), 2384-2393 (1980). https://doi.org/10.1063/1.439486
[30] S. Nosé, "A unified formulation of the constant temperature molecular dynamics methods," The Journal of Chemical Physics, **81**(1), 511-519 (1984). https://doi.org/10.1063/1.447334
[31] Samsonov, V. M., Vasiliev, S. A., and Samsonov, M. V. (2017). A study of the energy characteristics of silver nanoclusters using molecular dynamics. Journal of Structural Chemistry, **58**(7), 1415–1420. https://doi.org/10.26902/JSC20170714
[32] LAMMPS Documentation, "LAMMPS Molecular Dynamics Simulator – User Manual," [Online]. Available: https://docs.lammps.org/Manual.html [Accessed: 10-Jul-2025].
[33] Jmol Documentation, "Jmol: an open-source Java viewer for chemical structures in 3D," [Online]. Available: https://chemapps.stolaf.edu/jmol/docs/ [Accessed: 10-Jul-2025].

ОБЧИСЛЮВАЛЬНЕ МОДЕЛЮВАННЯ СТРУКТУРНОЇ СТАБІЛЬНОСТІ МЕТАЛІЧНИХ НАНОКЛАСТЕРІВ НА ОСНОВІ МЕТОДУ МОЛЕКУЛЯРНОЇ ДИНАМІКИ

Акбаралі М. Расулов, Нодірбек І. Іброхімов, Азамат Г. Тухтасінов, Джахонгір М. Ходжиматов
Ферганський державний технічний університет, Фергана, Узбекистан

У статті розглядаються результати моделювання молекулярної динаміки металевих кластерів міді (Cu), срібла (Ag) та кобальту (Co). Основна увага приділялася тому, як змінюються геометричні властивості та енергетична стабільність нанокластерів залежно від їх розміру. Чисельні розрахунки проводилися за допомогою програмного пакету Lammps. Цей програмний пакет широко використовується для задач атомістичного моделювання та добре зарекомендував себе при вивченні систем з великою кількістю частинок. Міжатомні взаємодії описувалися за допомогою потенціалів EAM та MEAM, а моделювання проводилося у високопродуктивному обчислювальному середовищі з підтримкою MPI/OpenMP. Робота проводилася у два послідовні етапи. На першому етапі кластери були релаксовані при температурі 0K для отримання конфігурацій, що відповідають мінімальному енергетичному стану. Потім системи поступово нагрівали до 300K, що дозволило відстежити зміни в їхній стабільності та оцінити можливі структурні перебудови під час термічної еволюції. Результати обчислень показали, що зі збільшенням кількості атомів загальна геометрія кластерів наближається до сферичної форми, а енергетична стабільність системи посилюється завдяки збільшенню об'єму внутрішніх атомів. Ми представляємо систематичне дослідження молекулярної динаміки структурної еволюції та енергетичної стабільності в нанокластерах Cu, Ag та Co, що містять від 13 до 55 атомів. Ідентифікуючи кластери з магічними числами та порівнюючи композиційну поведінку від 0K до 300K, ми виявляємо різні залежні від розміру тенденції стабільності для трьох металів. Ці результати пропонують кількісне розуміння механізмів формування нанокластерів, що стосуються каталізу та наноматеріальної інженерії.

Ключові слова: *моделювання молекулярної динаміки; міжатомні взаємодії; термостатизація; баростатизація; зовнішній тиск; модель NVE, NVT та NPT; атомні конфігурації; геометричні структури; енергія зв'язку; магічні числа; структурна стабільність*

EAST EUROPEAN JOURNAL OF PHYSICS. **2.** 341-346 (2026)
DOI:10.26565/2312-4334-2026-2-35 ISSN 2312-4334

STRUCTURAL TRANSITIONS IN $Cu_{1.85}S$ SINGLE CRYSTALS

J.I. Ismayilov[1], **Kh.Kh. Hashimov**[1], **O.A. Aliyev**[1,2]*
[1]*Azerbaijan State Oil and Industry University, Azadliq Ave. 34, Baku AZ1010, Azerbaijan*
[2]*Ministry of Science and Education, Republic of Azerbaijan, Institute of Physics, H. Javid Ave 131., AZ-1143 Baku, Azerbaijan*
**Corresponding Author E-mail: o.a.amea@gmail.com*

Received February 19, 2026; revised April 4, 2026; accepted May 1, 2026

$Cu_{1.85}S$ is of significant current interest due to its complex crystal chemistry, wide homogeneity range, and unique physicochemical properties. These materials belong to the class of digenites and exhibit various structural transformations and reversible phase transitions that are highly sensitive to copper content. The synthesis, growth, and investigation of the structural behavior of $Cu_{1.85}S$ single crystals provide essential insights into phase stability and transformation mechanisms in the $Cu_{2-x}S$ system. Such knowledge is crucial for potential applications in semiconductor devices, catalysts, and energy conversion systems, where the crystal structure and phase composition directly influence material performance. This paper presents the results of the synthesis, growth of single crystals, and X-ray phase analysis of the nonstoichiometric compound $Cu_{1.85}S$, which belongs to the class of digenites. The single crystals were obtained by combining the Bridgman directional crystallization method with slow cooling. A comprehensive microstructural and X-ray analysis was carried out, including the use of Weissenberg photographs and temperature-dependent diffraction studies in the range from room temperature to 420°C. It was established that at room temperature, the $Cu_{1.85}S$ sample is biphasic and consists of orthorhombic (P_{nma}) and monoclinic ($P2_{1/n}$) phases. Upon heating, two structural transitions were observed: first to a tetragonal phase at approximately 93°C, and then to a high-temperature face-centered cubic (FCC) lattice at around 120°C. All transitions are reversible and occur via a single-crystal-to-single-crystal mechanism with well-defined orientational relationships between the lattices. The biphasic nature at room temperature is attributed to the accumulation of copper atoms in twin regions. This work contributes to understanding structural transformations in the $Cu_{1.85}S$ system and confirms the existence of stable interphase transitions that depend on copper content.

Keywords: *Crystal; Phase transitions; X-ray diffraction; Digenite; Lattice*
PACS: 61.66.Dk, 61.05.fm

1. INTRODUCTION

Compounds of the $Cu-S$ system are among the most complex materials in crystal chemistry due to their nonstoichiometric nature, broad homogeneity range, and diverse phase states. Particular attention is given to copper sulfides of the $Cu_{2-x}S$ composition, which belongs to the class of digenites. These compounds are characterized by a high level of lattice defects, a variety of structural transformations, and unique physicochemical properties. They offer potential applications in semiconductor devices, catalysis, and energy conversion systems.

An analysis of the literature reveals that no universal method exists for synthesizing nonstoichiometric compounds of the $Cu-S$ system. While some studies utilized natural crystals, others involved powdered mixtures of the starting components, subjected to prolonged heat treatment or the slow-cooling method [3, 13]. However, variations in sample preparation conditions lead to discrepancies in structural study results. Thus, developing synthesis methods that ensure the production of homogeneous, single-phase, and well-crystallized samples is crucial.

It is known that at room temperature, $Cu_{2-x}S$ compounds often exist as two-phase systems. The most characteristic phases include the orthorhombic modification of the anilite type ($Cu_{1.75}S$, space group P_{nma}) and the monoclinic modification of the yarrowite type ($Cu_{1.96}S$, space group $P2_{1/n}$). These phases are close in both composition and unit cell parameters, making their identification by microstructural methods particularly challenging. Additionally, many compositions exhibit a metastable high-temperature cubic (FCC) modification.

Previous studies have shown that phase transformations in $Cu_{1.75}S$, $Cu_{1.80}S$, and $Cu_{1.90}S$ compounds exhibit different characteristics. Even small variations in copper content led to changes in both transition temperatures and transformation sequences [1,3]. This highlights the high sensitivity of the crystal structure to defect concentration and confirms the complexity of the phase behavior in digenite.

In this context, systematically investigating structural transformations in $Cu_{1.85}S$, a composition lying between the previously studied phases, is of particular interest. This study will help refine the understanding of phase stability within the $Cu_{2-x}S$ system, trace regularities in structural variations with respect to copper content, and elucidate the mechanisms of reversible phase transitions.

The objective of this work is to synthesize and grow $Cu_{1.85}S$ single crystals, perform comprehensive microstructural and X-ray phase analyses, and investigate temperature-dependent structural transformations from room temperature to 420°C.

MATERIALS AND METHODS

Synthesis of nonstoichiometric $Cu_{2-x}S$ compounds. Synthesis of nonstoichiometric $Cu_{2-x}S$ compounds. There is no single method reported in the literature for the synthesis of nonstoichiometric compounds of the $Cu-S$ system.

Cite as: J.I. Ismayilov, Kh.Kh. Hashimov, O.A. Aliyev, East Eur. J. Phys. 2, 341 (2026), https://doi.org/10.26565/2312-4334-2026-2-35

Some authors used natural crystals, whereas in [4,5,6] samples of the desired phases with various compositions were obtained by mixing the individual components in powder form and then heat-treating. In one case, ampoules containing the corresponding components were held at 593–743 K for 7 days [4]; in another, Cu and S components in the desired stoichiometric ratios were heated to 773–873 K for 24 hours [5]; and in a third case, powdered Cu and S were maintained in an evacuated Pyrex ampoule for 7 days at 723 K [6].

In [3], pressed powders of Cu_2S and CuS were placed in an open glass ampoule and annealed for 12 hours at 383 K. In [10,11,12], samples of some nonstoichiometric $Cu-S$ compositions were obtained using the slow-cooling method.

An analysis of these studies shows that the existing discrepancies in structural investigations are primarily determined by the different conditions used to prepare various nonstoichiometric $Cu-S$ samples.

To obtain homogeneous samples of composition $Cu_{1.85}S$, we employed the direct synthesis method, i.e., the chemical reaction of the starting components. Double-walled ampoules made of high-quality quartz, possessing high thermal stability, were used as reactors. The main ampoules, with an inner diameter of 1.5 cm and a length of 10 cm, were filled with the starting materials – Cu (electrolytic) and S (grade “Ultra-pure”) in the required amounts for each composition – and evacuated to a pressure of 10^{-5} mmHg.

All ampoules containing the respective compositions were placed in the stable zone of the furnace. The furnace temperature was raised to the melting point of sulfur ($393\ K$) and maintained at this temperature for 3 hours to ensure thorough interaction of molten sulfur with copper and to prevent ampoule rupture. The temperature was then increased at a rate of 50 K per hour up to the melting point of Cu_2S ($1403\ K$) with cyclic vibration. After a two-hour dwell at this temperature, the ampoules containing the samples were slowly cooled to $373\ K$ and annealed at this temperature for 300 hours to achieve homogenization, while the phase composition was monitored using microstructural and X-ray phase analyses.

Growth of $Cu_{1.85}S$ Single crystals. Given that nonstoichiometric $Cu_{2-x}S$ compounds are defect-containing crystals, the optimal method for obtaining single crystals of the desired $Cu_{1.85}S$ composition was determined experimentally to be a combination of the Bridgman method and slow cooling.

The synthesized $Cu_{1.85}S$ compositions were placed in specially designed high-quality quartz ampoules tailored for the Bridgman technique (length: 10 cm, inner diameter: 1 cm). The ampoules were evacuated to a pressure of 10^{-5} mmHg and subsequently placed in a two-zone furnace, where a temperature controller maintained the desired temperature. The furnace temperature was gradually increased above the melting point of Cu_2S. Following a three-hour dwell at this temperature, an electric motor was activated to lower the ampoule at a rate of 6 mm/h. Once the ampoule reached the lower zone of the furnace, it was transferred to an electric furnace and annealed at 573 K for 3 weeks. This annealing process corresponds to the lower zone of the two-zone furnace.

The samples obtained via this method were high-quality single crystals, exhibiting well-defined structural properties suitable for subsequent analysis.

Microstructural analysis. To reveal the microstructures, samples were prepared from each of the synthesized $Cu_{1.85}S$ composition. The surfaces of all samples were washed, degreased with ethanol, and dried after grinding and polishing. Experimentally, an etchant consisting of $50\%\ HNO_3\ +\ 50\%\ H_2O$, with the addition of 5% acetic acid to prevent oxidation was selected.

Microstructural analysis. To reveal the microstructures of the synthesized $Cu_{1.85}S$ compositions, samples were carefully prepared by grinding and polishing the surfaces of each specimen. Once polished, the samples were washed, then degraded with ethanol to remove surface contaminants, and finally dried. To reveal the structural details, an etching solution was applied to the samples. The etching solution consisted of 50% nitric acid (HNO_3) and 50% distilled water (H_2O), with 5% acetic acid added to prevent oxidation of the sample surface during etching.

This microstructural preparation method ensured the samples were adequately prepared for further analysis. The etchant enabled the identification of key microstructural features, including grain boundaries, phase distribution, and lattice defects, providing important insights into the overall quality and homogeneity of the synthesized $Cu_{1.85}S$ single crystals.

Debye-Scherrer patterns for all synthesized compositions were obtained using Cu Kα radiation under identical conditions. The calculations and indexing of interplanar spacings (see Tables 1-3) indicated that in $Cu_{1.85}S$ crystals, a second phase appears at room temperature. The amount in this second phase decreases as copper deficiency increases. Furthermore, in all $Cu_{1.85}S$ crystals, a metastable high-temperature face-centered cubic (FCC) phase also exists at room temperature.

The first phase in these compositions corresponds to anilite ($Cu_{1.75}S$), which crystallizes in an orthorhombic structure with unit cell parameters: $a = 7.89$ Å, $b = 7.84$ Å, and $c = 11.01$ Å, belonging to the space group Pnma, with $Z = 4$ formula units per unit cell. The second phase corresponds to yarrowite ($Cu_{1.96}S$), which crystallizes in a monoclinic structure with unit cell parameters: $a = 26.897$ Å, $b = 15.745$ Å, $c = 13.565$ Å, $\beta = 90.13°$, and space group $P2_1/n$. The unit cell contains 8 $Cu_{31}S_{16}$ formula units.

Due to the close composition and similar unit cell parameters of these two phases, distinguishing them in micrographs is practically impossible. However, their identification is essential as the two-phase nature of $Cu_{1.85}S$ at room temperature significantly influences the material's structural properties.

For the study of structural transformations, flat-parallel crystals were cleaved from the two-phase sample along the (111) cleavage plane, which corresponds to the high-temperature FCC phase. Diffraction measurements were taken from crystals mounted on a temperature-controlled stage of the diffractometer. At room temperature, nine diffraction peaks were recorded (see Table 3). These diffraction peaks are consistent with the existence of both phases.

Upon heating the crystal without changing its orientation, subsequent diffraction recordings were made at various temperatures. At higher temperatures, four of the nine diffraction peaks transitioned to tetragonal symmetry, indicating the formation of an intermediate phase. The equilibrium temperature between these phases, determined according to the method described in, corresponds to the transformation temperature from the low-temperature yarrowite phase to the intermediate tetragonal phase.

RESULTS AND DISCUSSION

Structural transitions in $Cu_{2-x}S$ crystals ($x = 0.10, 0.20$, and 0.25) were studied in detail in [1]. It was shown that at room temperature, these samples consist of two phases. One of them crystallizes in an orthorhombic lattice with unit cell parameters $a = 7.89$ Å$, b = 7.84$ Å$, c = 11.01$ Å; space group P$_{nma}$, $Z = 4$ [2]. The second phase has a monoclinic lattice with parameters $a = 26.897$ Å$, b = 15.745$ Å$, c = 13.565$ Å$, \beta = 90°\,08', Z = 8$ $Cu_{31}S_{16}$; space group $P2_{1/n}$, corresponding to the yarrowite ($Cu_{1.96}S$) lattice described in the literature [3].

For the samples of the specified compositions, the structural data and transformation temperatures are presented in Table 1. As in Table 1, the sequence of structural transformations in Cu$_{1.75}$S and Cu$_{1.80}$S samples is identical, whereas the transitions in Cu$_{1.90}$S occur according to a different sequence. In the Cu$_{1.75}$S and Cu$_{1.80}$S samples, the first phase (α_1) corresponds to the tetragonal phase, followed by a transformation to a second phase (α_2) at a higher temperature. The sequence of transformations for these samples is consistent, with α_1 transforming to α_2 at 116°C and 104°C, respectively. In contrast, the Cu$_{1.90}$S sample exhibits a distinct transformation pattern, with its first phase (α_1) remaining stable until a much higher transition temperature is reached.

Table 1. Structural and temperature transformations in $Cu_{2-x}S$ [1-3].

Composition	Phase	Transformation temperature, °C	Intermediate phases	Temperature of the intermediate transformation, °C	Lattice parameters of the high-temperature phase
$Cu_{1.75}S$	α_1	35	Tetragonal	116	(FCC) ($a = 5.5$)
	α_2	80			
$Cu_{1.80}S$	α_1	38	»	118	(FCC) ($a = 5.58$ Å)
	α_2	83			
$Cu_{1.90}S$	α_1	-	Orthorhombic + Hexagonal Close-Packed (HCP) ($a_{hex} = 3.97$ Å; $c_{hex} = 6.69$ Å)	157	(FCC) ($a = 5.62$ Å)
	α_2	104			

It was of interest to investigate how the structure and the sequence of structural transformations vary with the composition, specifically from Cu$_{1.80}$S to Cu$_{1.90}$S, as demonstrated by the X-ray study of structural transformations in these compounds.

The main X-ray measurements were carried out using an "Enraf-Nonius" goniometer and a D8 ADVANCE diffractometer (Cu Kα radiation; $5^{\circ} \leq 2\theta \leq 100^{\circ}$), operating in the temperature range from room temperature to $420\ °C$, with the use of the EVA and Topas 4.2 software packages supplied with the diffractometer.

To determine the unit cell parameters and the crystal system of the $Cu_{1.85}S$ single crystal at room temperature, a Weissenberg photograph of the zero-layer line along the ($1\bar{1}0$) direction [1] and a powder pattern were recorded, the calculation of which is presented in Table 2 (diffraction lines of the α$_2$-phase were indexed based on a pseudo-monoclinic crystal system).

Table 2. Recording of the $Cu_{1.85}S$ debaegram (sample radius – 0.8 mm; Cu Kα radiation, Ni filter)

No. lines	d_{exsp}, Å		α_1 **- phase**		α_2**- phase**	
		I/I	$d_{theoretical}$, Å	hkl	$d_{theoretical}$, Å	hkl
1	3.334	2	3.3239	013	3.3183	233
2	3.209	8	3.2066	202	3.2172	214
3	2.960	1	2.9600	122	2.9505	143
4	2.770	1	2.7807	220	2.7855	234
5	2.681	4	2.6870	203	2.6736	015
6	2.540	3	2.5368	123	2.5371	253(704)
7	2.417	1	2.4201	131	2.4202	505
8	2.365	6	2.3731	302	2.3714	235
9	2.260	4	2.2617	132	2.2608	006
10	2.172	1	2.1692	214	2.1701	316(026)
11	2.132	5	2.1372	231	2.1349	072(470)
12	2.023	10	2.0258	232	2.0219	336(255)
13	1.866	8	1.8654	215	1.8675	407(265)
14	1.821	1	1.8280	331	1.8193	482(256)
15	1.743	2	1.7426	116	1.7425	483
16	1.690	1	1.6963	413	1.6956	008
17	1.670	9	1.6723	242	1.6720	384(218)
18	1.652	1	1.6505	315	1.6512	547(057)
19	1.600	1	1.6033	404	1.6016	457(238)

No. lines	d_{exsp}, Å		α_1 **- phase**		α_2**- phase**	
		I/I	$d_{theoretical}$, Å	hkl	$d_{theoretical}$, Å	hkl
20	1.551	2	1.5506	325	1.5510	476(3.10.0)
21	1.442	2	1.4419	0.53	14400	239(748)
22	1.385	4	-	-	1.3836	3.11.2(096)
23	1.305	3	1.3067	0.60	1.3045	3.11.4(0.12.1)
24	1.287	1	1.2878	254	1.2878	4.12.0
25	1.265	2	1.2644	353	1.2651	4.12.2
26	1.204	1	1.2049	318	1.2037	4.12.4
27	1.140	6	1.1411	256	1.1406	0.13.4(5.13.3)
28	1.119	3	1.1188	633	1.1188	4.12.6
29	1.087	2	1.0867	641	1.0873	6.14.1(5.14.2)
30	1.072	3	1.0721	455	1.0723	4.12.7
31	0.989	5	0.9893	636(800)	0.9896	5.14.6(0.12.9)
32	0.947	7	0.9462	654	0.9465	5.16.3(3.15.6)

Analysis of the Debye and Weissenberg patterns reveals that, as in the case of $Cu_{1.75}S$, $Cu_{1.80}S$, and $Cu_{1.90}S$, two systems of reflections are observed. One of these corresponds to the $Cu_{1.85}S$ sample, which possesses an orthorhombic lattice with unit cell parameters: α = 7.94 Å, b = 7.86 Å, c = 11.12 Å, and space group Pbnm, while the other corresponds to variscite.

For the study of structural transformations, flat-parallel $Cu_{1.85}S$ crystals were cleaved from the two-phase sample along the cleavage plane (111), which belongs to the high-temperature FCC phase. From a crystal mounted on the diffractometer's temperature stage, nine diffraction peaks were recorded at room temperature (see Table 3).

Table 3. Calculations of the $Cu_{1.85}S$ Diffractogram; Cu Kα Radiation

$No.$ lines	$\theta, °$	$d,$Å	$hkl\ (\alpha_1)$	$hkl\ (\alpha_2)$	Unit Cell Parameters	$t, °C$
1	13°22'	3.334	013	233	α_1 - Phase ($a = 7.84;\ b = 7.89;\ c = 11.01$ Å)	22
2	13°53'	3.209	202	214		
3	16°43'	2.680	203	015		
4	26°15'	1.743	116	483		
5	27°20'	1.679	242	384	α_2- Phase ($a = 26.864$ Å; $b = 15.759$ Å; $c = 13.565$ Å; $\beta = 90.13°$)	
6	28°40'	1.607	404	457		
7	43°33'	1.119	633	4.12.6		
8	45°10'	1.087	641	6.14.1		
9	45°58'	1.072	455	4.12.7		
1	13°50'	3.224	102		Tetragonal ($a = 4.00;\ c = 11.18$ Å)	100
2	26°16'	1.742	203			
3	28°34'	1.612	204 (007)			
4	45°46'	1.076	323			
1	13°48'	3.232	111		FCC ($a = 5.603$ Å)	150
2	28°27'	1.618	222			
3	45°37'	1.079	333			

Then, without changing the crystal orientation, control recordings were performed every $10\ °C$ to observe changes in the diffraction pattern. Only at $100\ °C$ were four out of nine diffraction peaks recorded (see Table 3), which can be indexed on the basis of a tetragonal symmetry. The equilibrium temperature between the phases, $t = (93 \pm 1)\ °C$ (determined according to the method described in [4]), corresponds to the transformation temperature of the low-temperature yarrowite phase into the intermediate phase.

The intermediate tetragonal phase in $Cu_{1.85}S$ transforms into a phase with a face-centered cubic (FCC) lattice at $(120 \pm 1)\ °C$ (see Table 3). A series of temperature-dependent diffractometric recordings and Laue photographs taken before and after each transformation showed that all structural transitions in the $Cu_{1.85}S$ single crystal are reversible, with rigid orientational relationships between the lattices of the modifications, and that the transitions occur via a single-crystal-to-single-crystal mechanism.

Once the temperatures and the number of structural phase transitions were determined, Weissenberg photographs of each phase were taken at $t_1 > 93\ °C$ and $t_2 > 120\ °C$.

Zero-layer line projections were obtained by rotating the crystal around the direction that, at temperatures above $120\ °C$, corresponds to the $(1\bar{1}0)$ direction of the FCC lattice.

The Weissenberg photograph recorded at room temperature contains two systems of reflections, corresponding to the α_1 (orthorhombic) and α_2 (monoclinic) lattices, which merge into a single tetragonal lattice in the Weissenberg photograph obtained at $t_1 > 90\ °C$. The Weissenberg photograph was recorded at $t_2 > 120\ °C$ corresponds to the FCC lattice.

It should be noted that, unlike the first α_1 phase, the α_2 phase is characterized by twins, where each main reflection from the crystal on the radiograph corresponds to a weaker spot arising from rotation of the sample by precisely fixed angles of $70°12'$ and $109°48'$ (angles between the body diagonals of the cube). As in the $Cu_{1.75}S$ and $Cu_{1.80}S$ samples, for the high-temperature form of $Cu_{1.85}S$, the twin lattice nodes can be obtained by mirror reflection in four noncoplanar

(111) planes of the primary cubic lattice or by rotation around the $(1\bar{1}0)$ axes. The elements of twinning are the (111) plane and the $(11\bar{2})$ direction – typical for FCC metals [5].

Upon cooling the sample to room temperature, the diffraction pattern is completely restored in reverse sequence; that is, the single FCC phase passes through the intermediate tetragonal phase and transforms into a mixture of monoclinic and orthorhombic phases. The formation of two phases at room temperature is explained as follows. The anion lattice is fully occupied by sulfur atoms, while the copper atom positions are nonequivalent. Therefore, during the transition from the intermediate phase to the low-temperature phase, some copper atoms can accumulate in the twin regions, where a structure closer to the stoichiometric composition, i.e., $Cu_{1.96}S$, is formed. The amount of the $Cu_{1.96}S$ phase is minimal for $Cu_{1.75}S$ and increases as the alloy's copper deficiency decreases.

From this, it follows that digenite and yarrowite occupy different concentration ranges.

CONCLUSIONS

1. The $Cu_{1.85}S$ single crystal at room temperature consists of two coexisting phases: an orthorhombic (Pnma) phase and a monoclinic ($P2_1/n$) phase. This biphasic nature is attributed to the non-uniform distribution of copper atoms, which accumulate in twin regions, thereby contributing to the material's structural complexity.

2. X-ray phase analysis demonstrated the occurrence of two consecutive, reversible phase transitions in $Cu_{1.85}S$. The first transition occurs from the orthorhombic phase to an intermediate tetragonal phase at approximately 93°C, followed by a transformation to a high-temperature face-centered cubic (FCC) lattice at around 120°C. These transitions are well-defined and occur via a single-crystal-to-single-crystal mechanism.

3. The phase transitions in $Cu_{1.85}S$ are characterized by preserved orientational relationships between the lattices, indicating high structural order. The transitions are reversible and exhibit stable interphase transitions, with their behavior strongly influenced by the copper content, confirming the sensitivity of the material's structural properties to composition variations.

ORCID

Kh.Kh. Hashimov, https://orcid.org/0009-0002-9674-5578; **O.A. Aliyev,** https://orcid.org/0009-0000-5699-3054

REFERENCES

[1] N. Alsen, “Über Kristallstrukturen von Covelline (CuS) und Kupferglanz (Cu_2S),” Geologiska Föreningens I. Stockholm Förhandlingar, **53**, 111–120 (1931).
[2] P. Rahlfs, “Über die kubischen Hochtemperaturmodifikationen der Sulfide, Selenide und Telluride des Silbers und des einwertigen Kupfers,” Zeitschrift für Physikalische Chemie, (B), **31**, 157–194 (1936).
[3] M.J. Buerger, aand N.W. Buerger, “Low Chalcocite and High Chalcocite,” American Mineralogist, **29**(1–2), 55–65 (1944).
[4] S. Djurle, “An X-ray Study on the System Cu-S,” Acta Chemica Scandinavica, **12**(7), 1415–1427 (1958). https://doi.org/10.3891/acta.chem.scand.12-1415
[5] E.H. Roseboom, “An Investigation of the System Cu-S and Some Natural Copper Sulfides between 25 and 700°C,” Economic Geology, **61**(1), 641–672 (1966). https://doi.org/10.2113/gsecongeo.61.4.641
[6] O. Kimihiko, and K. Shichie, “Electrical Conduction and Phase Transformation of Copper Sulfides,” Journal of the Physical Society of Japan, **16**(8), 1130–1138 (1973).
[7] W. Kurz, “Chemisch-röntgenographische Untersuchungen an Kuban Kupferglanz,” Zeitschrift für Kristallographie - Crystalline Materials, **92**(1-6), 408–434 (1935). https://doi.org/10.1524/zkri.1935.92.1.408
[8] Kh.Kh. Hashimov, and N. Suleymanov, “Diffractometric Study of Structural Phase Transformations in $Cu_{2-x}S$ and $Cu_{2-x}Fe_{0.05}S$ Crystals,” Advanced Physical Research, **7**(1), 123-132 (2025). https://doi.org/10.62476/apr.71123
[9] T. Howard, and I. Evans, “The crystal structures of low chalcocite and djurleite,” Zeitschrift für Kristallografie, **150**, 299–320 (1979). https://doi.org/10.1524/zkri.1979.150.14.299
[10] Hashimov Kh.Kh. T.M. Isayeva, "X-ray Graphic Study of Structural Transformations in Crystals of Cu_2–x$Ni_{0.05}S$ (x = 0.05, 0.25, 0.30),” New Materials Compounds and Applications, **8**(1), 121-134 (2024). https://doi.org/10.62476/nmca8121
[11] Kh.Kh. Hashimov, “Synthesis of $Cu_{2-x}Ni_{0.5}S$ (x = 0.05, 0.25, 0.30) Compounds and Study of Single Crystals”, Asian Journal of Physical and Chemical Sciences, **11**(3), 45-51 (2023). https://doi.org/10.9734/AJOPACS/2023/v11i3205
[12] Kh.Kh. Hashimov, “Investigation of Crystal Structure and Polymorphic Transformations of Cu-S System Compounds,” in: *V International Scientific and Practical Conference “Modern Science: Actual Problems*”, (Manchester, UK, 2023), pp. 55-59. https://doi.org/10.5281/zenodo.7950997
[13] Kh.Kh. Hashimov, “Investigation of Polymer Transformations in Crystals,” in: *International Scientific-Practical Conference on Mathematical Methods and Mechatronic Systems in Engineering*, (2023), pp.25–27.

СТРУКТУРНІ ПЕРЕХОДИ В МОНОКРИСТАЛАХ $Cu_{1,85}S$

Дж.І. Ісмайлов[1], Х.Х. Гашімов[1], О.А. Алієв[1,2]
[1]*Азербайджанський державний університет нафти та промисловості, проспект Азадлік, 34, Баку AZ1010, Азербайджан*
[2]*Міністерство науки та освіти, Азербайджанська Республіка, Інститут фізики,*
проспект Х. Джавіда, 131, AZ-1143 Баку, Азербайджан

$Cu_{1,85}S$ представляє значний сучасний інтерес завдяки своїй складній кристалохімії, широкому діапазону однорідності та унікальним фізико-хімічним властивостям. Ці матеріали належать до класу дигенітів і демонструють різні структурні перетворення та оборотні фазові переходи, які є дуже чутливими до вмісту міді. Синтез, вирощування та дослідження структурної поведінки монокристалів $Cu_{1,85}S$ дають важливе розуміння фазової стабільності та механізмів перетворення в системі $Cu_{2-x}S$. Такі знання є вирішальними для потенційного застосування в напівпровідникових пристроях, каталізаторах та системах перетворення енергії, де кристалічна структура та фазовий склад безпосередньо впливають на характеристики матеріалу. У цій статті представлені результати синтезу, вирощування монокристалів та рентгенофазового аналізу нестехіометричної сполуки $Cu_{1.85}S$, яка належить до класу дигенітів. Монокристали були отримані шляхом поєднання методу спрямованої кристалізації Бріджмена з повільним охолодженням. Було проведено комплексний мікроструктурний та рентгеноструктурний аналіз, включаючи використання фотографій Вайсенберга та температурно-залежних дифракційних досліджень в діапазоні від кімнатної температури до 420°C. Було встановлено, що за кімнатної температури зразок $Cu_{1,85}S$ є двофазним і складається з орторомбічної (Pnma) та моноклінної $P2_{1/n}$ фаз. При нагріванні спостерігалися два структурні переходи: спочатку до тетрагональної фази приблизно при 93°C, а потім до високотемпературної гранецентрованої кубічної (ГЦК) решітки приблизно при 120°C. Усі переходи є оборотними та відбуваються за механізмом від монокристала до монокристала з чітко визначеними орієнтаційними зв'язками між ґратками. Двофазний характер за кімнатної температури пояснюється накопиченням атомів міді в двійникових областях. Ця робота сприяє розумінню структурних перетворень у системі $Cu_{1.85}S$ та підтверджує існування стабільних міжфазних переходів, залежних від вмісту міді.

Ключові слова: *кристал; фазові переходи; рентгенівська дифракція; дигеніт; ґратка*

East European Journal of Physics. **2.** 347-351 (2026)
DOI:10.26565/2312-4334-2026-2-36 ISSN 2312-4334

STRUCTURAL STUDY OF COPPER DOPED SINGLE-CRYSTAL SILICON BY DIFFUSION

Akramjon Y. Boboev[1], **Sherzod A. Makhmudov**[2], **Shukhrat K. Makhkamov**[1], **Nuritdin Y. Yunusaliyev**[1], **Murodiljon M. Xotamov**[1], **Mokhirabonu M. Arabboeva**[1]
[1]*Andijan state university named after Z.M. Babur, Andijan, Uzbekistan*
[2]*Institute of Nuclear Physics Academy of Sciences of the Republic of Uzbekistan*
**Corresponding Author e-mail: aboboevscp@gmail.com*

Received February 21, 2026; revised March 26, 2026; accepted April 16, 2026

The paper presents the results of a structural study of single-crystal silicon doped with copper by thermodiffusion at 1423K. The object of the study was n-Si crystals grown by the Czochralski method, containing SiO_2 oxygen precipitates. Structural analysis was performed on an X-ray diffractometer with an improved optical scheme, which made it possible to detect weak additional reflections and changes in lattice parameters. It was established that copper doping leads to the appearance of elastic stresses in the surface layers of the crystal, a change in the interplanar distance (111) and a redistribution of the intensities of reflections (222) and (333). Diffuse scattering and additional selective reflections were detected, indicating the formation of new phases. For the first time, a direct structural method has shown the formation of CuO nanocrystals with a monoclinic structure and an average size of 14–14.5 nm and Cu_2O nanocrystals with a cubic structure and an average size of about 17 nm. Their lattice parameters were measured experimentally and are slightly different from the standard reference values, which shows that the silicon matrix and internal stresses affect their structure. It has been shown that SiO_2 oxygen precipitates create local elastic fields that promote diffusion, nucleation, and separation of copper in the form of oxide nanophases. The results obtained clarify the mechanism of structural transformations in copper-doped silicon.

Keywords: *X-ray diffraction; Subcrystallite, Nanocrystal; Copper-doped silicon; Thermal diffusion; Copper oxides; Oxygen precipitates*
PACS: 61.72.Ss

INTRODUCTION

In the production of semiconductor devices, doping is one of the most important technological processes, along with etching and deposition. The main purpose of doping is to change the type of conductivity and concentration of carriers in the semiconductor volume to obtain the specified electrical properties (conductivity and the required smoothness of the p-n junction) [1]. The introduction of foreign atoms, including those that diffuse rapidly into the silicon lattice, causes stress within the crystal and, as a result, a change in the lattice parameters. Since the movement of impurity atoms occurs with the participation of intrinsic point defects (vacancies and interstitial silicon atoms), diffusion will lead to a change in the equilibrium concentration of point defects, resulting in most cases in the formation of precipitates, usually in the form of a compound of impurities with silicon atoms [2]. Such precipitates can create sufficiently large stresses, leading to the formation of new defects. At high temperatures, particularly in the presence of SiO_2 particles, the local stresses are strong enough to attract rapidly diffusing impurities (e.g., copper, gold, and iron), which promotes their precipitation and leads to the formation of dislocation clusters. In particular, the presence of such particles is associated in the literature with the occurrence of defects in the form of a star with a central core from which complex-shaped dislocations propagate [3].

Copper impurities in silicon have attracted the attention of researchers since the advent of silicon technology. This interest is driven both by academic curiosity about the unusual properties of this *3d* transition metal and by its practical importance. The latter is determined by the fact that copper easily precipitates, forming electrically active centres that degrade the parameters of electronic devices. To avoid unwanted precipitation, it is necessary to understand, in particular, the process of nucleation. However, to date, only the properties of isolated copper atoms in silicon (interstitial Cu_i and in the substitution position Cu_s) have been studied sufficiently well, while there is no reliable identification for most even the simplest copper aggregates with background and other alloying impurities [4,5]. The concentrations at which copper and other rapidly diffusing impurities form precipitates are too low to be determined by conventional analytical methods. At the same time, even at a concentration of $2\cdot10^{-4}$ %, these impurities can cause noticeable structural changes after annealing the crystal at a high temperature (> 900°C). The difficulty of determining small amounts of metallic impurities in silicon (e.g., copper and similar) is a long-standing problem in semiconductor technology. Often, the presence of rapidly diffusing impurities is detected only by their effect on the distribution of crystallographic defects or on the electrical properties of the crystal [6,7].

Below, experimental results of structural studies of copper-doped silicon single crystals are presented for the first time. The aim of the work is to determine the structural perfection of single crystals, to establish the formation of copper aggregates with background impurities and their types using an X-ray diffractometer with an improved optical scheme.

Cite as: A.Y. Boboev, Sh.A. Makhmudov, Sh.K. Makhkamov, N.Y. Yunusaliyev, M.M. Xotamov, M.M. Arabboeva, East Eur. J. Phys. 2, 347 (2026), https://doi.org/10.26565/2312-4334-2026-2-36

MATERIALS AND METHODS

The objects of the study were n-Si (KEF) single crystals grown by the Czochralski method with a resistivity $\rho_o \approx (3 \div 10)\ \Omega\cdot$cm, dislocation density $N_D \approx 10^1 \div 10^3$ cm^{-2}, and oxygen concentration $N_O \approx 2 \div 4\cdot 10^{17}$ cm^{-3}. Before measurements, the samples underwent mechanical and chemical polishing with removal of a surface layer approximately 20 µm thick and had a working surface (111) with an area of 5.4 ×15.8 mm² and a thickness of 0.6 mm. The samples were doped with copper at a temperature of 1423K using the surface thermodiffusion method. The copper concentration in the samples was 10-14 cm^{-3}. Structural studies were performed on an XRD-7000 X-ray diffractometer (CuK$_\alpha$ radiation, $\lambda = 0.15418$ nm) with an improved optical scheme, according to the Θ–2Θ scheme in step scanning mode at 300 K. The angular dependence of the intensity was measured in two ways: after adjusting the samples for reflection (111) and (333). The intensity of the incident beam was approximately $5\cdot 10^5$ imp·s^{-1}, and the intensity measurement error was ~ 0.6 %. The resistivity was measured using the conventional four-probe method, also at room temperature.

RESULTS AND DISCUSSION

Fig. 1 shows an X-ray diffraction pattern of copper-doped single-crystal silicon - n – Si (Cu), tuned to reflect (111) of the sample. It differs significantly from the X-ray diffraction pattern of unalloyed silicon samples, despite their similarity in appearance. The X-ray diffraction pattern of n-Si (Cu) showed no diffuse reflection at small scattering angles ($2\theta \approx 17.6°$). The intensity of the forbidden reflection (222) ($2\theta = 58.9°$) decreased by 9.5%, and the intensity of the structural line (333) ($d/n = 0.1046$ nm; $2\theta = 95°$) decreased by 11% compared to the intensity of similar reflections from unalloyed samples. In addition, a decrease in the intensity of the $(110)_{SiO2}$ reflection ($d/n = 0.2495$ nm; $2\theta = 36°$) of the impurity phase of crystalline quartz - SiO_2 - was also observed, by 11.5%. As for the intensity and interplanar spacing of the main reflection (111) ($d/n = 0.3143$ nm; $2\theta = 28.4°$), they increased by 2.6% and 0.7%, respectively, compared to the intensity and interplanar distance of the same reflection of the initial sample. The average level of the inelastic background of the n - Si (Cu) sample decreased by 9% compared to the level of the inelastic background of unalloyed silicon.

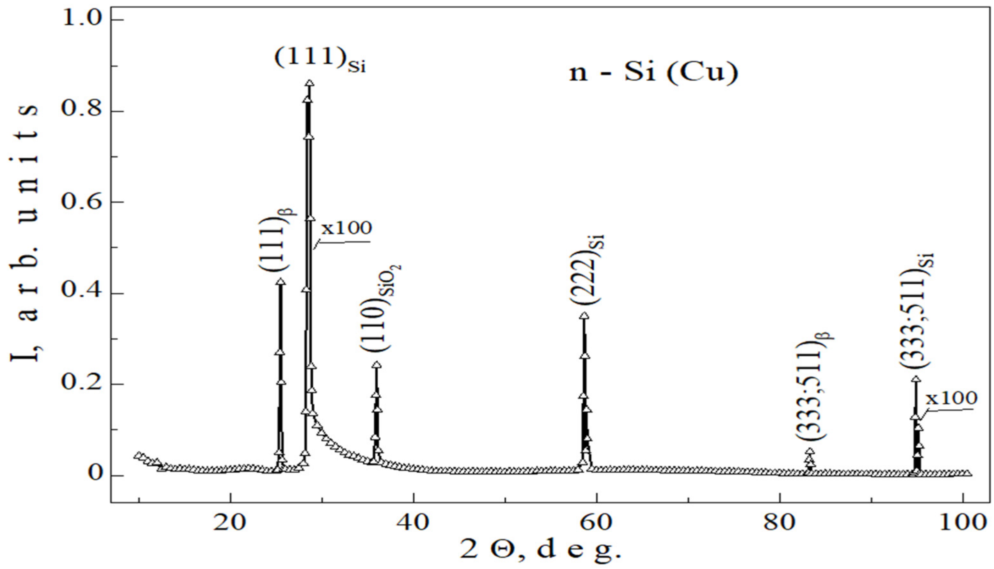

Figure 1. X-ray diffraction pattern of copper-doped single-crystal n-Si

In addition, diffuse scattering with weak intensity in the middle scattering angles with $d/n \approx 0.1467$ nm; $2\theta \approx 63.4°$ was detected on the X-ray diffraction pattern of copper-doped samples. Precision measurement showed the presence in this angle range against the background of diffuse reflection, in addition to the forbidden reflection (222) of silicon, of three additional selective reflections ($d/n = 0.1707$ nm; $2\theta = 53.7°$; $d/n = 0.1572$ nm; $2\theta = 58.6°$; $d/n = 0.1361$ nm; $2\theta = 69°$) with weak intensity from an unknown phase. The X-ray diffraction patterns of samples tuned to third-order reflection (333) differed from those tuned to first-order reflection (111) in the presence of an additional selective reflection ($d/n = 0.3079$ nm; $2\theta = 29°$) with noticeable intensity on the right wing of the main reflection (111). This reflection is not characteristic of silicon and silicon dioxide single crystals.

The narrow width ($FWHM = 2.62\cdot 10^{-3}$ rad) and high intensity ($2\cdot 10^5$ imp·sec^{-1}) of the main reflection (111) indicate a high degree of perfection of the crystal lattice of doped n-Si (Cu). Structural measurements showed that the cutting plane of the samples corresponded to the crystallographic plane (111). The dimensions of subcrystals (blocks), estimated by the width of this peak using the Selakov–Sherrer method [8], were approximately ~ 57 nm. However, the slight splitting of this reflection into α_1 and α_2 emissions (Fig. 2a) indicates the presence of elastic stresses in the silicon matrix lattice associated with the presence and uneven distribution of oxygen and the possible substitution of silicon atoms by copper atoms in silicon single crystals. Since the ionic radii of silicon, oxygen and copper atoms are $r^{4+}_{Si} = 0.042$, $r_o^{-2} = 0,140$ nm and r^{2+}_{Cu} = 0.072 nm, respectively [9]. Considering the significant chemical activity of copper towards oxygen [10], it can be assumed that molecules of silicon ion pairs are replaced by molecules of copper-oxygen ions in defect-prone areas of the silicon lattice [10]. This conclusion is confirmed by the presence of a forbidden reflection $(222)_{Si}$ with *d/n* = 0.1571 nm on the X-ray diffractogram (Fig. 1, 3), which should be absent for an ideal silicon lattice without elastic stress. In addition, the intensity of the main (111) reflection of doped silicon samples is 2.6% greater than the intensity of the same line in undoped samples. This fact also indicates the partial replacement of some silicon ion pairs with copper-oxygen ion molecules. Since the intensity of X-ray scattering is proportional to the atomic number (Z) of the elements, such ion replacement should lead to an increase in the intensity of this reflection in doped samples, because $Z_{Si} = 14$, $Z_O = 8$, $Z_{Cu} = 29$ [11]. However, with a noticeable increase in the intensity of this reflection, the X-ray diffraction pattern shows a significant decrease in the intensity of its second (222) and third (333) order reflections by 9.5% and 11%, respectively. In addition, an increase in the interplanar distance of the diffraction reflection (111) by 0.7% was observed on the X-ray diffraction pattern of the alloyed samples, which was absent in its higher orders - in the reflections (222) and (333). The almost complete splitting of the (333) reflection, close to the calculated value ($3.79 \cdot 10^{-3}$ rad) with a characteristic ratio of intensities for α_1 and α_2 radiation [$I_{333}(\alpha_1) \approx 2 \cdot I_{333}(\alpha_2)$] (Fig. 2 b) shows the absence of distortion of the silicon lattice in the deeper layers from the surface of the doped samples [12]. All these facts indicate an uneven distribution of copper-oxygen molecules in the lattice of doped samples. Their content in the surface layer is significantly higher than in deeper layers.

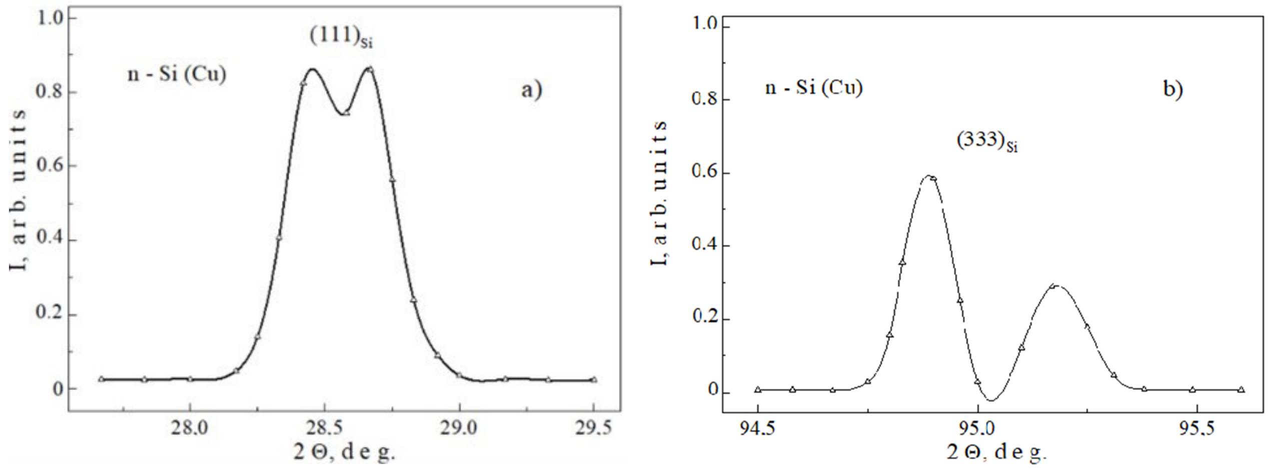

Figure 2. Reflection patterns (111) and (333) of single-crystal n-Si (Cu)

It should be noted that the observed increase in interplanar spacing in the case of structural reflection (111) shows that the arrangement of atoms in the surface layers of doped samples has a noticeable shift from their ideal position in the [111] direction while maintaining the existing initial symmetry, which cannot be said about atoms located in deeper layers. This situation leads to a partial violation of the Wolff-Bragg diffraction condition for high-order reflections (222) and (333). As a result, the normals of high-order atomic planes of the {HHH} type acquire a slightly distorted orientation with respect to the direction of the normals of the near-surface planes (111). This leads to a partial loss of intensity of the diffraction reflections (222) and (333), which is observed in the experiment. In addition, the decrease in the intensity of the (222) and (333) reflections may also be associated with a noticeable increase in primary extinction (weakening of the first-order intensity) for reflections from planes with large indices [13]. The decrease in the intensity of the diffraction reflection (110) of the SiO_2 impurity phase may also be associated with the distortion of its lattice as a result of the partial replacement of Si-O molecules by Cu-O molecules at the boundary areas between the blocks of doped samples.

In copper-doped samples, the presence of the silicon dioxide (SiO_2) impurity phase is indicated by the presence of a diffraction reflection (110) on the X-ray diffractogram with a slightly lower intensity (11.5%) than the intensity of this reflection in undoped samples. The characteristic size of the structural fragments - nanocrystals of the impurity phase - was ~ 75 nm. Such particles can create local elastic stresses around themselves, the magnitude of which is sufficient to attract rapidly diffusing impurities, in particular copper at elevated temperatures, and initiate processes of their separation in the form of clusters or nanoparticles. This assumption is confirmed by the presence of diffuse reflection at medium scattering angles with d/n ≈ 0.1467 nm; 2θ ≈ 63.4° and, against the background of this broad maximum, the presence of three not very narrow structural reflections with weak intensity (Fig. 3-a). Analysis of the nature of these structural lines showed that all these reflections belonged to the same newly formed impurity phase – CuO, which has monoclinic symmetry. They are caused by nanocrystals of this phase with average sizes of $L_{CuO} \approx 14$–14.5 nm. The experimental values of the lattice parameters of this phase were: $a_{exp} = 0.4573$, $b_{exp} = 0.3413$, $c_{exp} = 0.5239$ nm and β = 98.9°, which differ slightly from the tabulated values ($a_{tab} = 0.4662$, $b_{tab} = 0.3417$, $c_{tab} = 0.5118$ nm and β = 99.85°, respectively) [14]. The specific volume of the CuO impurity phase is $V_{CuO} \approx 0.0808$ nm^3, which is two times less than the specific volume of silicon - $V_{Si} \approx 0.160$ nm^3. The difference in specific volume is one of the factors stimulating the formation of copper oxide nanoparticles in a silicon environment.

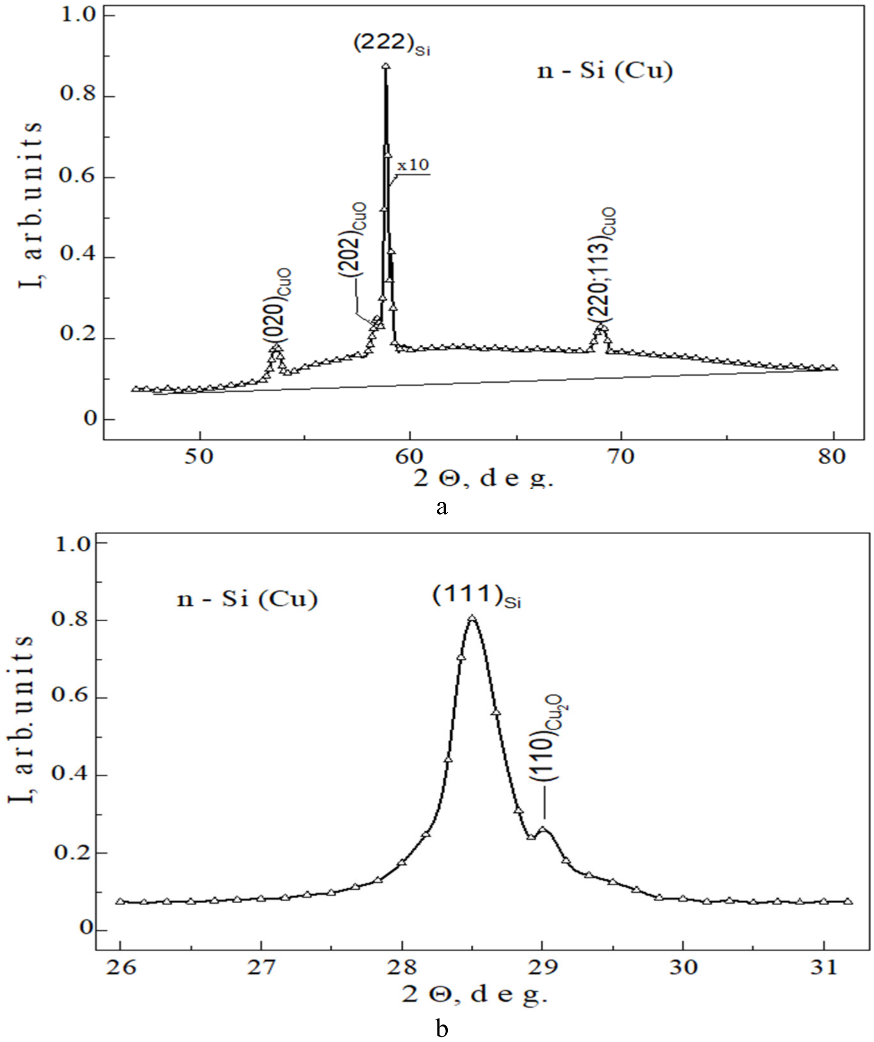

a

b

Figure 3. (a) Section of the X-ray diffraction pattern of single-crystal n-type Si doped with copper. (b) The sample is aligned for the (111) reflection

The X-ray diffraction pattern of the same sample, but tuned to reflection (333), did not differ significantly from the X-ray diffraction pattern tuned to reflection (111). Only a strong loss of intensity of the main reflection (111) (~ 3 times) and the appearance of a new selective reflection from an unknown phase on its right wing (Fig. 3-b). Analysis of the nature of the new reflection showed that nanocrystals of copper monoxide – Cu_2O, which has cubic symmetry, caused it. The characteristic dimensions of the nanocrystals are ~ 17 nm. The experimentally determined lattice parameter of copper monoxide was $a_{exp} = 0.4354$ nm, which slightly exceeds the tabulated value $a_{tab} = 0.4263$ nm [15].

CONCLUSIONS

In this work, the structure of single-crystal silicon doped with copper by thermodiffusion at a temperature of 1200°C was studied using X-ray diffraction. The results showed that when copper atoms are introduced into the silicon crystal lattice, elastic stresses arise in the surface layers and the interplanar distances change slightly. The study revealed the formation of new phases - nanocrystals of CuO and Cu_2O oxides. Their average sizes were approximately 14 - 15 nm and about 17 nm, respectively. It was also shown that SiO_2 oxygen precipitates promote copper diffusion and the formation of oxide nanophases. The results obtained provide a better understanding of the mechanism of structural transformations in copper - doped silicon and create a scientific basis for controlling such processes in semiconductor technologies.

Conflict of Interests

The authors declare that they have no conflict of interests

Funding

The present research work was financed under project FZ-292154210 granted by the Ministry of Higher Education, Science and Innovations of the Republic of Uzbekistan.

ORCID

A.Y. Boboev, https://orcid.org/0000-0002-3963-708X; **Sh.A. Makhmudov,** https://orcid.org/0009-0003-6539-9278;
Sh.K. Makhkamov, https://orcid.org/0009-0002-3491-4380; **N.Y. Yunusaliyev**, https://orcid.org/0000-0003-3766-5420;
M.M. Arabboeva, https://orcid.org/0009-0008-5181-4844; **Murodiljon M. Xotamov,** https://orcid.org/0009-0003-6011-4405

REFERENCES

[1] Utamuradova S., Daliev S., Khamdamov J., Matchonov K and Khaitbaev A. “Phase Transformations and Structural Transformations of Manganese Silicides in the Si-Mn System,” East European Journal of Physics, (4), 484-495 (2025). https://doi.org/10.26565/2312-4334-2025-4-49

[2] Boboev A. Y., Ergashev B. M., Yunusaliyev N. Y., and Xotamov M. M. “Study of the Formation of Low-Dimensional Defect States in Single-Crystal Silicon with the Participation of Oxygen,” East European Journal of Physics, (2), 299–306 (2025). https://doi.org/10.26565/2312-4334-2025-2-36

[3] Lin C.-Y., Zhao Z., Niu J., and Xia Z. “Synthesis, Properties and Applications of 3D Carbon Nanotube–Graphene Junctions,” *Journal of Physics D: Applied Physics*, 49, 443001 (2016). https://doi:10.1088/0022-3727/49/44/443001

[4] Fukuoka N. “New Donor Formation in n-Type Czochralski–Crown Silicon,” Japanese Journal of Applied Physics, **24**, 1450-1453 (1985). https://doi.org/10.1143/JJAP.24.1450

[5] Istratov A. A. and Weber E. R. “Electrical Properties and Recombination Activity of Copper, Nickel and Cobalt in Silicon,” Applied Physics A: Materials Science & Processing, **66**, 123–136 (1998). https://doi.org/10.1007/s003390050649

[6] Sabah S., Le T. T., Zhou Z., Sun C., Wang Y., Fu N., Rougieux F., and Liu A. “Recombination Activity of Chromium–Gallium Pairs in Silicon,” Solar Energy Materials and Solar Cells, **271**, 113989 (2025). https://doi.org/10.1016/j.solmat.2025.113989

[7] Isaev M. Sh., Asatov U. T., Tulametov M. A., Kodirov S. R., Rajabov A. E., “Study of the Inhomogeneities of Overcompensed Silicon Samples Doped with Manganese,” East European Journal of Physics, (2), 341–344 (2024). https://doi.org/10.26565/2312-4334-2024-2-40

[8] Zainabidinov S. Z., Boboev A. Y., Rasulova M. B., Yunusaliyev N. Y., “X-Ray Diffraction Analysis, Optical Characteristics and Electro-Physical Properties of the n-ZnO/p-NiO Structure Grown by the Spray Pyrolysis Method,” *New Materials, Compounds and Applications*, **8**(3), 411–421 (2024). https://doi.org/10.62476/nmca83411

[9] Shannon R. D. “Revised Effective Ionic Radii and Systematic Studies of Interatomic Distances in Halides and Chalcogenides,” Acta Crystallographica Section A, **32**, 751–767 (1976). https://doi.org/10.1107/S0567739476001551

[10] Chen P., Li Y., Qin F., An T., Dai Y., Zhang M., Liu M., Zhang L., “First-Principles Study of Copper Contamination in Silicon Semiconductor,” Surfaces and Interfaces, **31**, 102084 (2022). https://doi.org/10.1016/j.surfin.2022.102084

[11] Murin, L. I., Medvedeva, I. F., & Markevich, V. P. (2010). Interaction of copper atoms with radiation-induced defects in silicon. *Inorganic Materials*, **46**(4), 333–338. https://doi.org/10.1134/s0020168510040011

[12] Karimov M., Machkamov Sh., Tursunov N. A., Bakiev S. A., Machmudov Sh. A., Sattiev A. R., Akramov F. S., “Formation of Copper Impurity-Defect Complexes and Their Impact on Electrical Properties of Silicon,” Russian Physics Journal, **57**(1), 63–68 (2014). https://doi.org/10.1007/s11182-014-0208-8

[13] Pateras A., Park J., Ahn Y., Tilka J. A., Holt M. V., Kim H., Mawst L. J., and Evans P. G. “Dynamical Scattering in Coherent Hard X-Ray Nanobeam Bragg Diffraction,” Physical Review B, **97**, 235414 (2018). https://doi.org/10.1103/PhysRevB.97.235414

[14] Villars P. and Cenzual K. “Pearson’s Crystal Data: Crystal Structure Database for Inorganic Compounds,” ASM International, Materials Park, Ohio (2019). https://doi.org/10.31399/asm.hb.v03a.a0006856

[15] Ram S., Mitra C., “Formation of Stable Cu_2O Nanocrystals in a New Orthorhombic Crystal Structure,” Materials Science and Engineering: A, **304–306**, 805–809 (2001). https://doi.org/10.1016/S0921-5093(00)01578-1

СТРУКТУРНІ ДОСЛІДЖЕННЯ МОНОКРИСТАЛІЧНОГО КРЕМНІЮ, ЛЕГОВАНОГО МІДДЮ, МЕТОДОМ ДИФУЗІЇ

Акрамжон Ю. Бобоєв[1], Шерзод А. Махмудов[2], Шухрат К. Махкамов[1], Нурітдін Ю. Юнусалієв[1],
Муродільжон М. Хотамов[1], Мохірабону М. Араббоєва[1]
[1]Андижанський державний університет імені З.М. Бабура, Андижан, Узбекистан
[2]Інститут ядерної фізики Академії наук Республіки Узбекистан

У статті представлено результати структурного дослідження монокристалічного кремнію, легованого міддю методом термодифузії за температури 1423 K. Об'єктом дослідження були кристали n-Si, вирощені методом Чохральського, що містять кисневі преципітати SiO_2. Структурний аналіз проводився на рентгенівському дифрактометрі з удосконаленою оптичною схемою, що дозволило виявити слабкі додаткові відбиття та зміни параметрів кристалічної решітки. Встановлено, що легування міддю призводить до появи пружних напружень у поверхневих шарах кристалу, зміни міжплощинної відстані (111) та перерозподілу інтенсивності відбиття (222) і (333). Виявлено дифузне розсіювання та додаткові селективні відбиття, що свідчать про утворення нових фаз. Вперше прямим структурним методом показано формування нанокристалів CuO з моноклінічною структурою та середнім розміром 14–14,5 нм, а також нанокристалів Cu_2O з кубічною структурою та середнім розміром близько 17 нм. Їхні параметри решітки були виміряні експериментально та дещо відрізняються від стандартних еталонних значень, що свідчить про вплив кремнієвої матриці та внутрішніх напружень на їхню структуру. Було показано, що кисневі преципітати SiO_2 створюють локальні пружні поля, які сприяють дифузії, зародкоутворенню та розділенню міді у вигляді оксидних нанофаз. Отримані результати уточнюють механізм структурних перетворень у кремнії, легованому міддю.

Ключові слова: *рентгенівська дифракція; субкристаліт; нанокристал; легований міддю кремній; термічна дифузія; оксиди міді; кисневі преципітати*

East European Journal of Physics. **2**. 352–360 (2026)

DOI: 10.26565/2312-4334-2026-2-37 ISSN 2312-4334

FINITE ELEMENT MODELING OF SCANNING SPEED EFFECTS IN FEMTOSECOND LASER-INDUCED GRAPHENE FABRICATION

J.O. Sadullayev[1], **M.M. Akhmedov**[1*], **M.E. Vapayev**[1], **A.E. Rajabov**[1], **I.Y. Davletov**[1], **G.S. Boltaev**[2]
[1]*Department of Electrical Engineering and Power Engineering, Urgench State University named after Abu Raykhan Beruni, Urgench, 220100, Uzbekistan*
[2]*Department of Physics, American University of Sharjah, Sharjah 26666, United Arab Emirates*
[*]*Corresponding Author e-mail: munisbek95@urdu.uz*

Received February 22, 2026; revised April 4, 2026; accepted April 8, 2026

Laser-induced graphene (LIG) enables mask free direct writing of conductive carbon structures on polyimide substrates for flexible electronic and sensing applications. In femtosecond laser-induced graphene (FLIG), the scanning speed strongly affects the local temperature field, and thus the extent and quality of graphitization, but this dependence is still not fully quantified. In this study, a time dependent finite element model is implemented in COMSOL Multiphysics to resolve the temperature distribution generated by a femtosecond laser beam on a polyimide surface as a function of scanning speed. The laser is described as a moving Gaussian surface heat source, and the transient heat conduction equation is solved to capture ultrafast heating and cooling during a pulse train. Simulations for scan speeds between 0.05 and 0.20 m/s show that decreasing the speed increases the peak temperature and enlarges the heat affected zone, whereas higher speeds reduce both quantities. By comparison of the predicted peak temperatures with the graphitization thresholds in the literature for polyimide derived graphene, an intermediate scan speed window is identified in which the thermal budget is sufficient for graphene formation while avoiding excessive overheating and damage. This modeling framework provides a practical tool for pre selecting femtosecond laser parameters and for accelerating the optimization of FLIG processes for flexible graphene based devices.

Keywords: *Laser-induced graphene; Polyimide; Scanning speed; Ultrafast heat transfer; Moving Gaussian heat source; Finite element modeling; Temperature distribution; Graphitization window*

PACS: 42.70.Hj, 42.62.Fi

1. INTRODUCTION

Laser-induced graphene (LIG) has emerged as a versatile and scalable technique for the direct writing of conductive graphene-like networks on polymer substrates due to its simplicity, mask-free patterning capability, and compatibility with large-area processing. Typically, LIG is synthesized by scanning a focused laser beam across a carbon-rich precursor such as polyimide, where localized photothermal conversion induces carbonization and graphitization, resulting in a porous turbostratic graphene structure with tunable morphology and electrical conductivity [1–5]. These unique structural and electrical properties, combined with the ability to fabricate arbitrary planar geometries, have enabled numerous applications in flexible and wearable electronics, including strain sensors, pressure sensors, and biointerfaces [6–9]. Furthermore, the high specific surface area and excellent electrical conductivity of LIG make it particularly attractive for energy harvesting and storage applications, such as microsupercapacitors and electrochemical electrodes [10–12].

More recently, femtosecond laser processing has been introduced as an advanced approach to improve the spatial confinement of laser energy deposition and minimize collateral thermal damage. Ultrafast laser pulses can induce nonlinear absorption and highly localized energy transfer, leading to rapid heating and graphitization while significantly reducing heat diffusion into surrounding material regions [13–16]. As a result, femtosecond laser-induced graphene (FLIG) often exhibits improved structural uniformity, higher electrical conductivity, and enhanced material quality compared to graphene produced using continuous wave or long-pulse lasers [13]. However, FLIG formation is highly sensitive to laser processing parameters, including laser power, repetition rate, scanning speed, and hatch spacing. These parameters strongly influence the thermal history of the material and determine whether graphitization, partial carbonization, or material ablation occurs [10, 16].

In many previous studies, optimization of laser processing parameters—particularly scanning speed—has been performed using empirical approaches or design-of-experiments methodologies to balance electrical performance, structural integrity, and fabrication throughput [17–26]. Although these experimental approaches are effective for identifying suitable processing windows, they often require extensive experimental effort and do not provide direct insight into the underlying thermal mechanisms governing graphene formation. In ultrafast laser processing regimes, direct experimental measurement of transient temperature fields at the laser–material interface is extremely challenging due to the short timescales involved. Therefore, numerical modeling has become an essential tool for investigating ultrafast laser–material interactions. Time-dependent heat transfer simulations based on the finite element method (FEM) have been successfully

---

Cite as: J.O. Sadullayev, M.M. Akhmedov, M.E. Vapayev, A.E. Rajabov, I.Y. Davletov, G.S.Boltaev, East Eur. J. Phys. 2, 352 (2026), https://doi.org/10.26565/2312-4334-2026-2-37

applied to laser processing problems and can be extended to femtosecond laser irradiation by incorporating appropriate heat source formulations and ultrafast heat transfer models [27–29].

COMSOL Multiphysics provides a powerful and flexible framework for implementing such models, including moving Gaussian heat sources and advanced heat transfer formulations suitable for ultrafast laser–material interactions [27, 29]. By representing the femtosecond laser beam as a moving Gaussian surface heat flux on a polymer substrate, it is possible to simulate the spatiotemporal evolution of temperature distributions under different scanning speeds while maintaining constant laser parameters [28, 29]. From these simulations, key physical quantities such as peak temperature, thermal gradients, heat-affected zone dimensions, and cooling dynamics can be extracted and correlated with the experimental conditions required for graphene formation. This combined numerical and experimental approach provides a rational foundation for optimizing the processing parameters and improving the efficiency and quality of FLIG fabrication [13, 17, 26, 40, 43].

In this work, a numerical investigation of the evolution of temperature during femtosecond laser-induced graphene formation on a polymer substrate is presented, with particular emphasis on the effected of laser scanning speed. A time-dependent finite element model is developed in COMSOL Multiphysics using a moving Gaussian heat source to represent laser irradiation [28, 29]. The model is used to evaluate the influence of scanning speed on peak temperature, spatial temperature distribution, and thermal relaxation behavior. The results provide fundamental insight into the thermal mechanisms governing femtosecond laser-induced graphene formation and offer practical guidance for selecting optimal laser processing parameters for controlled and efficient FLIG fabrication.

In addition, the obtained results are consistent with analytical and mathematical approaches reported in recent studies on semiconductor structures, where the influence of temperature and material parameters on electronic and thermal characteristics has been systematically investigated [30–39], further confirming the reliability of the developed finite element model for describing temperature-dependent processes.

In this context, the present work makes three specific contributions.First, it establishes a systematic finite element model to quantify how femtosecond laser scanning speed controls the full spatiotemporal temperature field during laser-induced graphene formation on polymer substrates. Second, the model is used to identify a scan speed window in which the peak temperature and heat affected zone dimensions are compatible with graphene formation, thus providing a thermally grounded definition of an "optimal" processing regime. Third, the simulated temperature metrics are formulated in a way that can be directly correlated with experimentally accessible indicators such as Raman signatures, sheet resistance, and morphology, offering a practical route to integrate numerical predictions with future femtosecond FLIG optimization studies.

2. METHODOLOGY

2.1. Geometrical Model and Material Properties

The numerical simulations were performed in COMSOL Multiphysics using a two-dimensional representation of a polyimide (PI) substrate irradiated by a scanning femtosecond laser beam. The substrate was modeled as a rectangular domain with a thickness of $H_1 = 1.29 \times 10^{-4}$ m and a width of $W_1 = 2.0 \times 10^{-3}$ m. These dimensions represent a typical PI film geometry, while ensuring that the lateral boundaries remain sufficiently far from the heated region to minimize edge effects on the computed temperature field.

The initial temperature of the entire domain was set equal to the ambient temperature, $T_a = 293.15\,\mathrm{K}$.

Temperature-dependent thermophysical properties of polyimide—namely density (ρ), specific heat capacity (C_p), and thermal conductivity (k)—were obtained from literature and the COMSOL material library over the temperature range from room temperature up to the onset of carbonization.

Convective heat transfer to the surrounding air was modeled on the exposed surfaces using a heat transfer coefficient of $h_1 = 17\,\mathrm{W\,m^{-2}\,K^{-1}}$. Radiative heat losses were also taken into account using a surface emissivity of $\varepsilon = 0.7$. These parameters are consistent with previous numerical studies on laser heating of polymeric substrates and provide a realistic approximation of typical laboratory conditions.

2.2. Governing Equation and Assumptions

Heat transfer in the PI substrate was described by the transient heat-conduction equation in the lattice (continuum) approximation,

$$\rho C_p \frac{\partial T}{\partial t} = \nabla \cdot (k \nabla T) + Q(x, y, t), \tag{1}$$

where T is the temperature and $Q(x, y, t)$ denotes the volumetric heat source associated with laser absorption.

Given the spatial and temporal scales considered (spot radius on the order of 10^{-4} m and pulse duration $P_\mathrm{w} = 250\,\mathrm{fs}$), classical Fourier conduction was adopted as a first-order approximation; non-Fourier or two-temperature descriptions may be incorporated in future work to capture electron–phonon nonequilibrium more rigorously. Phase change, ablation, and temperature-dependent variations in optical properties were neglected so that the model isolates the role of scanning-speed-controlled thermal fields within the regime relevant to the onset of graphitization.

2.3. Laser Heat Source and Scanning Motion

The femtosecond laser was modeled as a train of Gaussian pulses incident on the upper surface of the substrate. The pulse repetition rate was set to $f = 10$ kHz, leading to an average power P_{avg} delivered to the surface. The beam was characterized by a diameter $D = 100\ \mu$m ($1/e^2$ intensity width), corresponding to a beam radius $w_0 = D/2 = 50\ \mu$m. The laser operated at a central wavelength of $\lambda = 1060$ nm. An effective absorptivity $A_1 = 0.8$ was assumed for the PI surface at this wavelength, such that the absorbed power entering the thermal model is $P_{\text{abs}} = A_1 P_{\text{avg}}$. The temporal width of each pulse was $P_{\text{w}} = 250$ fs, implemented as a short top-hat function within each $1/f$ period to approximate femtosecond energy deposition followed by longer-time heat diffusion.

The spatial distribution of the absorbed heat flux at the surface was described by a moving Gaussian profile,

$$q(x,y,t) = \frac{2P_{\text{abs}}}{\pi w_0^2}\exp\left(-\frac{2\big(x - x_c(t)\big)^2 + 2\big(y - y_c\big)^2}{w_0^2}\right) g(t), \tag{2}$$

where $(x_c(t), y_c)$ denotes the instantaneous beam center and $g(t)$ specifies the temporal envelope of the pulse train. The beam center followed a linear trajectory along the x-direction,

$$x_c(t) = x_0 + vt, \tag{3}$$

with $x_0 = D$ used as the reference entrance position and v denoting the scanning speed. In this work, v was varied between 0.05 and 0.20 m/s, while all other laser parameters were kept constant. This moving-source description was implemented in COMSOL Multiphysics via analytic functions defining the Gaussian heat flux and a time-dependent boundary condition applied at the top surface.

2.4. Boundary and Initial Conditions

At $t = 0$, the temperature throughout the substrate was set to the ambient value $T_a = 293.15$ K. The top surface received the laser heat flux described in Section 2, in addition to convective and radiative heat losses. The lateral boundaries were treated as adiabatic, reflecting the assumption that the computational domain is sufficiently wide to minimize lateral heat leakage over the time scales of interest. The bottom surface was coupled to the environment through convection and radiation, approximating thermal contact with a support stage exposed to air.

3. RESULTS AND ANALYSIS

Time-dependent COMSOL Multiphysics simulations were employed to quantify how the femtosecond laser scanning speed governs the spatial and temporal evolution of the temperature field during laser-induced graphene formation. Figures 1-4 present the surface temperature distributions along the laser track for scan speeds of 0.05, 0.10, 0.15, and 0.20 m/s, respectively. A clear monotonic trend is observed: decreasing the scanning speed substantially increases the peak temperature and broadens the thermally affected zone, whereas higher speeds lead to more confined and cooler heating profiles.

Figure 1. Simulated temperature distribution at a scanning speed of 0.20 m/s (peak surface temperature $T_{\max} \approx$ 2400 K). At 0.20 m/s, the train of femtosecond pulses produces a sequence of sharp temperature spikes that cumulatively drive the surface temperature to a quasi-steady peak around 2400 K. This peak remains slightly below the $\approx$ 2500 K level typically associated with the formation of well-ordered graphene domains, so the local thermal budget is sufficient for graphitization but not ideal for extensive defect healing. Consequently, the resulting graphene layer along the scan track is expected to be at least partially defective, with a higher density of structural imperfections compared with layers formed under conditions where the peak temperature significantly exceeds 2500 K.

Figure 2. Simulated temperature evolution at a scanning speed of 0.15 m/s (peak surface temperature $T_{\max} \approx$ 2480 K). At 0.15 m/s, the sequence of femtosecond pulses leads to a progressive build-up of temperature, and the surface repeatedly experiences sharp spikes that rise to a maximum of about 2480 K. This peak value lies very close to the lower bound of the $\approx$ 2500–3500 K window associated with the formation of well-developed graphene networks in polyimide-derived LIG [41]. Consequently, the local thermal conditions at this speed are expected to support more extensive graphitization and partial defect healing compared with 0.20 m/s, although the graphene layer may still contain a noticeable density of structural imperfections relative to regimes where $T_{\max}$ comfortably exceeds 2500 K.

Figure 3. Simulated temperature evolution at a scanning speed of 0.10 m/s (peak surface temperature $T_{\max} \approx$ 2500 K). At 0.10 m/s, the femtosecond pulse train generates a sequence of sharp temperature spikes with noticeable cumulative heating, and the surface temperature gradually approaches a maximum of about 2500 K without exceeding this level for any of the pulses. Since 2500 K is close to the lower boundary of the graphitization window for polyimide-derived graphene, the thermal conditions at this speed are sufficient to support graphene formation along the scan track but only marginally adequate for pronounced defect healing. Consequently, the resulting graphene layer is expected to be relatively continuous yet still contain a considerable density of structural defects compared with regimes where $T_{\max}$ clearly exceeds the optimal graphitization range.

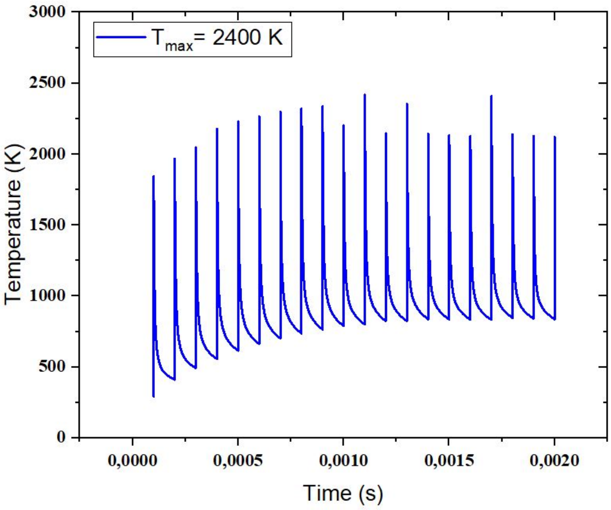

Figure 1. Temporal temperature evolution under pulsed laser irradiation at a scanning speed of 0.2 m/s ($T_{\max}$ = 2400 K)

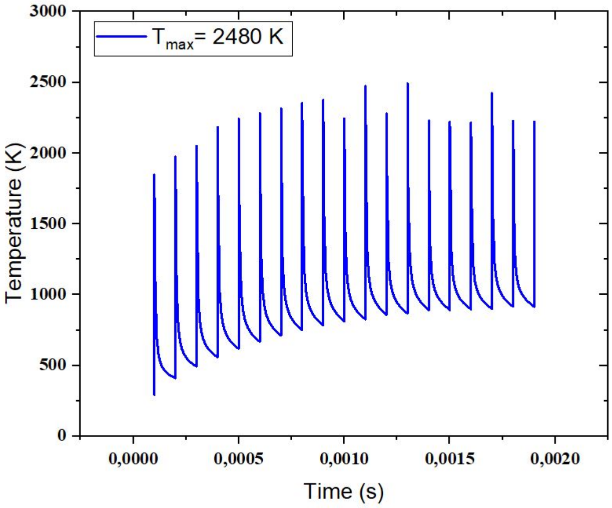

Figure 2. Temporal temperature evolution under pulsed laser irradiation at a scanning speed of 0.15 m/s ($T_{\max}$ = 2480 K)

Figure 4. Simulated temperature evolution at a scanning speed of 0.05 m/s (peak surface temperature $T_{\max} \approx$ 2600 K). At this lowest scanning speed, the laser–material interaction time is longest, so the cumulative effect of successive femtosecond pulses leads to a strong build-up of temperature and a maximum surface value of about 2600 K. This peak lies clearly inside the 2500–3500 K graphitization window reported for polyimide-derived graphene, indicating that the thermal conditions are highly favorable for the formation of a well-developed graphene network and for partial annealing of pre-existing defects. However, the pronounced heat accumulation also implies a wider heat-affected zone and a higher risk of local overheating or ablation in comparison with higher scanning speeds, which may compromise fine feature control even though the graphene layer quality is expected to be relatively high along the scan track.

Figure 5 presents the dependence of the maximum surface temperature $T_{\max}$ on the laser scanning speed in the range from 0.05 to 0.20 m/s. The curve shows a clear monotonic decrease: as the scanning speed is increased, the peak temperature achieved at the surface systematically drops from about 2600 K at 0.05 m/s to roughly 2400 K at 0.20 m/s. This trend is consistent with the reduced interaction time and lower effective energy input per unit length at higher scan speeds, which restrict heat accumulation in the polyimide substrate. At the lowest speed considered (0.05 m/s), $T_{\max}$ lies well inside the graphitization window 2500–3500 K, indicating favorable conditions for the formation of a well-developed

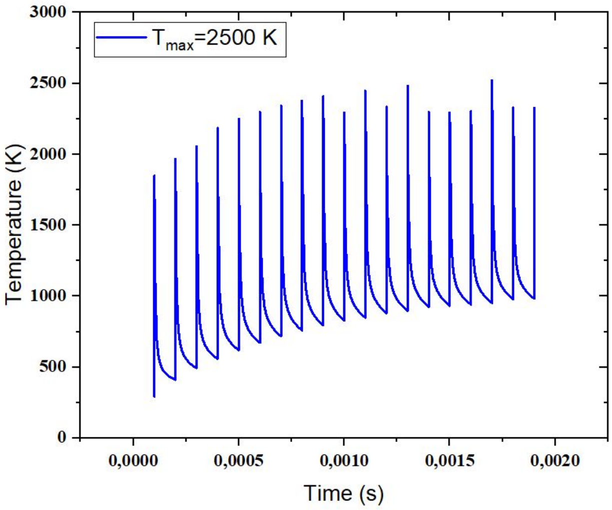

Figure 3. Temporal temperature evolution under pulsed laser irradiation at a scanning speed of 0.1 m/s ($T_{\max}$ = 2480 K)

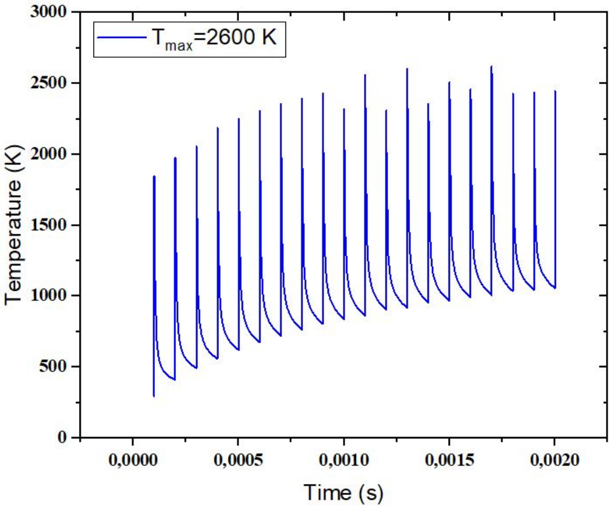

Figure 4. Temporal temperature evolution under pulsed laser irradiation at a scanning speed of 0.05 m/s ($T_{\max}$ = 2600 K)

graphene layer, while at 0.20 m/s the peak temperature falls closer to the lower boundary of this window and is expected to produce a thinner or more defective graphene film [41, 42]. The error bars in Figure 5 reflect the variation in peak temperature extracted from different probe locations along the scan track and highlight that, despite this variability, the overall decreasing trend with increasing scanning speed remains robust.

This trend aligns with the experimental findings of Murray et al. [16], where lower scanning speeds (e.g., 70–200 mm/s) produced high-quality LIG with low sheet resistance (∼16 Ω/sq) and sharp Raman 2D peaks, indicating better graphitization. Our FEM model complements this by quantifying the underlying thermal mechanism: peak temperatures systematically decrease from 2600 K at 0.05 m/s to 2400 K at 0.20 m/s, defining a graphitization window of 2500–3500 K consistent with MD simulations in recent studies [41, 42].

The simulation results reveal a clear and systematic dependence of the transient thermal field on scanning speed, confirming that this parameter is a primary handle for controlling femtosecond laser-induced graphene formation on polyimide. At low scanning speeds, cumulative heating drives the peak surface temperature deep into the graphitization window and generates a wide heat-affected zone, which supports extensive carbonization but increases the risk of structural damage and local ablation. Intermediate speeds yield more moderate peak temperatures and tighter thermal footprints

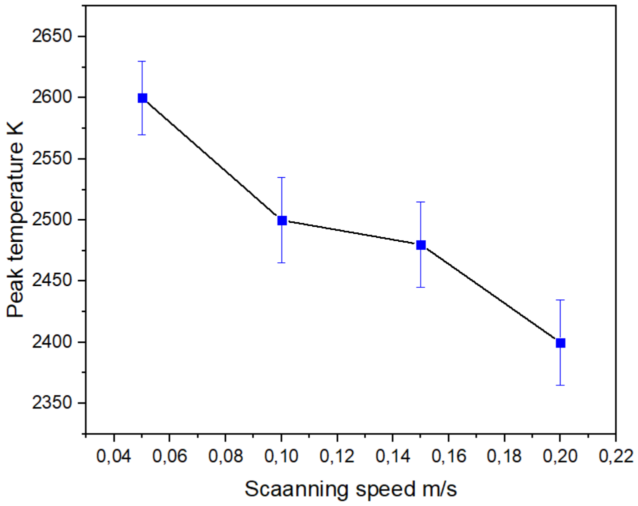

Figure 5. Peak surface temperature as a function of scanning speed (0.05–0.20 m/s).

while preserving a continuous high-temperature region along the scan path, making them particularly attractive as an operational window where graphene can form reliably with reduced thermal loading of the surrounding material. At the highest speeds considered, the thermal budget becomes marginal for robust graphitization, so although throughput is improved, the resulting graphene is expected to be thinner and more defective or even discontinuous along the track. Altogether, these observations delineate a finite scan-speed range in which the peak temperature and spatial extent of the heated zone jointly favor continuous, higher-quality graphene while limiting unnecessary overheating, and they provide a predictive basis for linking thermal metrics to future experimental measurements such as Raman spectra, sheet resistance, and morphology.

4. CONCLUSIONS

This study has established a time-dependent finite-element framework in COMSOL Multiphysics to quantify how femtosecond laser scanning speed governs the spatiotemporal temperature field during laser-induced graphene formation on polyimide. By modeling the laser as a moving Gaussian surface heat source and systematically varying the scanning speed in the range 0.05–0.20 m/s, the simulations revealed a monotonic decrease of the peak surface temperature from ≈ 2600 K at 0.05 m/s to ≈ 2400 K at 0.20 m/s, accompanied by a gradual contraction of the heat-affected zone. Comparison of these peak temperatures with reported graphitization windows for polyimide-derived graphene indicates that low and intermediate scan speeds fall within or close to the 2500–3500 K range associated with well-developed graphene networks, whereas higher speeds approach the lower bound of this window and are likely to produce thinner or more defective graphene layers.

The results therefore delineate a finite scan-speed window in which the thermal budget is sufficient to drive robust graphitization while limiting excessive overheating and damage. In practical terms, very low scanning speeds provide favorable conditions for high-quality graphene formation but at the cost of a wide heat-affected zone and an increased risk of ablation, whereas excessively high speeds enhance throughput but undermine graphene continuity and structural quality. Intermediate speeds, where peak temperatures lie safely within the graphitization window and the thermal footprint remains compact, emerge as promising candidates for defining an optimal processing regime for femtosecond laser-induced graphene.

From an application standpoint, the insights gained here are directly relevant to the design of FLIG-based flexible sensors, microsupercapacitor electrodes, and other planar graphene devices, where a balance between electrical performance, pattern resolution, and substrate integrity is critical. The presented modeling strategy can be used as a predictive tool to pre-screen scanning speeds and laser settings before fabrication, thereby reducing experimental iteration and accelerating process development. Future work should combine the thermal simulations with experimental characterization—such as Raman spectroscopy, sheet-resistance mapping, and microscopy—to quantitatively link the predicted temperature metrics to defect density and device performance, and to refine the graphitization thresholds for different polyimide grades and laser systems.

Acknowledgments

We acknowledge the F-FA-2021-510 Grant from the Ministry of Innovative Development of Uzbekistan.

ORCID

J.O. Sadullayev, https://orcid.org/0000-0002-5577-2644; **M.M. Akhmedov**, https://orcid.org/0000-0003-1208-1736; **M.E. Vapayev**, https://orcid.org/0009-0007-5194-131X; **A.E. Rajabov**, https://orcid.org/0000-0003-1687-2113; **I.Y. Davletov**, https://orcid.org/0009-0006-5971-7649; **G.S. Boltaev**, https://orcid.org/0000-0003-0354-1251

REFERENCES

[1] S. P. Lee, H. Kim, and J. Park, "A review on laser-induced graphene in flexible energy storage and conversion devices," Chem. Eng. J. **499**, 156110 (2024). https://doi.org/10.1016/j.cej.2024.156110.

[2] J. Yang, J. Yu, K. Zhang, F. Qiao, and G. Yu, "Laser-Induced Graphene Toward Flexible Energy Harvesting and Storage Electronics," Advanced Materials Technologies, **9**(22), 2301602 (2024). https://doi.org/10.1002/admt.202301602

[3] M. R. Bedilov, Kh. B. Beisembaeva, and I. Yu. Davletov, "Formation of the spectra of multiply charged ions from the plasma of Nd-doped glass irradiated with a neodymium laser," Technical Physics, **47**(8), 1019–1023 (2002). https://doi.org/10.1134/1.1501684

[4] Bedilov, M. R., Davletov, I. Y., Sabitov, M. S., Berdierov, G. R., Tsoi, T. G., "Multiply charged ion spectra of a laser plasma produced on both sides of the target," Quantum Electronics, **31**(5), 453 (2001). https://doi.org/10.1070/QE2001v031n05ABEH001977

[5] M. R. Bedilov, R. T. Khaidarov, B. K. Yakubov, and U. S. Kunishev, "Charge and energy spectra of multiply charged ions of a two-element laser plasma formed from targets of different densities," Quantum Electronics, **26**(9), 814 (1996). https://doi.org/10.1070/QE1996v026n09ABEH000788

[6] M. S. Isaev, U. T. Asatov, M. A. Tulametov, S. R. Kodirov, and A. E. Rajabov, "Study of the Inhomogeneities of Overcompensated Silicon Samples Doped with Manganese," East European Journal of Physics, (2), 341–344 (2024). https://doi.org/10.26565/2312-4334-2024-2-40

[7] J. S. Abdullayev, J. S. Abdullayev, I. B. Sapaev, J. I. Razzokov, D. A. Juraev, E. E. Elsayed, "Modeling of Optoelectronic Properties in p-Si/n-$Cd_mZn_{1-m}S$ Heterojunctions: Effects of Composition and Temperature," Journal of Electronic Materials, **54**, 11607–11617 (2025). https://doi.org/10.1007/s11664-025-12480-8

[8] A. T. Mamadalimov, M. S. Isaev, M. N. Mamatkulov, S. R. Kodirov, and J. T. Abdurazzokov, "Study of Silicide Formation in Large-Diameter Monocrystalline Silicon," East European Journal of Physics, (2), 366–371 (2024). https://doi.org/10.26565/2312-4334-2024-2-45

[9] M. S. Isaev, A. I. Khudayberdieva, M. N. Mamatkulov, U. T. Asatov, and S. R. Kodirov, "The Surface Layer Morphology of Si⟨Cr⟩ Samples," East European Journal of Physics, (4), 297–300 (2024). https://doi.org/10.26565/2312-4334-2024-4-32

[10] H. Wang, Z. Zhao, P. Liu, and X. Guo, "Laser-Induced Graphene Based Flexible Electronic Devices," Biosensors, **12**(2), 55 (2022). https://doi.org/10.3390/bios12020055

[11] C. Francis, A. Rektor, T. Valayil-Varghese, N. McKibben, I. Estrada, J. Forbey, and D. Estrada, "Laser-induced graphene gas sensors for environmental monitoring," Front. Chem. **12**, (2024). http://doi.org/10.3389/fchem.2024.1448205

[12] T. Han, A. Nag, R.B.V.B. Simorangkir, N. Afsarimanesh, H. Liu, S.C. Mukhopadhyay, and Y. Xu, *et al.*, "Multifunctional Flexible Sensor Based on Laser-Induced Graphene," Sensors, **19**, 3477 (2019). https://doi.org/10.3390/s19163477

[13] X. Zhao, J. Zhai, Y. Zhou, J. Hu, and L. Wang, "Femtosecond laser-driven synthesis of laser-induced graphene: Optimizing microstructure and electrochemical performance for flexible electrodes," Journal of Colloid and Interface Science, **703**, Part 1 (2026). https://doi.org/10.1016/j.jcis.2025.139061

[14] M. R. Bedilov, I. Yu. Davletov, and Sh. D. Sultanov, "Charge and energy spectra of fast multicharged ions in a laser plasma," Plasma Physics Reports, **28**(12), 1038–1040 (2002). https://doi.org/10.1134/1.1528235

[15] R.T. Khaydarov, H.B. Beisinbaeva, M.M. Sabitov, Milan Kalal, and G.R. Berdiyorov, "Conditions defining the mechanisms of the formation of light gas ions in multicomponent laser-produced plasmas," Nuclear Fusion, **50**(10), 105007 (2010). https://doi.org/10.1088/0029-5515/50/10/105007

[16] M. Guan, Z. Zhang, W. Zhu, Y. Gao, S. Wang, and X. Li, "Femtosecond laser-induced graphene for temperature and ultrasensitive flexible strain sensing," Front. Mater. Sci. **18**(3), 240696 (2024). https://doi.org/10.1007/s11706-024-0696-6

[17] R. Murray, M. Burke, D. Iacopino, and A.J. Quinn, "Design of Experiments and Optimization of Laser-Induced Graphene," ACS Omega, **6**(26), 6736–16743 (2021). https://doi.org/10.1021/acsomega.1c00309

[18] G. S. Boltaev, M. Iqbal, S. R. Kamalov, M. Vapaev, I. Y. Davletov, and A. S. Alnaser, "Impact of plasma conditions on the shape of femtosecond laser-induced surface structures of Ti and Ni," Applied Physics A, **128**(6), 488 (2022). https://doi.org/10.1007/s00339-022-05614-w

[19] B. X. Eshchanov, G. I. Mukhamedov, N. S. Khalilova, B. R. Sobirov, M. Vapaev, G. S.Boltaev, "Ultrafast laser nanostructured silicon coated with silver nanoparticles for efficient SERS detection of R6G," Applied Physics A, **132**(2), 111 (2026). https://doi.org/10.1007/s00339-025-09179-2

[20] A. I. Japakov, M. E. Vapaev, R. M. Bedilov, Z. T. Azamatov, and I. Y. Davletov, "Spectra of Multiply Charged Ions in Laser Plasma Formed from Gas-Containing Targets," East European Journal of Physics, (3), 490-494 (2023). https://doi.org/10.26565/2312-4334-2023-3-55

[21] A. I. Japakov, R. M. Bedilov, J. O. Kamalova, I. Y. Davletov, and A. R. Matnazarov, "The impact of laser radiation frequency on the formation of the main characteristics of ions in a mono-element laser plasma," EPJ Web of Conferences, **318**, 05002 (2025). https://doi.org/10.1051/epjconf/202531805002

[22] M. E. Vapaev, F. M. Tojinazarov, B. R. Sobirov, S. R. Kamalov, I. Y. Davletov, and G. S. Boltaev, "Laser fluence-dependent LIPSS formed on the surface of niobium alloys," EPJ Web of Conferences, **318**, 05005 (2025). https://doi.org/10.1051/epjconf/202531805005

[23] M. Akhmedov, J. Sadullayev, M. Vapayev, A. Matnazarov, I. Davletov, and J. Rayimbaev, "Picosecond-pulsed laser ablation of aluminum foils: crater morphology and plasma parameters," Engineering Research Express, **7**(3), 035362 (2025). https://doi.org/10.1088/2631-8695/ae0092

[24] M. Akhmedov, J. Sadullayev, M. Vapayev, F. Tojinazarov, I. Davletov, and J. Rayimbaev, "Effects of picosecond pulsed laser radiation on crater formation on copper foil surfaces," Engineering Research Express, **8**, 035401 (2026). https://doi.org/10.1088/2631-8695/ae3b9d

[25] Z. Ruziev, U. Sapaev, H. Eshkuvatov, R. Karimov, I. Egamberdiev, M. Musurmonov, and R. Turniyazov, "Surface ionization of diamond by femtosecond laser pulses: A comparative study of analytical models," Results in Optics, **23**, 100942 (2026). https://doi.org/10.1016/j.rio.2025.100942

[26] F.F. Franco, M.H. Malik, L. Manjakkal, A. Roshanghias, C.J. Smith, C. Gauchotte-Lindsay, "Optimizing Carbon Structures in Laser-Induced Graphene Electrodes Using Design of Experiments for Enhanced Electrochemical Sensing Characteristics," ACS Appl. Mater. Interfaces, **16**(47), 65489–65502 (2024). https://doi.org/10.1021/acsami.4c13124

[27] COMSOL AB, "Modeling ultrafast heat transfer with COMSOL Multiphysics," COMSOL Blog, 2026. https://www.comsol.com/blogs/modeling-ultrafast-heat-transfer-with-comsolmph

[28] J. Fernandes, and M.-J. Kim, "Probing ultrafast heat transfer mechanisms in plasmonic gold nanostructures: FEM analysis of core–shell configurations under femtosecond laser irradiation," Phys. Chem. Chem. Phys. (23), (2025). https://doi.org/10.1039/D5CP00715A

[29] COMSOL AB, "Ultrafast heat transfer due to femtosecond laser heating," COMSOL Application Gallery, 2025. https://www.comsol.com/model/ultrafast-heat-transfer-due-to-femtosecond-laser-heating-142421

[30] J. S. Abdullayev, L. Abdullayeva, L. Agamalieva, and R. Ismailova, "Correlating Ni microstructure with Schottky barrier homogeneity in monolayer MoS_2 field-effect transistors," Advanced Physical Research, **7**(3), 350–357 (2025). https://doi.org/10.62476/apr.73350

[31] J. S. Abdullayev, and I. B. Sapaev, (2025). Analytic analysis of the features of GaAs/Si radial heterojunctions: Influence of temperature and concentration. East European Journal of Physics, (1), 204–210. https://doi.org/10.26565/2312-4334-2025-1-21

[32] J. S. Abdullayev, I. B. Sapaev, N. Esanmuradova, S. Kadirov, and Sh.M. Kuliyev, "Mathematical analysis of the features of radial p-n junction: Influence of temperature and concentration," East European Journal of Physics, (2), 220–225 (2025). https://doi.org/10.26565/2312-4334-2025-2-24

[33] A. Mustafoqulov, R. Baratov, Z. Radjapov, S. Kadirov, and B. Urinov, "Angular displacement measurement and control sensors of agricultural robot-manipulators," in: *IV International Conference on Agricultural Engineering and Green Infrastructure for Sustainable Development (AEGISD-IV 2024)*, **105**, 03003 (2024). https://doi.org/10.1051/bioconf/202410503003

[34] A. Y. Boboev, N. Y. Yunusaliyev, G. G. Tojiboyev, O. S. Muminov, and S. R. Kadirov, "SRIM simulation of irradiation damage by protons in ZnO: S compound," Journal of Ovonic Research, **21**(6), 781-788 (2025). https://doi.org/10.15251/JOR.2025.216.781

[35] A. Y. Boboev, U. Karimberdiev, S. Kadirov, and N. Y. Yunusaliyev, "Growth of Solid Solutions $(Ge_2)(GaAs_{1-\delta}Bi_\delta)_x(ZnSe)_y$ on Silicon Substrates by Liquid Phase Epitaxy," Chalcogenide Letters, **22**(11), 951-957 (2025). https://doi.org/10.15251/CL.2025.2211.951

[36] A. T. Mamadalimov, M. S. Isaev, S. R. Kodirov, T. U. Atamirzaev, M. N. Mamatkulov, A. UT, "Comparative Analysis of the Properties of Manganese Silicide," J. Nano- Electron. Phys. **17**(5), 05011 (2025). https://doi.org/10.21272/jnep.17(5).05011

[37] S. R. U. Qodirov, and I. Y. Davletov, "Improving thinking and imagining skills in school students by training the physics using simulations," AIP Conference Proceedings, **3268**(1), 060006 (2025). https://doi.org/10.1063/5.0257234

[38] I. Davletov, N. Khakimov, A. Qodirov, M. Akhmedov, J. Sadullayev, and O. Khamraev, "Soft start of induction electric motors using rezistor and denistor devices," E3S Web of Conferences, **461**, 01066 (2023). https://doi.org/10.1051/e3sconf/202346101066

[39] I. Y. Davletov, N. Z. Khakimov, A. K. Qodirov, M. M. Akhmedov, J. O. Sadullayev, O. O. Khamraev, "Increasing the Efficiency of Asynchronous Motors by Improving the Quality of the Electric Current," in: *2023 IEEE XVI International Scientific and Technical Conference Actual Problems of Electronic Instrument Engineering (APEIE)*, (2023), pp. 1820-1824). https://doi.org/10.1109/APEIE59731.2023.10347842

[40] R.D. Crapnell, E. Bernalte, R. A. A. Muñoz, and C. E. Banks, "Electroanalytical overview: the use of laser-induced graphene sensors," Anal. Methods, **17**, 635-651 (2025). https://doi.org/10.1039/d4ay01793e

[41] C.H. Kim, J.H. Kim, S.Y. Jeong, and B.S. Shine, "Atomistic and data-driven modeling of laser-induced graphene formation on sustainable polymer substrates," Sci. Rep. **15**, 31627 (2025). https://doi.org/10.1038/s41598-025-15945-2

[42] S.V. Pavlov, "Defect Engineering in Laser-Induced Graphene (LIG) Through Temperature Control: A Reactive Molecular Dynamics Study," Molecules, **30**, 4344 (2025). https://doi.org/10.3390/molecules30224344

[43] J.O. Sadullayev, M.M. Akhmedov1, M.E. Vapayev, I.Y. Davletov, and G.S. Boltaev, "Modeling of Thermal Effects in a Polyimide Target Under Pulsed Laser Irradiation," East European Journal of Physics, (1), 274–280 (2026). https://doi.org/10.26565/2312-4334-2026-1-31

КІНЦЕВО-ЕЛЕМЕНТНЕ МОДЕЛЮВАННЯ ВПЛИВУ ШВИДКОСТІ СКАНУВАННЯ НА ФОРМУВАННЯ ГРАФЕНУ, ІНДУКОВАНОГО ФЕМТОСЕКУНДНИМ ЛАЗЕРОМ

Дж.О. Садуллаєв[1], **М.М. Ахмедов**[1], **М.Є. Вапаєв**[1], **А.Е. Раджабов**[1], **І.Й. Давлетов**[1], **Г.С. Болтаєв**[2]
[1]*Кафедра електротехніки та енергетики, Ургенчський державний університет імені Абу Райхана Беруні, Ургенч, 220100, Узбекистан*
[2]*Кафедра фізики, Американський університет Шарджі, Шарджа 26666, Об'єднані Арабські Емірати*

Індукований лазером графен (LIG) забезпечує безмаскове пряме записування провідних вуглецевих структур на підкладках із поліїміду для застосувань у гнучкій електроніці та сенсорних системах. У випадку графену, індукованого фемтосекундним лазером (FLOG), швидкість сканування суттєво впливає на локальне температурне поле, а отже — на ступінь і якість графітизації, однак ця залежність досі не є повністю кількісно визначеною. У цьому дослідженні в середовищі COMSOL Multiphysics реалізовано нестаціонарну скінченно-елементну модель для визначення розподілу температури, що формується фемтосекундним лазерним пучком на поверхні поліїміду залежно від швидкості сканування. Лазер описано як рухоме гаусівське поверхневе джерело тепла, а нестаціонарне рівняння теплопровідності розв'язується для відтворення надшвидкого нагрівання та охолодження під час серії імпульсів. Результати моделювання для швидкостей сканування в діапазоні 0,05–0,20 м/с показують, що зменшення швидкості призводить до зростання пікової температури та розширення зони термічного впливу, тоді як збільшення швидкості зменшує обидва ці параметри. Порівняння розрахованих пікових температур із порогами графітизації, наведеними в літературі для графену, отриманого з поліїміду, дозволило визначити проміжне вікно швидкостей сканування, за якого тепловий бюджет є достатнім для формування графену без надмірного перегрівання та пошкодження матеріалу.Запропонована модельна схема є практичним інструментом для попереднього вибору параметрів фемтосекундного лазера та прискорення оптимізації процесів FLIG у виробництві гнучких графенових пристроїв.

Ключові слова: *графен, індукований лазером; поліімід; швидкість сканування; надшвидкий теплоперенос; рухоме гаусівське джерело тепла; кінцево-елементне моделювання; розподіл температури; вікно графітизації*

East European Journal of Physics. **2.** 361-367 (2026)
DOI:10.26565/2312-4334-2026-2-38 ISSN 2312-4334

MODELING THE EFFECT OF Co-ION IMPLANTATION ON ZnO, Mg-DOPED ZnO THIN FILMS USING MONTE CARLO SRIM

Akramjon Y. Boboev[1], **Nuritdin Y. Yunusaliyev**[1], **Biloliddin M. Ergashev**[2], **Gaybullo G. Tojiboyev**[1], **Sardor R. Kadirov**[3], **Mokhirabonu M. Arabboeva**[1]
[1]*Andijan State University, named after Z.M. Babur, Andijan, Uzbekistan*
[2]*Andijan State Pedagogical Institute, Andijan, Uzbekistan*
[3]*Urgench State University, Urgench, Uzbekistan*
**Corresponding Author e-mail: aboboevscp@gmail.com*

Received February 28, 2026; revised May 6, 2026; accepted May 20, 2026

The interaction behavior of 1.25 MeV Co ions with Si, ZnO, and Mg-doped ZnO (ZnO:Mg) targets has been systematically analyzed using the latest SRIM 2013 simulations. The findings show that atomic displacements, the production of vacancies and energy loss are greatly influenced by the composition and structural density of the target. The results reveal that the highest number of atomic displacements is observed in crystalline Si, followed by ZnO, whereas Mg-doped ZnO exhibits the lowest displacement level. On the other hand, ZnO exhibits moderate defect generation, as its high atomic density and bonding energy make it harder for the lattice to become disordered. Moreover, the presence of Mg in the ZnO matrix slightly reduces overall damage, indicating that the lattice is more stable and tolerant to radiation. These results indicate that Mg doping improves the structural robustness of ZnO against high-energy Co-ion bombardment, thereby making ZnO:Mg films more appropriate for radiation-resistant optoelectronic and sensing applications.

Keywords: *Stopping power; ZnO; Mg-doped ZnO; SRIM; Ion implantation; Vacancy; Defect; Radiation damage; Monte Carlo simulation*
PACS: 61.72.U

INTRODUCTION

In recent years, ion implantation techniques have become one of the most widely used methods for manipulating the physical, structural, and electronic properties of semiconductor materials. The ability to precisely control the energy, flux, and type of ions allows researchers to modify the properties of materials at the atomic level. This is especially important for creating materials that will operate in high-radiation environments or under extreme conditions. Among the various ions studied for this purpose, cobalt (Co) stands out due to its medium atomic mass, its ability to interact strongly with electronic and nuclear systems, and its ability to simultaneously induce magnetic and structural changes in oxide-based semiconductors [1].

Zinc oxide (ZnO) is a group II–VI compound with a wide band gap ($E_g \approx 3.3$ eV). Due to its unique properties such as high optical transparency, piezoelectric properties, and chemical stability, it is used as a key material in the development of optoelectronic devices [2], gas sensors [3], ultraviolet photodetectors [4], and transparent conductive films. However, ZnO can change its crystal structure and form defects when exposed to high-energy particles or radiation [5]. The defects formed by such radiation, for example, oxygen vacancies, zinc interstitial atoms, or complex defect clusters, can significantly change electrical and optical conductivity, carrier mobility, and even the type of conductivity [6]. Therefore, improving the radiation resistance and defect stability of ZnO materials is one of the most important issues in modern semiconductor physics today.

One of the most effective ways to improve the radiation resistance of ZnO is to introduce other elements instead of cations (doping), and magnesium (Mg) atoms are especially widely used in this process. The incorporation of Mg^{2+} cations into the Zn^{2+} sublattice leads to a noticeable widening of the band gap energy [7], accompanied by an improvement in the crystalline rigidity and enhancement of the overall lattice stability of the ZnO matrix [8].Therefore, ZnO doped with Mg (ZnO:Mg) is considered a promising material for optoelectronic and sensor systems that operate stably under radiation and high-temperature conditions. However, the interaction process of high-energy ions with pure and doped ZnO systems has not been sufficiently studied. To understand this process in depth, an analysis of the atomic-level interaction mechanisms between ions and solids is required. When Co ions with an energy of 1.25 MeV pass through a solid, they lose their energy mainly through two main processes: electron stopping (inelastic collisions with electrons of target atoms) and nuclear stopping (elastic collisions with atomic nuclei) [9]. The ratio of these two mechanisms determines the depth of ion penetration (ion range) and the nature and spatial distribution of structural damage. The degree of energy scattering and the processes of atom recoil are determined by the mass and charge of the ion, as well as the density, atomic mass and binding energy of the target material. These parameters reflect changes in the material's properties under radiation and determine its operational stability. To accurately describe and predict these interaction processes, Monte Carlo-type

---

Cite as: A.Y. Boboev, N.Y. Yunusaliyev, B.M. Ergashev, G.G. Tojiboyev, S.R. Kadirov, M.M. Arabboeva, East Eur. J. Phys. 2, 361 (2026), https://doi.org/10.26565/2312-4334-2026-2-38

computational models, in particular the Stopping and Range of Ions in Matter (SRIM) software package, are widely used [10]. SRIM simulations enable accurate calculations of parameters such as ion trajectories, stopping powers, recoil distributions, ion ranges, and defect formation rates. This allows for microscopic analysis of energy distribution processes and lattice failure mechanisms. While experimental measurements are often performed under complex and constrained conditions, SRIM-based calculations provide a fully theoretical, yet informative method for comparing different material systems.

In this work, the interaction of Co ions with 1.25 MeV energy with silicon (Si), pure ZnO, and Mg-doped ZnO (ZnO:Mg) thin films was modeled using Monte Carlo SRIM-2013 simulations. The selection of these materials enables a comparative analysis of the radiation response of semiconductors with different atomic masses and structural characteristics. The research primarily focuses on evaluating the mechanisms of energy loss, the behavior of stopping power, and the tendencies of damage formation. Particular attention was given to analyzing how incorporating Mg into the ZnO lattice alters energy-dissipation pathways and structural response mechanisms under cobalt-ion irradiation. These findings serve as an important theoretical basis for designing radiation-resistant variants of oxide semiconductors.

THEORETICAL DETAILS

Simulation tools are essential to modern materials science and semiconductor physics for understanding ion interactions with solid targets. Through these computational approaches, scientists can at least partly represent the atomic-scale phenomena that are otherwise difficult to observe in the laboratory. One of the most popular and trusted Monte Carlo–based programs is SRIM (Stopping and Range of Ions in Matter). SRIM programs enable the determination of ionic trajectories, energy-loss mechanisms, and defect formation within complex multilayer structures [11]. The SRIM code provides a self-consistent framework for estimating the energy loss and scattering of Co ions as they pass through the Si, ZnO, and ZnO:Mg thin films. The present study, using SRIM 2013, simulated the implantation of 1.25 MeV Co ions into the three systems mentioned above to analyze their stopping power, penetration depth, and structural damage characteristics. The program simulates the trajectory of each ion as a sequence of discrete elastic and inelastic collisions with the target atoms, represented by a statistical Monte Carlo algorithm. Kinetic energy loss occurs with every collision and is shared between the two processes: nuclear stopping (elastic scattering) and electronic stopping (inelastic ion–electron interactions). The ions slowly lose their energy as they pass through the target material, where their paths are also slightly altered by small-angle scattering events. The total energy loss per unit distance (stopping power or –dE/dx) is a crucial metric that indicates the extent to which a material either absorbs or dissipates the energy of the ion [12,13]. At high energies in this scenario, electronic stopping power is the primary factor, as the incident ions dissipate their kinetic energy primarily through ionization and excitation of target atoms. This kind of interaction that leads to the path of the Co ions in Si and ZnO lattices. As energy loss continues, nuclear stopping becomes increasingly dominant at lower energies, especially in the end-of-range (EOR) region, where ions move slowly, and interactions lead to large atomic displacements and the creation of vacancies [14]. The simulations play a crucial role in anticipating material responses during and after irradiation, especially in semiconductor production, where ion implantation is a common practice for doping and modifying interfaces. The precision of SRIM in calculating stopping powers, recoil distributions, and ionization profiles makes it an essential tool for microelectronics, thin-film technology, and radiation protection research. Besides SRIM, there are other computational packages like TRIM, TRIDYN, and SDTrimSP that also employ Monte Carlo algorithms to simulate dynamic ion–solid interactions; nevertheless, SRIM remains the most convenient and widely compared to other methods owing to its well-validated physics models and user-friendly interface [15]. Theoretically, SRIM simulations are consistent with analytical models, such as the Bethe–Bloch equation, which quantifies the electronic energy loss of fast-moving charged particles in solids. Although Bethe–Bloch provides a continuous slowing-down approximation, SRIM not only goes beyond it but also accounts for stochastic (random) collision processes associated with angular scattering, secondary atom recoils, and defect cascades. This mixed theory-numerical method provides a clear view of both the spatial and energetic distributions of ion-induced damage. In the current situation, SRIM simulations are in accord with the following atomic density and structural stiffness; therefore, the total damage energy, vacancy concentration, and atomic displacements have been systematically decreased from Si to ZnO to ZnO:Mg. The propagation of electronic stopping at the initial stage of penetration and the rise in the nuclear-collision contribution near the EOR are the reasons behind the characteristic Bragg-like energy-deposition profiles for each material. Knowledge of these phenomena is important for guiding the development of radiation-resistant semiconductors and for altering material properties through compositional engineering. So, the SRIM-based Monte Carlo framework not only provides a clear method but also a robust one for visualizing and quantifying the energy loss of different materials due to Co ions and the resulting structural changes. The results of such computational experiments are useful not only for explaining radiation-matter interactions but also for producing advanced oxide semiconductors with improved resilience and greater control over defect architecture.

The aforementioned prospects render SRIM a necessary tool in present-day materials research, as it connects theoretical models, experimental verification, and technological applications in ion-beam engineering.

RESULTS AND DISCUSSION

The implant simulation of 1.25 MeV cobalt (Co) ions was performed using the SRIM 2013 code for three different target materials: silicon (Si), zinc oxide (ZnO), and magnesium-doped zinc oxide (ZnO:Mg). The physical parameters used in the study were based on experimentally reported values and verified literature data [16-18]. The simulation geometry created a Co ion beam of uniform density that was incident normally on the planar target layers, as depicted in Figure 1.

The density of crystalline silicon was set at 2.321 g/cm^{-3} and that of pure ZnO was fixed at 4.074 g/cm^{-3}. The density of Mg-doped ZnO layer was decreased to 3.972 g/cm^{-3}, which was equivalent to atomic ratios of Zn (44.3 %), O (51.7 %), and Mg (4.0 %). The displacement energies were determined according to the elemental composition: 15 eV for Si, and 25 eV (Zn) and 28 eV (O) for the ZnO-based systems. The surface and lattice binding energies were also modified according to the stronger ionic covalent bonding nature of the Zn-O and Zn-Mg lattices.

Table 1. Chemical formula of the samples.

Material	Chemical Formula
Silicon Substrate	Si
Zinc oxide	ZnO
Magnesium-doped zinc oxide	ZnO:Mg

RESULTS AND DISCUSSION

The different target layers and recoiled atoms are visualized through these graphs (Figure 1). The sketched trajectories indicate the energy consumption, scattering, and material transformation that happened during ion penetration. Silicon (Fig. 1a) allowed Co ions to form the longest and most extensive tracks, as they penetrated deep into the substrate and straggled widely laterally. This behavior is due to Silicon's relatively low atomic mass and density (2.321 g/cm^{-3}), which results in lower resistance to incident ions. The spatial distribution of ion trajectories is thick and elongated, showing that ions still have a considerable fraction of their kinetic energy before considerable deceleration takes place. The large scattering angle distribution indicates that elastic nuclear collisions significantly contribute to energy dissipation close to the end of the range, resulting in higher defect concentration and displacement density within the silicon matrix. According to SRIM-derived data, the mean projected range of Co ions in silicon reached approximately 1.8 µm, confirming that Si possesses the deepest penetration path and the largest longitudinal straggling among the studied materials. This greater ion range correlates with the low stopping power of Si, allowing Co ions to retain high kinetic energy over longer distances before substantial deceleration. Consequently, silicon exhibits the most extended collision cascades and the largest damage region within its lattice.

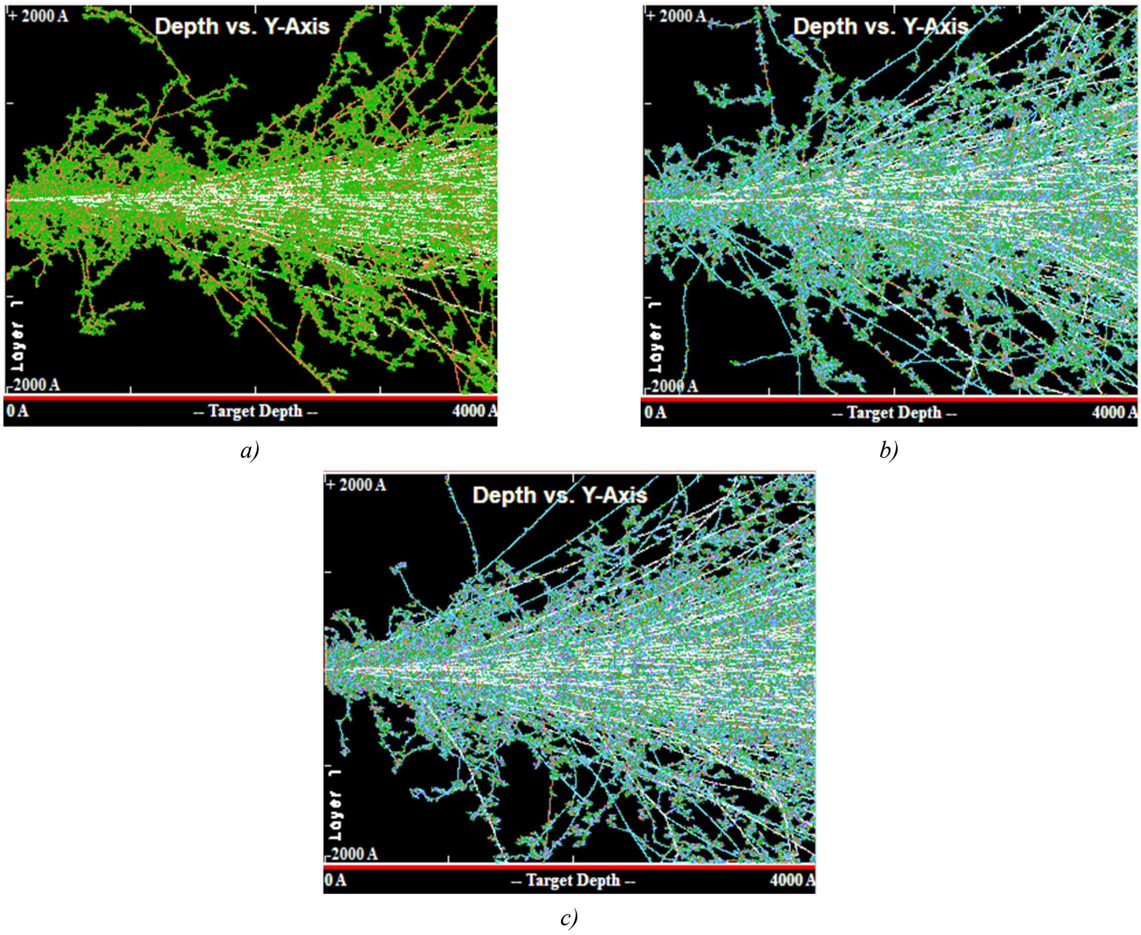

a) *b)*

c)

Figure 1. SRIM-simulated ion trajectories of 1.25 MeV Co ions in (a) ZnO, (b) ZnO:S, and (c) ZnO:S/Si targets showing the longitudinal distribution and scattering profiles of implanted ions through the target depth.

On the other hand, for ZnO (Fig. 1b), the ion trajectories are shorter and more compact compared to those in Si. The atomic arrangement is denser (4.074 g/cm^{-3}), and the ionic bonding is stronger (Zn–O bonding), which together restrict penetration depth and scattering amplitude. Most Co ions are stopped within a projected range of around 1.2 µm (or ≈ 276 nm in thin-film geometry), where the energy loss mainly occurs through the transition from electronic to nuclear stopping. The higher atomic masses of Zn and O atoms leads to reduced recoil mobility, thus confining the cascade within a very small volume. Hence the ZnO structure undergoes moderate atomic displacements and there is a distinct central collision zone that is followed by rapid energy attenuation. This behavior demonstrates that ZnO's stronger ionic–covalent bonding provides greater resistance to structural disorder than in silicon, leading to reduced defect density and shallower ion paths. The average displacement energy values of Zn = 25 eV and O = 28 eV ensure that most recoil events are localized near the end-of-range (EOR) region [19,20].

In ZnO:Mg (Fig. 1c), the Co ion paths are more uniformly scattered and their concentrations are lower at the end-of-range area. The presence of Mg atoms influences the lattice structure and decreases the average electron density slightly, this in turn leads to the reduction of both electronic and nuclear stopping probabilities. The resultant scattering pattern is therefore smoother and more uniform. The film doped with elements exhibits a lesser number of extended collision chains and lower lateral dispersion which signifies that the structural tolerance to energetic ion impact has been improved. The mean projected range for ZnO:Mg was estimated at 1.0–1.1 µm, indicating the shortest ion penetration depth among all materials studied. This reduction in range corresponds to an increase in the effective stopping power and lattice stability. Magnesium atoms, having a lighter atomic mass (24 amu), act as local energy buffers that moderate recoil cascades and mitigate defect accumulation, leading to enhanced radiation tolerance. ZnO:Mg is less affected by recoils and has a smaller energy dissipation profile when compared to pure ZnO, which means its lattice has a greater ability to relax and less damage to accumulate. All in all, the longitudinal trajectory maps in this work provide strong, unambiguous evidence that the penetration depth and scattering intensity take the order Si > ZnO > ZnO:Mg. The Si target not only suffers the most but also the disorder and range are the most extreme, while the introduction of Mg into the ZnO lattice leads to a more durable and less radiation-sensitive structure. These results agree with the assertion that modifying the composition—most notably, the addition of Mg—has a beneficial effect in the reduction of radiation-induced defects, thus making ZnO:Mg a more reliable material for semiconductor and thin-film applications where ion irradiation is involved. SRIM presents its calculations of total displacements, vacancies, and replacement collisions induced by 1.25 MeV Co ions in Si, ZnO, and ZnO:Mg targets. The simulated data shed light on the defect-formation tendencies of each material in a comparative manner [21]. The displacement and vacancy curves show how well each target resists atomic disorder under high-energy Co-ion bombardment (Figure 2).

In the case of silicon (Si), the total number of atomic displacements reaches its maximum, approximately 3090 displacements per ion, indicating that Si is the most susceptible to radiation-induced damage. This immense defect creation is ascribed to Silicon's low atomic mass and weak bonding forces which together allow for the easier transfer of kinetic energy from the impinging Co ions to the lattice atoms. Consequently, nuclear collisions and electronic energy losses greatly facilitate the creation of vacancies and interstitial defects. The high vacancy number (~3016/ion) and large replacement collision rate (74/ion) show that there is a lot of atomic mixing and cascade overlapping going on in the crystal lattice.

For zinc oxide (ZnO), the total number of atomic displacements is slightly lower, reaching approximately 3038 displacements per ion, indicating a comparable but slightly reduced level of damage relative to Si. This means that ZnO, although less damaged than Si by metal ion bombardment, nevertheless absorbs a whole lot of ion energy due to its higher density and mass (Zn = 65, O = 16) but its more rigid ionic–covalent bonds do not allow atom to migrate. Thus, zinc oxide's effective stopping power not only limits atomic displacements but also confines recoil cascades to compact near-surface regions, minimizing large-scale rearrangements. This confirms that ZnO exhibits moderate structural damage and enhanced defect localization under energetic Co ion exposure. The Zn and O sublattices tend to prevent not only the formation of large-scale atomic rearrangements but also the creation of deep collision cascades. Therefore, most of the recoil events take place near the end-of-range region, resulting in the formation of compact and shallow damage zones instead of deep ones In Mg-doped ZnO (ZnO:Mg), the total number of atomic displacements decreases further to approximately 2879 displacements per ion, demonstrating that Mg incorporation effectively suppresses radiation-induced defect formation. This decrease indicates that the incorporation of Mg atoms effectively suppresses lattice damage and mitigates the extent of defect cascade formation within the ZnO matrix [22]. The lighter Mg atoms are like local "energy buffers" that have the effect of softening the incoming energy and, at the same time, reducing the defect accumulation. The vacancy concentration (~2654/ion) still stays lower than that of pure ZnO and Si, thus the radiation tolerance is notably superior. The comparison among all the three targets gives a clear indication of one important fact, that is, the efficiency of ion-induced disorder has been systematically reduced according to the trend Si > ZnO > ZnO:Mg. This diminishing pattern is connected to the three factors of atomic bonding, density, and displacement energy among the materials [23]. Silicon, owing to its relatively low atomic mass, low density, and covalent bonding structure, is more susceptible to recoil displacement, whereas the ionic–covalent Zn–O framework exhibits greater resistance to such displacement. The better part is that the doping with Mg creates an even more stable situation with regard to the mentioned factors by increasing the overall scattering cross-section and, thus, slowing down the escape movement from the lattice. To conclude, the SRIM simulations reveal that Co ion implantation leads to the highest level of lattice defects in Si and moderate damage in ZnO, while the lowest defect density is observed in ZnO:Mg.

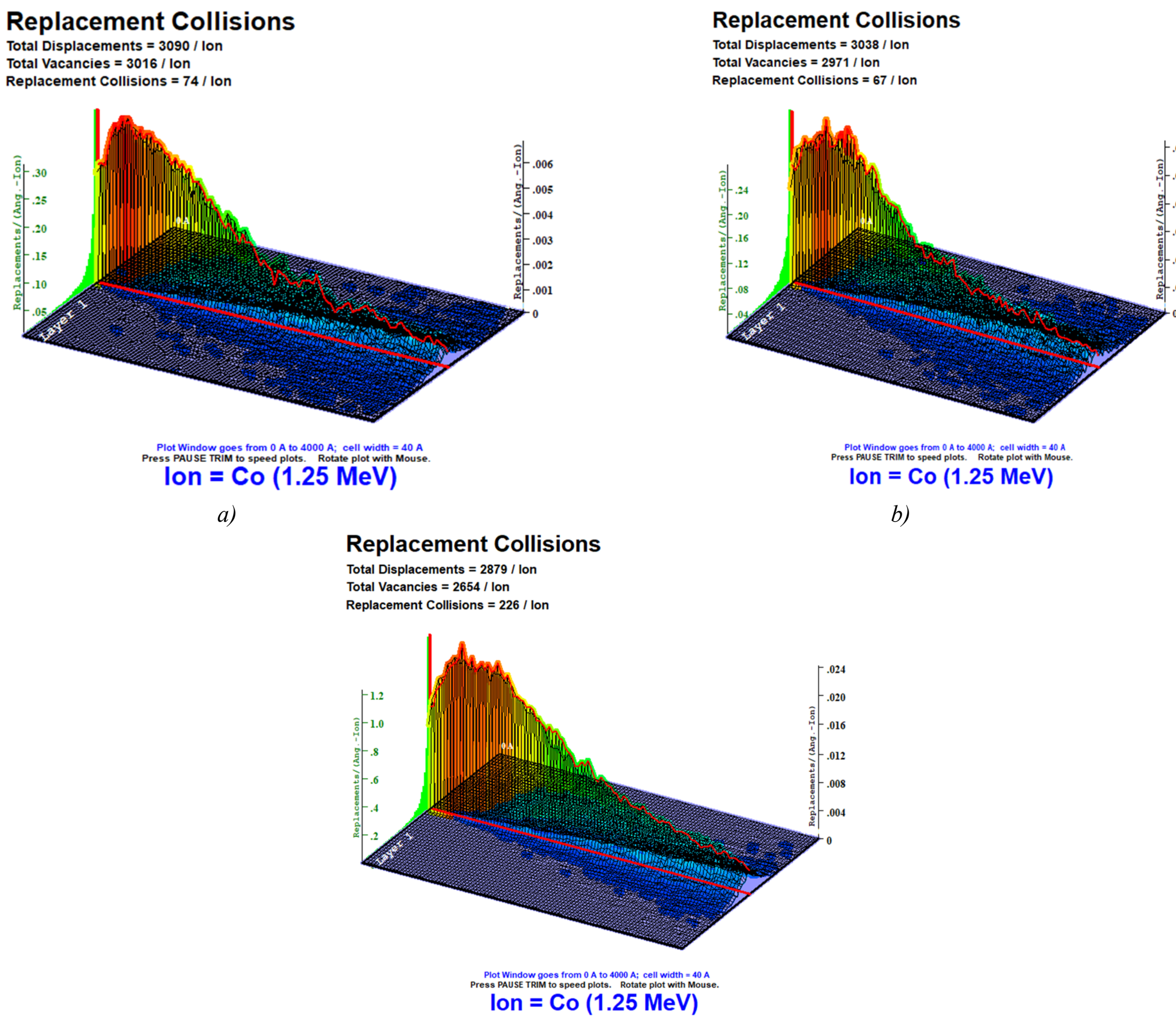

a) *b)*

c)

Figure 2. SRIM-simulated total displacements, vacancies, and replacement collisions produced by 1.25 MeV Co ion implantation in (a) Si, (b) ZnO, and (c) ZnO:Mg targets

The drop in total displacements and replacement collisions in Mg-doped ZnO demonstrates its great potential as a radiation-hardened oxide semiconductor for advanced optoelectronic and sensor applications that must operate in ionizing environments.

CONCLUSIONS

The Monte Carlo-based SRIM-2013 simulation was used to analyze the stopping behavior, energy dissipation, and defect formation processes of 1.25 MeV Co ions in Si, ZnO, and ZnO:Mg targets. The following main conclusions were drawn from the calculation results:

1. The ion penetration depth showed a strong dependence on the material composition, and the average projection range values were ≈ 1.8 µm for Si, ≈ 1.2 µm for ZnO, and ≈ 1.0–1.1 µm for ZnO:Mg.

2. The SRIM results show that the total number of atomic displacements is highest in Si ($\sim 3.09\times10^3$ displacements per ion), slightly lower in ZnO ($\sim 3.04\times10^3$ displacements per ion), and lowest in ZnO:Mg ($\sim 2.88\times10^3$ displacements per ion). This confirms that Mg incorporation into the ZnO lattice suppresses defect formation and enhances the radiation tolerance of ZnO:Mg.

3. The introduction of Mg^{2+} ions into the Zn^{2+} lattice changed the atomic mass and potential field, increased the lattice stability and smoothed the energy distribution. This significantly improved the radiation resistance of ZnO:Mg and reduced the depth distribution of defects.

4. The stopping power (–dE/dx) dominated at high energies in the electron stopping stage, and nuclear scattering mechanisms played a dominant role in the EOR (End-of-Range) region. Therefore, the energy distribution formed a Bragg-type profile for each material.

Thus, it was found that Mg-doped ZnO can be effectively used as the most stable and radiation-resistant oxide semiconductor against high-energy particles.

The results obtained serve as an important basis for improving the stability of optoelectronic and gas-sensing devices operating in ion-irradiation environments.

ORCID

A.Y. Boboev, https://orcid.org/0000-0002-3963-708X; **B.M. Ergashev**, https://orcid.org/0009-0007-9392-6548;
S.R. Kadirov, https://orcid.org/0009-0000-7584-3799; **N.Y. Yunusaliyev,** https://orcid.org/0000-0003-3766-5420;
G.G. Tojiboyev, https://orcid.org/0009-0000-5022-8108; **M.M. Arabboeva,** https://orcid.org/0009-0008-5181-4844

REFERENCES

[1] A. N. Zinoviev and P. Yu. Babenko, "Nuclear stopping powers of hydrogen and helium isotopes in beryllium, carbon, and tungsten," Technical Physics Letters, **46**(18), 23–26 (2020). https://doi.org/10.1134/S106378502009031X

[2] F. T. Yusupov, V. T. Mirzaev, T. I. Rakhmonov, O. R. Nurmatov, and D. Sh. Khidirov, "Enhanced optoelectronic properties of ZnO thin films through boron and fluorine co-doping," Journal of Ovonic Research, **21**, 285–296 (2025).

[3] M. Mishra, V. P. Banga, M. Kumar, and M. Gupta, "Effect of aging on transmittance, and effect of annealing temperature on CO_2 sensing of ZnO thin film deposited by spin coating," E-Prime – Advances in Electrical Engineering, Electronics and Energy, **7**, 100405 (2024). https://doi.org/10.1016/j.prime.2023.100405

[4] S. S. Zainabidinov, S. Kh. Yulchiev, A. Y. Boboev, B. D. Gulomov, and N. Y. Yunusaliyev, "Structural properties of Al-doped ZnO films," East European Journal of Physics, (3), 282–286 (2024). https://doi.org/10.26565/2312-4334-2024-3-28

[5] Z. Mirzajonov, K. Sulaymonov, T. Rakhmonov, F. Yusupov, D. Khidirov, and J. Rakhimjonov, "Advancements in zinc oxide (ZnO) thin films for photonic and optoelectronic applications: A focus on doping and annealing processes," E3S Web of Conferences, **549**, 03013 (2024). https://doi.org/10.1051/e3sconf/202454903013

[6] S. Z. Zainabidinov, A. Y. Boboev, and N. Y. Yunusaliev, "Effect of γ-irradiation on structure and electrophysical properties of S-doped ZnO films," East European Journal of Physics, (2), 321–326 (2024). https://doi.org/10.26565/2312-4334-2024-2-37

[7] L. Gao and J.-M. Zhang, "Photoluminescence of diluted Mg-doped ZnO thin films and band-gap change mechanisms," Acta Physica Sinica, **59**(2), 1263–1268 (2010). https://doi.org/10.7498/aps.59.1263

[8] N. R. Khalid et al., "Mechanistic investigation of Mg^{2+}-ion-induced ZnO nanorods for enhanced photocatalytic performance," Applied Nanoscience, 11(6), 1917–1927 (2021). https://doi.org/10.1007/s13204-021-01891-8

[9] A.Y. Boboev, N.Y. Yunusaliyev, G.G. Tojiboyev, O.Sh. Muminov, and S.R. Kadirov, "SRIM simulation of irradiation damage by protons in ZnO:S compound," Journal of Ovonic Research, **21**(6), 781–788 (2025). https://doi.org/10.15251/JOR.2025.216.781

[10] A. Y. Boboev, Kh. A. Makhmudov, N. Y. Yunusaliyev, M. O. G'ofurjonova, F. A. Abdulkhaev, and G. G. Tojiboyev, "Simulation of radiation-induced structural and optical modifications in ZnO:S/Si thin film structures," East European Journal of Physics, (3), 382–389 (2025). https://doi.org/10.26565/2312-4334-2025-2-36

[11] M. Hoseini, S. Hamidi et al., "The use of the SRIM code for calculating radiation damage induced by γ-rays," Pramana – Journal of Physics, **98**, 207 (2024). https://doi.org/10.1016/j.nimb.2017.08.036

[12] J. Gulomov, O. Accouche, J. Ziyoitdinov, and A. Mirzaalimov, "Optimizing CZTSe solar cell architecture: Comparative study of ZnO, TiO_2, and MoO_3 as electron transport layers," IEEE Access, **12**, 8313–8324 (2024). https://doi.org/10.1109/ACCESS.2024.3351675

[13] A. Y. Boboev, B. M. Ergashev, N. Y. Yunusaliev, and M. M. Xotamov, "Study of the formation of low-dimensional defect states in single-crystal silicon with the participation of oxygen," East European Journal of Physics, (2), 292–296 (2025). https://doi.org/10.26565/2312-4334-2025-2-36

[14] J. Gellanki, R. Kumari, R. Rani, H. Kumar Chourasiya, and S. Kumar, "In situ electrical characterization of the Au/n-Si Schottky barrier structure under 1.2 MeV Ar ion irradiation," Nuclear Instruments and Methods in Physics Research Section B: Beam Interactions with Materials and Atoms, **552**, 165373 (2024). https://doi.org/10.1088/1361-6641/acb45e

[15] Z. Ali, F. Liu et al., "Advancements in primary radiation damage models and SRIM simulations: A review of radiation damage predictions," Nuclear Engineering and Technology, **57**, 103570 (2025). https://doi.org/10.1016/j.net.2025.103570

[16] A. Jogi, A. Alanthattil, and B. V. Rajendra, "Modulation of optical and photoluminescence properties of ZnO thin films by Mg dopant," Journal of Materials Science: Materials in Electronics, **34**(7) (2023). https://doi.org/10.1007/s10854-023-09999-z

[17] T. Ivanova, A. Harizanova, T. Koutzarova, B. Vertruyen, and R. Closset, "Deposition of sol-gel ZnO:Mg films and investigation of their structural and optical properties," Materials, **15**(24), 8883 (2022).

[18] A. Y. Boboev, N. Y. Yunusaliev, Kh. A. Makhmudov, F. A. Abdulkhaev, G. G. Tojiboyev, and M. O. G'ofurjonova, "Surface morphology and roughness of sulfur-doped ZnO thin films: analysis based on atomic force microscopy," East European Journal of Physics, (3), 319–324 (2025). https://doi.org/10.26565/2312-4334-2025-3-30

[19] B. Patra et al., "Significant transformation in the point defects evidenced via theoretical simulations supported by Raman and photoluminescence studies in vertically grown 1D ZnO nanorods triggered by titanium ion implantation," Physica B: Condensed Matter, **672**, 415016 (2024). https://doi.org/10.1016/j.physb.2024.415745

[20] B. Oryema, I. G. Madiba, and C. B. Mtshali, "Atomistic simulation of primary radiation damage profiles in fluorine-doped tin oxide thin film target using SRIM code," Nano-Horizons: Journal of Nanosciences and Nanotechnologies **3**, 44–55 (2024). https://doi.org/10.25159/3005-2602/15610

[21] J. Zhang, Y. Niu et al., "An extension of first-principle combined Monte Carlo method to simulate secondary electron yield of anisotropic crystal Al_2O_3," Journal of Applied Physics, **135**, 085102 (2024). https://doi.org/10.1063/5.0182083

[22] A. N. Zinoviev, P. Yu. Babenko et al., "Contribution of molecular orbital excitation to the electronic stopping cross section in slow collisions of atoms with solids," Nuclear Instruments and Methods in Physics Research Section B **558**, 165217 (2024). https://doi.org/10.1016/j.nimb.2023.165219

[23] A. T. Mamadalimov, M. Sh. Isaev, M. N. Mamatkulov, S. R. Kodirov, and J. T. Abdurazzakov, "Study of silicide formation in large diameter monocrystalline silicon," East European Journal of Physics, (2), 366–370 (2024). https://doi.org/10.26565/2312-4334-2024-2-45

МОДЕЛЮВАННЯ ВПЛИВУ Co-ІОННОЇ ІМПЛАНТАЦІЇ НА ТОНКІ ПЛІВКИ ZnO, ЛЕГОВАНІ Mg ЗА ДОПОМОГОЮ МОНТЕ-КАРЛО SRIM

Акрамжон Й. Бобоєв[1], Нурітдін Ю. Юнусалієв[1], Білоліддін М. Ергашев[2], Гайбулло Г. Тоджибоєв[1], Сардор Р. Кадіров[3], Мохірабону М. Араббоєва[1]
[1]Андижанський державний університет імені З.М. Бабура, Андижан, Узбекистан
[2]Андижанський державний педагогічний інститут, Андижан, Узбекистан
[3]Ургенчський державний університет, Ургенч, Узбекистан

Поведінка взаємодії іонів Co з енергією 1,25 МеВ з мішенями ZnO (ZnO:Mg), легованими Si, ZnO та Mg, була систематично проаналізована за допомогою останньої версії симуляційного пакета SRIM 2013. Результати показують, що атомні зміщення, утворення вакансій та втрати енергії значною мірою залежать від складу та структурної щільності мішені. Результати показують, що найвища концентрація дефектів спостерігається в кристалічному Si через його нижчу порогову енергію зміщення та меншу атомну масу, що підвищує ймовірність зіткнень віддачі. З іншого боку, ZnO демонструє помірне утворення дефектів, оскільки його висока атомна щільність та енергія зв'язку ускладнюють упорядкування решітки. Крім того, присутність Mg у матриці ZnO дещо зменшує загальне пошкодження, що означає, що решітка стабільніша та стійкіша до впливу радіації. З цих результатів можна зробити висновок, що легування Mg дійсно покращує структурну стійкість ZnO до бомбардування високоенергетичними іонами Co і таким чином робить плівки ZnO:Mg більш придатними для радіаційно стійких оптоелектронних та сенсорних застосувань.

Ключові слова: *гальмівна здатність; ZnO; ZnO, легований Mg; SRIM; іонна імплантація; вакансія; дефект; радіаційне пошкодження; моделювання методом Монте-Карло*

EAST EUROPEAN JOURNAL OF PHYSICS. 2. 368-372 (2026)
DOI:10.26565/2312-4334-2026-2-39 ISSN 2312-4334

STUDY OF THERMOPHYSICAL PROPERTIES OF Cu_2NiTe_2 COMPOUND AT HIGH TEMPERATURES BY DSC SPECTROSCOPY

Y.I. Aliyev[1,2]*, **Kh.M. Guliyeva**[3], **N.N. Mursakulov**[3], **Kh.N. Ahmadova**[3,4,5],
A.I. Bayramova[2], **L.N. Ibrahimova**[6]
[1]*Azerbaijan State Pedagogical University, Baku, AZ-1000, Azerbaijan*
[2]*Azerbaijan University of Architecture and Construction, Baku, AZ-1073, Azerbaijan*
[3]*Institute of Physics, Ministry of Science and Education, Republic of Azerbaijan, Baku, AZ-1143, Azerbaijan*
[4]*Azerbaijan State Oil and Industry University, Baku, AZ-1010, Azerbaijan*
[5]*Khazar University, Baku, AZ-1096, Azerbaijan*
[6]*Nakhchivan State University, Nakhchivan, AZ-7012, Azerbaijan*
Corresponding Author email: yusifafshar@gmail.com

Received February 27, 2026; revised May 8, 2026; accepted May 14, 2026

The crystal structure and thermophysical properties of the chalcogenide semiconductor Cu_2NiTe_2 were comprehensively investigated using X-ray diffraction and differential scanning calorimetry. Structural characterization at room temperature revealed that the synthesized compound crystallizes in the hexagonal crystal system with the space group $P6_3/mmc$, indicating the formation of a highly ordered polycrystalline phase. The diffraction peaks were sharp and well-defined, confirming the material's good crystallinity and structural homogeneity. The absence of additional impurity peaks in the diffraction pattern also suggests that the synthesized compound possesses a predominantly single-phase structure.

Key words: *Cu_2NiTe_2; Chalcogenide; Semiconductor; DSC; X-ray diffraction; Crystal structure; Thermal properties*
PACS: 61.10.Nz, 67.80.Gb.

1. INTRODUCTION

Studying the thermal properties of semiconductor compounds provides information on both their structure and various physical properties. Thermal energy significantly influences the formation of these properties. Changing the temperature of a system alters the thermodynamic parameters, which in turn influence its physical properties. Therefore, extensive research has recently been conducted on the thermal properties of condensed systems and the influence of temperature on their physical properties [1-5].

The development of analytical methods allows for both increasing the accuracy of the results obtained and conducting comparative analysis. These methods enable the study of structural changes and thermal effects in various systems [6-8]. One of them is Differential Scanning Calorimetry (DSC). It has been established that, in studies conducted using the DSC method, it is possible to investigate structural transformations, thermal effects, melting, and other processes occurring in semiconductors, and to determine the mechanism of changes in thermodynamic parameters during these processes [9-11]. The thermodynamic functions of many semiconductor crystals have been studied by the DSC method. The thermal properties of the $Cu_2NiSeTe$ compound at high temperatures have been studied [12]. It has been established that 4 thermal transitions occur within the specified temperature range. The transition at $T = 144°C$ is attributed to the escape of water molecules from the sample. It has been shown that thermal transitions at $T = 587$ and $647°C$ increase system stability by rupturing weak bonds in polycrystals, whereas the transition at $T = 714°C$ corresponds to a structural phase transition.

There are certain difficulties in studying the thermal properties of chalcogenide semiconductors. Since these compounds are non-oxide materials, an oxide layer forms on their surfaces as the temperature increases. To avoid this, the thermophysical properties of chalcogenide semiconductors are studied in vacuum conditions [13]. When conducting studies in vacuum conditions, the mass of the samples does not change. Therefore, studies by Thermogravimetric Analysis (TGA) cannot be performed. However, by analyzing the DSC spectra, it is possible to study the processes of evaporation, decomposition, phase transitions, and melting occurring in the system.

Copper chalcogenides are compounds with interesting physical properties. Since Cu atoms have variable valence, various structures and physical properties are observed in the compounds they form [14-16]. One of such compounds is Cu_2NiTe_2. Although many properties of this compound have been studied, its thermal properties at high temperatures remain underexplored. In this work, a Cu_2NiTe_2 crystal was synthesized, its crystal structure at room temperature and thermophysical properties at elevated temperatures were studied.

2. EXPERIMENTAL PART

Sample synthesis. The Cu_2NiTe_2 compound was synthesized using a standard method typical for chalcogenide semiconductors. To prevent oxidation, the synthesis was carried out under vacuum. In a single-zone furnace, the elements

---

Cite as: Y.I. Aliyev, Kh.M. Guliyeva, N.N. Mursakulov, Kh.N. Ahmadova, A.I. Bayramova, L.N. Ibrahimova, East Eur. J. Phys. 2, 368 (2026), https://doi.org/10.26565/2312-4334-2026-2-39

(copper, nickel, and tellurium), deposited in stoichiometric proportions, were collected in a quartz ampoule. Air was evacuated from the ampoule to a vacuum of 10^{-4} Hg, and the ampoule's neck was closed. The ampoule's temperature was stabilized at T = 300°C inserted into the furnace. After holding the process for 1 hour, the furnace temperature was gradually increased. The temperature was stopped at 800°C, 900°C, and 1000°C for 30 minutes in the range of T = 700-1050°C. To ensure homogeneity, the synthesis ampoule was shaken while the furnace was running. After this, the temperature was also increased by T = 1050°C and maintained for 1.5 hours. In the next step, the temperature was gradually reduced to T = 600°C. After holding at the homogenization temperature for 3 days, the process was stopped. To study the structure of the resulting sample, X-ray diffraction analysis was performed. Based on the data obtained, the Cu_2NiTe_2 crystal was synthesized as a single-phase polycrystalline material.

Study of crystal structure. There are various methods for studying the crystal structure of solids. The research method is selected depending on the shape and chemical composition of the samples being studied. One such method is X-ray diffraction (XRD). It was used to study the crystal structure of the Cu_2NiTe_2 compound. Modern X-ray diffractometers make it possible to study the structure of crystalline solids and determine crystallographic parameters. The studies were conducted on a D8 ADVANCE diffractometer (Bruker, Germany). Its parameters were: 40 kV, 40 mA, CuK_α radiation, λ = 1.54184 Å. After the synthesis, samples for study were prepared from a polycrystal of Cu_2NiTe_2. For X-ray diffraction studies, the sample was crushed and ground into powder. The X-ray diffraction spectrum obtained at room temperature was analyzed using the Rietveld method in Mag2Pol. Miller indices were determined from the diffraction maxima. The symmetry, syngony, space group, and lattice parameters of the crystal were determined.

Study of thermophysical properties. Various approaches are used to investigate the thermophysical properties of condensed matter systems. Each experimental technique has its own advantages and limitations, depending on the nature of the material under investigation and the measurement conditions. Among the existing experimental techniques employed for thermophysical characterization, Differential Scanning Calorimetry (DSC) and Thermogravimetric Analysis (TGA) hold particular importance due to their high sensitivity and broad applicability [17-19]. The DSC method is based on the passage of heat flux through the sample, and the temperature dependence of the heat flux function is given in the DSC spectrum. The TGA method is based on the temperature dependence of a substance's mass. In studies conducted under vacuum conditions, it is not possible to control the change in mass. Because the mass of the ampoule generally remains unchanged. However, it is possible to obtain a DSC spectrum. Therefore, the thermophysical properties of the Cu_2NiTe_2 compound were studied at high temperatures using the DSC method. Those measurements were carried out using the DSC3 STAR Systems manufactured by METTLER TOLEDO, and temperature-corrected MULTISTAR sensors. The standard adiabatic calorimetry was performed in the temperature range from 20 °C up to 1000 °C at a heating rate of 5 °/min in argon atmosphere at a flow rate of 20 $mL \cdot min^{-1}$ (which is previously calibrated with indium). The cooling process was achieved with the help of the NITROGEN UN 1977 REFRIGERATED LIQUID analyzer cooling system and "digital temperature controller". The error of weight determination did not exceed **0.02**% at 20 °C and 1% at 1000 °C.

3. RESULTS AND DISCUSSION

The crystal structure of the Cu_2NiTe_2 compound was studied by X-ray diffraction at room temperature and normal conditions. The spectrum, obtained in the diffraction angle range of $25° \leq 2\theta \leq 70°$, is shown in Figure 1.

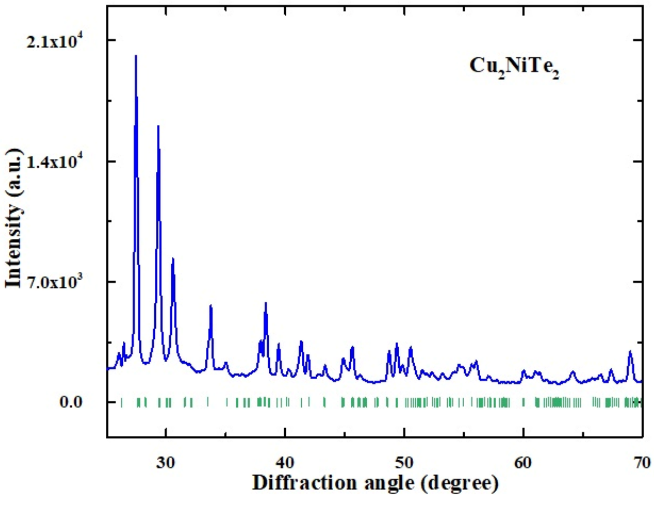

Figure 1. X-ray diffraction spectrum of the compound Cu_2NiTe_2. The experimentally obtained spectrum is shown by the blue line, and the diffraction planes are shown by the green lines

An analysis of the X-ray spectrum using the Rietveld method in the Mag2Pol program revealed that the crystal structure of the Cu_2NiTe_2 compound has high symmetry. The values of the crystallographic parameters were determined for this compound. It was found that the crystal structure of the Cu_2NiTe_2 compound has hexagonal symmetry and space group P6$_3$/mmc. The values of the lattice parameters were determined: $a = b = 3.9447(5)$ Å, $c = 17.1382(6)$ Å. The results are consistent with those from studies of the structure of copper- and nickel-containing chalcogenide dielectrics. Previous studies have established that the crystal structure of the $Cu_2NiSeTe$ compound is also hexagonal [12]. Certain variations were observed in the lattice parameters of these compounds. Such changes are mainly associated with the nature and atomic characteristics of the elements forming the crystal structure. In the $Cu_2NiSeTe$ compound, a portion of the Te atoms is substituted by Se atoms, resulting in modifications of the lattice parameters. This behavior can be explained by the mismatch between the ionic radii of selenium and tellurium atoms, which influences the interatomic distances and consequently affects the crystal lattice dimensions. It has been established that in the divalent state, the ionic radius of the selenium atoms is $R_{\mathrm{Se2-}} = 0.69$ Å, and the ionic radius of the tellurium atoms is $R_{\mathrm{Te2-}} = 0.85$ Å [20]. Between the ionic radii of these atoms, there is a distance of $\Delta R = 0.16$ Å. When a covalent chemical bond is formed between the metal and chalcogen atoms, the distance ΔR has a significant effect. Therefore, differences in the lattice parameters of the $Cu_2NiSeTe$ and Cu_2NiTe_2 compounds arise.

The results from structural studies indicate that the Cu_2NiTe_2 compound has a single-phase, highly symmetric hexagonal structure. Covalent bonds formed by Cu and Ni metals with Te chalcogen atoms are capable of forming a dense, highly symmetric system in a small volume. Such systems are resistant to external influences.

Semiconductor materials are known as functional materials with potential applications across various fields. Cu_2NiTe_2, in particular, has a wide range of applications. Therefore, it is important to study the processes occurring under external influences. When considering external influences, temperature is primarily considered, since heating occurs in electronic devices. As the temperature increases, the functionality of semiconductor converters changes. Therefore, when studying each research object, it is necessary to examine the fundamental physical properties that arise with temperature. With this in mind, the thermophysical properties of Cu_2NiTe_2 at high temperatures were studied.

Thermal properties were studied at high temperatures using DSC. The heat flow spectrum in the temperature range $20°C \leq T \leq 1000°C$ is shown in Figure 2.

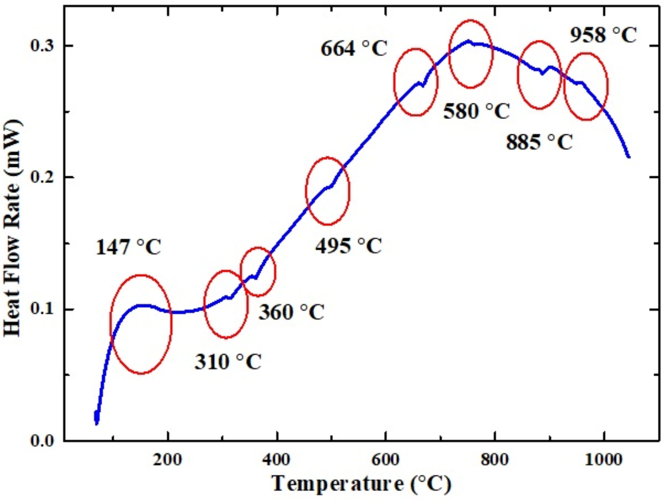

Figure 2. Heat flow rate function of Cu_2NiTe_2 sample at the $20\ °C \leq T \leq 1000\ °C$ temperature ranges

As can be seen from Figure 2, the temperature dependence of the heat flux spectrum can be divided into four distinct regions, each corresponding to specific thermophysical processes occurring within the investigated material. In the first region, the heat flux value increases abruptly to $\Phi = 0.1$ mW. In the second region, it remains practically at the level of $\Phi \sim 0.1$ mW. In the third region, a abrupt increase in the heat flux value to $\Phi = 0.3$ mW is observed. In the last region, a decrease in the value of the heat flux function is observed. The abrupt increase in the heat flux in a small temperature range is associated with the quantum region of heat capacity in high-entropy compounds. At this time, the frequencies of harmonic oscillations of the atoms forming the structure begin to increase. When analyzing the DSC spectrum of the Cu_2NiTe_2 compound, it was determined that the thermal properties of this compound are quite complex. Each of the 4 different regions observed at high temperatures has its own thermal properties. In some regions, the lattice vibration frequencies increase due to thermal energy, in some regions they remain stable, and in some regions a decrease is observed. The observation of these effects is associated with thermal transitions occurring in the system. From the spectrum presented in Figure 2, it is evident that 8 different thermal effects were observed at high temperatures. These effects occurred at temperatures of $T = 147$ °C, 310 °C, 360 °C, 495 °C, 664 °C, 580 °C, 885 °C, and 958 °C. As can be seen from the spectrum, the effect centered at $T = 147$ °C differs from the others. This effect is caused by a small number of water molecules leaving the sample. Beginning at approximately $T = 100$ °C, water molecules undergo evaporation and gradually leave the sample in the gaseous phase. Although water molecules are free, in some cases they combine with metal atoms in the material, forming hydroxide groups. In this case, as the temperature increases, the hydroxide groups first break down and water molecules form. Then, the water molecules begin to leave the substance. Thermal effects in this case occur at higher temperatures.

The spectrum in Figure 2 shows that the remaining thermal effects are endoeffects, which are virtually identical to each other. The energy required to generate the effects is of the same order. These effects, which arise with low energy absorption, are primarily associated with the release of air gases from the substance. For example, gas atoms adsorbed from the air, primarily carbon dioxide, exist in a space between grains. These molecules exist both freely and form specific chemical bonds with the metal atoms within the sample. As the temperature increases, the vibrational amplitudes of the bonds between the atoms increase, breaking weak chemical bonds. When bonds are broken, the gas molecules escape the sample. This effect is observed by energy absorption in the DSC spectrum. The thermal effects observed for the Cu_2NiTe_2 compound at high temperatures are virtually identical. No phase transition is observed in the system.

4. CONCLUSIONS

The crystal structure and thermophysical properties of the Cu_2NiTe_2 compound were comparatively studied. Structural studies revealed that this compound has a highly symmetrical hexagonal crystal structure. The thermal properties of Cu_2NiTe_2 were studied in the temperature range of $T = 20\text{-}1000°C$. Eight thermal effects were observed in this temperature range. The transition at $T = 147°C$ is attributed to the release of water molecules from the sample. Other effects, occurring at higher temperatures, are explained by the rupture of bonds between gas atoms within the sample and the release of gases from it. It was determined that the hexagonal system is sufficiently stable at this temperature, and no phase transition occurs in this temperature range.

ORCID

Y.I. Aliyev, https://orcid.org/0000-0001-8896-2180; **Kh.M. Guliyeva,** https://orcid.org/0000-0001-8061-3189; **N.N. Mursakulov,** https://orcid.org/0000-0001-5121-9289; **Kh.N. Ahmadova,** https://orcid.org/0000-0001-5974-5400

REFERENCES

[1] N.T. Dang, V.S. Zakhvalinskii, D.P. Kozlenko, T.-L. Phan, S.E. Kichanov, S.V. Trukhanov, A.V. Trukhanov, *et al.*, "Effect of Fe doping on structure, magnetic and electrical properties $La_{0.7}Ca_{0.3}Mn_{0.5}Fe_{0.5}O_3$ manganite," Ceramics International, **44**(13), 14974-14979 (2018). https://doi.org/10.1016/j.ceramint.2018.05.124

[2] E.B. Asgerov, D.I. Ismailov, R.N. Mehdiyeva, S.H. Jabarov, M.N. Mirzayev, E.M. Kerimova, and N.T. Dang, "Differential-thermal and X-ray analysis of $TlFeS_2$ and $TlFeSe_2$ chalcogenides," Journal of Surface Investigation: X-ray, Synchrotron and Neutron Techniques, **12**(4), 688-691 (2018). https://doi.org/10.1134/S1027451018040043

[3] Y.G. Asadov, Y.I. Aliyev, A.O. Dashdemirov, S.H. Jabarov, and T.G. Naghiyev, "High-temperature X-ray diffraction study of Ag_2S-Cu_2S system," Modern Physics Letters B, **34**, 2150018 (2020). https://doi.org/10.1142/S0217984921500184

[4] M.N. Mirzayev, R.N. Mehdiyeva, Kh.F. Mammadov, S.H. Jabarov, and E.B. Asgerov, "Calculation of the thermal parameters of boron silicide by differential scanning calorimetry," Physics of Particles and Nuclei Letters, **15**(6), 673-677 (2018). https://doi.org/10.1134/S1547477118060146

[5] S.H. Jabarov, A.Kh. Nabiyeva, E.M. Huseynov, G.T. Imanova, A.V. Trukhanov, and S.V. Trukhanov, "Dielectric and electrical properties of $La_{0.5}Ba_{0.5}MnO_3$ and $La_{0.97}Ba_{0.03}MnO_3$ perovskites," Journal of Porous Materials, **31**(5), 1811-1816 (2024). https://doi.org/10.1007/s10934-024-01632-6

[6] Kh.N. Ahmadova, Sh.N. Aliyeva, Sh.R. Mammadova, and L.N. Ibrahimova, "Comparative optical characterization of CdSe and CdS thin films by spectroscopic ellipsometry for photovoltaic applications," Advanced Physical Research, **7**(3), 358-365 (2025). https://doi.org/10.62476/apr.73358

[7] S.M. Bashirova, "Study of radiation-thermal decomposition of water in the nano-Si/H_2O system using Fourier infrared spectroscopy," Scientific Works, Azerbaijan University of Architecture and Construction, (1), 113-116 (2025). https://doi.org/10.58225/sw.2025.1-113-116

[8] S.H. Jabarov, "Structural and thermal analysis of $BaFe_{11.9}Ga_{0.1}O_{19}$ and $BaFe_{11.7}Ga_{0.3}O_{19}$," International Journal of Modern Physics B, **32**(27), 1850303 (2018). https://doi.org/10.1142/S0217979218503034

[9] A.O. Dashdemirov, Y.I. Aliyev, T.M. Ilyasli, R.E. Huseynov, S.R. Azimova, and H.J. Huseynov, "Heat flux and mass effect in the $Cu_{2-x}Tm_xSe$ system at high temperatures," Advanced Physical Research, **7**(1), 111-117 (2025). https://doi.org/10.62476/apr.71011

[10] A. Raudino, M.G. Sarpietro, and M. Pannuzzo, "4 – Differential scanning calorimetry (DSC): theoretical fundamentals, Drug-Biomembrane Interaction Studies, The Application of Calorimetric Techniques Woodhead Publishing Series in Biomedicine, 127-168 (2013). https://doi.org/10.1533/9781908818348.127

[11] E.M Huseynov, and A.S. Abiyev, "Investigating gamma radiation-induced modifications in titanium nitride (TiN) nanocrystals using DSC spectroscopy," Radiation Physics and Chemistry, **232**, 112652 (2025). https://doi.org/10.1016/j.radphyschem.2025.112652

[12] Kh.M. Guliyeva, N.N. Mursakulov, N.A. Aliyeva, and Y.I. Aliyev, "Synthesis, structure and thermal properties of the $Cu_2NiSeTe$," Integrated Ferroelectrics, **237**, 67-72 (2023). https://doi.org/10.1080/10584587.2023.2227048

[13] S.R. Azimova, N.M. Abdullayev, Y.I. Aliyev, M.N. Mirzayev, V.A. Skuratov, A.K. Mutali, and S.H. Jabarov, "Study on the thermodynamic behavior of Sb-Te binary systems with swift heavy-ions irradiation at the high temperatures," Journal of the Korean Physical Society, **77**(3), 240-246 (2020). https://doi.org/10.3938/jkps.77.240

[14] I.I. Mazin, "Structural and electronic properties of the two-dimensional superconductor CuS with 1 -valent copper," Physical Review B, **85**, 115133 (2012). https://doi.org/10.1103/PhysRevB.85.115133

[15] Yu.I. Aliyev, A.G. Babaev, Yu.G. Asadov, G.F. Ganizade, R.D. Aliyeva, S.G. Jabarov, and A.V. Trukhanov, "Temperature-induced structural phase transformations in $Cu_{1.50}Zn_{0.30}Te$ and $Cu_{1.75}Cd_{0.05}Te$ single crystals," Crystallography Reports, **62**(4), 610-617 (2017). https://doi.org/10.1134/S1063774517040022

[16] K. Fujinuma, D. Takegami, A. Melendez-Sans, M. Yoshimura, K.-D. Tsuei, R. Higashinaka, T.D. Matsuda, *et al.*, "Effect of S *3p* and Se *4p* holes on charge fluctuations in pyrite-type CuS_2 and $CuSe_2$ revealed by hard x-ray photoemission spectroscopy," Physical Review B, **111**, 115147 (2025). https://doi.org/10.1103/PhysRevB.111.115147

[17] E. Ghanbari, S.J. Picken, and J.H. van Esch, “Analysis of differential scanning calorimetry (DSC): determining the transition temperatures, and enthalpy and heat capacity changes in multicomponent systems by analytical model fitting,” Journal of Thermal Analysis and Calorimetry, **148**, 12393-12409 (2023). https://doi.org/10.1007/s10973-023-12356-1
[18] H. Chang, R. Murugan, and A. Ghule, “Coupling of thermogravimetric analysis and thermo-Raman spectroscopy for in situ dynamic thermal analysis,” Thermochimica Acta, **374**(1), 45-49 (2001). https://doi.org/10.1016/S0040-6031(01)00488-9
[19] A.J. Shapiro, R.M. O’Dea, and T.H. Epps III, “Thermogravimetric analysis as a High-throughput lignocellulosic biomass characterization method,” ACS Sustainable Chemistry & Engineering, **11**(49), 17216-17223 (2023). https://doi.org/10.1021/acssuschemeng.3c03769
[20] L.T. Bugaenko, S.M. Ryabykh, and A.L. Bugaenko, A nearly complete system of average crystallographic ionic radii and its use for determining ionization potentials, Moscow University Chemistry Bulletin, **63**, 303-317 (2008). https://doi.org/10.3103/S0027131408060011 (in Russian)

ДОСЛІДЖЕННЯ ТЕПЛОФІЗИЧНИХ ВЛАСТИВОСТЕЙ СПОЛУКИ Cu_2NiTe_2 ЗА ВИСОКИХ ТЕМПЕРАТУР МЕТОДОМ ДСК-СПЕКТРОСКОПІЇ

Ю.І. Алієв[1,2], Х.М. Гулієва[3], Н.Н. Мурсакулов[3], Х.Н. Ахмадова[3,4,5], А.І. Байрамова[2], Л.Н. Ібрагімова[6]
[1]*Азербайджанський державний педагогічний університет, Баку, AZ-1000, Азербайджан*
[2]*Азербайджанський університет архітектури та будівництва, Баку, AZ-1073, Азербайджан*
[3]*Інститут фізики, Міністерство науки та освіти, Азербайджанська Республіка, Баку, AZ-1143, Азербайджан*
[4]*Азербайджанський державний університет нафти та промисловості, Баку, AZ-1010, Азербайджан*
[5]*Хазарський університет, Баку, AZ-1096, Азербайджан*
[6]*Нахчиванський державний університет, Нахчивань, AZ-7012, Азербайджан*

Кристалічну структуру та теплофізичні властивості халькогенідного напівпровідника $Cu2NiTe_2$ було всебічно досліджено за допомогою рентгенівської дифракції та диференціальної скануючої калориметрії. Структурна характеристика за кімнатної температури показала, що синтезована сполука кристалізується в гексагональній кристалічній системі з просторовою групою $P6_3/mmc$, що вказує на утворення високовпорядкованої полікристалічної фази. Дифракційні піки були різкими та добре визначеними, що підтверджує добру кристалічність та структурну однорідність матеріалу. Відсутність додаткових домішкових піків на дифракційній картині також свідчить про те, що синтезована сполука має переважно однофазну структуру.

Ключові слова: *Cu_2NiTe_2; халькогенід; напівпровідник; ДСК; рентгенівська дифракція; кристалічна структура; теплові властивості*

East European Journal of Physics. **2.** 373-378 (2026)
DOI:10.26565/2312-4334-2026-2-40 ISSN 2312-4334

FABRICATION AND ELECTRICAL TRANSPORT PROPERTIES OF TRIPLE-BARRIER GaAs-BASED M–p–n–M STRUCTURES

Bahodir M. Abdukahhorov, Oybek A. Abdulkhaev, Damir B. Istamov*, Shukurullo M. Kuliyev, Dilbara M. Yodgorova
Physical-Technical Institute of Uzbekistan Academy of Sciences, Tashkent 100084, Uzbekistan
**Corresponding Author e-mail: istamov@uzsci.net*

Received February 28, 2026; revised March 31, 2026; April 16, 2026

Engineering multi-barrier potential profiles provides an effective approach to controlling charge-carrier transport in semiconductor structures. In this work, three configurations of triple-barrier *GaAs*-based metal–p–n–metal (M–p–n–M) structures were fabricated on semi-insulating *GaAs* substrates using liquid phase epitaxy (LPE). The layer composition and semitransparent metal contacts (*Ag*, *Au*) were deliberately designed to form a coupled system of metal–semiconductor and *p - n* junctions. The electrical transport properties were investigated over a wide voltage range, and the current–voltage characteristics were comparatively analyzed. In the low-bias regime, the current follows a power-law dependence $I \sim V^{0.5}$, indicating generation-dominated transport. With increasing bias, a transition to a quasi-ohmic region and subsequent breakdown behavior was observed. In the high-field regime, linear regions in the $ln(I/U^2)$ versus $1/U$ dependence confirm the dominance of field-assisted transport mechanisms within the barrier regions. The results demonstrate that electric-field redistribution and barrier coupling play key roles in governing charge transport in triple-barrier structures, providing a foundation for the further development of advanced semiconductor devices.

Keywords: *Gallium arsenide; Metal–semiconductor junction; p–n junction; Triple-barrier structure; Liquid phase epitaxy; Electrical transport; High-field effects*
PACS: 73.40.Sx, 73.40.-c, 72.20.Ht, 72.20.Jv, 85.60.Gz

1. INTRODUCTION

The rapid development of optical communication and high-speed signal processing systems requires photodetector architectures that combine low dark current, high responsivity, and a wide operational voltage range[1–6]. Gallium arsenide ($GaAs$)-based metal-semiconductor-metal (MSM) photodetectors offer intrinsic advantages such as low capacitance and fast response. However, their performance is often limited by relatively low Schottky barrier heights, which lead to increased dark current levels [7–10]. In addition, the high density of surface states in $GaAs$ can give rise to surface leakage currents, further degrading sensitivity [11–13].

Traditional photoresistors previously employed in optoelectronic circuits have largely been replaced by semiconductor photostructures based on $p-n$ junctions. Avalanche photodiodes, $p-i-n$ photodiodes, and phototransistors with internal gain mechanisms are widely used in high-speed and high-sensitivity applications [14–18]. Such devices can also operate in unconventional biasing modes to enable advanced functional capabilities [19].

For ultraviolet and visible spectral regions ($200 \div 900\ nm$), photodetectors are typically fabricated using compound semiconductors such as GaP, $GaAsP$, and $GaAs$ [20,21]. Various contact metals, including Au [22], Pt [23], Ni [24], Al [25], and Cu [26], are employed to tailor metal-semiconductor interfaces. The introduction of thin interfacial insulating layers has been shown to suppress reverse leakage currents and increase breakdown voltages without significantly compromising photosensitivity.

In recent years, several approaches have been proposed to mitigate dark current and enhance performance, including modified Schottky contacts, nBn architectures, and double-barrier heterostructures [27–29]. In multi-barrier systems, the sequential limitation of current by individual junctions enables improved control over breakdown processes and reduced leakage currents.

High-field carrier transport in barrier structures is commonly described within the Fowler–Nordheim tunneling framework [30], while charge transport across thin potential barriers can be further interpreted using the Simmons model [31].

Owing to its direct bandgap, high electron mobility, and stable metal-semiconductor interface formation, $GaAs$ remains one of the most attractive compound semiconductors for photodetectors and photovoltaic applications [7,32].

Despite these advances, most reported MSM and heterostructure devices rely on nanostructuring, plasmonic enhancement, or complex epitaxial techniques. In contrast, the electrophysical behavior of classical multi-barrier $M-p-n-M$ architectures fabricated by liquid phase epitaxy (LPE) have not been systematically investigated. In particular, the role of controlled $p-$layer thickness in barrier coupling and in the transition between transport regimes under high electric fields has not been experimentally clarified.

In this context, the present study is focused on electrical transport under dark conditions as a fundamental step toward understanding carrier dynamics in multi-barrier semiconductor structures.

Cite as: B.M. Abdukahhorov, O.A. Abdulkhaev, D.B. Istamov, Sh.M. Kuliyev, D.M. Yodgorova, East Eur. J. Phys. 2, 373 (2026), https://doi.org/10.26565/2312-4334-2026-2-40

The objective of this work is to develop baseline structural designs and fabrication technologies for semiconductor structures, to fabricate experimental samples, and to elucidate the mechanisms governing their electrical transport properties.

In this study, triple-barrier $GaAs$-based $M-p-n-M$ structures were fabricated by liquid phase epitaxy, and their carrier transport mechanisms in the high-field regime were comparatively analyzed based on current–voltage characteristics.

2. STRUCTURE AND FABRICATION

2.1 Structural Design of Triple-Barrier $m-p-n-m$ structures

The investigated structures were designed as triple-barrier $metal-p-n-metal$ $(M-p-n-M)$ architectures fabricated on semi-insulating (SI) $GaAs$ substrates (Fig. 1). The structure consists of a top metal-semiconductor $(M-S)$ junction, a central $p-n$ junction, and a bottom metal–semiconductor junction, thereby forming three sequentially coupled potential barriers. Such a configuration enables electric field redistribution across the layers under applied bias and promotes inter-barrier coupling effects.

a) ***b)***

Figure 1. Structural concept and electrical measurement configuration of the fabricated triple-barrier $m-p-n-m$ $GaAs$-based structures: (a) layered schematic representation of the vertical architecture, and (b) planar cross-sectional view illustrating the coupled metal-semiconductor and p-n junctions.

(100)-oriented $SI\ GaAs$ single-crystal substrates were employed, with a carrier concentration of approximately $2.0 \times 10^8\ \mathrm{cm}^{-3}$ and a thickness of 350 µm. Three sample types (Sample-01, Sample-02, and Sample-03) were fabricated, differing in layer sequence, conductivity type, and homo-/heterojunction configuration (Table 1). The epitaxial layer thickness ranged from $1.2\ to\ 2$ µm, with the p-layer intentionally designed to be significantly thinner than the n-type base region.

2.2 Liquid Phase Epitaxy Growth Parameters

The epitaxial layers were grown by liquid phase epitaxy (LPE) using a graphite boat system with a sliding (shift) mechanism (Fig. 2). Growth was carried out in a purified hydrogen (H_2) ambient. Crystallization was initiated at approximately 860 °C, and the cooling rate was carefully controlled within the range of $0.33-0.4\ ^\circ\mathrm{C/min}$. This slow cooling regime ensured a stable supersaturation level in the melt and promoted uniform layer formation.

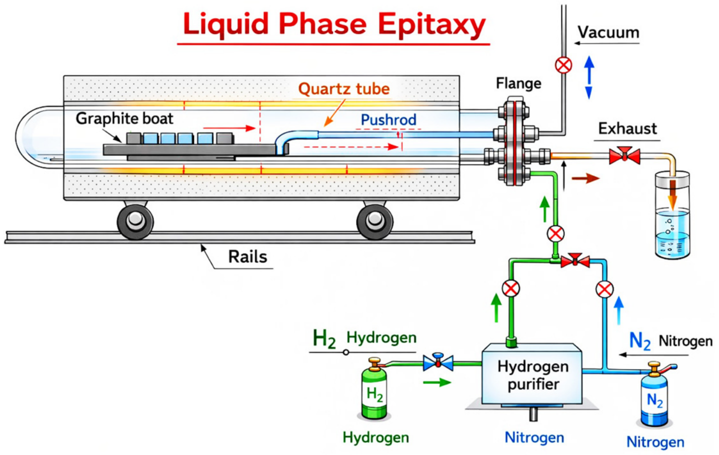

Figure 2. Schematic diagram of the liquid phase epitaxy (LPE) system used for the growth of triple-barrier GaAs-based m-p-n-m structures, showing the graphite boat assembly, quartz tube reactor, gas flow control (H_2/N_2), and sliding mechanism for controlled melt-substrate interaction.

Table 1. Structural parameters of fabricated triple-barrier $m-p-n-m$ $GaAs$-based structures

No.	Sample ID	Layer Sequence	Conductivity Type	Contact Metals	Barrier Configuration
1	Sample -01	$Ag-nGaAs-\pi GaAs-Ag$	n / p^-	Ag / Ag	$M-S / n-p / S-M$
2	Sample-02	$Ag-nAlxGa_{1-x}-As-\pi GaAs-Ag$	n / p	Ag / Ag	$M-S / n-p / S-M$
3	Sample -03	$Au-pAlInGaAs-\nu GaAs-Au$	p / n^-	Au / Au	$M-S / p-n / S-M$

For $n-$type layers, the melt composition consisted of $Ga + nGaAs{:}\,Sn + Al$, whereas $p-$type layers were formed from $Ga + \ pGaAs{:}\,Zn + Al$ solutions. The growth duration followed the relation $\Delta t_n = 1.7 \times 2^n \ (n = 1 \div 4)$.

The dopant concentration in the epitaxial layers was at least $2 \times 10^{15}\mathrm{cm}^{-3}$; Sn-doped sources exhibited concentrations $\leq 2 \times 10^{15}\mathrm{cm}^{-3}$, while Zn-doped sources reached approximately $5 \times 10^{17}\mathrm{cm}^{-3}$.

The intentionally reduced $p-$layer thickness facilitates the coupling of adjacent space-charge regions under high electric fields, which subsequently influences the transition of the dominant transport mechanism.

2.3 Contact Formation and Device Geometry

Metal contacts were deposited onto the epitaxial surface by vacuum evaporation. A semitransparent rectifying contact (Ag or Au) with a thickness of approximately 70 Å was formed on the top epitaxial layer. An identical semitransparent (~70 Å) rectifying metal layer was deposited on the backside of the substrate.

These symmetric metal–semiconductor interfaces establish two Schottky-type barriers that, together with the central $p - n$ junction, complete the triple-barrier $M - p - n - M$ configuration. The ultrathin semitransparent contacts preserve carrier injection characteristics while enabling efficient electric field redistribution within the structure.

The active device area ranged from $2\ to\ 25\ \mathrm{mm}^2$, with some samples fabricated up to $1 \times 1\ \mathrm{cm}^2$. The n-type base thickness was 350 µm, whereas the epitaxial layer thickness was $1.2 - 2$ µm.

3. Electrical Measurement Method

The current-voltage (I-V) characteristics were measured under dark and illumination conditions using a standard two-probe configuration. The bias voltage was applied and controlled by a Keithley 2460 SourceMeter with a step increment of 0.05 V. Current and voltage values were recorded using the instrument's high-precision internal measurement modules.

The minimum detectable current was 0.1 nA. The relative measurement uncertainty ranged between 0.2-0.4%, determined by the metrological specifications of the Keithley 2460 system.

Measurements in the breakdown region were performed in current-stabilization mode using the built-in current source and protection functions of the instrument to ensure device safety and data reliability.

4. RESULTS

4.1 Current–Voltage Characteristics

The current-voltage $(I - V)$ characteristics of the fabricated triple-barrier $M - p - n - M$ structures are presented in Fig. 6. All samples (Sample-01, Sample-02, and Sample-03) exhibit pronounced nonlinear current-voltage behavior, which originates from the sequential arrangement of two metal–semiconductor $(M - S)$ junctions and one central $p - n$ junction.

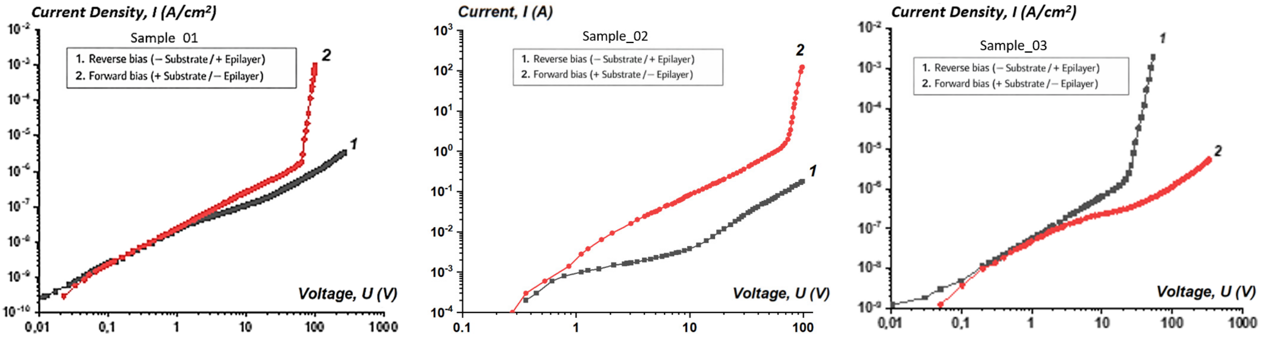

a) *b)* *c)*

Figure 3. Dark current-voltage $(I - V)$ characteristics of the fabricated triple-barrier $m - p - n - m$ GaAs-based photostructures: (a) Sample-01 (homojunction, p-type substrate), (b) Sample-02 (heterojunction, p-type substrate), and (c) Sample-03 (homojunction, n-type substrate).

Under dark conditions, the $I - V$ characteristics reflect the collective response of the three coupled barriers. In the low-bias region, the current follows a power-law dependence $I{\sim}V^{0.5}$, indicating the dominance of generation processes in the reverse-biased junction. As the applied voltage increases, a broad ohmic region emerges. Beyond a characteristic voltage U_0, a sharp current rise (breakdown region) appears in only one bias polarity.

A notable feature common to all structures is that breakdown consistently initiates when the current density reaches approximately $J \approx 1\ \mu\mathrm{A/cm}^2$.

The breakdown voltage U_{br} depends on the thickness of the base region, with thinner bases leading to lower breakdown voltages. Furthermore, the polarity at which breakdown occurs is governed by the conductivity type of the substrate.

4.2 High-Field Transport Analysis

In the breakdown region, the dependence $ln(I/U^2) \sim 1/U$ exhibits clear linear behavior for all samples (Fig. 7), supporting the hypothesis of a tunneling-dominated breakdown mechanism. Although slope values were not explicitly extracted, the observed linearity indicates that field-assisted carrier transport across the barrier becomes dominant at high electric fields.

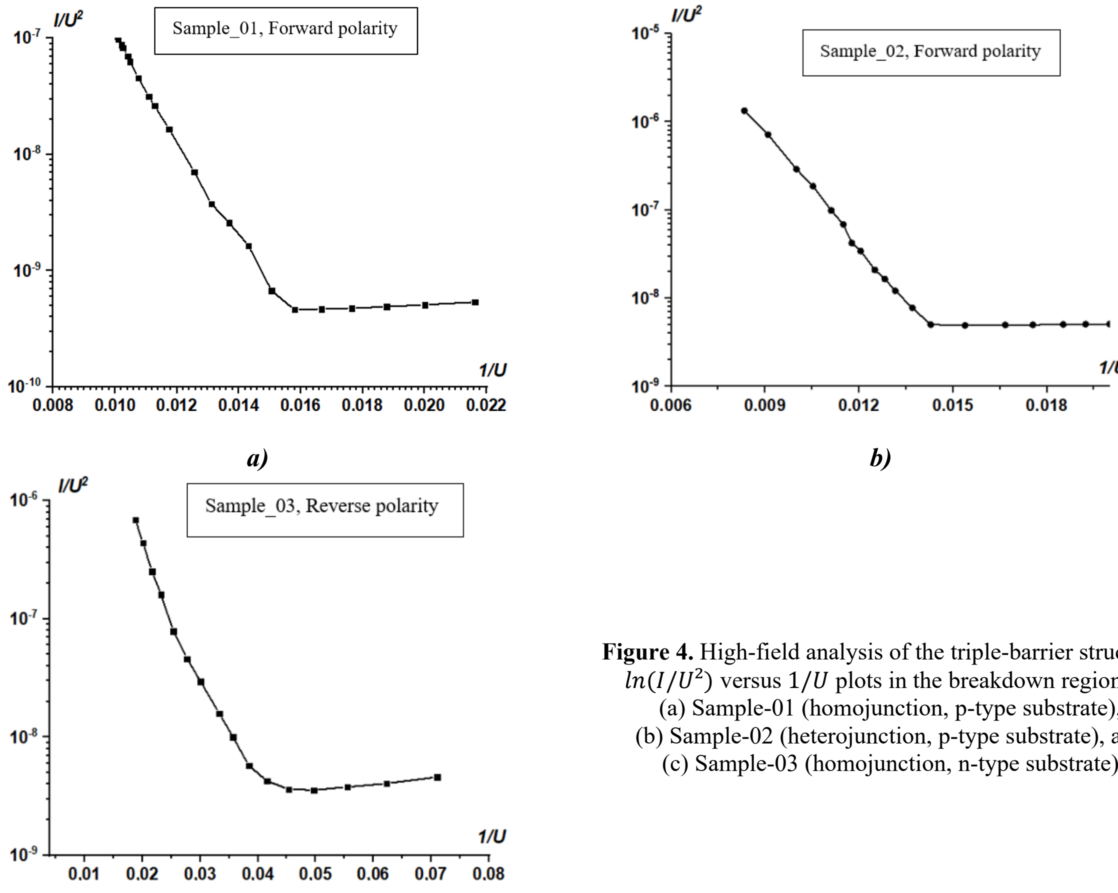

a) *b)*

c)

Figure 4. High-field analysis of the triple-barrier structures: $ln(I/U^2)$ versus $1/U$ plots in the breakdown region for (a) Sample-01 (homojunction, p-type substrate), (b) Sample-02 (heterojunction, p-type substrate), and (c) Sample-03 (homojunction, n-type substrate)

The triple-barrier structure is model-wise analogous to a thyristor; however, it differs due to the presence of a thick $n-$type base (≈ 350 μm) and a comparatively thinner secondary region. This configuration promotes the coupling (merging) of adjacent space-charge regions prior to the onset of avalanche multiplication. As a result, the wide ohmic region and the occurrence of breakdown in only one bias regime represent characteristic features of the multi-barrier architecture.

5. SHORT DISCUSSION

The obtained results reveal that increasing bias voltage in the triple-barrier $M-p-n-M$ architecture leads to a pronounced redistribution of the electric field across the layered structure. In the low-voltage regime, the current follows a $I \sim V^{0.5}$ dependence, indicating the predominance of generation–recombination processes in the reverse-biased junction. With further increases in voltage, the influence of the blocking junction becomes dominant, and the structure transitions into an extended ohmic region.

The combination of a thin $p-$layer and a relatively thick $n-$type base facilitates the convergence of adjacent space-charge regions. At a critical bias, these regions couple (barrier coupling), resulting in a sharp increase in current. This behavior precedes classical avalanche multiplication and reflects the intrinsic interaction between sequentially connected barriers.

In the breakdown regime, the linear dependence of $ln(I/U^2)$ on $1/U$ indicates the dominance of a tunneling-assisted transport mechanism under high electric fields. Thus, breakdown in the multi-barrier architecture is governed by field-controlled carrier transport, with its characteristics tunable through structural parameters. These features may be of interest for further studies aimed at evaluating the dynamic properties of such structures.

6. CONCLUSIONS

Triple-barrier $GaAs$-based $M-p-n-M$ structures were successfully fabricated using liquid phase epitaxy (LPE). The deliberate selection of structural and technological parameters enabled the formation of a coupled barrier system composed of two metal–semiconductor junctions and a central $p-n$ junction.

The current–voltage characteristics demonstrate generation-dominated transport ($I \sim V^{0.5}$) at low bias and the emergence of a breakdown region under high electric fields. Breakdown consistently occurs when the current density approaches approximately 1 $\mu A/cm^2$, while the breakdown voltage is strongly dependent on the base-region thickness. The observed linearity in the $ln(I/U^2) \sim 1/U$ relation confirms the predominance of tunneling-assisted transport in the high-field regime.

These findings demonstrate that electric field redistribution and barrier coupling are the key mechanisms governing carrier transport in triple-barrier architectures. The proposed structural approach provides a promising platform for advanced semiconductor devices operating under high-field conditions.

ORCID

Oybek A. Abdulkhaev, https://orcid.org/0000-0002-8822-1187; **Damir B. Istamov,** https://orcid.org/0009-0007-4654-1880; **Bahodir M. Abdukahhorov,** https://orcid.org/0009-0002-0932-0281

REFERENCES

[1] B. Fang, Y. Tian, and Z. Ma, "High carrier collection efficiency in graphene/GaAs heterojunction photodetectors," J. Semicond. **46**, (2025). https://doi.org/10.1088/1674-4926/24110002

[2] Y. Tian, H. Liu, J. Li, B. Liu, and F. Liu, "Recent Developments of Advanced Broadband Photodetectors Based on 2D Materials," Nanomaterials, **15**, (2025). https://doi.org/10.3390/nano15060431

[3] R.R. Kabulov, L.O. Shuhratova, K.T. Suyarov, F.A. Akbarov, D.B. Istamov, Structural, Compositional, and Photoluminescence Properties of $CsPbBr_3$ Thin Films Grown by Single-source Thermal Vacuum Chemical Vapor Deposition, E-Journal Surf. Sci. Nanotechnol. **367**, 364–367 (2025). https://doi.org/10.1380/ejssnt.2025-051

[4] F. Li, J. Zeng, Y. Zhao, L. Zhu, Y. Zhou, Z. Wang, Z. Wang, *et al.*, "High Hole Mobility van der Waals Junction Field-Effect Transistors Based on Te/GaAs for Multimode Photodetection and Logic Applications," ACS Appl. Mater. Interfaces, **17**, 18655-18665 (2025). https://doi.org/10.1021/acsami.5c00891

[5] I.I. Maripov, S.A. Radzhapov, S.F. Xasanov, D.B. Istamov, Y.T. Yuldashev, D. Axnazarova, and S.A. Ashirov, "Electrophysical Characterization of Photodetectors Based on Semiconductor Structures Si (Li) And Si(Au)," East Eur. J. Phys. (4), 435–441 (2025). https://doi.org/10.26565/2312-4334-2025-4-43

[6] E. Balcı, H. Durmuş, Ç. Bilkan, and Ş. Altındal, "On the electrical parameters, conduction mechanisms depend on temperature and voltage, and thermal sensor applications in the Re/n-GaAs/Au Schottky diodes," J. Mater. Sci. Mater. Electron. **37**, (2026). https://doi.org/10.1007/s10854-025-16561-6

[7] F. Lin, J. Cui, Z. Zhang, Z. Wei, X. Hou, B. Meng, Y. Liu, *et al.*, "GaAs Nanowire Photodetectors Based on Au Nanoparticles Modification," Materials (Basel). **16**, 1–11 (2023). https://doi.org/10.3390/ma16041735

[8] F. Capasso, "Band-Gap Engineering: From Physics and Materials To New Semiconductor Devices," Science, **235**, 172-176 (1987). https://doi.org/10.1126/science.235.4785.172

[9] A. Rogalski, "Infrared detectors: Status and trends," Prog. Quantum Electron. **27**, 59–210 (2003). https://doi.org/10.1016/S0079-6727(02)00024-1

[10] B.F. Levine, "Quantum-well infrared photodetectors," J. Appl. Phys. **74**, (1993). https://doi.org/10.1063/1.354252

[11] S. Mohammadnejad, and M. Aasi, "Analysis of structures and technologies of various types of photodetectors used in laser warning systems: a review," Opt. Eng. **62**, (2023). https://doi.org/10.1117/1.oe.62.9.090901

[12] H.J. Lee, M.M.A. Gamel, P.J. Ker, M.Z. Jamaludin, Y.H. Wong, and J.P.R. David, "Absorption Coefficient of Bulk III-V Semiconductor Materials: A Review on Methods, Properties and Future Prospects," J. Electron. Mater. **51**, 6082–6107 (2022). https://doi.org/10.1007/s11664-022-09846-7

[13] Z. Sun, "Electron Transport in High Aspect Ratio Semiconductor Nanowires and Metal-Semiconductor Interfaces," 2016. http://rave.ohiolink.edu/etdc/view?acc_num=ucin1479821421998919

[14] D.B. Istamov, O.A. Abdulkhayev, and S.M. Kuliyev, "Limiting characteristics of silicon diode temperature sensors for determining the maximum temperature with specified measurement accuracy," UNEC J. Eng. Appl. Sci. **5**, 63–69 (2025). https://doi.org/10.61640/ujeas.2025.0507

[15] R. Bebitov, O. Abdulkhaev, D. Yodgorova, D. Istamov, G. Khamdamov, S. Kuliyev, J.S. Abdullaev, *et al.*, "Potential distribution over temperature sensors of p-n junction diodes with arbitrary doping of the base region," E3S Web Conf. **401**, (2023). https://doi.org/10.1051/e3sconf/202340103062

[16] R.R. Bebitov, O.A. Abdulkhaev, D.M. Yodgorova, D.B. Istamov, G.M. Khamdamov, S.M. Kuliyev, A.A. Khakimov, and A.Z. Rakhmatov, "Dependence of the accuracy of the silicon diode temperature sensors for cryogenic thermometry on the spread of their parameters," Low Temp. Phys. **49**, 256–260 (2023). https://doi.org/10.1063/10.0016843

[17] R.R. Bebitov, O.A. Abdulkhaev, D.M. Yodgorova, D.B. Istamov, S.M. Kuliyev, A.A. Khakimov, A.B. Bobonazarov, and A.Z. Rakhmatov, "Distribution of impurities in base-depleted region of diode temperature sensor," Low Temp. Phys. **50**, 418-424 (2024). https://doi.org/10.1063/10.0025635

[18] D.B. Istamov, O.A. Abdulkhayev, S.M. Kuliyev, N. Abdullayev, S.A. Ashirov, and D.M. Yodgorova, "Temperature Response Curve of Silicon Diode Temperature Sensors," East Eur. J. Phys. (2), 287–291 (2025). https://doi.org/10.26565/2312-4334-2025-2-35

[19] Z. Ma, P. Tang, J. Xue, and J. Zhou, "Enhancing Photoresponse of GaAs-Based Photodetector by Plasmon Grating Structures," Plasmonics, **18**, 1571–1579 (2023). https://doi.org/10.1007/s11468-023-01849-2

[20] A. Komilov, O. Abdulkhaev, Y. Nasrullayev, B. Abdurasulov, and B. Abdukahhorov, "Error Minimization in PV Characterization When Using Unfiltered Light Sources," Appl. Sol. Energy (English Transl. Geliotekhnika), **60**, 179–188 (2024). https://doi.org/10.3103/S0003701X24602059

[21] S.D. Lin, and C.P. Lee, "GaAs metal-semiconductor-metal photodetectors with low dark current and high responsivity at 850 nm," Semicond. Sci. Technol. **17**, 1261–1266 (2002). https://doi.org/10.1088/0268-1242/17/12/309

[22] L. Boudjemila, *et al.*, "Study Of Polarization Photosensitiveness of Nanostructured Au-Palladium-N-Gap Schottky Barriers," in: *Handb. XXII Int. Sci. Conf. "Ecology. Human. Soc.*" 99–102 (2021). https://doi.org/https://doi.org/10.20535/EHS.2021.233065

[23] S.M. Sze, D.J. Coleman, and A. Loya, "Current transport in metal-semiconductor-metal (MSM) structures," Solid State Electron. **14**, 1209–1218 (1971). https://doi.org/10.1016/0038-1101(71)90109-2

[24] V.P. Maxniy, "UV photodetectors with a Schottky barrier based on Zinc Selenide," Tech. Phys. J. **68**, 123–125 (1998).

[25] H.H. Gullu, D.E. Yıldız, M. Yıldırım, I. Demir, and I. Altuntas, "Electrical characteristics of Al/AlGaAs/GaAs diode with high-Al concentration at the interface," J. Mater. Sci. Mater. Electron. **35**, (2024). https://doi.org/10.1007/s10854-023-11907-4

[26] E.H. Rhoderick, "Metal-Semiconductor Contacts," IEEE Proc. I Solid State Electron Devices, **129**, 1–14 (1982). https://doi.org/10.1049/ip-i-1.1982.0001

[27] A. Rogalski, P. Martyniuk, M. Kopytko, P. Madejczyk, and S. Krishna, "InAsSb-based infrared photodetectors: Thirty years later on," Sensors (Switzerland), **20**, 1–74 (2020). https://doi.org/10.3390/s20247047

[28] V. Gúriaux, A. Nedelcu, and P. Bois, "Double barrier strained quantum well infrared photodetectors for the 3-5 μm atmospheric window," J. Appl. Phys. **105**, 1–9 (2009). https://doi.org/10.1063/1.3143102

[29] B.S. Ma, W.J. Fan, Y.X. Dang, W.K. Cheah, W.K. Loke, W. Liu, D.S. Li, *et al.*, "GaInNAs double-barrier quantum well infrared photodetector with the photodetection at 1.24 μm," Appl. Phys. Lett. **91**, 3–5 (2007). https://doi.org/10.1063/1.2767185

[30] R.H. Fowler, and L. Nordheim, "Electron emission in intense electric fields," Proc. R. Soc. London. Ser. A, Contain. Pap. a Math. Phys. Character, **119**, 173–181 (1928). https://doi.org/10.1098/rspa.1928.0091

[31] J.G. Simmons, "Generalized Formula for the Electric Tunnel Effect between Similar Electrodes Separated by a Thin Insulating Film," J. Appl. Phys. **34**, 1793–1803 (1963). https://doi.org/10.1063/1.1702682

[32] F.X. Liang, J.Z. Wang, Z.P. Li, and L.B. Luo, "Near-Infrared-Light Photodetectors Based on One-Dimensional Inorganic Semiconductor Nanostructures," Adv. Opt. Mater. **5**, 1–14 (2017). https://doi.org/10.1002/adom.201700081

ВИГОТОВЛЕННЯ ТА ЕЛЕКТРИЧНІ ТРАНСПОРТНІ ВЛАСТИВОСТІ ТРЬОХБАР'ЄРНИХ СТРУКТУР GaAs ТИПУ M–p–n–M

Баходір М. Абдукахоров, Ойбек А. Абдулхаєв, Дамір Б. Істамов, Шукурулло М. Кулієв, Ділбара М. Йодгорова
Фізико-технічний інститут Академії наук Узбекистану, Ташкент 100084, Узбекистан

Інженерне формування багатобар'єрних потенціальних профілів є ефективним підходом до керування транспортом носіїв заряду в напівпровідникових структурах. У цій роботі виготовлено три конфігурації трьохбар'єрних структур $GaAs$ типу метал–p–n–метал ($M-p-n-M$) на напівізоляційних підкладках $GaAs$ із використанням методу рідкофазної епітаксії (LPE). Склад шарів і напівпрозорі металеві контакти (Ag, Au) були цілеспрямовано підібрані для формування зв'язаної системи переходів метал–напівпровідник і $p-n$. Електричні транспортні властивості досліджувалися в широкому діапазоні напруг, а вольт-амперні характеристики були піддані порівняльному аналізу. У режимі малих напруг струм підкоряється степеневій залежності $I \sim V^{0,5}$, що свідчить про домінування генераційних процесів. Із зростанням напруги спостерігається перехід до квазіомічної області та подальше формування пробою. У режимі високих електричних полів лінійні ділянки залежності $ln(I/U^2)$ від $1/U$ підтверджують домінування польово-асистованих механізмів транспорту в бар'єрних областях. Отримані результати демонструють, що перерозподіл електричного поля та взаємодія бар'єрів відіграють ключову роль у визначенні транспорту носіїв заряду в трьохбар'єрних структурах, забезпечуючи основу для подальшого розвитку перспективних напівпровідникових приладів.

Ключові слова: *арсенід галію; перехід метал–напівпровідник; p–n перехід; трьохбар'єрна структура; рідкофазна епітаксія; електричний транспорт; ефекти високих електричних полів*

East European Journal of Physics. **2.** 379-384 (2026)

DOI:10.26565/2312-4334-2026-2-41 ISSN 2312-4334

STRUCTURAL AND PHASE STATES OF RHODIUM DOPED SILICON MONOCRYSTALS

Akramjon Y. Boboev[1], **Sherzod A. Makhmudov**[2], **Avaz K. Rafikov**[2], **Ziyodjon M. Ibrokhimov**[3], **Rakhmat M. Mansurov**[4], **Nuritdin Y. Yunusaliyev**[1], **Biloliddin M. Ergashev**[5]
[1]*Andijan State University named after Z.M. Babur, Andijan, Uzbekistan*
[2]*Institute of Nuclear Physics, Academy of Sciences of the Republic of Uzbekistan*
[3]*Andijan State Technical Institute, Andijan, Uzbekistan*
[4]*Academic Lyceum No. 1 of the Ministry of Internal Affairs of the Republic of Uzbekistan*
[5]*Andijan State Pedagogical Institute, Andijan, Uzbekistan*
**Corresponding Author e-mail: aboboevscp@gmail.com*

Received February 28, 2026; revised April 22, 2026; accepted May 6, 2026

In this paper, the structural and phase states of silicon (Si) monocrystals doped with rhodium (Rh) atoms were investigated. For the study, n-type silicon samples doped with rhodium, grown by the Chokralsky method, were selected. Rhodium atoms were introduced via thermal diffusion at 1300°C, and the samples were cooled under both slow and rapid cooling regimes. The resulting data were evaluated using X-ray diffraction (XRD) analysis. In the control samples, heat treatment resulted in the formation of secondary phases such as SiP_2 and SiO_2, which were shown to be associated with background impurities, particularly oxygen atoms. In the rhodium-alloyed and slow-cooled sample, the $SiRh_3$ phase formed, and the crystal lattice remained relatively stable. This indicates that the rhodium atoms have the ability to reduce internal stresses and relax the lattice. In the rapid cooling regime, the RhO_2 oxide phase appeared, and an increase in micro-stresses and crystal defects was observed. The results indicate that rhodium doping is an effective method for controlling the structure, phase composition, and electrical properties of silicon monocrystals. This research is of significant importance for semiconductor materials, microelectronics, and solar cells.

Keywords: *Silicon; Rhodium; Phosphorus; Diffusion; Impurity; Oxygen; Secondary phases; XRD; Defects; Microstrain*
PACS: 61.72.U

INTRODUCTION

At present, one of the key priorities in solid-state physics and semiconductor technology is the atomistic control of materials' electro-physical properties. Single-crystal silicon (Si), owing to its technological versatility and widespread natural abundance, remains the “foundation” of modern micro- and nanoelectronics. However, the reduction of modern devices (high-frequency transistors, power thyristors, and high-efficiency solar cells) to the nanometre scale has drastically increased the demand for structural perfection of the material. Any uncontrolled defect or impurity atom in the crystal lattice serves as a primary factor in reducing the device's useful coefficient of performance. Moreover, oxygen atoms, which give rise to both “beneficial” and “deleterious” states in silicon monocrystals grown by the Czochralski method, are also the most common technological background impurities (with a concentration of up to 10^{17}–10^{18} cm^3) [1]. In some cases, oxygen atoms strengthen the crystal lattice and restrict dislocation movement [2]. During heat treatment processes (at around 450 °C and 650 °C), oxygen atoms form ‘thermal donors’, which unexpectedly alters the material's relative resistance [3]. Furthermore, the uneven distribution of oxygen precipitates (SiO_x) induces high mechanical stresses within the crystal, leading to the scattering of charge carriers and energy loss [4].

Legating silicon with 4d transition metals, particularly rhodium (Rh), is considered one of the most promising methods for modifying material properties. Rhodium atoms in silicon's forbidden band give rise to deep energy levels (for example, at $E_c - 0.32$ eV and $E_v + 0.35$ eV) that exhibit both donor and acceptor characteristics [5]. This allows for the wide range control of the charge carriers' recombination rate. Furthermore, due to the high diffusion coefficient of rhodium in silicon, a uniform distribution of the impurities throughout the monocrystal can be achieved by introducing it via thermal diffusion [6]. Furthermore, rhodium atoms also possess the ability to clean the crystal's active areas by collecting (gettering) oxygen and other technological impurities around them [7]. The formation of Rh-O complexes enhances the semiconductor's resistance to high temperatures [8]. This prevents the material from degrading during the high-temperature thermal oxidation and diffusion stages of the manufacturing process. At the same time, in rhodium-doped silicon, radiation-induced defects (for example, A centres or E centres) interact with the rhodium atoms and lose their electrical activity [9]. In this regard, the investigation of the structural properties and phase states of complexes of silicon with rhodium and oxygen atoms not only allows for an understanding of fundamental processes in solid-state physics, but also allows for the creation of new materials that can operate stably under extreme conditions for practical nanoelectronics. However, despite the great interest in rhodium-doped silicon crystal, research has been mainly limited to studying its electrical and recombination-related properties. The structural changes and phase formation processes that occur in bulk silicon single crystals during rhodium diffusion have not been sufficiently studied. In particular, the

---

Cite as: A.Y. Boboev, Sh.A. Makhmudov, A.K. Rafikov, Z.M. Ibrokhimov, R.M. Mansurov, N. Y. Yunusaliyev, B.M. Ergashev, East Eur. J. Phys. 2, 379 (2026), https://doi.org/10.26565/2312-4334-2026-2-41

relationship between high-temperature rhodium diffusion, the formation of secondary phases, and the relaxation of internal micro-strains in the silicon lattice has not yet been systematically experimentally determined.

Therefore, in this research work, we aimed to conduct a fundamental analysis of the mechanisms of structural changes and phase formation that occur in bulk silicon single crystals during rhodium diffusion. The scientific novelty of the work lies in the first experimental confirmation that the formation of secondary phases $SiRh_3$ and RhO_2 under high-temperature diffusion and controlled cooling regimes leads to a significant reduction in internal micro-strains in the silicon crystal lattice. Thus, in contrast to previous studies that focused mainly on electrical properties, this work reveals the unique role of rhodium in the structural stabilization of the silicon matrix and provides new insights into the phase formation processes in the Rh-Si-O system.

MATERIALS AND METHODS

As the research object, n-type monocrystalline silicon samples, phosphorus-doped and grown by the Czochralski method, were selected. For the experiments, the samples were prepared with dimensions of 10 × 10 × 1 mm³. To ensure the cleanliness of the sample surfaces, they underwent a two-stage treatment: first the surfaces were mechanically polished, then chemically treated to completely remove organic and inorganic contaminants. The doping process of the silicon samples was carried out in two distinct stages. In the first stage, rhodium (Rh) metal was deposited onto the surface of the silicon substrates using a VUP-4 vacuum system. Subsequently, the samples were placed into high-purity quartz ampoules, which were then evacuated to a residual pressure of $5\text{-}6\cdot10^{-2}$ mmHg and hermetically sealed. Thermal diffusion was performed at a constant temperature of 1300 °C for 10 hours. This specific duration was selected to ensure equilibrium and facilitate a uniform distribution of Rh atoms throughout the bulk volume of the samples. Following the diffusion process, the samples were subjected to two different cooling regimes to investigate their structural impact: a) rapid Quenching: Samples were quickly removed from the furnace and immersed in a specialized cooling oil achieving a cooling rate of approximately 300 °C/min; b) Slow Cooling: Samples remained inside the furnace, where the temperature was gradually decreased at a controlled rate of 5–20 °C/min. These contrasting cooling modes allowed for a comparative analysis of the phase transformations and the relaxation of internal micro-strains within the Rh-Si system.

The structural and phase states of the investigated samples were monitored using an Empyrean Malvern X-ray diffractometer. X-ray diffraction measurements were carried out in Bragg–Brentano geometry, with a continuous scan speed of 1°/min over a 2θ range of 10° to 80°. The angular step was set to 0.02 degrees. The graphical analysis and peak integration were performed using Origin software package.

RESULTS AND DISCUSSION

In the study, the X-ray diffraction state of n-Si<P> samples prepared without deliberately introducing impurity atoms (for example, rhodium) was evaluated (Figure 1, green line).

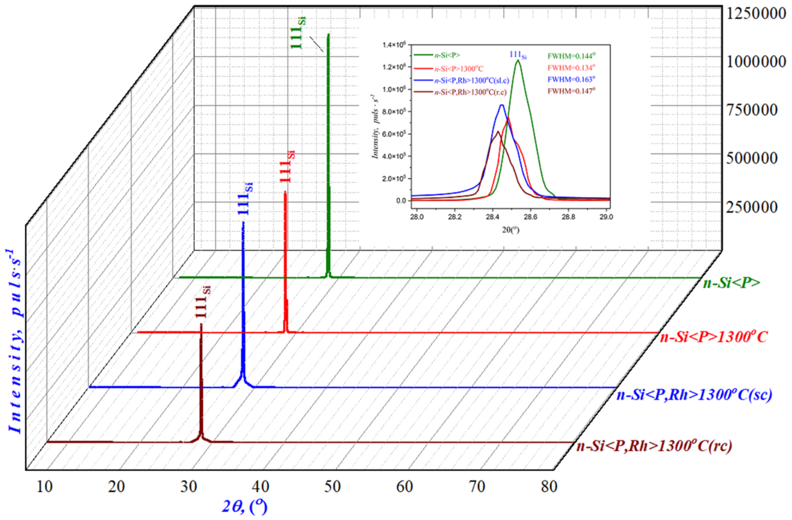

Figure 1. XRD patterns of n-Si<P> and Rh-doped n-Si<P,Rh> samples before and after 1300°C heat treatment under slow-cooling (sc) and rapid-cooling (rc) regimes.

This, in turn, involves identifying the secondary phases that arise from the natural structural changes in the silicon crystal lattice under heat treatment, from background impurities (particularly oxygen) and from the redistribution of phosphorus atoms. In the X-ray diffraction pattern of the control sample, a high-intensity (I = 1268300 imp/s) diffraction reflection corresponding to the $(111)_{Si}$ crystallographic plane was observed at 2θ = 28.54°. The high intensity and selective nature of this peak indicate that the sample surface is oriented with respect to the (111) crystallographic direction. Using the interplanar distance d = 3.125 Å for the (111) reflection, the lattice constant of the n-Si<P> samples was determined to be $a \approx 5.4126$ Å. Furthermore, using the experimental values of this orientation, the size of the constituent sub-crystallites was calculated to be $D \approx 59.7$ nm. This value indicates that, while the silicon remains monocrystalline, there are a certain number of boundary regions and microdefects within the volume [10]. At the same time, additional low-intensity peaks were also observed in the X-ray diffraction spectrum of the control sample (see Figures 2*a, b* and *c*). In particular, the observation of the (200) reflection of the SiP_2 phase at $2\theta = 30.90°$ suggests that part of the phosphorus impurity may be locally concentrated in regions prone to chemical bonding with silicon. Using the experimental values of this reflection, recalculations based on these compounds determined that the size of the resulting polycrystallite domains is $D \approx 75.1$ nm. The observation of the SiP_2 phase is often explained by the redistribution of phosphorus and its binding at certain “energetically favorable” centres during high-temperature treatments [11]. In the control sample, traces of oxide phases formed in the presence of oxygen were also detected. At $2\theta = 42.43°$, the (211) reflection corresponding to the SiO_2 phase was observed. The FWHM for this reflection was larger, and the calculated nanocrystallite size was around $D \approx 25$ nm. Furthermore, for this SiO_2 phase, the lattice constants characteristic of the trigonal $P3_221$ space group was determined to be $a = b \approx 5.031$ Å and $c \approx 5.527$ Å. The relatively small size of the oxide nanocrystals is explained by the precipitation of oxygen atoms mainly at the grain boundaries, around dislocations, or in near-surface layers.

In the next stage, the X-ray diffraction characteristics of n-Si<P> samples heat-treated at 1300°C for ten hours were studied (Figure 1, red line). Typically, heat treatment leads to a redistribution of internal stresses in the crystal lattice, are used to redistribute internal stresses in the crystal lattice following heat treatment, accelerate diffusion processes, change the configuration of defects, and bring background impurities (oxygen, carbon) and phosphorus atoms to a dynamic equilibrium state [12]. Under such conditions, the structural evolution is assessed by changes in lattice constants, shifts in diffraction peaks at various angles, and variations in intensity and half-width. After heat treatment, the $(111)_{Si}$ reflection was observed to shift to $2\theta = 28.36°$. The shift of this reflection towards smaller angles indicates a slight change in the interplanar distance ($d = 3.131$ Å) and an increase in the lattice constant $a \approx 5.423$ Å. Furthermore, the intensity of the $(111)_{Si}$ reflection decreased to $I = 758700$ imp/s. This, in turn, indicates an increase in microdistortions at the surface, an increase in diffusion centres due to diffusion, and an increase in the proportion of secondary phases in some domains and at boundaries [13]. At the same time, it was determined that the size of the sub-crystals ($D \approx 64.9$ nm) increased, based on experimental values of the $(111)_{Si}$ reflection. It is associated with the ‘coarsening’ of subgrain boundaries resulting from heat treatment, a process that is thermodynamically favorable at elevated temperatures [14]. However, the increase in subgrain size accompanied by a decrease in intensity indicates an uneven structural order in the crystal lattice, i.e., enlargement in some areas and an increase in defects and micro-stresses in others [15]. After heat treatment at 1300°C, the phase corresponds to SiP_2. The (200) peak was observed at $2\theta = 30.86°$, but its intensity had decreased and the calculated polycrystallite domain size was around $D \approx 62.6$ nm. This suggests that some of the phosphorus undergoes re-melting or diffuses into less localized regions [16]. In other words, at elevated temperatures phosphorus atoms tend to distribute relatively uniformly throughout the silicon volume, although it is also possible that a stable phase state is maintained at certain energetically favourable centres [17]. During the growth of silicon monocrystals by the Czochralski method, the incorporation of a certain amount of background impurities such as oxygen and carbon into the crystal volume is well known in practice. Oxygen atoms often form clusters in interstitial sites or as Si–O bonds, and during thermal treatments can evolve into SiO_x and SiO_2 crystallites. Therefore, the appearance of peaks characteristic of the SiO_2 phase in the X-ray diffraction patterns confirms the active participation of the background impurities.

The formation of SiO_2 nanocrystallites with dimensions of around 20–30 nm acts as a barrier to the movement of charge carriers in the oxide precipitates, creating recombination centers or, conversely, under certain technological conditions, it can increase the bulk purity by collecting harmful impurities through a “gettering” effect. As a qualitative assessment of micro-stresses, the presence of ‘forbidden’ reflections such as $(222)_{Si}$, which are weakly visible in the normally ideal diamond-like structure, and their intensity ratios are used (see red line in Fig. 2c). The amount of formed micro-stresses can be estimated by I(222)/I(111) can be estimated from the I(222)/I(111) ratio $\approx 2.5 \cdot 10^{-3}$ [18]. This value is much larger than the ideal $\sim 10^{-4}$ order of magnitude, indicating the presence of local deformations, dislocations, boundary regions, and a non-uniform distribution of inclusions in the crystal lattice [18]. During heat treatment, such micro-stresses lead to a reduction in internal stresses through the annihilation and reorganization of defects, as well as the formation of oxygen precipitates, secondary phases (SiP_2, SiO_2) and their lattice constant mismatches.

Analysis of the X-ray diffraction patterns of n-Si<P,Rh> samples prepared under slow-cooling conditions (Figure 1, blue line) showed that the rhodium atoms have reached a relatively equilibrated state in the silicon crystal lattice. The main diffraction peak was observed at $2\theta = 28.45°$, and was identified as belonging to the $(111)_{Si}$ crystallographic orientation. The intensity of this peak was 860220 imp/s. The main The high intensity of the $(111)_{Si}$ reflection indicates that the overall order of the silicon crystal lattice is preserved. Despite the diffusion of the rhodium atoms, the main diamond structure of silicon has not been disturbed. The interlinear distance for this reflection was determined to be d = 3.136 Å. The angular distribution of the peaks indicates that there is no significant change in the lattice constant, showing that the slow cooling process has resulted in a state close to thermodynamic equilibrium [19].

At the same time, an additional diffraction peak was observed in the X-ray diffraction pattern at $2\theta = 32.2°$. This peak belongs to the $SiRh_3$ compound and corresponds to the (110) crystallographic direction. The $SiRh_3$ phase was found to possess tetragonal symmetry, with an interlinear spacing $d = 2.778$ Å. This phase indicates that the rhodium atoms have chemically bonded with silicon. The $SiRh_3$ phase, formed under slow cooling conditions, can be considered to be primarily located at the sub-granular boundaries and in the near-surface layers. This is explained by the fact that the rhodium atoms lose their mobility after diffusion and settle into energetically favorable centres [20].

To assess the level of micro-stresses formed in n-Si<P,Rh> samples prepared under slow cooling conditions, the intensity ratio of the $(222)_{Si}$ and $(111)_{Si}$ reflections was calculated (see Fig. 2c, blue line). In the slow cooling regime, this ratio was $I(222)/I(111) \approx 5.9 \cdot 10^{-4}$. This value is small compared to the control samples, indicating that internal stresses in the crystal lattice have been partially relieved under the influence of the rhodium atoms. In the n-Si<P,Rh> samples prepared under rapid cooling conditions, the X-ray diffraction pattern differed significantly from that of the slow-cooling regime (Figure 1, brown line). The main $(111)_{Si}$ reflection was observed at 2θ = 28.42°, and its intensity was noted to have decreased to 623 530 imp/s. The decrease in intensity is explained by the retention of a high degree of defects and micro-strains in the crystal lattice as a result of rapid cooling [21]. Under such conditions, the atoms do not have time to reach thermodynamic equilibrium and the existing structure remains in a 'frozen' state. X-ray diffraction patterns of n-Si<P,Rh> samples prepared under rapid cooling conditions show an additional peak at 2θ = 71.4°. This peak corresponds to the RhO_2 oxide phase, which is represented by the (301) crystallographic orientation. It was determined that the RhO2 phase has a tetragonal structure, with a crystallite size of approximately 8.5 nm and an interlinear distance of d = 1.325 Å. The formation of the RhO_2 phase indicates that the rhodium atoms actively reacted with oxygen under rapid cooling conditions [22]. This phenomenon clearly demonstrates the tendency of oxygen atoms to combine with rhodium, overcoming the background impurities present in silicon [23]. In n-Si<P,Rh> samples, the level of micro-stresses generated by rapid cooling increased significantly under the rapid cooling regime, $I(222)/I(111) \approx 1.0 \cdot 10^{-3}$ (see the brown line in Fig. 2*c*). This value is considerably larger than that for the slow cooling regime, indicating that the rapid cooling process retains a high degree of internal strains in the crystal lattice [24].

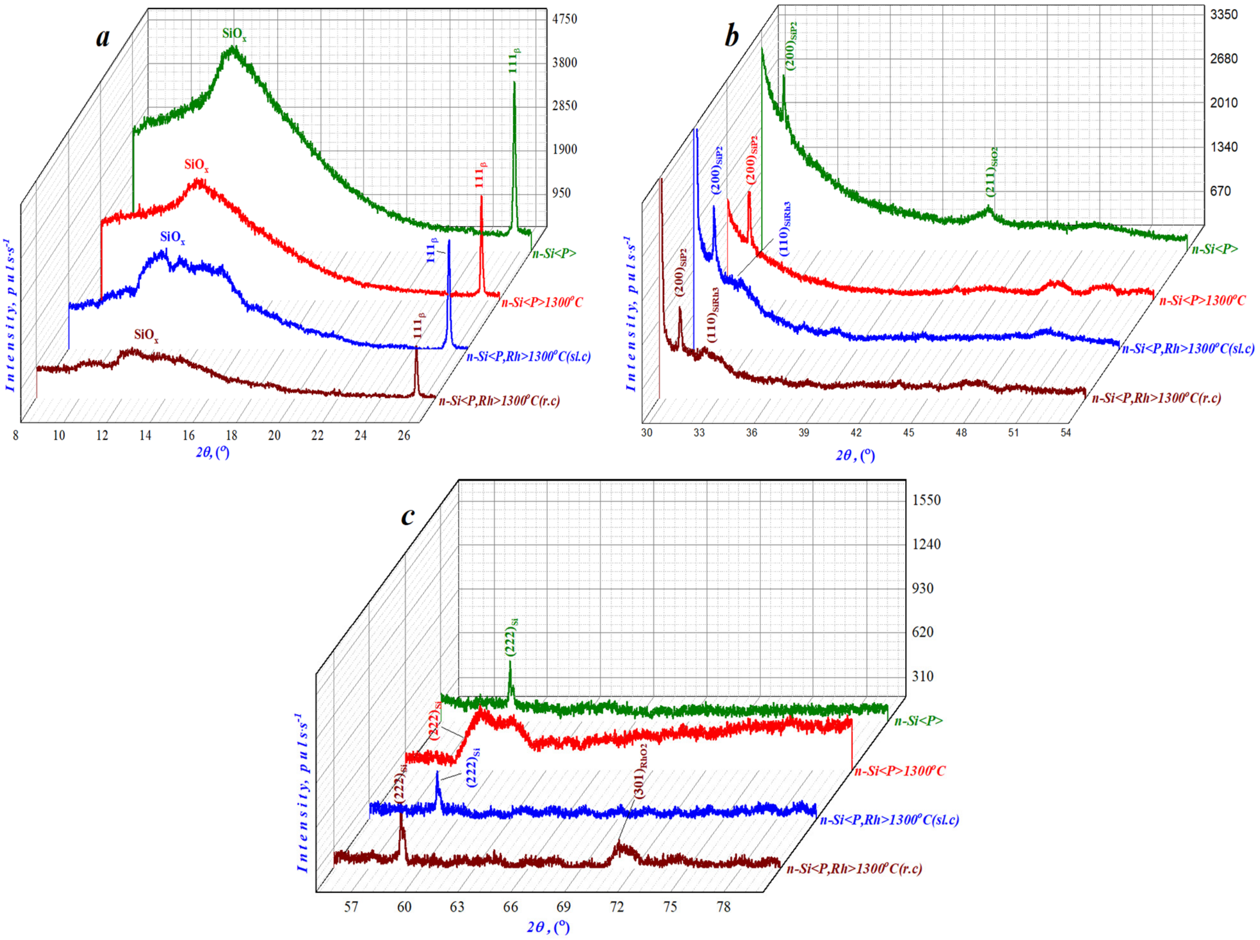

Figure 2. Enlarged XRD regions illustrating secondary phase formation and microstructural evolution in n-Si<P> and Rh-doped n-Si<P,Rh> single crystals: (a) low-angle region, (b) intermediate region, and (c) high-angle region.

CONCLUSIONS

In the control samples, due to the redistribution of oxygen atoms in phosphorus and vanadium impurities as a result of high-temperature treatment, SiP_2 (polycrystallite size $D \approx 88.4$ nm) and secondary phases such as SiO_2 ($D \approx 25$ nm) were identified.

Heating at 1300°C for 5 hours leads to an increase in the silicon lattice constant to $a \approx 5.4104$ Å and a decrease in the diffraction reflection intensity, which was found to lead to an increase in microdeformations and scattering centers.

It was found that at the slow cooling (sc) rate, at the sub-granular partition boundaries, rhodium atoms chemically combine with silicon to form the tetrahedral $SiRh_3$ phase.

In rhodium-doped and slow-cooled samples, the degree of micro-stresses ($I(222)/I(111) \approx 5.9 \cdot 10^{-4}$) is reduced compared to the control sample, indicating that the rhodium atoms possess the property of relieving internal lattice stresses.

It was found that during rapid cooling (rc), the rhodium atoms actively interact with the ambient oxygen to form the RhO_2 oxide phase (crystallite size ≈ 8.5 nm), indicating the strong gettering property of rhodium.

During the rapid cooling process, the atoms do not have time to reach equilibrium, resulting in a high concentration of “frozen” defects in the crystal lattice and the retention of maximum micro-stresses ($1.0 \cdot 10^{-3}$)

Funding

The present research work was financed under the project FZ-292154210 granted by the Ministry of Innovative Development of the Republic of Uzbekistan

ORCID

A.Y. Boboev, https://orcid.org/0000-0002-3963-708X; **B.M. Ergashev**, https://orcid.org/0009-0007-9392-6548;
N.Y. Yunusaliyev, https://orcid.org/0000-0003-3766-5420; **Z.M. Ibrokhimov**, https://orcid.org/0009-0003-6931-661X;
Sh.A. Makhmudov, https://orcid.org/0009-0003-6539-9278; **A.K. Rafikov**, https://orcid.org/0000-0001-9199-2428;

REFERENCES

[1] J. Li, J. Wang, Z. Zhong, Z. Li, Y. Wen, L. Wang, and L. Liu, “Pathway and control of oxygen transport in the melt during single crystal silicon growth by continuous-feeding Czochralski method,” Journal of Crystal Growth, **662**, 128183 (2025). https://doi.org/10.1016/j.jcrysgro.2025.128183

[2] W. Zhao, J. Li, and L. Liu, “Control of oxygen impurities in a continuous-feeding Czochralski-silicon crystal growth by the double-crucible method,” Crystals, **11**, 264 (2021). https://doi.org/10.3390/cryst11030264

[3] R. Newman, “Oxygen diffusion and precipitation in Czochralski silicon,” Journal of Physics: Condensed Matter, **12**, R335 (2000). https://doi.org/10.1088/0953-8984/12/25/201

[4] P. Dong, X. Liang, and D. Tian, “On the mechanism of carrier scattering at oxide precipitates in Czochralski silicon,” Journal of Materials Science: Materials in Electronics, **4**, (2015). https://doi.org/10.1007/s10854-015-2728-6

[5] Y. Boboev, K. A. Makhmudov, and Z. M. Ibrokhimov, “Long-term relaxation processes of electrical conductivity in compensated Si<B,S> and Si<B,Rh> monocrystals,” East European Journal of Physics, (2), 436–440 (2025). https://doi.org/10.26565/2312-4334-2025-2-54

[6] Sh. A. Makhmudov, A.A. Sulaymonov, and A.K. Rafikov, “Study of the concentration of Si impurities and their electrical state,” Nauchnyi Zhurnal Fizika, (1), 16 (2023). (in Russian, Kyrgyzstan)

[7] J. Golubović, M. Varničić, and S. Štrbac, “Study of oxygen reduction reaction on polycrystalline rhodium in acidic and alkaline media,” Catalysts, **14**, 327 (2024). https://doi.org/10.3390/catal14050327

[8] M. Trzcinski, G. Balcerowska-Czerniak, and A. Bukaluk, “XPS studies of the initial oxidation of polycrystalline Rh surface,” Catalysts, **10**, 617 (2020). https://doi.org/10.3390/catal10060617

[9] Y. Boboev, B. M. Ergashev, N. Y. Yunusaliyev, and J. S. Madaminjonov, “Electrophysical nature of defects in silicon caused by implanted platinum atoms,” East European Journal of Physics, (2), 431–435 (2025). https://doi.org/10.26565/2312-4334-2025-2-53

[10] Y. Boboev, S. K. Yulchiev, Z. M. Ibrokhimov, and N. Y. Yunusaliyev, “The impact of various lighting conditions on the photosensitive properties of Si<B,S> and Si<B,Rh> structures,” East European Journal of Physics, (4), 620-626 (2025). https://doi.org/10.26565/2312-4334-2025-4-65

[11] X. Zhang and S. Wang, “Structure and growth of single crystal SiP_2 using flux method,” Solid State Sciences, **37**, 1–5 (2014). https://doi.org/10.1016/j.solidstatesciences.2014.08.009

[12] A.Y. Boboev, B.M. Ergashev, N.Y. Yunusaliyev, and M.M. Xotamov, “Study of the formation of low-dimensional defect states in single-crystal silicon with the participation of oxygen,” East European Journal of Physics (2), 299-306 (2025). https://doi.org/10.26565/2312-4334-2025-2-36

[13] K. Kayed and D. Kurd, “The effect of annealing temperature on the structural and optical properties of Si/SiO_2 composites synthesized by thermal oxidation of silicon wafers,” preprint, (2021). https://doi.org/10.21203/rs.3.rs-246154/v2

[14] I.I. Gorbachev, E.I. Korzunova, V.V. Popov, D.M. Khabibulin, and N.V. Urtsev, “Simulation of austenite grain growth in low-alloyed steels upon austenitization,” Physics of Metals and Metallography, **124**(3), 303–309 (2023). https://doi.org/10.31857/S0015323022601738

[15] K.S. Daliev, Sh.B. Utamuradova, J.J. Khamdamov, M.B. Bekmuratov, O.N. Yusupov, Sh.B. Norkulov, and Kh.J. Matchonov, “Defect formation in MIS structures based on silicon with an impurity of ytterbium,” East European Journal of Physics, (4), 301–304 (2024). https://doi.org/10.26565/2312-4334-2024-4-33

[16] Geiskopf, M. Stoffel, and X. Devaux, “Formation of SiP_2 nanocrystals embedded in SiO_2 from phosphorus-rich SiO1.5 thin films,” The Journal of Physical Chemistry C, **124**(14), 7973–7978 (2020). https://doi.org/10.1021/acs.jpcc.9b11416

[17] J. Safarian, and M. Tangstad, “Phase diagram study of the Si–P system in Si-rich region,” Journal of Materials Research, **26**(12), 1494–1503 (2011). https://doi.org/10.1557/jmr.2011.130

[18] L. Marot, R. Schoch, R. Steiner, V. Thommen, D. Mathys, and E. Meyer, “Rhodium and silicon system: II. Rhodium silicide formation,” Nanotechnology, *21*, 365707 (2010). https://doi.org/10.1088/0957-4484/21/36/365707

[19] L. Schellenberg, J. L. Jorda, and J. Muller, “The rhodium-silicon phase diagram,” Journal of the Less Common Metals, **109**(2), 261–274 (1985). https://doi.org/10.1016/0022-5088(85)90058-X

[20] K. Matsukawa, K. Shirai, and H. Yamaguchi, “Diffusion of transition-metal impurities in silicon,” Physica B: Condensed Matter, **401–402**, 151–154 (2007). https://doi.org/10.1016/j.physb.2007.08.134

[21] D. Garagnani, P. De Padova, C. Ottaviani, C. Quaresima, A. Generosi, B. Paci, B. Olivieri, *et al.*, “Evidence of sp2-like hybridization of silicon valence orbitals in thin and thick Si grown on α-phase Si(111)$\sqrt{3}\times\sqrt{3}$R30°-Bi,” Materials, **15**(5), 1730 (2022). https://doi.org/10.3390/ma15051730

[22] M. Trzcinski, G. Balcerowska-Czerniak, and A. Bukaluk, “XPS studies of the initial oxidation of polycrystalline Rh surface,” Catalysts, **10**, 617 (2020). https://doi.org/10.3390/catal10060617
[23] M.E. Turano, E.A. Jamka, M.Z. Gillum, and K.D. Gibson, “Emergence of subsurface oxygen on Rh(111),” The Journal of Physical Chemistry Letters, **12**(25), 5844–5849 (2021). https://doi.org/10.1021/acs.jpclett.1c01820
[24] Z.N. Weinrich, X. Li, S. Sharma, V. Craciun, M. Ahmed, E.A.C. Sanchez, S. Moffatt, and K.S. Jones, “Dopant-defect interactions in highly doped epitaxial Si:P thin films,” Thin Solid Films, **685**, (2019). https://doi.org/10.1016/j.tsf.2019.05.059

СТРУКТУРНО-ФАЗОВІ СТАНИ МОНОКРИСТАЛІВ КРЕМНІЮ, ЛЕГОВАНИХ РОДІЄМ

Акрамжон Й. Бобоєв[1], Шерзод А. Махмудов[2], Аваз К. Рафіков[2], Зійоджон М. Іброхімов[3], Рахмат М. Мансуров[4], Нурітдін Ю. Юнусалієв[1], Білоліддін М. Ергашев[5]
[1]*Андижанський державний університет імені З.М. Бабур, Андижан, Узбекистан*
[2]*Інститут ядерної фізики Академії наук Республіки Узбекистан*
[3]*Андижанський державний технічний інститут, Андижан, Узбекистан*
[4]*Академічний ліцей № 1 МВС Республіки Узбекистан*
[5]*Андижанський державний педагогічний інститут, Андижан, Узбекистан*

У цій роботі досліджено структурний та фазовий стан монокристалів кремнію (Si), легованих атомами родію (Rh). Для дослідження було обрано зразки кремнію n-типу, леговані родієм, вирощені методом Чокральського. Атоми родію вводили шляхом термічної дифузії при 1300°C, а зразки охолоджували як у режимах повільного, так і швидкого охолодження. Отримані дані оцінювали за допомогою рентгеноструктурного аналізу (XRD). У контрольних зразках термічна обробка призвела до утворення вторинних фаз, таких як SiP_2 та SiO_2, які, як було показано, пов'язані з фоновими домішками, зокрема атомами кисню. У зразку, легованому родієм та повільно охолодженому, утворилася фаза $SiRh_3$, а кристалічна решітка залишалася відносно стабільною. Це вказує на те, що атоми родію мають здатність зменшувати внутрішні напруження та релаксувати решітку. У режимі швидкого охолодження з'явилася фаза оксиду RhO_2, а також спостерігалося збільшення мікронапружень та кристалічних дефектів. Результати показують, що легування родієм є ефективним методом контролю структури, фазового складу та електричних властивостей монокристалів кремнію. Це дослідження має важливе значення для напівпровідникових матеріалів, мікроелектроніки та сонячних елементів.

Ключові слова: *кремній; родій; фосфор; дифузія; домішка; кисень; вторинні фази; рентгенівська дифракція; дефекти; мікродеформація*

East European Journal of Physics. **2.** 385-391 (2026)
DOI:10.26565/2312-4334-2026-2-42 ISSN 2312-4334

THERMODYNAMIC PROPERTIES OF Mn-DOPED DILUTED MAGNETIC SEMICONDUCTOR SUPERLATTICES

Mehdi M. Mahmudov[1], **Ragib Y. Damirov**[1]*, **Naila S. Sardarova**[2], **Arzu M. Ahmadova**[3]
[1]*Department of Solid State Physics, Baku State University, Z. Khalilov Street, 23, AZ1148, Baku, Azerbaijan*
[2]*Department of Natural Sciences, Sumgait State University, Baku Street, 1, AZ5008, Sumgait, Azerbaijan*
[3]*Department of Engineering and Applied Science, Azerbaijan State University of Economic,*
Istiglaliyyat Street 6, AZ1001, Baku, Azerbaijan
**Corresponding Author e-mail: damirovraghib@gmail.com*

Received March 5, 2026; revised May 18, 2026; accepted May 20, 2026

This work investigates the thermodynamic properties of a two-dimensional electron gas in manganese-doped diluted magnetic semiconductor superlattices, with particular emphasis on the chemical potential. Within the grand canonical formalism, a general expression for the chemical potential is derived that is valid for both degenerate and nondegenerate cases. In the nondegenerate limit, the chemical potential decreases with increasing temperature and exhibits a logarithmic dependence on carrier density; the temperature sensitivity is most pronounced at low carrier concentrations, where entropic effects dominate. In the degenerate regime, Landau quantization leads to a characteristic stepwise oscillatory dependence of the chemical potential on the applied magnetic field. The influence of the exchange interaction is analyzed in two limiting cases: in the weak-coupling limit, the correction to the chemical potential is linear in the Mn concentration and exchange constant, whereas in the strong-coupling limit, the system approaches complete spin polarization with carriers confined predominantly to a single spin channel. The exchange interaction introduces an additional spin-dependent contribution described by the Brillouin function, resulting in the most pronounced modifications at low temperatures and in strong magnetic fields.

Keywords: *Diluted magnetic semiconductors; Superlattices; Chemical potential; Exchange interaction; Landau quantization; Spin polarization*
PACS: 75.50.Pp, 68.65.Cd, 75.30.Kz

1. INTRODUCTION

Diluted magnetic semiconductor superlattices (DMSSs), which combine semiconductor heterostructures with magnetic impurities, have attracted considerable attention as promising candidates for spintronic applications [1,2]. Their distinctive physical properties arise from the interplay between quantum confinement and exchange coupling between itinerant charge carriers and localized magnetic moments [3,4]. The incorporation of transition-metal ions, particularly Mn, into III-V semiconductor superlattice structures gives rise to pronounced phenomena such as giant Zeeman splitting, enhanced Faraday rotation, and strong negative magnetoresistance [5,6]. A detailed understanding of the thermodynamic behavior of a two-dimensional electron gas in diluted magnetic semiconductor superlattices is therefore essential for controlling and optimizing their electronic and magnetic properties. Among the relevant thermodynamic quantities, the chemical potential plays a central role, as it governs carrier statistics, transport properties, and magnetic response [7]. In low-dimensional systems, the chemical potential differs substantially from that of bulk materials due to modifications of the density of states and quantum-size effects [8]. Previous theoretical studies of two-dimensional electron gases have primarily focused on nonmagnetic quantum-well structures [9, 10], whereas investigations that explicitly incorporate exchange interactions in superlattice configurations remain relatively limited [11-12]. Recent advances in molecular beam epitaxy have enabled the growth of high-quality diluted magnetic semiconductor superlattices, such as $(Ga,Mn)As/AlGaAs$ [13,14], further emphasizing the need for a comprehensive theoretical description of their thermodynamic properties. The exchange interaction between conduction electrons and localized d electrons of magnetic ions is a key mechanism governing the electronic structure and magnetic behavior of these materials [15]. This coupling can significantly modify the band structure and may give rise to carrier-induced ferromagnetism [16-18]. Consequently, analyzing its influence on thermodynamic quantities, particularly the chemical potential, is crucial for the development of efficient spintronic devices [19].

The present work differs from previous theoretical studies in several important aspects. We derive a unified analytical expression for the chemical potential within a single grand canonical formalism that remains valid in both the degenerate and nondegenerate cases, without introducing separate approximations for each limit. Second, the role of the exchange interaction is investigated in two distinct coupling regimes, namely the weak-coupling limit ($\alpha x \ll 1$) and the strong-coupling limit ($\alpha x \gg 1$). This approach leads to compact analytical expressions (Eqs. 13–15) that describe the crossover from linear to saturated behavior of the spin-polarization-induced correction to the chemical potential. To the best of our knowledge, such an analytical description has not previously been obtained for diluted magnetic semiconductor superlattices. Third, unlike strictly two-dimensional quantum-well models [9–12], the present treatment explicitly retains the superlattice miniband dispersion along the growth direction through the $\cos a\, k_z$ term in Eq. (1).

Cite as: M.M. Mahmudov, R.Y. Damirov, N.S. Sardarova, A.M. Ahmadova, East Eur. J. Phys. 2, 385 (2026), https://doi.org/10.26565/2312-4334-2026-2-42

In this work, the thermodynamic properties of a two-dimensional electron gas in manganese-doped diluted magnetic semiconductor superlattices are theoretically investigated, with particular emphasis on the chemical potential. Using the grand thermodynamic potential formalism [20], which naturally incorporates the effects of temperature, magnetic field, and carrier concentration, a general expression for the chemical potential is derived. Within this framework, the nondegenerate regime of the electron gas is analyzed, taking into account the exchange interaction between conduction electrons and localized magnetic moments of Mn ions. The results demonstrate that, in the nondegenerate case, the chemical potential decreases with increasing temperature and exhibits a logarithmic dependence on carrier density. Furthermore, the exchange interaction modifies the chemical potential through a contribution described by the Brillouin function, with the most pronounced effects occurring at low temperatures and in strong magnetic fields.

2. ENERGY SPECTRUM AND CHEMICAL POTENTIAL OF DMSS

In a strong magnetic field applied perpendicular to the superlattice layers, the electronic motion in diluted magnetic semiconductor superlattices becomes quantized within the plane of the layers, while the spin degeneracy of the electronic spectrum is removed. Under these conditions, the electron energy spectrum can be expressed as [21]:

$$\varepsilon(N,\sigma,k_z) = (2N+1)\mu B + \varepsilon_0(1-\cos a\,k_z) + g^*\sigma\mu_B B + 3AS, \tag{1}$$

where $N = 1, 2, \ldots$ are the Landau quantum numbers, k_z is the quasi-momentum component along the z-axis, $\mu = (m_0/m_\perp)\mu_B$, m_0 is the mass of a free electron, $m_\perp$ is the mass of the electron in the plane of the layer, ε_0 is the half-width of the conduction band in the direction k_z, a is the superlattice period in the direction z, g^* is the effective g-factor determined from the band structure, and the rest are standard constants, S is spin of magnetic impurity, $A = -(N_0\alpha\langle|S_z|\rangle x)/6$- the magnitude of the exchange splitting, N_0 is the number of cells per unit volume, α is constant describing the change in the structure of the band caused by the exchange interaction, x is the molar concentration of the impurity. It can be seen that each Landau level is split into two spin sublevels, and the splitting of the *N*th Landau level is equal to $\Delta\varepsilon = g^*\mu_B B$. In this work, manganese ions with spin 5/2 are taken as impurities, and then Eq. (1) takes the form:

$$\varepsilon = (2N+1)\mu B \pm \tfrac{1}{2} g\mu_B B \mp \tfrac{5}{2}\alpha x f(B,T) + \varepsilon_0(1-\cos a\,k_z). \tag{2}$$

where x is the molar concentration of manganese, and $f(B,T) = \frac{2}{5}B_{5/2}\left(\frac{g_{Mn}\mu_B B}{k_B T}\right)$, with $B_S(x) = \frac{2s+1}{2}cth\frac{2s+1}{2} - \frac{1}{2}cth\frac{x}{2}$ being the Brillouin function.

The chemical potential ζ of the electron gas can be obtained via the Gibbs method from the grand thermodynamic potential $\Omega = \Omega(T,V,\zeta,B)$ [20]:

$$n = -\frac{1}{V}\left(\frac{\partial\Omega}{\partial\zeta}\right)_{T,B} \tag{3}$$

where the grand potential in a quantizing magnetic field is given by [21]:

$$\Omega = -k_\mathrm{B}T\frac{V}{2a(\pi R)^2}\sum\nolimits_{N,S,\sigma}\int_0^{Z_0} ln(1+e^{\eta^*+\varepsilon_0^*\cos Z})dZ, \tag{4}$$

where $R = (\hbar/eB)^{1/2}$ is the magnetic length, $\eta^* = \zeta^* - \varepsilon_N^* - \varepsilon_0^*$, $\zeta^* = \zeta/k_B T$, $\varepsilon_N^* = \varepsilon_N/k_B T$, ζ is the chemical potential, $Z(\varepsilon) = ak_z = arccos(1-(\varepsilon-\varepsilon_z)/\varepsilon_0)$, $\varepsilon_N = (2N+1)\mu B$, $\varepsilon_0^* = \varepsilon_0/k_B T$, $\varepsilon_z = \varepsilon(N,\sigma,k_z) - (2N+1)\mu B - g^*\sigma\mu_B B - 3AS$. The upper limit of the integral is defined as [22]:

$$Z_0 = \begin{cases} \pi, & \varepsilon > 2\varepsilon_0 \\ arccos\left(1 + \frac{\mu B + \frac{g\mu B}{2} - \frac{5\alpha x f(B,T)}{2} - \varepsilon}{\varepsilon_0}\right), & \varepsilon < 2\varepsilon_0 \end{cases}. \tag{5}$$

Changing the integration variable from dZ to $d\varepsilon$, the grand potential becomes:

$$\Omega = \frac{k_B T V}{2(\pi R)^2}\sum\nolimits_{N,S,\sigma}\int_{\varepsilon_N}^{\infty}\frac{dk_z(\varepsilon,N)}{d\varepsilon} ln\left(1 + exp\left(\frac{\zeta-\varepsilon}{k_B T}\right)\right)d\varepsilon. \tag{6}$$

Substituting this expression into account in (3) yields a general formula for the chemical potential, valid for arbitrary magnetic field strength and electron gas degeneracy:

$$n = \frac{1}{2(\pi R)^2}\sum\nolimits_{N,S,\sigma}\int_0^{2\varepsilon_0}\frac{f(\varepsilon)d\varepsilon}{a\sqrt{(\varepsilon-\varepsilon^*)(2\varepsilon_0-(\varepsilon-\varepsilon^*))}}\,, \tag{7}$$

where $\varepsilon^* = \mu_B B(2N+1) \pm \frac{1}{2} g\mu_B B \mp \frac{5}{2}\alpha x f(B,T)$, and $f(\varepsilon)$ is the Fermi distribution function.

In the nondegenerate limit $(\zeta - \varepsilon \ll k_B T)$, this expression reduces to:

$$n = \frac{1}{2a(\pi R)^2}\sqrt{\frac{\pi k_B T}{2\varepsilon_0}}\sum_{N,S,\sigma} e^{\frac{\zeta-\varepsilon^*}{k_B T}}. \tag{8}$$

or equivalently,

$$\zeta = k_B T ln\left[2na(\pi R)^2\sqrt{\frac{2\varepsilon_0}{\pi k_B T}}\left(\sum_{N,S,\sigma} e^{-\frac{\varepsilon^*}{k_B T}}\right)^{-1}\right]. \tag{9}$$

Eq. (9) indicates that, for a nondegenerate electron gas, the chemical potential increases logarithmically with carrier concentration and decreases with increasing temperature. Temperature elevation facilitates the occupation of higher-energy states, resulting in a reduction of the chemical potential, while the dependence on the magnetic field arises through the quantized energy levels ε^*.

3. RESULTS AND DISCUSSION

The chemical potential of a two-dimensional electron gas in diluted magnetic semiconductor superlattices is determined by the combined effects of carrier concentration, temperature, magnetic field, and exchange interactions. In the nondegenerate case, to obtain the explicit dependence of the chemical potential on carrier concentration, exchange interaction, and temperature, the corresponding plots (Figs. 1-3) were constructed using the following parameters: $\varepsilon_0 = 10\ meV$, $a = 5\ nm$, $g = 2$, $x = 0.05$, $\alpha = 0.22\ eV$ [1].

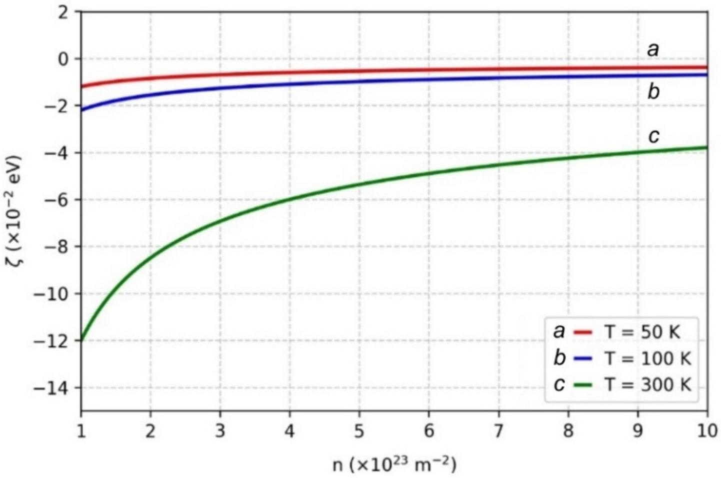

Figure 1. Chemical potential dependence on electron concentration ζ(n)

As shown in Fig. 1, the chemical potential increases monotonically with electron concentration for all considered temperatures at a fixed magnetic field $(B = 1\,T)$, following a logarithmic dependence $\zeta \propto k_B T ln(n)$, characteristic of a nondegenerate electron gas. At low carrier concentrations, the large number of available states leads to high entropy and strongly negative values of ζ. As the concentration increases, low-energy states become progressively occupied, entropy decreases, and the chemical potential shifts toward zero. An increase in temperature lowers the chemical potential due to enhanced thermal excitation, which redistributes electrons over higher-energy states. The exchange interaction between conduction electrons and localized Mn moments further modifies the chemical potential through the Brillouin function, with the strongest effects occurring at low temperatures and in strong magnetic fields. In addition, Landau quantization alters the density of states, introducing further corrections to ζ. The exchange interaction significantly influences the chemical potential in systems containing magnetic impurities. An increase in the exchange parameter α lowers the energy spectrum and reduces the chemical potential by shifting electrons toward lower-energy states, with the most pronounced effect observed at low temperatures. As shown in Fig. 2, at low temperature $(T = 50K)$ the chemical potential decreases most rapidly due to nearly complete spin polarization of Mn ions. At higher temperatures, thermal fluctuations reduce the degree of spin polarization and weaken the exchange-induced shift, resulting in a smaller variation of the chemical potential. As seen from Fig. 3, the chemical potential decreases monotonically with increasing temperature for all considered carrier concentrations, in accordance with Eq. (9). This behavior reflects the fundamental statistical nature of the nondegenerate electron gas: as temperature rises, thermal excitation redistributes carriers over a broader range of energy states, increasing the configurational entropy and driving the chemical potential to more negative values.

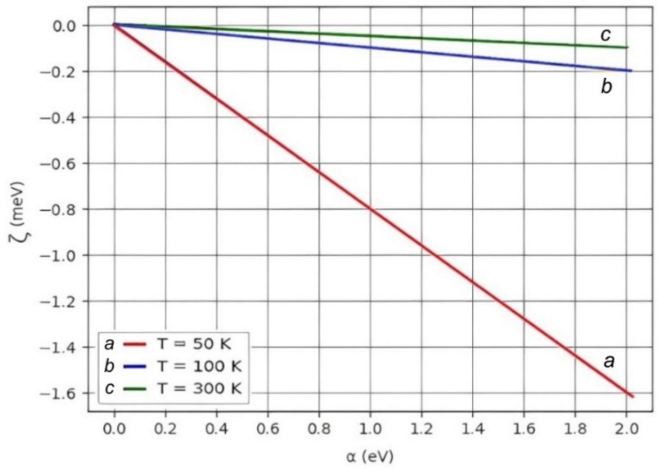

Figure 2. Chemical potential dependence on exchange interaction $\zeta(\alpha)$

At higher carrier concentrations, the chemical potential remains less negative over the entire temperature range. This follows directly from the logarithmic dependence in Eq. (9): a larger carrier density reduces the number of unoccupied low-energy states available per electron, thereby increasing the chemical potential relative to the low-concentration case. The temperature sensitivity of the chemical potential is more pronounced at lower concentrations. For $n = 10^{14} m^{-2}$, the chemical potential decreases steeply with temperature because the sparse carrier distribution leaves many thermally accessible states, leading to strong entropic effects. For $n = 10^{16} m^{-2}$, the lower-energy states are more strongly occupied, which moderates the temperature-induced reduction of the chemical potential. The exchange interaction between conduction electrons and localized Mn moments introduces an additional correction through the Brillouin function, as described by Eqs. (13)–(14). At the magnetic field value considered ($B = 1\,T$), this correction remains moderate; its influence becomes most significant at low temperatures, where the Mn spin polarization approaches saturation and the Brillouin function approaches unity.

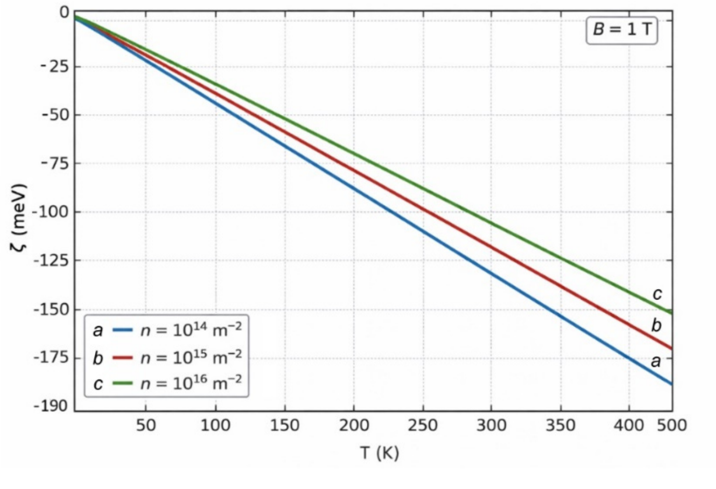

Figure 3. Chemical potential dependence on temperature $\zeta(T)$

To assess the quantitative validity of the analytical results, we compare the temperature dependence predicted by Eq. (9) with the self-consistent numerical calculations reported by Dietl and Ohno [9] for $(Ga, Mn)As$ at low Mn concentrations ($x = 0.05$) and $B = 1\,T$. Using the material parameters adopted in the present work ($\varepsilon_0 = 10\,meV, a = 5\,nm, g = 2, \alpha = 0.22\,eV$), Eq. (9) reproduces the correct order of magnitude of the chemical potential and the characteristic logarithmic decrease with temperature observed in those calculations. The quantitative agreement is satisfactory in the nondegenerate case ($T > 50\,K$), while deviations at lower temperatures are expected due to the onset of degeneracy effects not captured by Eq. (9) alone. We note that direct experimental measurements of the chemical potential as a function of magnetic field and exchange coupling strength are not yet available for Mn-doped superlattice geometries specifically; such measurements would provide a stringent test of the present theory and are identified as an important direction for future experimental work.

In the degenerate case ($\zeta - \varepsilon \gg k_B T$), all quantum states up to N_{max} are filled (quantum limit):

$$n = \frac{\pi}{2a(\pi R)^2} N_{\max}, \tag{10}$$

and the chemical potential equals the energy of the highest occupied level:

$$\zeta = \varepsilon_{N_{max}}(B). \tag{11}$$

This leads to stepwise variation of $\zeta(B)$ with quantum oscillation character as the magnetic field varies (Fig.4).

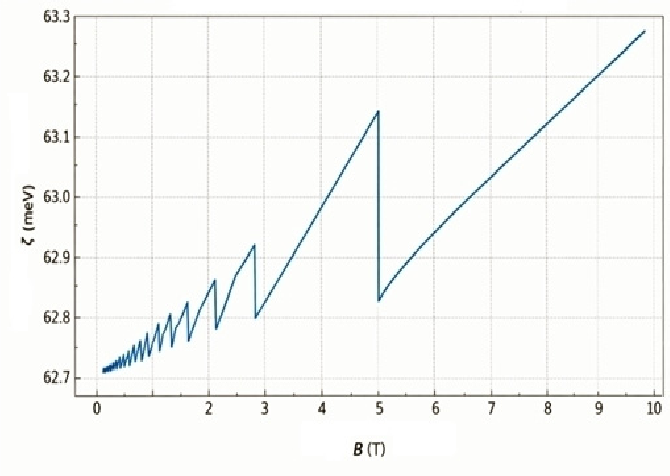

Figure 4. Chemical potential dependence on magnetic field $\zeta(B)$

Fig. 4 demonstrates the stepwise decrease of ζ with increasing magnetic field, reflecting the sequential depopulation of Landau levels. Each plateau corresponds to a fully occupied level, and its width is determined by the Landau level spacing $\hbar\omega_C$, which increases linearly with B (here, ω_C is the cyclotron frequency of an electron in a magnetic field). At low magnetic fields, closely spaced levels produce almost smooth variation of ζ , whereas at higher fields the oscillations become clearly resolved. The miniband dispersion along the z-direction introduces additional broadening, distinguishing the superlattice from an ideal strictly two-dimensional system. The exchange interaction further shifts the spin-split sublevels and modifies the positions of the steps.

Let us determine the influence of exchange interaction on the chemical potential. Separating the spin contributions in the summation yields:

$$\textstyle\sum_{N,S,\sigma} e^{-\frac{\varepsilon^*}{k_BT}} = \sum_{N,S,\sigma} e^{-\frac{\varepsilon_N^0}{k_BT} \pm \frac{5\alpha x f(B,T)}{2k_BT}}. \tag{12}$$

For weak exchange coupling, the chemical potential becomes:

$$\zeta(x,\alpha) = \zeta_0 - k_BTln\left[1 + \frac{5\alpha x f(B,T)}{2k_BT}\sinh\left(\frac{\mu_B g^* B}{2k_BT}\right)\right]. \tag{13}$$

In the limit of weak exchange interaction $(\alpha x \ll 1)$, expansion yields:

$$\zeta = \zeta_0 - \frac{5\alpha x f(B,T)}{4}\tanh\left(\frac{\mu_B g^* B}{2k_BT}\right). \tag{14}$$

Thus, in this case, the exchange correction to the chemical potential is linear in both doping concentration x and exchange constant α.

In the case of strong exchange interactions $(\alpha x \gg 1)$, one obtains:

$$\zeta = k_BTln\left[4na(\pi R)^2\sqrt{\frac{2\varepsilon_0}{\pi k_BT}}e^{\frac{5\alpha x f(B,T)}{2k_BT}}\right]. \tag{15}$$

Thus, a strong spin polarization develops, and electrons predominantly occupy a single spin channel. In the weak-coupling limit $(\alpha x \ll 1)$, Eq. (14) indicates that the exchange correction to the chemical potential is linear in both x and α, with the hyperbolic tangent term reflecting thermally induced spin polarization. In the strong-coupling limit $(\alpha x \gg 1)$, Eq. (15) describes a fully spin-polarized electron gas in which carriers occupy essentially one spin subband. The factor of 4 in Eq. (15), compared with the factor of 2 in Eq. (9), reflects the effective modification of the density of states associated with occupation of a single spin channel. The transition from partial to complete spin polarization with increasing exchange interaction strength is directly relevant to spintronic applications, as it determines the conditions under which the superlattice can operate as an efficient spin filter.

4. CONCLUSIONS

A theoretical framework describing the chemical potential of a quasi-two-dimensional electron gas in Mn-doped diluted magnetic semiconductor superlattices has been developed within the grand canonical formalism. Analytical expressions valid in both the degenerate and nondegenerate cases have been derived and numerically analyzed. In the degenerate limit, Landau quantization gives rise to a characteristic stepwise oscillatory dependence of the chemical potential on the magnetic field. In the nondegenerate case, the chemical potential is determined by the interplay among carrier concentration, temperature, and exchange coupling. Weak exchange interaction introduces a correction proportional to the Mn concentration and the exchange constant, whereas strong exchange coupling leads to nearly complete spin polarization, with carriers predominantly confined to a single spin channel. The obtained results establish a direct quantitative relationship between the microscopic exchange parameters of diluted magnetic semiconductor superlattices and their macroscopic thermodynamic properties. These findings may provide a theoretical basis for tailoring material parameters in the design of future spintronic devices.

ORCID

Mehdi M. Mahmudov, https://orcid.org/0009-0007-4154-6199; **Ragib Y. Damirov,** https://orcid.org/0009-0008-8712-1310; **Naila S. Sardarova,** https://orcid.org/0000-0003-0896-9126; **Arzu M. Ahmadova,** https://orcid.org/0000-0002-2392-9774

REFERENCES

[1] J. Kossut, and J.A. Gaj, *Introduction to the physics of diluted magnetic semiconductors*, (Springer, Berlin, Heidelberg, 2010), p. 469, https://doi.org/10.1007/978-3-642-15856-8

[2] P. Kacman, “Spin interactions in diluted magnetic semiconductors and magnetic semiconductor structures”, Semiconductor Science and Technology, **16**(4), R25-R39 (2001). https://doi.org/10.1088/0268-1242/16/4/201

[3] A. Gupta, R. Zhang, P. Kumar, V. Kumar, and A. Kumar, “Nano-structured dilute magnetic semiconductors for efficient spintronics at room temperature”, Magnetochemistry, **6**(1), 1-22 (2020). https://doi.org/10.3390/magnetochemistry6010015

[4] A.M. Babanli, and B.G. Ibragimov, “Magnetic moment of electrons in diluted magnetic semiconductor quantum ring”, in: *Proceedings of the 6th International conference on Control and Optimization with Industrial Applications* (COIA, Baku, 2018), pp.122-124.

[5] Berry Habte Dulla, “Thermodynamic properties of diluted magnetic semiconductors using Heisenberg spin model in 3D”, Journal of Applied Physical Science International, **2**(3), 101-106 (2015). https://ikprress.org/index.php/JAPSI/article/view/2844

[6] J. Ricardo de Sousa, and N.S. Branco, “Two-dimensional quantum spin -½ Heisenberg model with competing interactions”, Physical Review B, **72**(13), 134421 (2005). https://doi.org/10.1103/PhysRevB.72.134421

[7] R.N. Bhatt, M. Berciu, M.P. Kennett, and X.Wan, “Diluted magnetic semiconductors in the low carrier density regime”, Journal of Superconductivity, **15**(1), 71-83 (2002), https://doi.org/10.1023/A:1014031327996

[8] W. Zawadzki, “Theory of optical transitions in inversion layers of narrow-gap semiconductors”, Journal of Physics C: Solid State Physics, **16**(1), 229-240 (1983). https://doi.org/10.1088/0022-3719/16/1/025

[9] T. Dietl, and H. Ohno, “Dilute ferromagnetic semiconductors: Physics and spintronic structures”, Reviews of Modern Physics, **86**(1), 187-251 (2014). https://doi.org/10.1103/RevModPhys.86.187

[10] T. Jungwirth, J. Sinova, J. Mašek, J. Kučera, and A.H. MacDonald, “Theory of ferromagnetic $(III, Mn)V$ semiconductors”, Reviews of Modern Physics, **78**(3), 809-864 (2006). https://doi.org/10.1103/RevModPhys.78.809

[11] G. Bastard, *Wave Mechanics Applied to Semiconductor Heterostructures, (Monographs of Physics (Les Editions de Physique))*, (Wiley-Interscience Publishing, Paris, 1991), p. 357.

[12] D.R. Yakovlev, A. Keller, et al. “Kinetic exchange between the conduction band electrons and magnetic ions in quantum-confined structures”, Physical Review Letters, **83**(7), 1431-1434 (1999). https://doi.org/10.1103/PhysRevLett.83.1431

[13] H. Ohno, “Making nonmagnetic semiconductors ferromagnetic”, Science, **281**(5379), 951-956 (1998). https://doi.org/10.1126/science.281.5379.951

[14] A.H. MacDonald, P. Schiffer, and N. Samarth, “Ferromagnetic semiconductors: moving beyond $(Ga, Mn)As$”, Nature Materials, **4**(3), 195-202 (2005). https://doi.org/10.1038/nmat1325

[15] T. Dietl, H. Ohno, F. Matsukura, J. Cibert, and D. Ferrand, “Zener model description of ferromagnetism in zinc-blende magnetic semiconductors”, Science, **287**(5455), 1019-1022 (2000). https://doi.org/10.1126/science.287.5455.1019

[16] S. Lee, S. Chung, H. Lee, X. Liu, M. Dobrowolska, and J.K. Furdyna, “Interlayer exchange coupling in $(Ga, Mn)As$ ferromagnetic semiconductor multilayer systems”, Journal of Semiconductors, **40**(8), 081503 (2019). https://doi.org/10.1088/1674-4926/40/8/081503

[17] K. Ando, H. Saito, Z. Jin, T. Fukumura, M. Kawasaki, Y. Matsumoto, and H. Koinuma, “Magneto-optical properties of ZnO-based diluted magnetic semiconductors”, Journal of Applied Physics, **89**(11), 7284-7286 (2001). https://doi.org/10.1063/1.1356035

[18] D.D. Awschalom, and M.E. Flatté, “Challenges for semiconductor spintronics”, Nature Physics, **3**, 153-159 (2007). https://doi.org/10.1038/nphys551

[19] I. Žutić, J. Fabian, and S. Das Sarma, “Spintronics: Fundamentals and applications”, Reviews of Modern Physics, **76**(2), 323-410 (2004). https://doi.org/10.1103/RevModPhys.76.323

[20] B.M. Askerov, and S.R. Figarova, *Thermodynamics, Gibbs Method and Statistical Physics of Electron Gases*, (Springer, Berlin, Heidelberg, 2010), p. 374. https://doi.org/10.1007/978-3-642-03171-7

[21] S.R. Figarova, M.M. Mahmudov, and R.Y. Damirov, “Magnetization of diluted magnetic semiconductor II type superlattices with impurities Mn (manganese) ions”, Journal of Baku Engineering University: PHYSICS, **8**(1), 9-15 (2024). https://doi.org/10.30546/09081.2024.101.5002

[22] M.M. Mahmudov, and R.Y. Damirov, “Entropy of diluted magnetic semiconductor superlattices with impurities Mn ions”, Baku State University: Journal of Physics and Space Sciences, **2**(2), 9-16 (2025). https://doi.org/10.30546/209501.101.2025.2.02.03

ТЕРМОДИНАМІЧНІ ВЛАСТИВОСТІ РОЗБАВЛЕНИХ МАГНІТНИХ НАПІВПРОВІДНИКОВИХ НАДГРАТОК, ЛЕГОВАНИХ Mn

Мехді М. Махмудов[1], Рагіб Й. Даміров[1], Наїла С. Сардарова[2], Арзу М. Ахмадова[3]
[1]Кафедра фізики твердого тіла, Бакинський державний університет, вулиця З. Халілова, 23, AZ1148, Баку, Азербайджан
[2]Кафедра природничих наук, Сумгаїтський державний університет, вулиця Баку, 1, AZ5008, Сумгаїт, Азербайджан
[3]Кафедра інженерії та прикладних наук, Азербайджанський державний економічний університет,
вулиця Істіглаліят, 6, AZ1001, Баку, Азербайджан

У цій роботі досліджуються термодинамічні властивості двовимірного електронного газу в розбавлених магнітних напівпровідникових надґратках, легованих марганцем, з особливим акцентом на хімічний потенціал. У рамках великого канонічного формалізму отримано загальний вираз для хімічного потенціалу, який є справедливим як для вироджених, так і для невироджених випадків. У невиродженій границі хімічний потенціал зменшується зі зростанням температури та демонструє логарифмічну залежність від густини носіїв; температурна чутливість є найбільш вираженою за низьких концентрацій носіїв, де домінують ентропійні ефекти. У виродженому режимі квантування Ландау призводить до характерної ступінчастої коливальної залежності хімічного потенціалу від прикладеного магнітного поля. Вплив обмінної взаємодії аналізується у двох граничних випадках: у границі слабкого зв'язку поправка до хімічного потенціалу є лінійною щодо концентрації Mn та константи обміну, тоді як у границі сильного зв'язку система наближається до повної спінової поляризації з носіями, обмеженими переважно одним спіновим каналом. Обмінна взаємодія вносить додатковий спінзалежний внесок, що описується функцією Бріллюена, і призводить до найбільш виражених модифікацій за низьких температур та в сильних магнітних полях.

Ключові слова: *розбавлені магнітні напівпровідники; надґратки; хімічний потенціал; обмінна взаємодія; квантування Ландау; спінова поляризація*

EAST EUROPEAN JOURNAL OF PHYSICS. **2.** 392-398 (2026)
DOI:10.26565/2312-4334-2026-2-43 ISSN 2312-4334

ELECTRONIC TRANSITIONS AND RECOMBINATION MECHANISMS Cu-DOPED CdIn_2S_4 SINGLE CRYSTALS

Zafar Kadiroglu[1]*, **G.D. Abdinova**[2]
[1]*Semiconductors and Materials Science Research Center, Baku, AZ1011, Azerbaijan*
[2]*Institute of Physics Public Legal Entity, Ministry of Science and Education, Republic of Azerbaijan, Baku, AZ1073 Azerbaijan*
**Corresponding Author email: zafarkadiroglu@gmail.com*

Received March 13, 2026; revised May 8, 2026; accepted May 15, 2026

The study investigates the spectral distribution of photoconductivity, optical quenching, transient characteristics, thermally stimulated currents, and the temperature dependence of both dark and photocurrent in Cu-doped CdIn_2S_4 single crystals. Detailed analysis of the experimental data reveals the presence of deep donor levels with ionization energies located at E_c - 0.17 eV, E_c - 0.66 eV, E_c - 1.2 eV, and E_c - 1.55 eV. At 110 K, optical quenching of the photoconductivity was observed within the photon energy range of 0.86 to 1.63 eV. The energy positions of the photosensitivity centers relative to the valence band maximum were identified, yielding optical ionization energy of $E^{o}_{vr} = 0.86$ eV and a thermal ionization energy for the r-type levels of $E^{t}_{vr} = 0.62$ eV. The capture cross-sections ratio for holes and electrons at these r-centers was found to be $S_{pr}/S_{nr} = 5\times10^4$. Both optical and thermal quenching phenomena are attributed to charge-state transitions and carrier-exchange dynamics between slow (r) and fast (s) recombination centers. The well-defined electronic structure and high photosensitivity of Cu-doped CdIn_2S_4 single crystals suggest they are promising candidates for advanced photodetector applications in the visible and near-infrared spectral regions.

Keywords: *CdIn_2S_4; Photoconductivity; Optical quenching; Recombination centers; Deep donor level; Near-infrared photodetectors*
PACS: 72.40.+w, 61.72.uj

1. INTRODUCTION

CdIn_2S_4 belongs to the family of ternary $A^{II}B_2^{III}C_4^{VI}$ semiconductors, where A represents divalent cations (Zn, Cd), B represents trivalent cations (Ga, In), and C represents chalcogens (S, Se). These compounds are characterized by a wide band gap, intense luminescence, and high photosensitivity in the visible region of the electromagnetic spectrum [1-- 13]. Among these materials, cadmium thioindate (CdIn_2S_4) is of significant interest for optoelectronics. However, the intrinsic properties of undoped CdIn_2S_4 are often limited by complex intrinsic defect structures. The activation of CdIn_2S_4 with copper (Cu) has been shown to significantly enhance its photosensitivity by creating a high density of deep-level sensitizing centers, known as r-centers [14]. These Cu-related centers introduce a high asymmetry in the capture cross-sections for charge carriers, thereby effectively suppressing recombination and increasing the lifetime of photo-excited electrons. Consequently, Cu-doping transforms CdIn_2S_4 into a high-performance material suitable for precision photodetectors. The CdIn_2S_4 compound crystallizes in a cubic structure with a lattice constant of a = 10.797 Å (space group O_h^7 - Fd3m). At room temperature, the energy of indirect transitions is $E_g^{\text{НП}} = 2.28$ eV [15]. The results of studies on the various photoelectric properties of CdIn_2S_4 are presented in [16-21]. Due to its high quantum efficiency and broad absorption in the visible range, CdIn_2S_4 is a promising photocatalyst [22-24].

Despite extensive studies, the carrier recombination mechanisms in Cu- doped CdIn_2S_4 crystals remain a subject of debate. One of the most informative methods for investigating the energy spectrum of local states and carrier trapping processes is the analysis of the optical and thermal quenching of photoconductivity. These effects allow for the determination of recombination center parameters and provide insight into the interaction dynamics between different types of centers under varying temperature and illumination conditions.

This work is devoted to a comprehensive study of the spectral distribution, kinetics of optical quenching, thermally stimulated currents, temperature dependence of the dark current, and thermal quenching of the photocurrent in Cu-doped CdIn_2S_4 single crystals. The primary focus is on determining the energy parameters of photosensitivity centers and clarifying the roles of slow (r) and fast (s) recombination centers in photosensitivity processes.

2. EXPERIMENTAL DETAILS

The copper-doped CdIn_2S_4 compound was synthesized from high-purity constituent elements (at least 99,99 wt.%). The copper (Cu) impurity concentration was fixed at 0.002 mol. Single crystals were subsequently grown from the synthesized material using the melt crystallization.

The resulting crystals were characterized using X-ray diffraction and Raman scattering spectroscopy. X-ray diffraction studies, performed with a Bruker D2 Phaser diffractometer, confirmed that $\text{Cdİn}_2\text{S}_4$ crystallizes in a space group O_h^7 - Fd3m. The unit cell parameters were determined to be a = 10.797Å.

Raman spectra of CdIn_2S_4 were recorded using a “Nanofinder 30” (Tokyo Instruments, Japan) confocal Raman microspectrometer. A Nd:YAG laser (532 nm second-harmonic output, 10 mW maximum power) served as the excitation source. Using a diffraction grating with 1800 lines/mm, the spectral resolution was better than 0.5 cm^{-1}. All spectra were

---

Cite as: Z. Kadiroglu, G.D. Abdinova, East Eur. J. Phys. 2, 392 (2026), https://doi.org/10.26565/2312-4334-2026-2-43

measured in a back scattering geometry. The Raman spectra are in good agreement with previously reported literature, together with X-ray diffraction findings, confirm the high structural quality of the synthesized crystals. The resulting crystals exhibited n-type conductivity. Notably, it was established that neither the introduction of Cu impurities nor a stoichiometric excess of sulfur (or deficiency of cadmium and indium) triggered a carrier type conversion from n-type to p-type. For this study, high-resistivity, photosensitive samples were selected with the following parameters: dark specific resistivity (ρ): $10^6 \div 10^8$ Ω·см. and photosensitivity ratio (R_{dark} / R_{light}) = $10^2 \div 10^5$ (measured at 300 K under 200 lx illumination). Samples were prepared as plane-parallel plates with dimensions of 3 x 2 x 1 мм^3. Metallic indium was used to create ohmic contacts. The applied electric field strength was maintained below 20 V/cm to ensure linear current-voltage (I-V) characteristics and to exclude effects related to space-charge-limited current.

To measure the thermally stimulated current, the sample was kept in the dark at room temperature for 15 hours before being cooled to 100 K. After remaining at this temperature for 30-40 minutes, the sample was illuminated within the intrinsic absorption region.

The experimental setup used to study the optical quenching of photoconductivity is described in Ref. [25]. Intrinsic photoconductivity (background or primary illumination) was excited using an SI-6-300 incandescent lamp. A combination of selective, neutral, and water filters was employed to ensure uniform light absorption throughout the crystal volume. Quenching of the photocurrent was induced using monochromatic radiation in the 0.4-2.0 μm wavelength range, generated by an incandescent lamp coupled with an SF-4A monochromator. The resulting current was recorded using a DC chart recorder. Spectral plots were constructed point-by-point under steady-state conditions using a sequential excitation mode. In order to obtain the true spectral dependence of the photoconductivity, the raw data were normalized by the incident light intensity. Finally, the temperature dependence of the photocurrent was measured as the sample was heated at a constant rate of 0.08 K/s.

3. RESULTS AND DISCUSSION

3.1. Spectral Distribution of Photoconductivity

Experiments show that Cu doped $CdIn_2S_4$ single crystals exhibit photoconductivity within the energy range of 0.62 to 3.0 eV (Figures 1 and 2). Figure 1 illustrates the photocurrent spectrum of these crystals at T = 110 K. Given that the photocurrent values are relatively low (ranging from 10^{-9} to 10^{-6} A), a logarithmic scale is employed to clearly resolve subtle "shoulders" and slopes in the data. Based on the long-wavelength limit of the impurity photocurrent, we identified energy levels at E_c - 0.7 eV, E_c - 1.2 eV, and E_c - 1.55 eV. These levels are associated with the transitions of electrons from deep levels to the conduction band. Figure 2 represents the intrinsic and near-intrinsic regions (1.5 to 3.0 eV). A sharp peak near 1.75 eV corresponds to transitions from impurity levels to the conduction band, while a second, broader peak near 2.48 eV represents the interband transitions. The distinct separation of these two peaks indicates a well-defined electronic structure, suggesting that this crystal is a promising candidate for photodetector applications in the visible to near-infrared ranges.

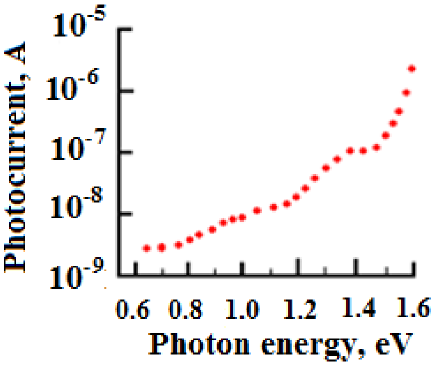

Figure 1. Spectral distribution of photoconductivity in Cu-doped $CdIn_2S_4$ single crystals at T = 110 K within the photon energy 0.6÷1.6 eV

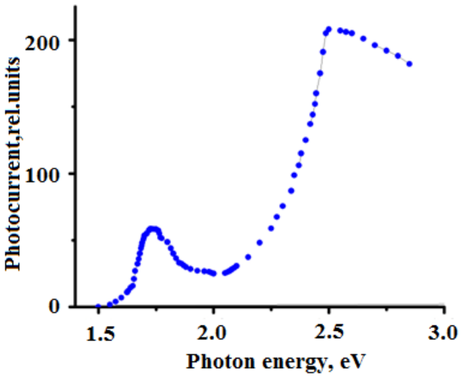

Figure 2. Spectral distribution of photoconductivity in Cu-doped $CdIn_2S_4$ single crystals at T = 110 K within the photon energy 1.5÷3.0 eV

3.2. Optical Quenching of Photoconductivity

Optical quenching of photoconductivity refers to the reduction of the steady-state intrinsic photocurrent when a sample is simultaneously exposed to additional light at impurity wavelengths. The study of optical quenching is an effective method for probing the band structure and the electronic-state system in semiconductors [25-30]. Specifically, this method provides valuable information regarding the parameters of photosensitivity centers (r-centers). The optical ionization energy (depth) of these centers relative to the valence band maximum (E^o_{vr}) is determined from the long - wavelength edge of the quenched spectrum.

The optical photocurrent quenching method was used to study slow r-recombination centers (Rose Class II centers [26]), which account for the high photosensitivity of $CdIn_2S_4$ single crystals. The optical quenching spectrum for copper-doped (Cu) samples is shown in Figure 3. The value of the current corresponding to optical quenching, $\Delta i_{ph} = i_{ph} - i_{ir}$, is plotted on the ordinate axis. Here, i_{ph} represents the primary (background) photocurrent, while i_{ir} is the photocurrent resulting from simultaneous illumination by both the primary and secondary light sources. As illustrated in Figure 3, optical quenching of the photocurrent is observed in the 0.86÷1.63 eV range at T = 110 K.

The quenching maximum is localized within the 1.13 - 1.27 eV interval. Based on the long-wavelength edge of the quenching spectrum, the optical ionization energy (depth) of the photosensitivity center levels relative to the valence band maximum was determined to be $E^o_{vr} = 0.86$ eV. In the secondary illumination energy range of 0.86 эВ < hν <1.2 eV, only photocurrent quenching is observed (Figure 3). When the secondary radiation is turned off, the photocurrent slowly increases, returning to the steady-state value determined by the primary illumination.

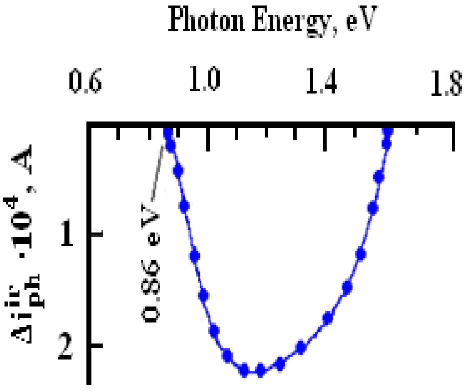

Figure 3. Optical quenching spectrum of intrinsic photoconductivity of $CdIn_2S_4$ single crystals doped with Cu

In $CdIn_2S_4$:Cu, a "flash" behavior of the photocurrent is observed under secondary light illumination. This is clearly illustrated in Figure 3, which displays the transient characteristics of the optical quenching of photoconductivity. Upon exposure to monochromatic light with photon energies hν > 1.2 eV, the photocurrent rises sharply, passes through a maximum and gradually recovers to the steady-state level maintained by the primary illumination at T = 110 K. This kinetic behavior confirms the competition between the rapid optical generation of electrons from donor levels and the subsequent slower recombination processes. This specific type of optical quenching-characterized by transient excitation-is determined by the ratio between the excitation and quenching rates at a given wavelength. As the energy of the secondary radiation increases, the amplitude of the "flash" also increases. At a fixed wavelength, two processes occur simultaneously: 1. Stimulation: An increase in photocurrent due to carrier generation from impurity levels into the conduction band. 2. A decrease in photocurrent resulting from the generation of holes from photosensitivity centers into the valence band. The unique nature of this kinetics allows for the separation of quenching and stimulation effects, as their respective amplitudes are proportional to the spectral dependencies of the photon capture cross - sections. This enables the determination of the long-wavelength excitation threshold. The long-wavelength edge of the photocurrent "flash" occurs at an energy of 1.2 eV. The emergence of this effect at hν > 1.2 eV suggests the presence of donor levels within the band gap, the shallowest of which is located 1.2 eV below the conduction band (E_c). The aforementioned facts indicate that the E_c -1.2 eV level plays an active role in the generation and recombination processes in $CdIn_2S_4$. Given that the optical quenching of the photoconductivity spectra extends up to 1.63 eV, the possibility of double optical transitions involving photosensitivity centers cannot be excluded.

3.3. The Temperature Dependence of Dark Current

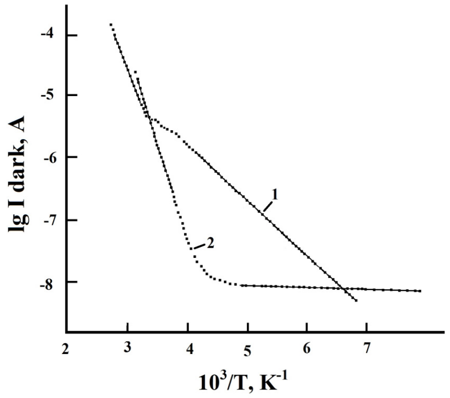

Figure 4. Temperature dependence of dark current in $CdIn_2S_4$ single crystals: 1-undoped; 2-Cu- doped

The temperature dependence of the dark current, I_{dark} (T), in $CdIn_2S_4$ single crystals was investigated in the temperature range of 110 - 410 K (Figure 4). For undoped $CdIn_2S_4$ single crystals, the activation energy values determined from of lg (I_{dark}) versus 10^3/T plot were E_c - 0.22 eV; E_c - 0.5 eV, and E_c - 1.0 eV (curve 1). In contrast, for Cu-doped crystals, no dark current activation was observed in the temperature dependence up to 230 K (Figure 4, curve 2).

This fact can be explained by an increase in the concentration of acceptor centers due to Cu doping. In thermodynamic equilibrium, these acceptors are compensated by the existing donors in the crystal, leading to a shift of the Fermi level toward the middle of the bandgap. Consequently, the activation of the dark current occurs at higher temperatures. For Cu-doped $CdIn_2S_4$ crystals, the dark current increases exponentially starting from 230 K. The activation energy for these crystals, determined from the slope of the temperature- dependent dark current, was found to be E_c - 0.66 eV. This result is in close agreement with the E_c - 0.7 eV value derived from the spectral distribution of photoconductivity.

3.4. The Temperature Dependenc of Photoconductivity

The temperature dependence of the intrinsic stationary photocurrent, $I_{ph}(10^3/T)$, in Cu-doped $CdIn_2S_4$ single crystals was investigated at various light intensities (L) within the range of 110-300 K (Figure 5). Experiments demonstrated that at constant light intensity (L), the photocurrent gradually increases with rising temperature. At approximately 230 K, a transition occurs from high to low photosensitivity, marking the onset of thermal quenching of the photocurrent. As the illumination intensity L increases, the rate of photocurrent grown decreases, and the onset of thermal quenching of the photoconductivity shifts toward higher temperatures. The activation of the photocurrent is likely due to electron trapping centers located below the conduction band. Effective recombination centers to acting trapping centers for holes.

At temperatures T< 230 K, electrons in these traps are thermally excited into the conduction band, thereby increasing the photocurrent. It is well-established that thermal quenching of the photoconductivity occurs due to the recharging of recombination centers. Since the r-photosensitive centers are located in the lower half of the band gap, the ratio of their capture cross-section is highly asymmetric (S_{pr}/S_{nr} >>1). In the thermal quenching of the photoconductivity region, an intensive exchange of charge carriers occurs between the valence band and r-centers. Consequently, the r-centers transition from acting as effective recombination centers to acting trapping centers for holes.

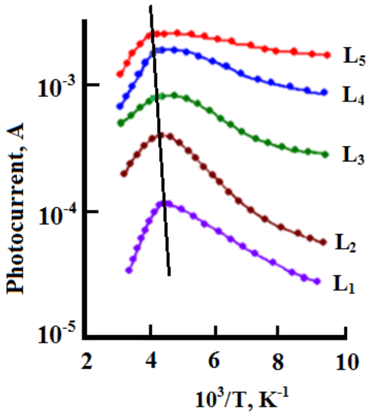

Figure 5. Temperature dependence of photocurrent in Cu-doped single crystals at different intensities of excitation light ($L_1 < L_2 < L_3 < L_4 < L_5$)

The transition from high to low photosensitivity at a fixed light intensity is determined by the following relation:

$$n = (C_{pr}/C_{nr})\, N_v \exp(-E^t_{vr}/kT).$$

Where n is the concentration of free electrons at the onset temperature of thermal quenching of the photoconductivity onset; N_v is the effective density of states in the valence band; E^t_{vr} is the "thermal" ionization energy of the r-centers relative to the top of the valence band. C_{pr} and C_{nr} are the capture probabilities of holes and electrons by the r-centers, respectively. Using the values $N_v = 7.10^{18}$ cm^{-3} and $\mu_p = 10$ $cm^2/V.sec$ (derived from thermoelectric power, conductivity, and photo-hole measurements), the following parameters were determined by analyzing the intersection of the straight line drawn through the thermal quenching onset points on the log I_{ph} vs. $10^3/T$ plot: the "thermal' ionization energy of the r-photosensitivity levels $E^t_{vr} = 0.62$ eV, as well as the ratio of capture cross-sections for holes and electrons by the r-centers $S_{pr}/S_{nr} = 5\times10^4$ indicates a very effective sensitizing center.

3.5. THERMALLY STIMULATED CURRENT

Thermally stimulated conductivity (TSC) was investigated within the temperature range of 110 - 300 K. Experimental results demonstrated that the temperature of the TSC maximum (T_m) is independent of both the duration and intensity of the initial illumination (Figure 6). The peak intensity increases with longer illumination duration due to a higher concentration of filled traps; the position of the maximum temperature remains constant. This invariance of T_m with respect to the initial trap filling level is a characteristic feature of first-order (monomolecular) kinetics, confirming the case of slow retrapping in Cu-doped $CdIn_2S_4$ crystals. This behavior suggests that the retrapping of carriers is negligible compared to the recombination rate. As the heating rate (β) increases from 0.08 K/s to 0.65 K/s, T_m shifts systematically toward higher temperatures (Figure 7).

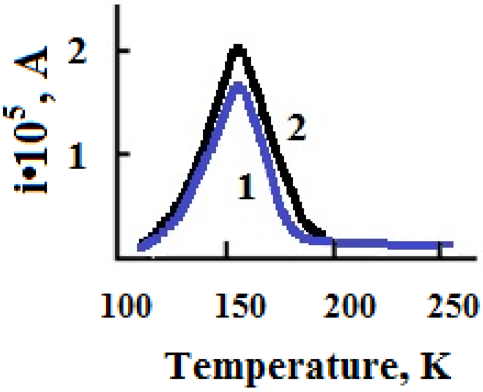

Figure 6. Temperature dependence of thermally stimulated current in Cu-doped $CdIn_2S_4$ single crystals at different illumination duration: (1) 5 min and (2) 60 min (at a constant heating rate β = 0.08 K/s).

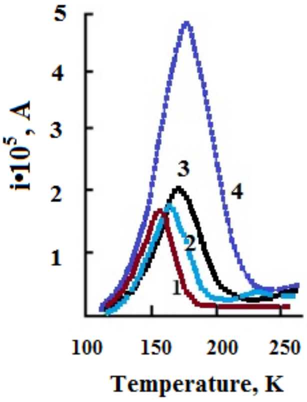

Figure 7. Temperature dependence of thermally stimulated current in Cu-doped $CdIn_2S_4$ single crystals at various heating rates: (1) $\beta_1 = 0.08$ K/s, (2) $\beta_2 = 0.24$ K/s, (3) $\beta_3 = 0.43$ K/s, (4) $\beta_4 = 0.65$ K/s

Following the theory for slow re-trapping, the activation energy (E_t) was determined using the following relation [31]:

$$\frac{E_t}{kT_m} = \ln\left(\frac{T_m^2}{\beta}\right) + \ln\left(\frac{\upsilon\, k\, S\, N_c}{E_t}\right),$$

where E_t is the trap depth, k is the Boltzmann constant, N_c is the effective density of states in the conduction band, S is the capture cross-section, and υ is the thermal velocity. The second term on the right-hand side is independent of temperature. From the slope of the Arrhenius plot (ln (T^2_m/β) vs. $1000/T_m$), the trap depth was calculated to be approximately $E_t \approx 0.14$ eV.

The activation energy (depth) of these levels can also be determined by the following formula [31,32]:

$$E_t = \frac{1.51\, k\, \mathrm{Tmax}\, \mathrm{T1}}{\mathrm{Tmax} - \mathrm{T1}}.$$

Where T_1 – is the temperature at which the thermally stimulated current reaches half of its maximum value on the rising side of the peak. A value of 0.17 eV was obtained for the activation energy of the trapping levels. This value is in satisfactory agreement with the previously calculated value of $E_t \approx 0.14$ eV.

4. DISCUSSION

Studies on optical and thermal quenching indicate that the recombination of non-equilibrium carriers in Cu-doped $CdIn_2S_4$ crystals is governed by a three-center model. This framework consists of:

1. Slow r-centers: Deep compensated acceptors responsible for high photosensitivity;
2. Fast s-centers: Centers for rapid recombination with significantly larger electron-capture cross-sections ($S_{nr} \ll S_{ns}$);
3. t-levels: Trapping levels located near the bottom of the conduction band (E_c - 0.17 eV) that regulate the population of the recombination centers via the charge neutrality condition.

In stoichiometric $CdIn_2S_4$, cationic vacancies (V_{Cd}) typically act as r-centers. However, in copper-doped samples, Cu atoms occupying tetrahedral lattice sites likely serve this role. The similar ionic radii of Cu^+ (0.96 Å) and Cd^{2+} (0.97 Å) facilitate the substitution of cadmium by copper. In thermodynamic equilibrium, the photosensitivity centers are located below the hole quasi-Fermi level (E_{fp}), acting primarily as hole traps. Upon illumination with intrinsic light, electrons are excited from the valence band to the conduction band, generating a primary photocurrent. As the intensity of intrinsic excitation increases, E_{fp} shifts toward the valence band, transforming the r-centers into active recombination centers.

This increases the electron lifetime and elevates the steady-state photocurrent.

Under secondary illumination (0.86 - 1.63 eV), electronic transitions occur from the valence band to the photosensitivity centers, which is physically equivalent to the release of holes from r-centers into the valence band. These holes are subsequently captured by the fast s-centers, leading to a redistribution of recombination fluxes: recombination through the slow r-centers decreases, while recombination through the fast s-centers increases sharply. The suppression of the r-center channel and the subsequent relocalization of holes to s-centers results in a significant reduction of free electrons in the conduction band, leading to the observed quenching of the photocurrent.

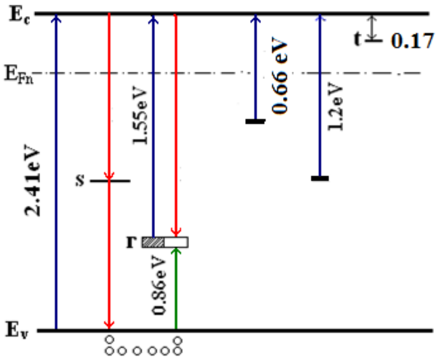

Figure 8. Energy level scheme and electronic transitions in Cu-doped $CdIn_2S_4$ singe crystals at 110 K. Transitions from r-center (1.55 eV) and the valence band (2.41eV) to the conduction band are indicated, alongside trapping levels (t) and fast recombination centers (s)

We attributed the 1.55 eV value obtained from the photoconductivity spectrum to electronic transitions from r-photosensitivity centers to the conduction band. This interpretation is supported by the energy balance: the sum of energy levels (1.55 + 0.86 = 2.41 eV) corresponds exactly to the band gap width (E_g) of the $CdIn_2S_4$ at T = 110 K. These results enable a comprehensive explanation of electronic transitions using a three-level energy scheme. By synthesizing our findings with existing literature, we propose this model for the excitation and recombination processes in Cu-doped $CdIn_2S_4$ single crystals (Figure 8).

CONCLUSIONS

In this study, the energy range for the optical quenching of photoconductivity in Cu-doped $CdIn_2S_4$ single crystals at 110 K was determined to be 0.86-1.63 eV. The ionization energies of deep donor levels were identified as E_c - 0.17 eV, E_c - 0.66 eV (refined based on spectral analysis), E_c - 1.2 eV, and E_c - 1.55 eV. Based on the spectral characteristics, the optical energy of the photosensitivity (r) centers relative to the valence band maximum was determined as $E^o_{vr} = 0.86$ eV. Additionally, the thermal energy of these r-centers was found to be $E^t_{vr} = 0.62$ eV, with a hole-to-electron capture cross-section ratio (Spr/Snr) of 5×10^4.

The results demonstrate that the quenching mechanisms are governed by the redistribution of charge carriers between slow (r) and fast (s) recombination centers. In summary, our investigation into the photoconductivity of $CdIn_2S_4$: Cu confirms the existence of several deep donor levels and highly efficient sensitizing r-centers. The high capture cross-section ratio suggests that these crystals possess superior photosensitivity. These findings indicate that Cu-doped CdIn$_2$S$_4$ crystals exhibit a well-defined electronic structure, making them excellent candidates for next-generation visible and near-infrared photodetectors.

ORCID

Zafar Kadiroglu, https://orcid.org/0009-0001-9735-5160; **G.D. Abdinova,** https://orcid.org/0009-0004-4172-1207

REFERENCES

[1] A. Liang, L.T. Shi, G. Perra, O. Gomis, D. Errandonea, L.M. Tiginyanu, V.V. Ursaki, and F. J. Manjon, “Pressure – induced band anticrossing in two adamantine ordered-vacancy compounds: CdGa$_2$S$_4$ and HgGa$_2$S$_4$,” J. Alloys Compd., 886, 161226 (2021). https://doi.org/10.1016/j.jallcom.2021.161226

[2] T. G. Kerimova, I. A. Mamedova, L. I. Kengerlinskiy, N. A. Abdullayev, Z. Kadiroglu, and N. T. Mamedov, “Temperature dependence of Raman spectrum of CdGa$_2$Se$_4$,” International Conference on Modern Trends in Physics, **5**(1), 125 (2019).

[3] A. Nayak, S. Jena, and P. Parida, “An ab-initio investigation of Cd-based chalcopyrite-type semiconductors; Promising candidates for sustainable energy goals,” J. Phys. Chem. Solids, 212,113537 (2026). https://doi.org/10.1016/j.jpcs.2026.113537

[4] T.G. Kerimova, Z.G. Mamedov, and A.G. Sultanova, “Stimulated impurity photoconductivity in CdGa$_2$S$_4$,” Fizika (Baku), **6** (3), 56-58 (2000).

[5] Z. Kadiroglu, “Promising Materials for Optoelectronics CdIn$_2$S$_4$: Experimental Studies of Electronics Properties,” in: *Proceedings 7th Advanced Chemistry World Congress*, (Roma, Italy, 2026), pp. 85.

[6] Z. A. Jahangirli, T. G. Kerimova, I. A. Mamedova, N. A. Abdullaev, and N. T. Mamedov, “Ab initio Calculations of Phonon Dispersion in CdGa$_2$S$_4$,” Phys. Solid State, **60**(11), 2305–2309 (2018). https://doi.org/10.1134/S1063783418110069

[7] Z. A. Jahangirli, T. G. Kerimova, I. A. Mamedova, S. A. Nabieva, and N. A. Abdullaev, “Ab Initio and Experimental Study of Electronic, Optical, and Vibrational Properties of CdGa$_2$Te$_4$”, Phys. Solid State, **62**(8), 1426–1433 (2020). https://doi.org/10.1134/S1063783420080120

[8] T. G. Kerimova, N. A. Abdullaev, I. A. Mamedova, Z. I. Badalova, R. A. Guliev, R. Raucar, K. Wakita, and N. T. Mamedov, “Optical Phonons in CdGa$_2$S$_{4x}$Se$_{4(1-x)}$ alloys,” Semiconductors, **47**(6), 761–766 (2013).

[9] I. G. Nasibov, I. A. Mamedova, Z. Kadiroglu, and T. G. Kerimova, “Photouminescence of ZnGa$_2$S$_4$ doped with atoms Nd,” Transactions of National Academy of Science of Azerbaijan, Series of physics-mathematical and technical sciences, Physics and Astronomy, **XXXVI** (2), 30-34 (2016) (in Russian).

[10] V.Yu. Rud, Yu.V. Rud, A.A. Vaipolin, I.V. Bodnar, and N Fernelius, “Photosensitive structure on CdGa$_2$S$_4$ single crystals,” Semiconductors, **37**, 1283-1290 (2003). https://doi.org/10.1134/1.1626209

[11] D.T. Gusejnov, Yu. G. Asadov, Z.G. Mamedov, and N.E. Gasanov, “Impurity photoconductivity in CdGa$_2$S$_4$,” Izv. Akad. Nauk SSSR, Neorg. Mater. **23**(10), 1736-1737 (1987).

[12] I. A. Mamedova, Z. A. Jahangirli, and N.A. Abdullayev, “Electronic properties of CdGa$_2$S$_4$: Ab-initio calculations and experimental studies by spectral ellipsometry,” Phys. Solid State, **66**, 365-374 (2024). https://doi.org/10.1134/S1063783424601310

[13] Z. A. Dzhakhangirli, T. G. Kerimova, N. A. Abdullayev, I. A. Mamedova, and N. T. Mamedov, “Ab Initio Calculations of Phonon Dispersion in CdGa$_2$Se$_4$,” Semiconductors, **51**(5), 556-558 (2017). https://doi.org/10.1134/S1063782617050074

[14] H. Koelmans, H.G. Grimmeiss,” The photoconductivity of activated with Cu and Au”, Physica, **25**(7), 1287-1288 (1959). https://doi.org/10.1016/0031-8914(59)90050-3

[15] H. Nakanishi, **“**Fundamental Absorption Edge in CdIn$_2$S$_4$” Jpn. J. Appl. Phys. **19** (1), 103-108 (1980). https://doi.org/10.1143/JJAP.19.103

[16] Z. Kadiroglu, “The role of cation deficiency and impurities in the formation of photosensitivity centers in CdIn$_2$S$_4$ compound,” Phys. Solid State, **67**,684-687 (2025). https://doi.org/10.1134/S1063783425601079

[17] K. Zhang, F. Chen, Sh. Han, Na Li, W. Sun, and Y. Tang, **“**Construction of a novel hierarchical 2D/3 D heterojunction Bi$_4$Ti$_3$O$_{12}$/CdIn$_2$S$_4$ with significantly boosted photocatalytic activity for degradation of tetracycline under visible light,” Inorg. Chem. Commun. **173**(3), 113820 (2025). https://doi.org/10.1016/j.inoche.2024.113820

[18] D.T. Guseinov, T. G. Kerimova, and Z. L. Kadyrogly, “Effects arising from a repulsive barrier in the compound CdIn$_2$S$_4$,” Semiconductors, **30**(6), 517-519 (1996).

[19] Z. Kadiroglu, T.G. Kerimova, R.A. Guliev, and M.A. Aliev, “Electrical and photoelectrical properties of CdIn$_2$S$_4$ doped Fe,” Transactions of the National Academy of Science of Azerbaijan, Series of physics-mathematical and technical sciences, Physics and Astronomy, **XXXII** (2), 36-40 (2012) (in Russian).

[20] D. T. Guseinov, and Z. G. Mamedov, “On the Phase Transitions in CdIn$_2$S$_4$,” Inorganic Materials, **30** (12), 1597 (1994).

[21] G. Yadav, and Md. Ahmaruzzaman, “CdIn$_2$S$_4$-based advanced composite materials: Structure, properties, and applications in environment and energy -A concise review,” Inorganic and Nano-Metal Chemistry, **55**(2),122-136 (2025). https://doi.org/10.1080/24701556.2023.2240775

[22] Sh. Sambyal, A. Sudhaik, S. Sonu, P. Raizada, V. Chaudhary, V.-H. Nguyen, A. A. Parwaz Khan, *et al.*, “Recent updates on cadmium indium sulfide (CdIn$_2$S$_4$ - CIS) photo-catalyst: Synthesis, enhancement strategies and applications,” Coord. Chem. Rev. **535**, 216653 (2025). https://doi.org/10.1016/j.ccr.2025.216653

[23] M.A. Hamza, G. Metha, and C.J. Shearer, “Recent advances and future directions of CdIn$_2$S$_4$-based photocatalysts: properties, synthesis, and modifications for energy and environmental applications,” J. Mater. Chem. A, **13**, 212292 (2025). https://doi.org/10.1039/D5TA02047F

[24] M. A. Hamza, A. J. Keltie, R. K. Matthews, M. L. Day, and C. J. Shearer, “CdIn$_2$S$_4$ Micro-Pyramids for Reductive Photocatalytic Degradation of Perfluorooctanesulfonic Acid,” Small, **21**, e04601 (2025). https://doi.org/10.1002/smll.202504601

[25] Z. Kadiroglu, “Optical quenching of photoconductivity in CdIn$_2$S$_4$ single crystals,” Transactions of the National Academy of Science of Azerbaijan, Series of Physics-Mathematical and Technical Sciences, Physics and Astronomy, **XLI** (5), 121-127 (2021). (in Russian).

[26] A. Rose, *Concepts in Photoconductivity and Allied Problems*, (Interscience Publishers, New York, 1963), p. 168.

[27] *Photoconductivity and Photoconductive Materials: Fundamentals, Techniques and Applications*, edited by S.O. Kasab, (John Wiley & Sons, Ltd, 2022). https//doi.org/10.1002/9781119579182

[28] R. H. Bube, *Photoconductivity*, (Wiley & Sons, Inc. 1999). https://doi.org/10.1002/047134608X.W6026

[29] Z. Kadiroglu, "Photoelectronic properties in $CdGa_2S_4$ single crystals," East Eur. J. Phys. (1), 281 (2026). http://doi.org/10.26565/2312-2026-1-32

[30] D.T. Guseinov, Z. G. Mamedov, N. E. Qasanov, and Yu.G. Asadov, "On the Two Types of Slow Recombination Centers in $CdIn_2S_4$," FTP, **21**(4), 738-741 (1987). (in Russian)

[31] A. G. Milnes, *Deep Impurities in Semiconductors*, (Garnegie-Mellon University, John Wiley & Sons, New York, 1973).

[32] L. I. Grossweiner, "A note on the Analysis of First-Order Glow Curves," J. Appl. Phys. **24**, 1306-1307 (1953). https://doi.org/10.1063/1.1721152

ЕЛЕКТРОННІ ПЕРЕХОДИ ТА МЕХАНІЗМИ РЕКОМБІНАЦІЇ МОНОКРИСТАЛІВ $CdIn_2S_4$, ЛЕГОВАНИХ МІДДЮ

Зафар Кадіроглу[1], Г.Д. Абдінова[2]
[1]Науково-дослідний центр напівпровідників та матеріалознавства, Баку, AZ1011 Азербайджан
[2]Інститут фізики, публічна юридична особа, Міністерство науки та освіти, Азербайджанська Республіка, Баку, AZ1073 Азербайджан

У дослідженні вивчаються спектральний розподіл фотопровідності, оптичне гасіння, перехідні характеристики, термостимульовані струми та температурна залежність як темнового, так і фотоструму в монокристалах CdIn2S4, легованих міддю. Детальний аналіз експериментальних даних показує наявність глибоких донорних рівнів з енергіями іонізації, розташованими при E_c - 0,17 еВ, E_c - 0,66 еВ, E_c - 1,2 еВ та E_c - 1,55 еВ. При 110 K оптичне гасіння фотопровідності спостерігалося в діапазоні енергій фотонів від 0,86 до 1,63 еВ. Було визначено енергетичні положення центрів фоточутливості відносно максимуму валентної зони, що дало енергію оптичної іонізації $E^o_{vr} = 0{,}86$ еВ та енергію теплової іонізації для рівнів r-типу $E^t_{vr} = 0{,}62$ еВ. Співвідношення перерізів захоплення для дірок та електронів у цих r-центрах було визначено як $S_{pr}/S_{nr} = 5\times10^4$. Як оптичне, так і теплове гасіння пояснюються переходами зарядових станів та динамікою обміну носіями між повільними (r) і швидкими (s) рекомбінаційними центрами. Чітко визначена електронна структура та висока фоточутливість монокристалів CdIn2S4, легованих міддю, свідчать про те, що вони є перспективними кандидатами для передових застосувань у фотодетекторах у видимому та ближньому інфрачервоному спектральних діапазонах.

Ключові слова: *$CdIn_2S_4$; фотопровідність; оптичне гасіння; рекомбінаційні центри; глибокий донорний рівень; фотодетектори ближнього інфрачервоного діапазону*

East European Journal of Physics. **2**. 399–410 (2026)

DOI: 10.26565/2312-4334-2026-2-44 ISSN 2312-4334

AN IN-DEPTH FIRST-PRINCIPLES STUDY OF THE STRUCTURAL, STABILITY, ELECTRONIC, THERMODYNAMIC, AND OPTICAL CHARACTERISTICS OF TWO-DIMENSIONAL BiBrO

Yadgar Hussein Shwan

Physics Department, College of Education, University of Sulaimani, Sulaymaniyah 46001, Kurdistan Region, Iraq

Corresponding Author e-mail: yadgar.shwan@univsul.edu.iq

Received March 7, 2026; revised May 16, 2026; accepted May 18, 2026

This study leverages DFT within the GGA framework to provide a thorough calculate of the stability, electronic properties, thermal performance, and optical responses of 2D BiBrO. The computed formation energy, along with phonon calulation findings and AIMD results, verifies the stable structural, dynamical and thermal stability of the BiBrO system. The 2D BiBrO material exhibits semiconducting behavior with a band gap of 2.42 eV, as confirmed by electronic band structure analysis. Optical properties analysis of BiBrO reveals powerful visible and ultraviolet (UV) light interaction, which supports its applications as a solar energy storage device. The large ability of BiBrO to store thermal energy is due to high heat capacity, because BiBrO has a greater phonon density of states. The entropy rises proportionally to the temperature which means that there is additional atomic disorder and more accessible microscopic states. Furthermore, the increase in entropy and the plateau in heat capacity at high temperatures imply a change toward a more disordered state, while yet allowing for effective thermal energy absorption. The low lattice thermal conductivity and smaller phonon group velocity of BiBrO are the characteristics that render the material useful in thermal insulation, while maintaining structural stability. These findings give critical information regarding how BiBrO may be used in energy storage systems as well as thermal barrier.

Keywords: *2D BiBrO; DFT; Electronic characteristics; Lattice thermal conductivity; Optical characteristics; Stability*

PACS: 71.15.Mb, 73.22.-f, 78.20.-e, 63.20.dk, 65.80.-g, 66.70.-f

1. INTRODUCTION

Since the discovery of Graphene in 2004, there is a significant interest in the two dimensional materials. Due to their small dimensions, which causes reduced dimensionality, their electrical, optical, and catalytic properties are promising platforms with respect to high-level electronic and energy applications. The materials covered in this category are quite diverse with Hexagonal boron nitride (h-BN), Hexagonal boron-carbon-nitride (B- C-N) transition metal oxides (TMOs), transition metal dichalcogenides (TMDs), and metal halides each with its own structural and physicochemical properties to support many technological applications [1–5]. In recent years, much research effort has been devoted to the study of novel two-dimensional materials for various applications such as spintronics, chemical and biological sensing, supercapacitors, solar cells and lithium-ion batteries. [6, 7].

The crystal structure of transition metal dichalcogenides (TMDs) is usually considered MX2, and is layered, which is most often implemented in two dimensions (2D). These materials have a large variety of physical properties such as semiconducting, superconducting and metallic. The MX2-type layered materials, including graphite (i.e., stacked sheets of graphene), include strong covalent bonds in each layer, and relatively weak van der Waals (vdW) forces between individual layers in their bulk phases. In the recent past, there is a proposal of a new category of MX-type 2D material and there has been a lot of concern as these materials have shown promising and wide-ranging physical characteristics [8–10]. Bismuth triiodide (BiI_3) is a layered semiconductor that has attracted considerable attention for optoelectronic and photovoltaic applications due to its suitable band gap and strong optical absorption. First-principles density functional theory (DFT) studies, demonstrated that bulk BiI_3 consists of weakly bonded van der Waals layers, making the exfoliation of a stable BiI_3 monolayer energetically feasible. Their calculations further revealed that monolayer BiI_3 exhibits semiconducting behavior with a band gap appropriate for visible-light absorption and a high absorption coefficient in the visible region, highlighting its potential for ultrathin solar cells and photodetectors [11–13]

Bismuth bromide oxide (BiOBr) crystallises in a layered matlockite-type tetragonal form of (space group P4/nmm). Being a part of the (BiOX, X = Cl, Br, I) group. BiOBr is a semiconductor, which has an indirect band gap of about 2.46 eV, which allows it to have a lot of absorption in the visible-light portion. Due to these structural and electronic properties, BiOBr has drawn a lot of attention to be used in photocatalysis, optoelectronics and photovoltaic devices [14–16]. These properties of the BiBrO provide a promising future because of its layered structure. This is a structure whereby a two dimension structure can be formed due to the weak van der Waals forces , which are used to stacked the layers. The layers are exfoliable to 2D nanosheets, as is the case with graphene which is made of graphite. This makes BiBrO a large surface area 2D material [17]. Theoretical calculations of a BiBrO singlayer with uncharacteristically high thermal stability as verified by dispersion-phonon calculation. In addition, the material is semiconducting and has a wide band gap [18].

Cite as: Y.H. Shwan, East Eur. J. Phys. 2, 399 (2026), https://doi.org/10.26565/2312-4334-2026-2-44

The crystal structure of BiBrO has not been fully analyzed, and its complete characterization remains limited. Further investigations are necessary to achieve a comprehensive understanding of the BiBrO structure. This study employes (DFT) computations to thoroughly calculate the fundamental features of BiBrO in its tetragonal crystal form. The present study offers a thorough investigation of both the low- and high-temperature behavior, in addition to the thermal stability of BiBrO, using ab initio molecular dynamics (AIMD) simulations. The formation energy is calculated to assess the energetic stability of the atomic configuration. Additionally, the electronic properties of BiBrO are analyzed in detail through an examination of its band structure and partial density of states (PDOS). The optical properties are further examined by calculating the real and imaginary components of the dielectric function, as well as the refractive index, reflectivity, absorption coefficient, and optical conductivity. The thermal characteristics of the material were comprehensively analyzed through heat capacity and entropy calculations, followed by investigations of the phonon-band structure to assess its dynamical stability. Bismuth oxybromide (BiOBr) demonstrates relatively low thermal conductivity, positioning it as a promising candidate for thermal insulation applications. Its capacity to restrict heat transport, along with its structural stability, underscores its potential in energy-related technologies.

The rest of this paper is arranged as follows. Section 2 explains the computational methods used in this investigation. Section 3 delves further into the structural, electrical, dynamical, thermal, and optical aspects of the researched atomic configurations. This section focuses on the material's electrical properties, thermal transport characteristics, and interaction with electromagnetic radiation. Finally, Section 4 summarizes the main findings and highlights the study's significant conclusions.

2. COMPUTATIONAL APPROACH

We examine a two-dimension unit cell of BiBrO with space group $P4/nmm$ consisting of 6 atom. Quantum espresso utilizes the projector augmented wave (PAW) framework for conducting first-principles calculations with DFT. Besides this, the exchange-correlation effects were modeled on the basis of the generalized gradient approximation (GGA) with the use of the Perdew Burke Ernzerhof functional (PBE) formulation. A convergence test establishes the suitable kinetic energy cutoff for Brillouin zone sampling through testing. A combination of $11 \times 11 \times 5$ Monkhorst-Pack k-point grid and 50 Ry plane-wave cutoff is used as the computational parameters. None self consistent field (*nscf*) calculations require a denser k-point grid of $50 \times 50 \times 5$ for their execution. Using the relax and vc-relax modes structural relaxation processes the unitcells and atomic arrangements to find optimal structures which can be analyzed well. The relaxation energy reaches convergence at 2.72×10^{-7} eV [**?**, 19].

The AIMD simulation run tests thermal stability on a unit cell maintained at 300 K for 5 ps. Structure undergo analysis of their electronic and optical characteristics when they reach full relaxation, where stress are less than 6×10^{-4} eV/Å. Phonopy program calculates dynamic stability, entropy and heat capacity using phonon-related parameters such as frequencies and density of states (DOS). Thermal conductivity of lattice was determined by iteratively solving the phonon Boltzmann transport equation using phono3py, using a $20 \times 20 \times 2$ q-mesh. XCRYSDEN and BURI 1.3. are used to visualize and design structures, as well as to improve our understanding of material characteristics by assuring correct modeling and guiding investigations [21–23]

3. RESULTS

In this part, the findings on the geometrical, stability, electrical, optical, and thermal characteristics of the 2D structure of BiBrO are provided.

3.1. Geometric properties

Before we begin understanding BiBrO structure we must determine its basic shape. The BiBrO structure visualization displays top and side views in Fig. 1. BiBrO crystallizes in the tetragonal $P4/nmm$ space group and takes on a structure similar to that of Matlockite. The crystal is made up of a single BiBrO unit cell layer in two dimensions. The Bi^{3+} cation interacts with four equivalent O^{2-} atoms and four equivalent Br^{1-} atoms, displaying a fourfold coordination environment. The measured lengths of the Bi-O and Bi-Br bonds are 2.33 Å and 3.19 Å, respectively. Matlockite compounds are characterized by a stable layered framework formed by the coordination of each O^{2-} anion to four equivalent Bi^{3+} atoms to form a mixture of corner and edge-sharing OBi_4 tetrahedra. The Br^{1-} anion is four-fold coordinated and bonds to four equivalent atoms of Bi^{3+}. The structural properties were evaluated with the help of the optimized lattice parameters (a, b, and c) that determine the size of the unit cell and the arrangement of atoms in the BiBrO crystal structure [24].

Accurate simulation models for BiBrO electronic and thermal as well as optical characteristics require an precise descriptions of its geometric features including unit cell dimensions, lattice and bond length parameters. Geometric variation factors produce substantial effects on both electronic band structure together with phonon dispersion and optical response. After fully relaxed structure. The best lattice values are $a = 3.93$Å, $b = 3.93,$Å which proves the tetragonal symmetry in the plane. To avoid unwanted interlayer interactions in the two-dimensional model, a vacuum gap of $c = 8.39$ Å was added along the out-of-plane direction, their description outlines how atoms are arranged within a unit cell structure. The physical properties of the BiBrO are evaluated using relaxation structure-parameters. The observed results matched previously recorded data [25, 26].

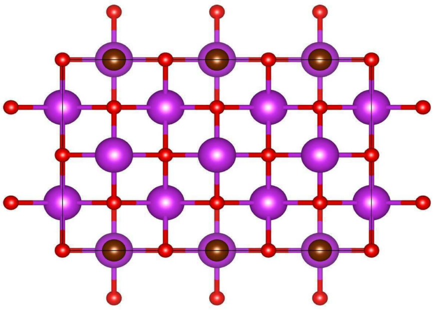

Top view

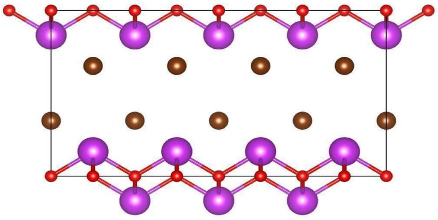

Side view

Figure 1. 2D BiBrO structure is shown from the top view (upper panel) and side view (lower panel).

3.2. Stability

Multiple approaches are used to investigate the stability of the BiBrO structure, including calculating formation energy and executing molecular dynamics simulations in combination with phonon dispersion analysis. An important thermodynamic quantity called formation energy (E_f) measures changes in energy during the process of creating compounds from their most stable standard state elements. When the formation energy becomes negative it indicates that the material's creation process remains energetically stable. Finding positive formation energy means decreased thermodynamic stability and increased disposition to decompose the material [27]. The study of BiBrO indicates stable structure due to its negative energy (-1.63 eV at a = 3.85Å), as is illustrated in Fig. 2(a).

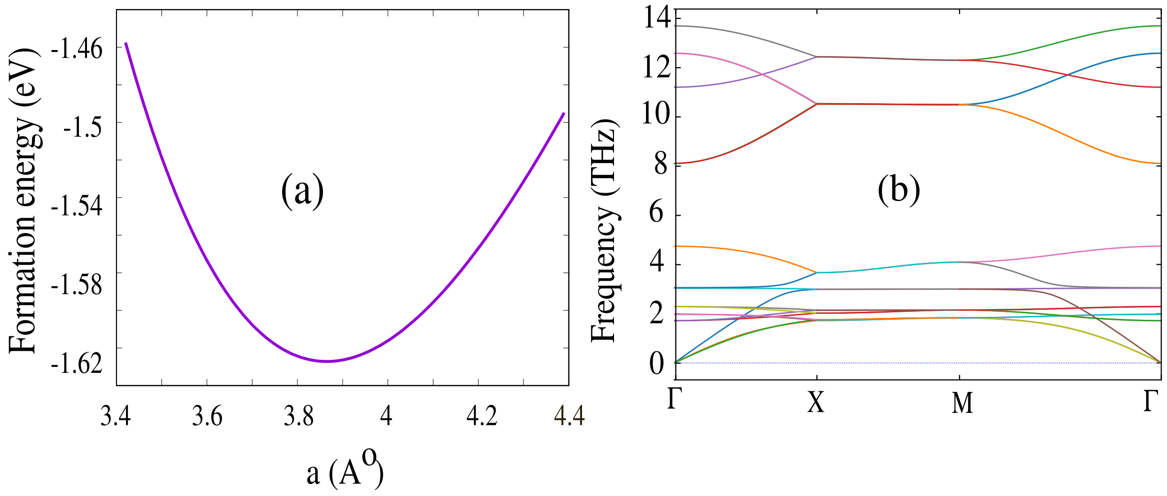

Figure 2. "Formation energy of 2D BiBrO as a function of its lattice constant (a), Phonon dispersion curve of 2D BiBrO(b).

The Fig. 3 presents the findings of the AIMD simulation that studied the thermal stability of 2D BiBrO at 300 K. The simulation duration consisted of 5 ps at each 1.0 fs time step. The temperature pattern varies minimally during the simulation because heat transport inside the 2D BiBrO structure is restricted at that temperature. Results from these simulated normal environmental assessments is shown that the structure maintained a stable state. The testing revealed neither substantial damage nor bond disruption to the structural makeup. The energy fluctuations per atom shown in Fig. 3(b) confirm this observation by staying under 0.17 Ry, which matches other reported DFT studies.

The simulation results confirm that no major energetic changes took place inside the BiBrO system during the computational period. The lack of observable structure deformation exists at each time step indicating varying temperature points [23, 28, 29].

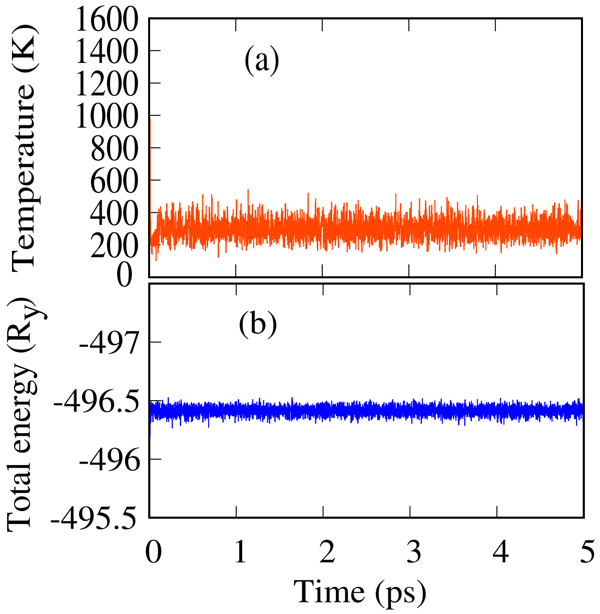

Figure 3. AIMD simulation for 2D BiBrO,(a) temperature,(b) total energy, as a function of time.

The frequencies of phonons identify key characteristics about material stability and physical behavior. Studying phonon dispersion is critical for understanding basic macroscopic properties of materials, such as their specific heat and thermal expansion responses. Phonon modes whose frequencies fall within the lower range are known as soft modes which have direct links to structural phase transitions, while the inspection of Fig. 2(b) demonstrates that BiBrO exhibits dynamic stability by showing no formation of imaginary phonon modes throughout the Brillouin zone which proves its resistance to spontaneous lattice distortions. Both transverse acoustic and longitudinal acoustic phonon branches show linear dispersion near the Γ point which defines the stable crystalline material behavior for sound wave propagation through the lattice. The flexural acoustic phonon branch has a parabolic form around the Γ point, indicating two-dimensional shapes material characteristics. The identical phonon dispersion pattern occurs routinely in other 2D materials such as graphene alongside transition metal dichalcogenides. The analysis of phonon dispersion shows that BiBrO acoustic branch frequencies stay below 2 THz which produces values much lower than h-BN and other two-dimensional materials.Due to the low frequencies and present heavy atoms (Bi and Br). This causes BiBrO naturally an inefficient heat conductor, therefore it may be used as insulation material [30–32]

3.3. Electronic properties

We first analyzed BiBrO's thermal stability. Then, we computed the electronic properties of BiBrO. It is mostly determined by the band structure and (PDOS) throughout the chosen path Γ→X→M→Γ. PDOS and bandstructure are related to the same energy level with the energy of Fermi set to be zero, they are depicted in Fig. 4 and Fig. 5. The electronic band structure of BiBrO shows that its valence band maximum (VBM) appears near the M point and its conduction band minimum (CBM) exists at the Γ point. Bandgap indirect behavior is confirmed by the VBM and CBM regions showing spatial separation as this reveals a momentum-changing electron transition between valence and conduction bands. Knowledge about this behavior stands essential for optical characterization because it influences how electrons interact with light. The calculated energy bandgap of 2.42 eV in Fig. 4 might be underestimated since the study uses GGA-PBE approach. The calculated 2.42 eV bandgap operates within the spectrum of visible light, which stands crucial for solar energy applications. The material exhibits a unique quality that makes it desirable for photovoltaic uses [33, 34].

BiBrO shows a non-flat band structure indicating that electrons display substantial dispersion together with non-localization across energy levels when momentum changes. Across the Brillouin zone, the band edges fail to match in alignment, which results in the formation of non-flat band structures. The change in energy level positions occurs as momentum shifts through the bands, the hybridization of atomic orbitals together with complex bonding relationships between Bi, Br, and O elements produces this variation. Lower BiBrO symmetry causes increased energy band dispersion through diminished degenerate energy states which generates extensive band gaps. The crystal structure demonstrates incomplete symmetry characteristics because of structural imperfections [35, 36].

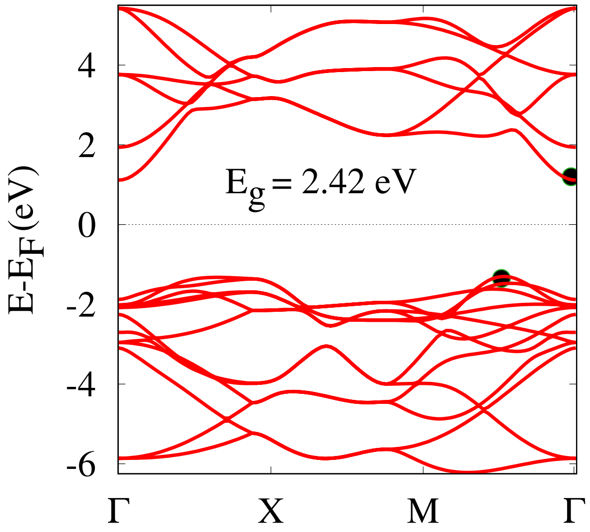

Figure 4. Electron band structure of 2D BiBrO with the Fermi energy referenced to zero.

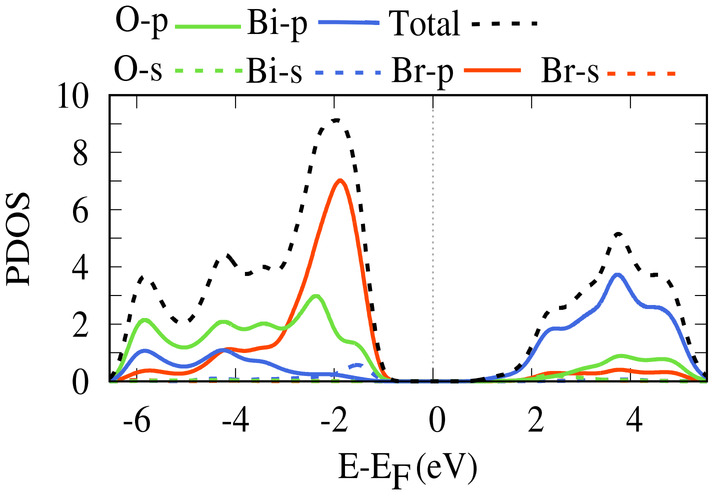

Figure 5. Total and (PDOS) of 2D BiBrO structure.

The (PDOS) analysis investigated orbital participation from each constituent atom across a -6.25 to 5.5 eV energy range of the band structure. The graphical representation of this analysis shown in Fig. 5 provides critical understanding of the bonding features in the material. The valence band predominantly contains Br-p orbitals because of extensive atomic interactions throughout the bismuth-oxygen-bromine system which produce an ionic bond framework. Bi-p orbitals contribute extensively to electronic as well as optical properties in the CB phase of BiBrO. The substantial electronic character gap between Br, Bi and O elements proves the ionic nature of BiBrO bonding. The material exhibits a band gap spanning (-1 to 1.4) eV leads to zero PDOS because electronic states are not allowed during this interval.

The PDOS study reveals that the Bi-p and Br-p orbitals, that involved in the interaction, remain mainly different. This implies that there is minimal hybridization of these orbitals, confirming that the interaction between bismuth and bromine remains primarily ionic or weakly covalent in nature. The separate orbitals function independently while avoiding mixing so they maintain their original characteristics which results in localized states distribtion. Cl-p orbitals have a smaller PDOS peak than Br-p orbitals, indicating that Br participates substantially more to the bond-intraction within the investigated energy range. This implies that Br-p orbitals are more delocalized or actively engaged in the electronic structure, while Cl-p orbitals might seem more localized or only partially participating in bonding interactions. The interactions among these orbitals, as well as the spatial configuration of atoms, result in diverse contributions to the levels of energy at various k-points in the Brillouin zone. The BiBrO structure exhibits an indirect band gap due to the appearance of the VBM and CBM along the M-Γ route [37]

3.4. Optical characteristics

This section discusses the optical characteristics of 2D BiBrO, with an emphasis on essential parameters such the dielectric function,ε, absorption coefficient,α, and optical conductivity σ. These values are computed using the Random

Phase Approximation (RPA) method on the Brillouin zone with a tighter k-point grid across the energy range 0 to 10 eV. These characteristics explain how the material reacts to incident electromagnetic spectrum and are essential for determining its optical applications such as solar energy harvesting. The dielectric response changes with the energy of photons through electric fields applied both parallel (E_x) and perpendicular (E_z) as seen in Fig. 6. The results from both x and y-polarized electric field testing show similar which demonstrate symmetry optical behavior of BiBrO. The material generates dissimilar polarization patterns along the x-axis and z-axis because of its lowest anisotropic structure [38, 39].

The real part Re(ε) is the active component related to the response of structures to electrical energy storage. The static dielectric constants at the energy of a zero photon are 5.8 for E_x and 6.9 for E_z. This implies that BiBrO has a high polarisation behaviour, which indicates that it is easily polarizable, given that its constituent atoms are relatively less sensitive to external electric fields. Around 3 eV the material exhibits its highest optical response and therefore shows relatively high dielectric values because of the limited anomalous dispersion at this energy, in agreement with the Kramers–Kronig relations. This would mean high potential for energy storage in electricity. Around 5 eV, the material enters a plasmonic regime defined by the negative value of the Re (ε) due to the presence of collective oscillations of electrons. This is where the material no longer accommodates propagating waves, highlighting its potential for plasmonic uses [40, 41].

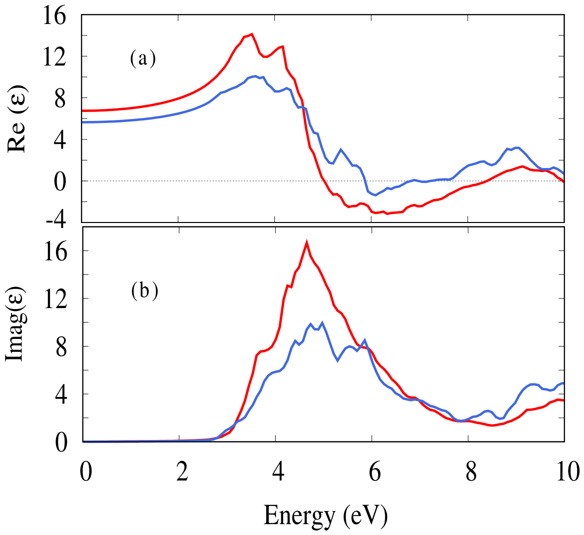

Figure 6. Re (ε) (a) and imag (ε) (b) parts of the dielectric function of 2D BiBrO under external electric fields applied parallel (E_x, red) and perpendicular (E_z, blue) to the plane.

The imag (ε) of the dielectric has a different response to various frequencies (viewed in Fig. 6,(b)). Imag(ε) reflects the material's ability to absorb energy. Its absence in the 0–2.41eV range suggests that the optical bandgap, which is consistent with the electronic bandgap. Significant peaks at high energies are indicative of the presence of interband transitions and a high joint density of states in these areas of frequencies. Imag(ε), the imaginary portion of the dielectric function, is linked to the material's shielding electromagnetic radiation capabilities via screening processes. Shielding efficiency enhances with higher Imag(ε), whereas lower Imag(ε) values result in poorer shielding. Surprisingly, the two absorption and screening performance are strongly correlated with the material's electronic structure and optical response. For both field orientations, both the real and imaginary parts of the dielectric function exhibit the same increasing tendency from visible region to deep UV region. Such behaviour indicates that the material is a good candidate for energy storage and UV photo detector application [24, 42].

Optical conductivity, σ, measures the ability of a material to transport electric currents when a material is exposed to an optical field. The optical conductivity has pronounced variation with photon energy as can be seen in Fig. 7. One important observation is that the optical conductivity σ is essentially zero in the energy range from (0 to 2.41) eV owing to a limited number of electronic states capable of taking part in optical transitions, Also, it can be described as the optical band gap. Over this threshold, there is a steep rise in the optical conductivity level which is indicative of quick onset of inter band transitions. This is a typical property of a wide band-gap semiconductor in which much energy is necessary to move electrons from the valence band to the conduction band. The photon energy which exceeds the band gap plays an important role in deciding the overall transition strength and the participation of most interband transitions. This data provides an insight into the patterns of the charge transport, the knowledge that is needed by the developers for the generation of the solar energy as well as the photodetectors, and also for the design of the optoelectronic systems [43, 44]

The way light travels through a substance is described by the dimensionless refractive index (n). It affects the dispersion of various wavelengths and establishes the phase velocity of light in the medium. The way the refractive index behaves, as seen in Fig. 7, gives insight into how electromagnetic waves interact with the material's electronic structure, especially how light is bent and slowed as it travels through. At zero photon energy, the material's stationary refractive index (n) is 2.56 which pointed to a significant response to external electric field. Initially the refractive index increases slightly as photon energy increases where in other words is a drop in phase velocity of light. This tendency is typical of normal dispersion in transparent zones. However at about 4 eV the refractive index gradually decreases, this drop is related to the photon energy surpassing the material's band gap, resulting in increasing absorption and eventually saturation, which decreases the material's capacity to further slow down light [45, 46].

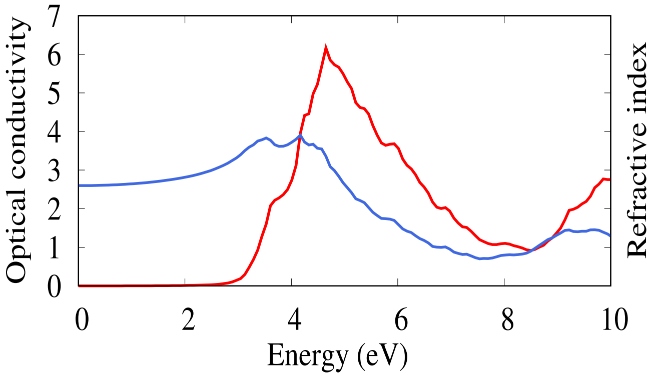

Figure 7. Optical conductivity (red) and Refractive index (blue) of 2D BiBrO in external electric field.

The absorption coefficient,α, defines the capability of a material to absorb photons depending on the photon energy (see Fig. 8). In extremely low photon energies, α is almost null because photons lack sufficient energy to spark electrons out of the VB to the CB. As the energy of photons approaches the band gap, α dramatically goes up, corresponding to a rise in Im(ε) owing to greater interband transitions, suggesting the start of substantial light-matter interaction. The capability to sense light from visible to Ultraviolet range as indicated by the absorption curve, is essential for opto-device applications. BiBrO exhibits intense absorption in the visible and deep-UV region, which suggests that it can serve as a highly effective light harvester and converter for a large range of light producing electricity. The absorption coefficient can therefore fall at very large photon energies, either because of a diminished joint density of states or because the transitions over step to the primary absorption edges themselves. Also, many-body effects, excitonic interactions and phonon scattering may affect on the absorption behavior but their roles are stronger in near the band edge and weaker at high energy [47].

The reflectivity of BiBrO is displayed in Fig. 8. From 0.0 eV to 2.8 eV, the reflectivity has a value of nearly 19%. At low photon energies (below the band gap), the free-electron dielectric response is weak. This means the material doesn't effectively reflect light, leading to very low reflectivity in that range. As photon energy increases above the band gap, reflectivity rises-potentially reaching values as high as 41% on average. This is because electrons can oscillate more strongly in response to the light. The reflectivity can be reduced to levels almost reaching zero at hight frequency. At this photon energy, the incident light is extremely transparent through it, as reflection is suppressed and absorption is negligible. Provided that this happens at around 8 eV, the material would effectively look transparent in that very limited ultraviolet wavelength. From this analysis, this material can be used as shielding in the UV range [48, 49].

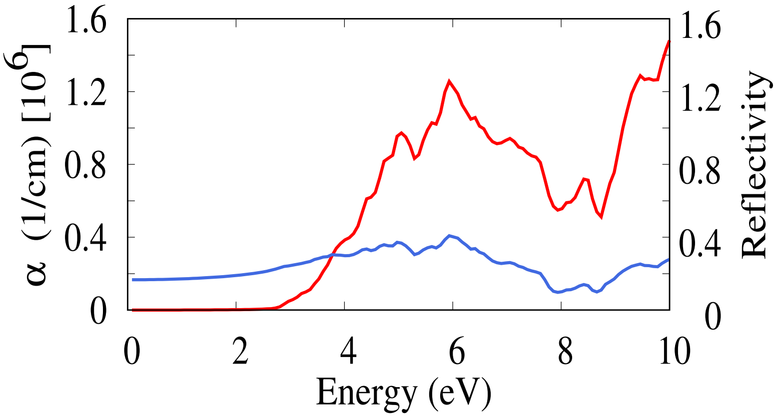

Figure 8. The absorption coefficient,α, (red) and reflectivity (blue) of BiBrO in external electric field.

3.5. Thermal properties

After verifying thermal stability. At intermediate high temperature ranges, we analyze BiBrO's thermal properties through temperature-dependent measurements of heat capacity C_V, entropy and phonon density of state which are displayed in Fig. 9, Fig. 10. The heat capacity of a substance is defined as the ratio of heat absorbed to temperature change. Entropy measures a number of possible microscopic arrangements of the system and this is measured by entropy. The graph shows how a material's heat capacity and entropy vary with temperature (red and blue lines, respectively). At lower temperatures, both heat capacity and entropy gradually rise because the number of low energy vibrational states grows, according to quantum statistics. The C_V shows a distinct plateau from 300-1000 K, suggesting that the thermal energy needed to increase the temperature becomes almost independent of temperature. This behavior indicates that BiBrO is approaching the classical Dulong-Petit limit, where most lattice vibrational modes become fully thermally activated. As a result, further increases in temperature do not significantly enhance the phonon contribution to the heat capacity, which reflects the saturation of vibrational degrees of freedom. At 1000 K the value of C_V is 24.66J.K.mol per atom, nearly close to the Dulong-Petit limit as the phonon modes become mostly completely saturated [45].

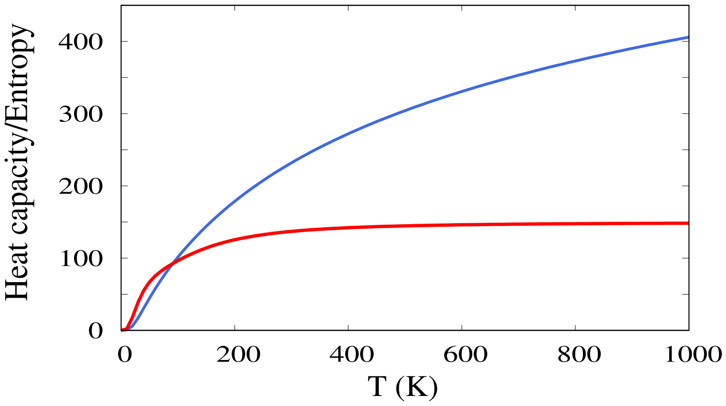

Figure 9. Capacity of heat(red) and entropy (blue) as a function of temperature of BiBrO.

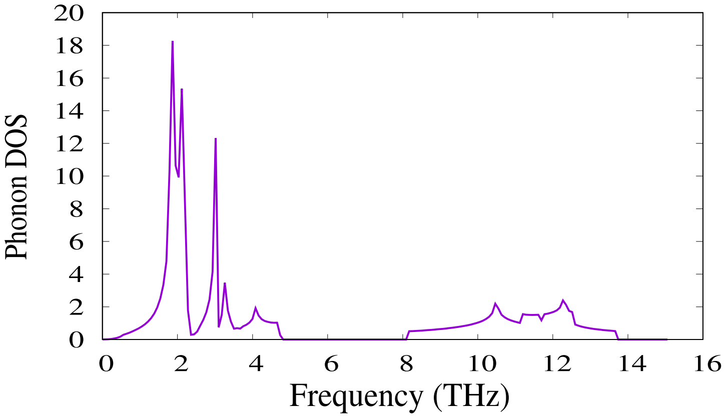

Figure 10. Calculate Phonon DOS of BiBrO.

Much like the blue curve of entropy, the entropy curve is rising with temperature but the rate of increase slows at high temperatures as the system gains more thermal energy, and the system is approaching maximum disorder. This is in line with the third law of thermodynamics.

As temperature approaches absolute zero, entropy tends to a finite constant (often zero for a perfect crystal), consistent with the Third Law of Thermodynamics, while the heat capacity vanishes because quantum mechanics restricts thermal excitations-only the ground state remains populated, leaving no accessible energy states to absorb heat. Conclude, the propagation of phonon, the major heat carriers in BiBrO material, is interrupted by the temperature induced disorder. Phonons are essentially vibrations of atoms in the material which are quantized. In the case of well-ordered atomic arrangement, These vibrations may effectively propagate through the lattice and thermal energy may be propagated. In a more disordered form, however, as is found in BiBrO at higher temperatures, the disordered atomic sites serve as scattering centres of phonon. These collisions can frequently hinder the natural propagation of vibrations, which in turn retard their effectiveness as a means of the transportation of heat. The outcome influences the thermal conductivity of BiBro in future. [**?**,50,51].

The Fig. 10 illustrates the phonon density of states. The phonon(DOS) of BiBrO shows that there are sharp and large concentrations of vibration modes in the low-frequency part of the spectrum (1-4 THz), and then a clear phononic gap and a set of weaker high-frequency modes, extending between about 8.1 and 13 THz. The heavy atomic masses of Bi and Br can explain the dominance of low-frequency vibrations by reducing vibrational frequencies based on the lattice dynamical principles $\omega \propto \sqrt{\frac{k}{m}}$, therefore, increasing the contribution of acoustic and low-energy optical phonons. The division of the low and high-frequency space points to the decoupling of the lattice dynamics, where the higher-frequency modes are probably related to the lightest vibrations involving oxygen and the tightest bond strength. Dynamical stability of the crystal structure can be established by the absence of imaginary frequencies. A bimodal phonon distribution is an indicator of constrained phonon group velocities and increased phonon scattering, which can be of benefit in lowering the thermal conductivity of the lattice, and thus make the material potentially useful in thermoelectric and thermal insulation [52,53].

Lattice thermal conductivity is a measure of the efficiency of the heat conduction through a substance owing to lattice vibration, specifically phonons. Phonons are the main carriers of thermal energy in semiconductors and insulators, as display in Fig. 11(a) [54]. At a temperature of 200K, the lattice usually reaches a maximum of 4.4 W/m.K, this is because the phonon population rises due to normal phonon scattering (N-process) and does not disrupt heat flow much, as well as because of the high group velocity. At elevated temperatures, a significant portion of the thermal energy is carried by high-frequency phonons, which become increasingly active, and the Umklapp scattering (U-process) dominates, phonons interact strongly and lose momentum, which reduces their capacity in conducting heat. Conductivity of heat is consequently lowered [55]. Studies indicate that phonons significantly affect the transfer of heat in various 2D layer material, as demonstrated by research on other 2D layer sructure. [56, 57]. The BiBrO exhibits weak lattice thermal conductivity, which is attributed to the material properties that limit the phonon transport. Due to the presence of the heavy Bi element, atom vibrations occur at very slow rates, ensuring that group phonon velocities are reduced. This leads to reduced efficiency in the transport of heat. In short, BiBrO has a moderate heat capacity poor thermal conductivity of the lattice, rendering it a good thermal insulator.

Thermal transport is governed by the group velocity because the lattice thermal conductivity is proportional to the product of the phonon group velocity and the heat capacity. When the temperature rises, the lattice becomes softer, and as a result, the group velocity of phonons reduces, leading to lower lattice thermal conductivity, the trend of this behavior is reflected well based on the trends observed in BiBrO material, as can be seen in Fig. 11 [58,59]. Phonon group velocities are large in the low-frequency regime (acoustic), indicating a fast propagation of the respective vibrational modes inside the BiBrO structure, which corresponds well to the speed of sound in the material. Conversely, at frequencies between (1-2) THz, the phonon group velocity remains mostly constant. This indicates that vibrational speeds stay relatively steady or increase gradually in this high-frequency range, the atoms participate in highly localized 'rattling' motions. The energy remains trapped there temporarily, which reduces thermal conductivity. Overall, the thermal properties of BiBrO make it an interesting candidate in many thermal management applications, especially when heat absorption and insulation play the most crucial role.

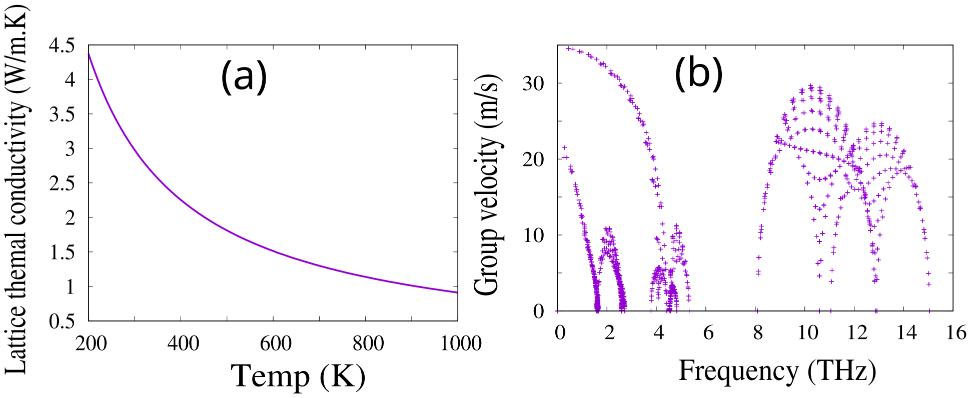

Figure 11. Lattice thermal conductivity (a),and Group velocity (b) in 2D BiBrO .

4. CONCLUSIONS

This study provides a thorough first-principles investigation of BiBrO's structural, stability, electronic characteristics, lattice dynamics, thermal stability, and optical characteristics. According to the band structure calculation, the material has an indirect band gap of 2.42 eV, making it suitable for usage as a semiconductor. The lattice dynamical analysis demonstrates that there do not exist imaginary phonon frequency, and AIMD calculation prove that the structure remains stable under thermal condition, showing good dynamical and thermal stability. The considerable contribution of low-frequency vibrational modes in the phonon density of states suggests that lattice vibrations are efficiently dispersed and dissipated, resulting in increased material stability. In addition to these properties, the high optical response in the visible and ultraviolet regions along with the high absorption coefficient highlights its significant potential in the application in solar energy collection and optoelectronics. BiBrO exhibits excellent heat capacity, which is (24.66 J/K.mol per atom). As a result, the heat capacity remains reach the Dulong-Petit limit even at moderate temperatures. BiBrO's comparatively low lattice thermal conductivity implies that it is a good thermal insulator, since lower phonon-mediated heat transfer improves its capacity to inhibit thermal diffusion. We discovered that the BiBrO has numerous applications in significant domains like as solar energy, energy conversion and thermal management applications.

5. ACKNOWLEDGMENT

The University of Sulaimani provided assistance for this research. The Computational Science Laboratory, Research and Development Center, University of Sulaimani, provided computational resources.

ORCID

Yadgar Hussein Shwan, https://orcid.org/0000-0002-0020-253X

REFERENCES

[1] D. Golberg, Y. Bando, Y. Huang, T. Terao, M. Mitome, C. Tang, and C. Zhi, "Boron nitride nanotubes and nanosheets," ACS nano, **4**(6), 2979-2993 (2010). https://doi.org/10.1021/nn1006495

[2] N. R. Abdullah, B. J. Abdullah, and V. Gudmundsson, "Modeling the electronic, phonon, magnetic, thermal, mechanical, and optical properties of a hybrid B3C2N3 nanosheet in the context of a bc6n single layer," Materials Science in Semiconductor Processing, **180**, 108581 (2024). https://doi.org/10.1016/j.mssp.2024.108581

[3] A. V. Kretinin, Y. Cao, J.-S. Tu, G. Yu, R. Jalil, K. S. Novoselov, S. J. Haigh, *et al.*, "Electronic properties of graphene encapsulated with different two-dimensional atomic crystals," Nano letters, **14**(6), 3270-3276 (2014). https://doi.org/10.1021/nl5006542

[4] P. Avouris, "Graphene: electronic and photonic properties and devices," Nano letters, **10**(11), 4285–4294 (2010). https://doi.org/10.1021/nl102824h

[5] P. Miró, M. Audiffred, and T. Heine, "An atlas of two-dimensional materials," Chemical Society Reviews, **43**(18), 6537–6554 (2014). https://doi.org/10.1039/C4CS00102H

[6] M. Xu, T. Liang, M. Shi, and H. Chen, "Graphene-like two-dimensional materials," Chemical reviews, **113**(5), 3766-3798 (2013). https://doi.org/10.1021/cr300263a

[7] D. Deng, K. Novoselov, Q. Fu, N. Zheng, Z. Tian, and X. Bao, "Catalysis with two-dimensional materials and their heterostructures," Nature nanotechnology, **11**(3), 218–230 (2016). https://doi.org/10.1038/nnano.2015.340

[8] Q. H. Wang, K. Kalantar-Zadeh, A. Kis, J. N. Coleman,and M. S. Strano, "Electronics and optoelectronics of two-dimensional transition metal dichalcogenides," Nature nanotechnology, **7**(11), 699–712 (2012). https://doi.org/10.1038/nnano.2012.193

[9] J. He, S. Ma, P. Lyu, and P. Nachtigall, "Unusual Dirac half-metallicity with intrinsic ferromagnetism in vanadium trihalide monolayers," Journal of Materials Chemistry C, **4**(13), 2518-2526 (2016). https://doi.org/10.1039/C6TC00409A

[10] W.-B. Zhang, L.-J. Xiang, and H.-B. Li, "Theoretical perspective of energy harvesting properties of atomically thin BiI 3," Journal of Materials Chemistry A, **4**(48), 19086–19094 (2016). https://doi.org/10.1039/C6TA06806E

[11] N. F. Coutinho, R. B. Merlo, N. F. Borrero, and F. C. Marques, "Thermal evaporated bismuth triiodide (BiI3) thin films for photovoltaic applications," MRS advances, **3**(55), 3233–3236 (2018). https://doi.org/10.1557/adv.2018.405

[12] Q. Wei, J. Chen, P. Ding, B. Shen, J. Yin, F. Xu, Y. Xia, and Z. Liu, "Synthesis of easily transferred 2D layered BiI3 nanoplates for flexible visible-light photodetectors," ACS applied materials & interfaces, **10**(25), 21527–21533 (2018). https://doi.org/10.1021/acsami.8b02582

[13] F. Ma, M. Zhou, Y. Jiao, G. Gao, Y. Gu, A. Bilic, Z. Chen, and A. Du, "Single layer bismuth iodide: computational exploration of structural, electrical, mechanical and optical properties," Scientific reports, **5**(1), 17558 (2015). https://doi.org/10.1038/srep17558

[14] Y. Zhang, P. Zhang, Y. Lan, L. Zhang, J. Yan, and X. Su, "Bismuth oxybromide photocatalysts for CO_2 reduction: modification methods, bottlenecks, and optimization strategies," Chemical Communications, **62**(2), 2877-2895 (2026). https://doi.org/10.1039/d5cc06774j

[15] I. H. Sabuj, Q. S. Hossain, S. S. Nishat, S. A. Jahan, M. Khan, U. S. Akhtar, M. S. Bashar, *et al.*, "Experimental and theoretical exploration of bismuth oxyhalide (BiOX, X= Cl, Br, I) nanoparticles in thermoelectric, optoelectronic, and photocatalytic applications," RSC advances, **16**(4), 3648–3661 (2026). https://doi.org/10.1039/D5RA07838E

[16] J. Zhang, Y. Liu, S. Xin, S. Lin, X. Zhang, J. Wang, X. Guo, *et al.*, "First-principles study of the effect of Bi content on the photocatalytic performance of bismuth bromide oxide-based catalysts," Physical Chemistry Chemical Physics, **27**, 3612-3621 (2025). https://doi.org/10.1039/D4CP04044A

[17] H. Fjellvåg, and P. Karen, "Crystal structure of $ScCl_3$ Refined from Powder Neutron Diffraction Data," Acta Chemica Scandinavica, **48**, 294–297 (1994). https://doi.org/10.3891/acta.chem.scand.48-0294

[18] X. Zhang, B. Li, J. Wang, Y. Yuan, Q. Zhang, Z. Gao, L.-M. Liu, and L. Chen, "The stabilities and electronic structures of single-layer bismuth oxyhalides for photocatalytic water splitting," Physical Chemistry Chemical Physics, **16**(47), 25854–25861 (2014). https://doi.org/10.1039/C4CP03166K

[19] A. Darmawan, E. Suprayoga, A. A. AlShaikhi, and A. R. Nugraha, "Thermoelectric properties of two-dimensional materials with combination of linear and nonlinear band structures," Materials Today Communications, **33**, 104596 (2022). https://doi.org/10.1016/j.mtcomm.2022.104596

[20] Y. H. Shwan, M. A. Ameen, A. S. Mahmood, DFT Study of the Stability, Electronic, Optical, and Thermal Properties of Two-Dimensional $BiBr_3$ Semiconductor, East European Journal of Physics (1) (2026) 191–202. https://doi.org/10.26565/2312-4334-2026-1-19

[21] P. Giannozzi, S. Baroni, N. Bonini, M. Calandra, R. Car, C. Cavazzoni, D. Ceresoli, *et al.*, "Quantum espresso: a modular and open-source software project for quantumsimulations of materials," Journal of physics: Condensed matter B, **39**, 395502 (2009). https://doi.org/10.1088/0953-8984/21/39/395502

[22] A. Togo, and I. Tanaka, "First principles phonon calculations in materials science," Scripta Materialia, **108**, 1–5 (2015). https://doi.org/10.1016/j.scriptamat.2015.07.021

[23] J. P. Perdew, K. Burke, and M. Ernzerhof, "Generalized gradient approximation made simple," Physical review letters, **77**(18), 3865 (1996). https://doi.org/10.1103/physrevlett.77.3865

[24] Z.-Y. Zhao, Q.-L. Liu, and W.-W. Dai, "Structural, electronic and optical properties of $BiOX_{1-x}Y_x$ (X, Y= F, Cl, Br and I) solid solutions from DFT calculations," Scientific reports, **6**(1), 31449 (2016). https://doi.org/10.1038/srep31449

[25] X. He, Y. Wu, S. Liu, W. He, S. Li, G. Huo, L. Jiang, Y. Kapitonov, *et al.*, "Large-scale ultrastable 2D inorganic molecular crystal $BiBr_3$ and heterostructures with superior photoluminescence enhancement," Advanced Functional Materials, **34**(39), 2403273 (2024). https://doi.org/10.1002/adfm.202403273

[26] W.-T. Ouyang, H.-T. Ji, Y.-Y. Liu, T. Li, Y.-F. Jiang, Y.-H. Lu, J. Jiang, and W.-M. He, "Tempo/O_2 synergistically mediated bibro-photocatalyzed decarboxylative phosphorylation of n-arylglycines," Chemistry–A European Journal, **30**(41), e202304234 (2024). https://doi.org/10.1002/chem.202304234

[27] A. Jehan, M. Husain, S. Bibi, N. Rahman, V. Tirth, A. Azzouz-Rached, M. Y. Khan, *et al.*, "Insight into the structural, optoelectronic, and elastic properties of AuXF3 (X= Ca, Sr) fluoroperovskites: Dft study, Optical and Quantum Electronics, **55**(14), 1242 (2023). https://doi.org/10.1007/s11082-023-05394-4

[28] H. van Gog, W.-F. Li, C. Fang, R. S. Koster, M. Dijkstra, and M. van Huis, "Thermal stability and electronic and magnetic properties of atomically thin 2D transition metal oxides," NPJ 2D Materials and Applications, **3**(1), 18 (2019). https://doi.org/10.1038/s41699-019-0100-z

[29] Y. H. Shwan, M. A. Ameen, and A. S. Mahmood, "DFT study of electronic, optical, and thermodynamic properties of the 2D shape of Bi_44O_6 structure," Solid State Communications, **404**, 116095 (2025). https://doi.org/10.1016/j.ssc.2025.116095

[30] N. R. Abdullah, B. J. Abdullah, Y. H. Azeez, and V. Gudmundsson, "Exploring electronic, optical, and phononic properties of MgX (X= C, N, and O) monolayers using first principle calculations," arXiv preprint arXiv:2307.11041 (2023). https://arxiv.org/pdf/2307.11041

[31] Z. Zhang, Y. Xie, Y. Ouyang, and Y. Chen, "A systematic investigation of thermal conductivities of transition metal dichalcogenides," International Journal of Heat and Mass Transfer, **108**, 417–422 (2017). https://doi.org/10.1016/j.ijheatmasstransfer.2016.12.041

[32] T. Gunst, T. Markussen, K. Stokbro, and M. Brandbyge, "First-principles method for electron-phonon coupling and electron mobility: Applications to two-dimensional materials," Physical Review B, **93**(3), 035414 (2016). https://doi.org/10.1103/PhysRevB.93.035414

[33] N. R. Abdullah, B. J. Abdullah, and V. Gudmundsson, "DFT study of tunable electronic, magnetic, thermal, and optical properties of a Ga_2Si_6 monolayer," Solid State Sciences, **125**, 106835 (2022). https://doi.org/10.1016/j.solidstatesciences.2022.106835

[34] R. Arora, A. R. Barr, D. T. Larson, M. Pizzochero, and E. Kaxiras, "Engineering interfacial charge transfer through modulation doping for 2D electronics," Physical Review Materials, **9**(2), L021601 (2025). https://doi.org/10.1103/PhysRevMaterials.9.L021601

[35] J. Xie, Z. Zhang, D. Yang, D. Xue, and M. Si, "Theoretical prediction of carrier mobility in few-layer BC_2N," The Journal of Physical Chemistry Letters, **5**(23), 4073–4077 (2014). https://doi.org/10.1021/jz502006z

[36] J.-C. Tung, C.-H. Lee, P.-L. Liu, and Y.-K. Wang, "Electronic band structures of the possible topological insulator pb2bibro6 and pb2seteo6 double perovskite: An ab initio study," Applied Sciences, **12**(12), 5913 (2022). https://doi.org/10.3390/app12125913

[37] N. R. Abdullah, H. G. Hussein, and V. Gudmundsson, "Controlling electronic, magnetic, thermal, and optical properties of boron-nitrogen codoped strontium oxide monolayer: Activation of optical transitions in the vl region," arXiv preprint arXiv:2307.09173 (2023). https://arxiv.org/pdf/2307.09173

[38] S. Qi, Y. Zhang, R. Zhang, X. Liu, and H. Xu, "First-principles and experiment investigation of bi2o3/bi2wo6 heterojunctions," Colloid and Interface Science Communications, **44**, 100502 (2021). https://doi.org/10.1016/j.colcom.2021.100502

[39] T. L. Wakjira, K. Tadele, A. B. Gemta, and G. B. Kassahun, "Effect of tin doping and tin-bromine co-doping on electronic and optical properties of biocl crystal: density functional theory," Materials Research Express, **11**(6), 065903 (2024). https://doi.org/10.1088/2053-1591/ad549c

[40] W. L. Huang, "Electronic structures and optical properties of BiOX (X = F, Cl, Br, I) via DFT calculations," Journal of computational chemistry, **30**(12), 1882–1891 (2009). https://doi.org/10.1002/jcc.21191

[41] Y. H. Shwan, B. N. Ghafoor, and G. H. Hamasalih, "Optimization of surface plasmon resonance (spr) for gold/air interface by using kretschmann configuration," Engineering and Technology Journal, **40**(10), 1334-1341 (2022). https://doi.org/10.30684/etj.2022.132902.1151

[42] M. Barhoumi, and M. Said, "Electronic and optical properties of bismuth oxyhalides from ab initio calculations," Materials Science and Engineering: B, **264**, 114921 (2021). https://doi.org/10.1016/j.mseb.2020.114921

[43] M. Fang, Z. Wang, H. Gu, B. Song, Z. Guo, J. Zhu, X. Chen, *et al.*, "Complex optical conductivity of Bi_2Se_3 thin film: Approaching two-dimensional limit," Applied Physics Letters, **118**(19), (2021). https://doi.org/10.1063/5.0049170

[44] L. Chhana, B. Lalroliana, R. C. Tiwari, B. Chettri, D. P. Rai, L. Vanchhawng, L. Zuala, and R. Madaka, "Strain-modulated electronic and optical properties of monolayer and bilayer CdS: A DFT study," Journal of Electronic Materials, **51**(11), 6556–6567 (2022). https://doi.org/10.1007/s11664-022-09897-w

[45] T. L. Wakjira, K. Tadele, A. B. Gemta, and G. B. Kassahun, "Electronic, optical, phonon, and thermodynamic properties of bismuth oxyhalides for photocatalysis application using density functional theory," Discover Materials, **4**(1), 56 (2024). https://doi.org/10.1007/s43939-024-00131-4

[46] A. M. Ganose, M. Cuff, K. T. Butler, A. Walsh, and D. O. Scanlon, "Interplay of orbital and relativistic effects in bismuth oxyhalides: BiOF, BiOCl, BiOBr, and BiOI," Chemistry of materials, **28**(7), 1980–1984 (2016). https://doi.org/10.1021/acs.chemmater.6b00349

[47] A. Ghaleb, and A. Ahmed, "Structural, electronic, and optical properties of sphalerite zns compounds calculated using density functional theory (DFT)," Chalcogenide Letters, 19(5), 309-318 (2022). https://doi.org/10.15251/CL.2022.195.309

[48] V. Márta, Z. Pap, E. Bárdos, T. Gyulavári, G. Veréb, K. Hernadi, "Effect of urea as a shape-controlling agent on the properties of bismuth oxybromides," Catalysts, **13**(3), 616 (2023). https://doi.org/10.3390/catal13030616

[49] S. Praveen, S. Veeralingam, and S. Badhulika, "A flexible self-powered uv photodetector and optical uv filter based on β-$Bi_2O_3$3/$SnO_2$2 quantum dots schottky heterojunction," Advanced Materials Interfaces, **8**(15), 2100373 (2021). https://doi.org/10.1002/admi.202100373

[50] X. Tan, H. Shao, T. Hu, G. Liu, J. Jiang, and H. Jiang, "High thermoelectric performance in two-dimensional graphyne sheets predicted by first-principles calculations," Physical Chemistry Chemical Physics, **17**(35), 22872–22881 (2015). https://doi.org/10.1039/C5CP03466C

[51] Z.-X. Xie, L.-M. Tang, C.-N. Pan, Q. Chen, and K.-Q. Chen, "Ballistic thermoelectric properties in boron nitride nanoribbons," Journal of Applied Physics, **114**(14), 144311 (2013). https://doi.org/10.1063/1.4824750

[52] D. Singh, M. Sajjad, J. A. Larsson, and R. Ahuja, "Promising high-temperature thermoelectric response of bismuth oxybromide," Results in Physics, **19**, 103584 (2020). https://doi.org/10.1016/j.rinp.2020.103584

[53] Y. Li, J. Li, J. Tian, H. Liu, and J. Shi, "A first-principles study of 2d bi-based bioclbr, biocli, and biobri monolayers with ultralow lattice thermal conductivities for thermoelectric application," ACS Applied Nano Materials, **7**(13), 15086–15095 (2024). https://doi.org/10.1021/acsanm.4c01799

[54] J. J. Plata, P. Nath, D. Usanmaz, J. Carrete, C. Toher, M. de Jong, M. Asta, *et al.*, "An efficient and accurate framework for calculating lattice thermal conductivity of solids: Aflow-aapl automatic anharmonic phonon library," npj Computational Materials, **3**(1), 45 (2017). https://doi.org/10.1038/s41524-017-0046-7

[55] Y.-Y. Wu, Q. Wei, J. Zou, and H. Yang, "Ultra-low thermal conductivity and high thermoelectric performance of monolayer BiP_3: a first principles study," Physical Chemistry Chemical Physics, **23**(35), 19834–19840 (2021). https://doi.org/10.1039/d1cp01383a

[56] M. Markov, "Prediction of thermal conductivity and strategies for heat transport reduction in bismuth: an ab initio study," Ph.D. thesis, Université Paris Saclay (COmUE) (2016).

[57] M. Wang, and D. Han, "Thermal properties of 2d dirac materials MN_4 (M= Be and Mg): a first-principles study," ACS omega, **7**(12), 10812–10819 (2022). https://doi.org/10.1021/acsomega.2c00785

[58] Y. Luo, X. Yang, T. Feng, J. Wang, and X. Ruan, "Vibrational hierarchy leads to dual-phonon transport in low thermal conductivity crystals," Nature communications, **11**(1), 2554 (2020). https://doi.org/10.1038/s41467-020-16371-w

[59] A. Togo, "First-principles phonon calculations with phonopy and phono3py," Journal of the Physical Society of Japan, **92**(1), 012001 (2023). https://doi.org/10.7566/jpsj.92.012001

ПОГЛИБЛЕНЕ ДОСЛІДЖЕННЯ СТРУКТУРНИХ, СТАБІЛЬНИХ, ЕЛЕКТРОННИХ, ТЕРМОДИНАМІЧНИХ ТА ОПТИЧНИХ ХАРАКТЕРИСТИК ДВОВИМІРНОГО BiBrO НА ОСНОВІ ПЕРШОПРИНЦИПІВ

Ядгар Хуссейн Шван

Фізичний факультет, Коледж освіти, Університет Сулеймані, Сулейманія 46001, Курдистан, Ірак

Це дослідження використовує DFT в рамках GGA для проведення ретельного розрахунку стабільності, електронних властивостей, теплових характеристик та оптичних відгуків 2D BiBrO. Обчислена енергія утворення, разом з результатами розрахунку фононів та результатами AIMD, підтверджує стабільну структурну, динамічну та теплову стабільність системи BiBrO. 2D матеріал BiBrO демонструє напівпровідникову поведінку із забороненою зоною 2,42 еВ, що підтверджено аналізом електронної зонної структури. Аналіз оптичних властивостей BiBrO виявляє потужну взаємодію видимого та ультрафіолетового (УФ) світла, що підтверджує його застосування як пристрою накопичення сонячної енергії. Велика здатність BiBrO накопичувати теплову енергію зумовлена високою теплоємністю, оскільки BiBrO має більшу щільність фононних станів. Ентропія зростає пропорційно температурі, що означає додатковий атомний безлад і більш доступні мікроскопічні стани. Крім того, збільшення ентропії та плато теплоємності при високих температурах означають зміну до більш невпорядкованого стану, водночас забезпечуючи ефективне поглинання теплової енергії. Низька теплопровідність решітки та менша швидкість груп фононів BiBrO є характеристиками, які роблять матеріал корисним для теплоізоляції, зберігаючи при цьому структурну стабільність. Ці результати дають важливу інформацію щодо того, як BiBrO може бути використаний у системах накопичення енергії, а також як тепловий бар'єр.

Ключові слова: *2D BiBrO; DFT; електронні характеристики; теплопровідність решітки; оптичні характеристики; стабільність*

EAST EUROPEAN JOURNAL OF PHYSICS. **2.** 411-418 (2026)
DOI:10.26565/2312-4334-2026-2-45 ISSN 2312-4334

COMPREHENSIVE ANALYSIS OF MORPHOLOGY, STRUCTURE, AND PHOTOVOLTAIC PROPERTIES OF *CdTe* and *CdTe*:*In* THIN FILMS

Iftikhorjon I. Yulchiev*, Dadakhon Sh. Khidirov, Jaxongir S. Raximjonov, Muminjon M. Madraximov, Sherzod Sh. Abdullaev, Valijon T. Mirzayev
Fergana State Technical University, Fergana, Uzbekistan
**Corresponding Author e-mail: iftixorjon.yulchiyev@gmail.com*

Received March 3, 2026; revised April 9, 2026; accepted May 17, 2026

In this work, the photovoltaic properties and short-circuit current spectra of indium (In)-doped CdTe films were comprehensively investigated. The study covers the spectral sensitivity and light-absorption characteristics of undoped, freshly prepared, and thermally treated CdTe:In films. The effects of doping level and thermal treatment temperature on photovoltaic effect parameters were analyzed. The results showed that indium doping and subsequent thermal treatment significantly improve the photovoltaic efficiency of CdTe films. Using spectroscopic and electron microscopy methods, the chemical composition, surface morphology, and bandgap width of the films were determined, and their interrelation with optical and electrical properties was revealed. The obtained results indicate that $CdTe:In$ films are promising for applications in solar energy devices.

Keywords: CdTe:In *thin films; Photovoltaic effect; Short-circuit current spectra; Anomalous photovoltage (APV); Deep energy levels; Thermal treatment; Solar energy materials*
PACS: 61.05.cp, 68.55.-a, 73.50.Pz, 78.66.-w, 81.15.Ef, 84.60.Jt

INTRODUCTION

Thin-film semiconductor materials occupy an important place in modern optoelectronic and photovoltaic technologies. In this field, controlling the structural, optical, and electrical properties of materials is of decisive importance for improving the functional efficiency of devices. Cadmium telluride (CdTe) is widely studied as a promising semiconductor material due to its high light-absorption coefficient and suitable energy structure. Doping and post-deposition thermal treatment are important technological factors in modifying the properties of CdTe films. In particular, doping with indium (In) affects carrier concentration, defect compensation mechanisms, and the formation of internal electric fields [1, 2, 3]. Thermal treatment, in turn, governs grain growth, the redistribution of defect levels, and band alignment, as evidenced by short-circuit current spectra and anomalous photovoltage characteristics. At the same time, comprehensive studies of the relationships among short-circuit current spectra, spectral sensitivity, and photovoltaic efficiency in indium-doped CdTe thin films are limited. In this work, the spectral and photovoltaic properties of undoped, freshly prepared, and thermally treated CdTe:In films are analyzed in their interrelation. The research results have important scientific significance for optimizing semiconductor processing technologies and developing high-efficiency photovoltaic devices.

TECHNOLOGY AND MEASUREMENT METHODS

To obtain the films, we used the thermal vacuum evaporation method. A vacuum system was assembled based on a VUP-5M automatically controlled vacuum unit and a VAKMA 2NVR-5 DM fore-vacuum pump, together with a VAKMA NVDM-160 vapor-oil diffusion pump providing a pressure of $\sim 10^{-2}$ Pa. The samples had dimensions of 7×25 mm² and a thickness of 0.8–1.5 µm. In this method, the films are formed as nanoscale polycrystalline layers; under vacuum conditions, the materials are heated to form a high-quality coating on the surface. Thickness and dimensions are precisely controlled, thereby improving the photovoltaic properties of the films [3, 4]. Using these methods, nanoscale polycrystalline films are produced under high-vacuum conditions. During preparation, the films were thermally treated in the 350–750 K range, resulting in a transition from the amorphous state to the polycrystalline state [5, 6]. The film thickness was accurately monitored using a special quartz crystal sensor of the equipment. At 77 and 300 K, the short-circuit current spectra and bandgap width of as-prepared and thermally treated $CdTe:In$ films were determined.

RESULTS

Short-circuit current spectra and bandgap width of CdTe:In films. Typical room-temperature spectra $I_{sc}(\nu)$ obtained for CdTe:In samples–undoped CdTe (curve 1), freshly prepared (2), and thermally treated (3)–are shown in Figure 1a. As can be seen from the curves, the spectral sensitivity of I_{sc} differs sharply for different samples. The spectral maxima are determined with an accuracy of ±0.05 eV and, with the same accuracy, correspond to the intrinsic absorption edge. The long-wavelength tail of the spectra is associated with impurity-related light absorption in the barrier regions of crystallites, i.e., anomalous photovoltage (APV), whose contribution increases significantly in the doped CdTe:In sample (curves 2 and 3 in Figure 1).

Cite as: I.I. Yulchiev, D.Sh. Khidirov, J.S. Raximjonov, M.M. Madraximov, Sh.Sh. Abdullaev, V.T. Mirzayev, East Eur. J. Phys. 2, 411 (2026), https://doi.org/10.26565/2312-4334-2026-2-45

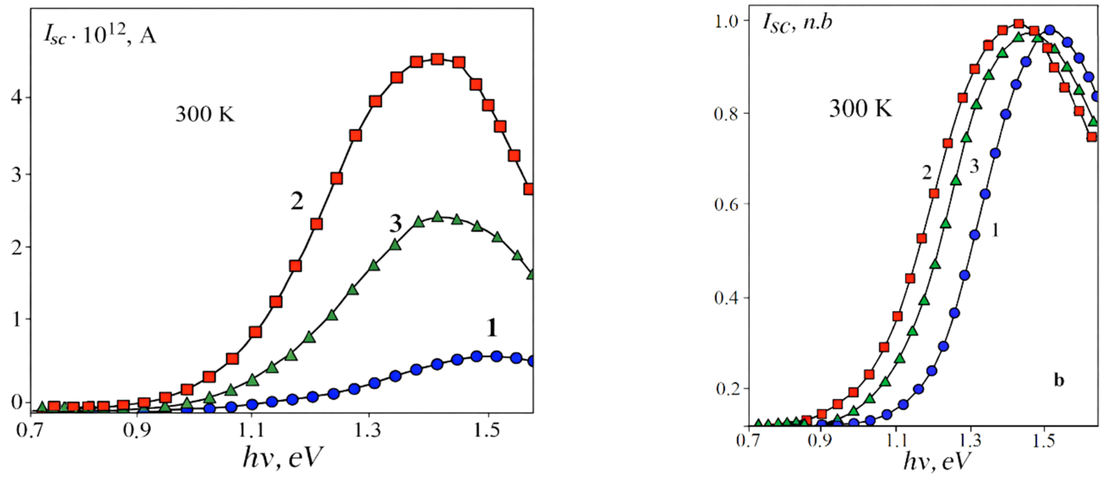

Figure 1. Short-circuit current Isc spectra of CdTe (curve 1) and CdTe:In films (curve 2 – freshly prepared; curve 3 – after thermal treatment) exhibiting AFK characteristics at T = 300 K, shown on (a) absolute and (b) normalized scales.

The short-wavelength decrease of the spectra appears to be due to light absorption in the quasi-neutral regions of the grains, which leads to bulk photoconductivity of the shunt layer and, consequently, to a decrease in the spectral value of the photovoltage, $V_{APV}(\nu)=I_{sc}(\nu)\cdot R_{pl}(\nu)$. The integral of the short-circuit current in doped films increases by more than two orders of magnitude compared to pure CdTe samples. This is achieved in the non-thermally treated CdTe:In case, where photoconductivity dominates in the films (V_{APV} is only 60–100 V/cm), and for thermally treated (TT) films, mainly due to the photovoltaic effect ($V_{APV}=3\cdot10^3$ V/cm). From the standpoint of analyzing the APV formation mechanism, it was even more effective to compare the I_{sc} spectra for the three samples discussed above obtained at liquid nitrogen temperature, T=77 K (Figure 2).

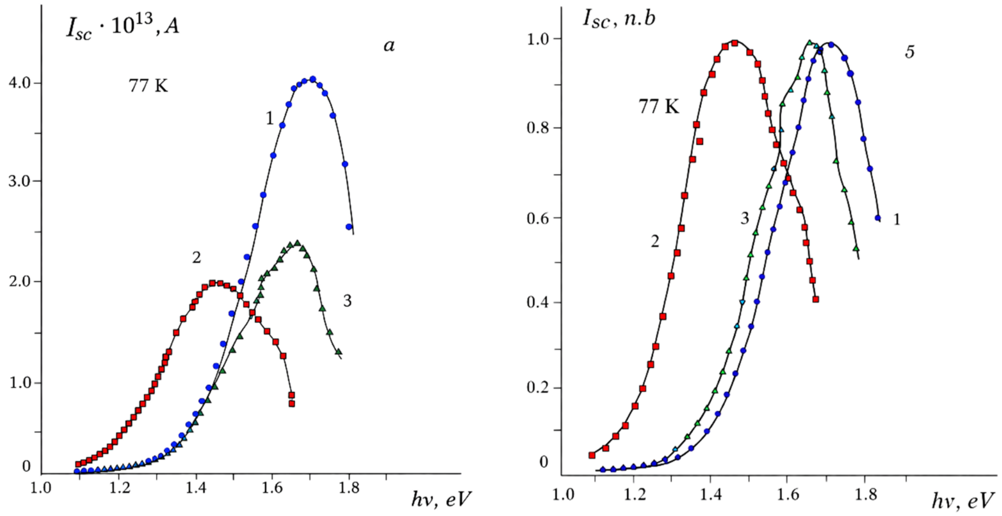

Figure 2. Short-circuit current I_{sc} spectra of CdTe (curve 1) and CdTe:In films (curve 2 – freshly prepared; curve 3 – after thermal treatment (TTE)) exhibiting AFK characteristics at T = 77 K, presented on (a) absolute and (b) normalized scales.

According to the results reported in [7, 8, 9], in our experiments for CdTe films the I_{sc} value practically did not change within the studied temperature range T = 77÷300 K. However, in doped CdTe:In samples, when the temperature decreases from 300 K to 77 K, both the integral value of Iqt and the level of its spectral maximum decrease by approximately one order of magnitude. For freshly prepared CdTe:In films, a noticeable long-wavelength shift of the $I_{sc}(\nu)$ spectrum is observed, and a doublet structure appears (Figure 2a, curve 2). The latter is associated with a twofold contribution to the AFK integral, arising from impurity-related and intrinsic absorption, which dominates over the grain-related intrinsic contribution (see curve 2 in Figure 2 for hν < 1.6 eV).

However, it should be emphasized that in annealed CdTe:In films the "intrinsic" contribution to APV, similar to that in CdTe films, exceeds the "grain-related" contribution (curves 1 and 3), and the doublet structure of the oppositely signed shoulder spectrum is preserved compared to curve 2. The short-wavelength shift of the maxima in spectral curves 1 and 3 in Figure 2 is associated with the increase in the CdTe bandgap as the temperature decreases. Thus, in obliquely evaporated CdTe:In films, APV formation occurs due to light absorption in both the intrinsic and grain-related spectral regions. Depending on technological conditions, the "grain-related" contribution may exceed the "intrinsic" one and may even change its sign. To determine the impurity level involved in AFK formation, the long-wavelength tails of the $I_{sc}(\nu)$

spectra shown by curves 1–3 in Figure 2 were analyzed in more detail by studying the photon capture cross-section [10, 11]. From the comparison of the experimental and theoretical spectral curves (Figure 3), the following deep levels of local centers were identified at T=77 K: $E_1=E_c-(1.43\pm0.02)$ eV, $E_2=E_c-(1.05\pm0.02)$ eV, $E_3=E_c-(1.31\pm0.02)$ eV, $E_4=E_c-(1.18\pm0.02)$ eV, and $E_5=E_c-(0.9\pm0.02)$ eV.

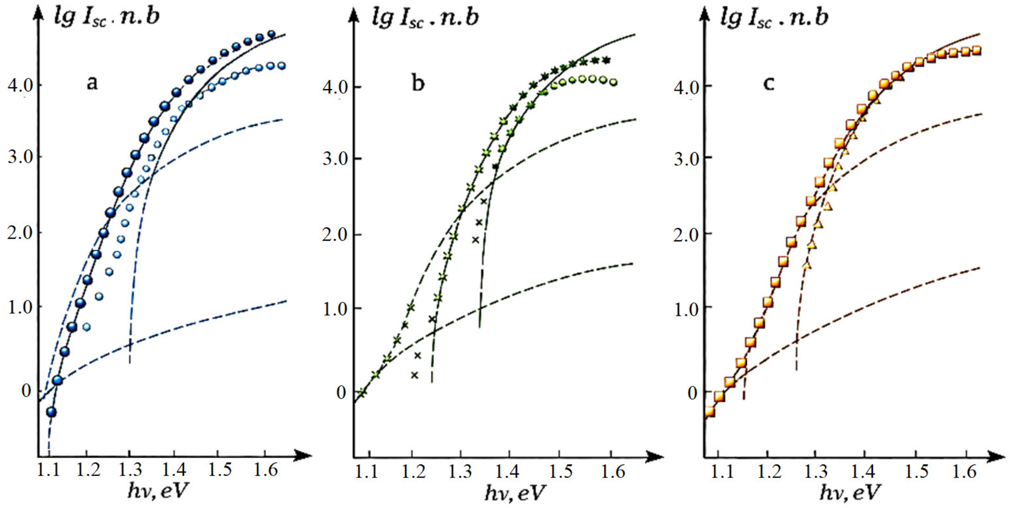

Figure 3. Short-circuit current spectra of CdTe (a) and CdTe:In films (b – freshly prepared; c – after thermal treatment) at T = 77 K (solid dots), and the theoretical spectra based on the photon capture cross-section (open dots, crosses, triangles, squares)

Surface morphology and crystal structure of the films studied by electron microscopy and spectroscopic methods

The surface morphology of CdTe polycrystalline thin films before and after thermal treatment was investigated using scanning electron microscopy (SEM). The obtained results clearly demonstrate that thermal treatment has a significant effect on the microstructural characteristics of the films.

The as-deposited (thermally untreated) CdTe film is characterized by an uneven and relatively disordered grain structure. The grains are irregular in shape, and their boundaries are poorly defined, with small particles and microdefects observed across the surface. This indicates a high density of grain boundaries and a relatively weakly compacted structure, which can increase the likelihood of charge carrier scattering and thus limit the film's electrophysical properties (Figure 4a).

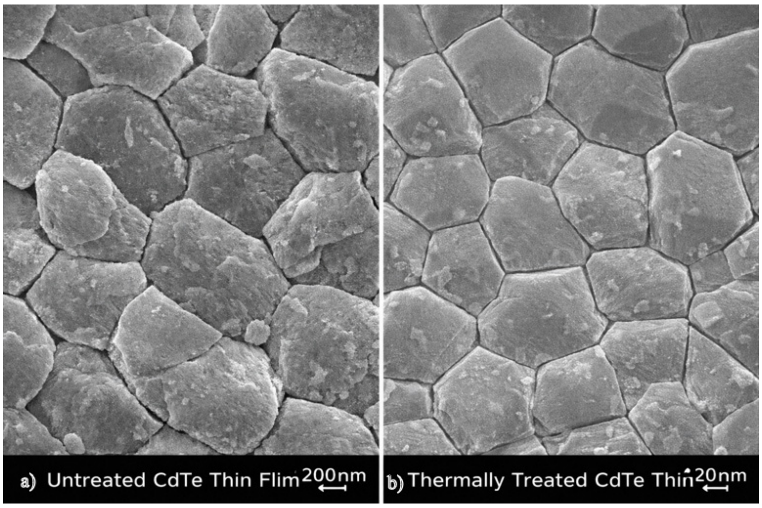

Figure 4. SEM images of CdTe films: (a) as-deposited and (b) after thermal treatment

In contrast, the thermally treated CdTe film exhibits a significantly improved microstructure. SEM images show an increase in average grain size, with grains appearing more regular and polyhedral. Grain boundaries are clear and smooth, and the film surface shows greater overall uniformity [12, 13]. This indicates that recrystallization and grain growth processes were activated during the thermal treatment (Figure 4b).

As a result of grain growth and structural densification, the number of grain boundaries decreases, thereby reducing charge-carrier recombination centers. Consequently, thermally treated CdTe films exhibit increased electrical conductivity, enhanced photosensitivity, and improved photoelectric properties. In addition, the reduction of surface defects can positively influence the film's optical absorption and interactions with photons.

Overall, the SEM results indicate that thermal treatment significantly improves the microstructural quality of polycrystalline CdTe thin films, promoting grain growth, structural densification, and enhanced surface uniformity. These microstructural changes are an important factor for increasing the efficiency of CdTe-based photovoltaic and photosensitive devices.

In the as-deposited CdTe:In sample (Figure 5a), the grains exhibit a relatively irregular and polygonal shape, with clearly defined grain boundaries. Numerous small spherical clusters (bright spots) are observed on the film surface. These clusters are associated with the uneven distribution of In dopants or the local formation of secondary phases. The non-uniform grain size and the high density of grain boundaries indicate a significant presence of structural defects in the film. As a result, strong charge-carrier scattering occurs at grain boundaries, leading to reduced electrical conductivity and an increase in recombination centers.

The morphological structure of thermally treated CdTe:In samples (Figure 5b) is significantly improved. The grains exhibit a more regular and larger polygonal shape, grain boundaries become smoother, and the surface density of the film increases [13, 14]. The reduction in the number of spherical clusters is explained by the redistribution of In atoms throughout the grain volume and the partial elimination of secondary phases. The increase in grain size reduces the number of grain boundaries, thereby enhancing charge-carrier mobility and decreasing resistivity.

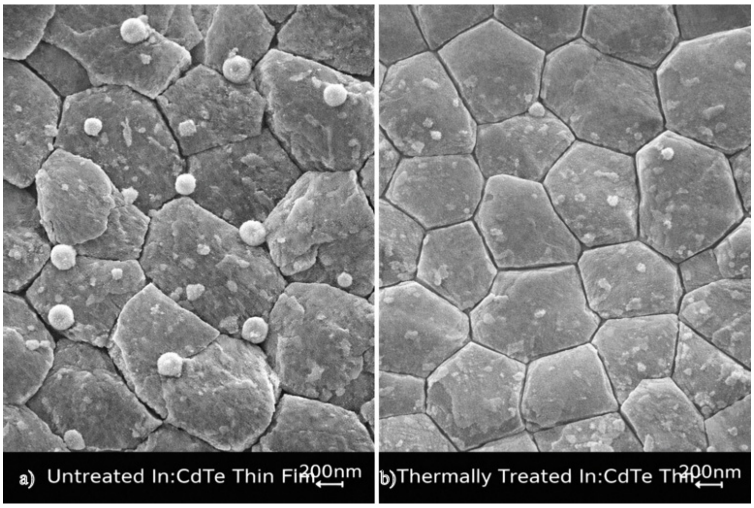

Figure 5. SEM images of as-deposited (a) and thermally treated (b) CdTe:In films

As a result of improved structural uniformity and reduced grain boundary effects in thermally treated CdTe:In samples:

- Charge carrier mobility increases;
- Resistivity decreases;
- Potential barriers at grain boundaries are reduced;
- Anomalous photovoltaic voltage is enhanced.

Thermal treatment significantly improves the morphological quality of In-doped CdTe polycrystalline films and optimizes their electrophysical and photoelectric properties. This makes these films a promising material for use in photodetectors and photovoltaic devices.

1. ***Phase identification:*** The main diffraction peaks in the experimental spectrum are located approximately at the following 2θ positions: ~23.8°, ~39–40°, ~46–47°, ~56°, and ~62–66° (Figure 6). These reflections correspond to the cubic CdTe crystal structure (zinc-blende, space group F-43m). By comparison with the ICDD reference card for CdTe (PDF 96-900-8841), the following crystallographic planes are identified:

2θ (°)	**Miller indices (hkl)**	**Phase attribution**
~23.8°	(111)	CdTe
~39.3°	(220)	CdTe
~46.5°	(311)	CdTe
~56.2°	(400)	CdTe
~62–66°	(331)/(422)	CdTe

2. ***Crystal structure and texture (preferential orientation):*** The (111) reflection exhibits the highest intensity in the diffraction pattern, indicating the presence of a strong (111) texture. This suggests that the crystallites predominantly grow along the (111) direction and that grain orientation is largely aligned with this energetically favorable plane. Such behavior reflects epitaxial or semi-oriented growth along the most thermodynamically stable crystallographic plane. For CdTe, the (111) plane possesses the lowest surface energy; therefore, this orientation is commonly dominant in polycrystalline thin films.

3. ***Presence of secondary phases:*** The lower panels also include separate reference cards for Cd and Te. In the experimental diffraction pattern, no distinct diffraction peaks corresponding to metallic Cd are detected. Likewise, no

dominant reflections attributable to the hexagonal Te phase are observed. This indicates that the segregation of free Cd or free Te is minimal, and the film is essentially composed of a single CdTe phase with well-controlled stoichiometry. If minor low-intensity additional peaks are present, they may be associated with micro-Te segregation or slight traces of Cd oxidation. Nevertheless, the dominant and clearly identified phase is CdTe.

4. ***Crystallite size estimation (Scherrer analysis):*** If the full width at half maximum (FWHM) of the (111) diffraction peak is known, the average crystallite size can be calculated using the Scherrer equation:

$$D = \frac{0.9\,\lambda}{\beta\cos\theta}. \tag{1}$$

Here: λ=1.5406 Å is the X-ray wavelength (CuKα radiation), β is the full width at half maximum (FWHM) of the diffraction peak expressed in radians, and θ is the Bragg angle corresponding to the diffraction peak position [15, 16].

The relatively narrow diffraction peaks observed in the spectrum indicate good crystallinity and the formation of relatively large crystallites, typically in the range of 30–100 nm.

5. ***Internal mechanical strain (IMS) and lattice parameter:*** If the (111) diffraction peak slightly shifts from its ideal position, this indicates the presence of internal mechanical strain in the film:

- A shift toward lower 2θ values (left shift) corresponds to lattice expansion (tensile strain).
- A shift toward higher 2θ values (right shift) corresponds to lattice contraction (compressive strain).

For cubic CdTe, the lattice parameter is approximately: $\alpha \approx 6.48$ Å

If the interplanar spacing d d is calculated from the experimental 2θ value using Bragg's law:

$$d = \frac{\lambda}{2\sin\theta} \tag{2}$$

where λ is the X-ray wavelength and $\theta = \frac{2\theta}{2}$, then the lattice parameter for cubic CdTe can be determined using:

$$a = d\sqrt{h^2 + k^2 + l^2} \tag{3}$$

Once calculated, the internal mechanical strain (IMS) in the film can be determined by comparing the experimentally obtained lattice parameter with the standard value.

6. ***Background level and amorphous component:*** The diffraction pattern exhibits a low background intensity along with well-defined and sharp crystalline peaks. This indicates a negligible amorphous component in the film and a high degree of crystallinity.

7. ***Photovoltaic significance:*** The strong (111) texture and high degree of crystallinity provide several important advantages, including reduced carrier recombination, a lower density of grain boundary defects, enhanced charge carrier mobility, and improved photoelectric response (optical response). These structural features are critical factors for enhancing the performance of CdTe-based solar cells.

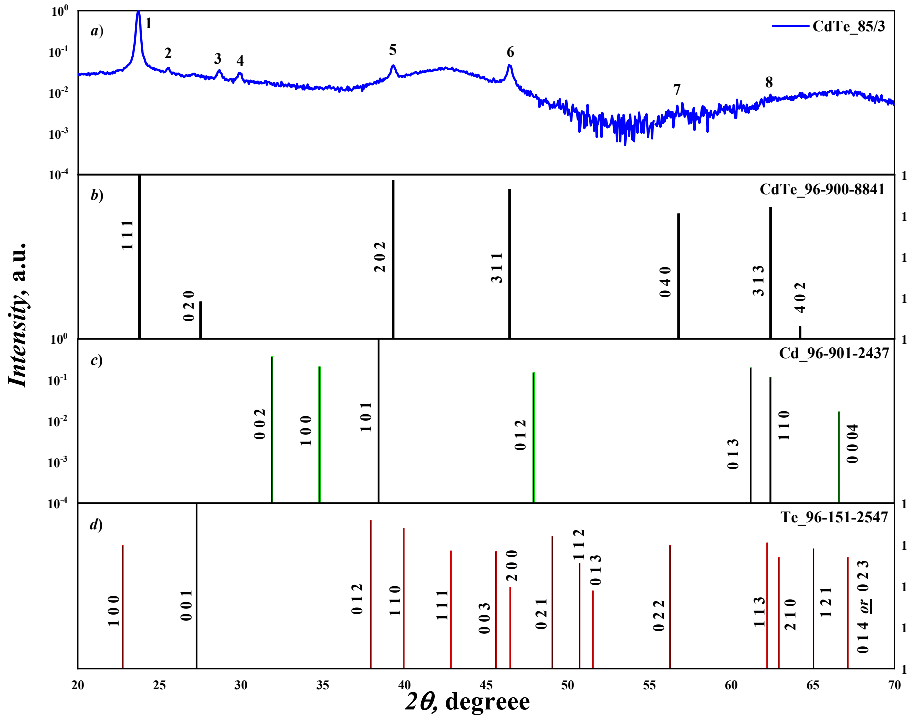

Figure 6. X-ray diffraction (XRD) patterns of the polycrystalline CdTe thin film: (a) experimental diffraction spectrum; (b) reference ICDD card for cubic CdTe (zinc-blende structure, PDF 96-900-8841); (c) Cd reference (PDF 96-901-2437); and (d) Te reference (PDF 96-151-2547).

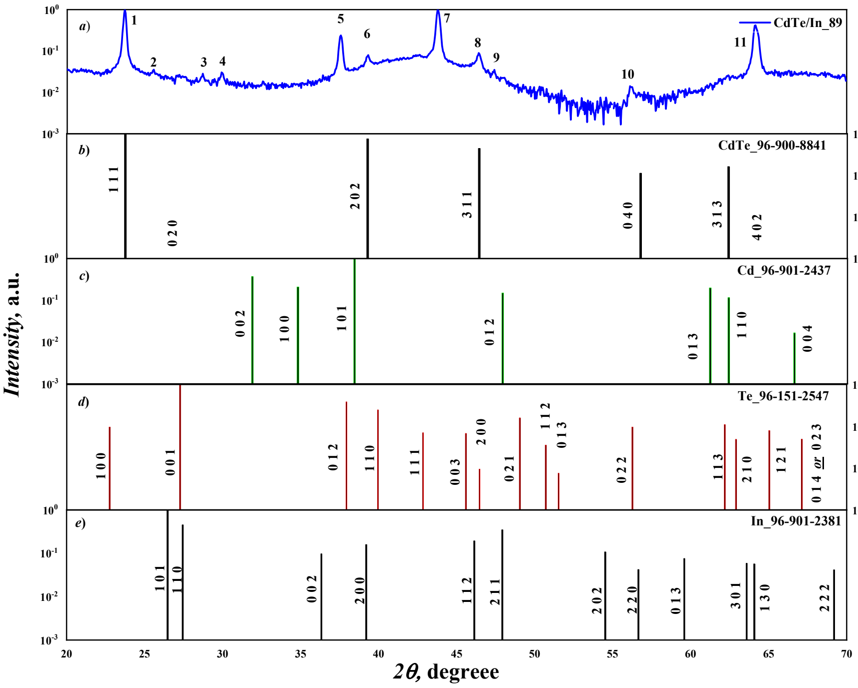

Figure 7. X-ray diffraction (XRD) patterns of the polycrystalline CdTe:In thin film: (a) experimental diffraction spectrum; (b) reference ICDD card of cubic CdTe (zinc-blende structure, PDF 96-900-8841); (c) Cd reference (PDF 96-901-2437); (d) Te reference (PDF 96-151-2547); and (e) In reference (PDF 96-901-2381).

1. ***Phase identification:*** In the experimental pattern (a), the main diffraction peaks are observed at approximately the following 2θ values: ~23.7° corresponding to (111), ~39.3° to (220), ~46.5° to (311), ~56° to (400), and ~62–66° to (331)/(422) (Figure 7). These reflections are fully consistent with the cubic zinc-blende crystal structure of CdTe (space group F-43m), in agreement with the ICDD reference card (PDF 96-900-8841). Therefore, the indium-doped film preserves the cubic CdTe phase as the dominant structural phase.

2. ***Effect of indium doping on the crystal structure:*** The lower panel includes the reference card for In (PDF 96-901-2381). In the experimental diffraction pattern, no distinct peaks corresponding to metallic indium are detected. Furthermore, no strong reflections associated with In_2Te_3 or other intermetallic phases are observed. This indicates that indium is incorporated substitutionally into the CdTe lattice, without phase segregation, leading to the formation of a single-phase solid solution.

3. ***Peak shift and lattice deformation:*** The atomic radius of indium is not smaller than that of cadmium (In ≈ 0.156 nm, Cd ≈ 0.148 nm). Therefore, when In atoms substitute Cd sites in the lattice, changes in the lattice parameter may occur, leading to slight shifts in the diffraction peak positions [17].

If the (111) diffraction peak shifts relative to that of pure CdTe: A shift toward lower 2θ values (left shift) indicates lattice expansion (tensile strain). A shift toward higher 2θ values (right shift) indicates lattice contraction (compressive strain).

Such peak shifts confirm the presence of internal mechanical strain (IMS) within the film.

4. ***Degree of crystallinity:*** In the diffraction pattern, the peaks are sharp and intense, the background level is relatively low, and the (111) reflection is dominant. These features indicate good crystallinity, a strong preferential texture, and oriented grain growth.

5. ***Texture:*** The (111) diffraction peak is significantly more intense than the other reflections, indicating preferential growth along the energetically stable (111) plane. This suggests a reduced grain boundary density and a lower concentration of recombination centers. Such structural characteristics positively influence the photovoltaic properties of the material.

6. ***Additional peaks:*** In the experimental diffraction pattern, additional peaks labeled 5, 6, 8, 9, 10, and 11 are observed. These features may be associated with lattice distortion induced by indium incorporation, microstrain effects, minor interstitial defects, or stress localized at grain boundaries. However, these peaks do not correspond to independent secondary phases, indicating that no separate crystalline phase is formed.

7. ***Structural quality assessment:*** The CdTe:In thin film is phase-pure, retains the cubic crystal structure, and exhibits a strong (111) preferential orientation. Indium is successfully incorporated into the lattice, and the film demonstrates a high degree of crystallinity.

8. ***Correlation with photovoltaic and electrical properties:*** Indium acts as a donor dopant in CdTe. Due to the improved structural quality, electrical conductivity increases, carrier concentration is enhanced, recombination processes are reduced, and the optical response is improved [18, 19].

DISCUSSION

In the CdTe photovoltaic sample, three defect levels are active: E_1, E_2, and E_3, which are associated with singly and doubly charged cadmium vacancies and excess tellurium, respectively [9]. In the as-prepared CdTe:In film, the E_1 level is not observed (Figure 3b), which is most likely attributed to charge-state saturation V_{Cd}^{--} and the formation of donor–acceptor pairs $I_n^+V_{Cd}^-$, with an electron transition energy to the conduction band of 1.18 eV. During heat treatment (HT) of the doped film, self-compensation between interstitial donors In^{+i} and vacancy-type acceptors V_{Cd}^{-j} occurs [3, 9], and the E_5 level appears in the Iqt spectrum (Figure 3c). This is most likely associated with the formation of defect pairs ($I_n^+V_{Cd}^-$) in the barrier region near the surface of the crystal grains. This is accompanied by a sharp increase in photoresistance and a simultaneous one-order-of-magnitude rise in U_{APV}. The contribution of the E_5 level to APV is associated with light absorption in the barrier region, which induces electron transitions from the E_5 level to the conduction band. Since the occupancy of this level decreases exponentially toward the grain surface, the contribution of E_5 centers to impurity-related APV is insignificant compared to that of the localized E_2, E_3, and E_4 centers (see Figure 3).

SEM analysis reveals that the surface morphology of CdTe and CdTe:In polycrystalline thin films is highly sensitive to heat treatment (HT). The as-deposited CdTe films exhibit irregular grains, indistinct grain boundaries, and dispersed microdefects, indicating insufficient structural compaction and a high grain boundary density. Such a microstructure promotes strong carrier scattering at grain boundaries, reduces mobility, enhances recombination, and consequently degrades electrical conductivity and photoelectric performance.

After HT, CdTe films exhibit significant grain growth, improved grain uniformity, and enhanced surface homogeneity, consistent with recrystallization processes. The increase in grain size reduces grain boundary density and recombination centers, thereby improving electrical conductivity and photosensitivity. Additionally, reducing surface defects stabilizes light absorption and enhances photon–matter interactions.

In CdTe:In films, the HT effect is more complex, influencing both grain morphology and the spatial redistribution of In dopants. In untreated samples, spherical clusters likely originate from non-uniform In distribution or localized secondary phases, acting as trap and recombination centers. HT significantly reduces these clusters, promotes grain enlargement, and enhances structural densification due to dopant redistribution toward energetically favorable configurations. The smoothing and reduction of grain boundaries decrease potential barriers, increase carrier mobility, and lower resistivity. This reduction in grain boundary density plays a crucial role in enhancing the anomalous photovoltage (APV).

XRD analysis confirms the preservation of the cubic CdTe lattice with strong (111) preferential orientation and high phase purity in both CdTe and CdTe:In films. Indium incorporation does not disrupt the crystal structure; instead, it maintains the structural quality required for efficient photovoltaic and optoelectronic applications. Overall, thermally treated CdTe:In thin films demonstrates improved structural, electrical, and photoelectric properties, confirming their strong potential for high-performance photodetectors and photovoltaic devices (Figure 6, 7).

CONCLUSIONS

XRD analysis confirms that both CdTe and CdTe:In thin films crystallize in the cubic zinc-blende structure (F-43m) with a strong (111) preferential orientation. The dominant (111) reflection and well-defined higher-order peaks ((220), (311), (400)) verify high phase purity and good crystallinity. No secondary phases related to metallic Cd, Te, or indium compounds were detected, indicating effective stoichiometric control and successful substitutional incorporation of In into the CdTe lattice. Slight peak shifts in CdTe:In suggest lattice distortion induced by indium doping.

Electrical and spectral measurements reveal a significant enhancement in photosensitivity and photoelectric response for CdTe:In films. Thermally treated samples exhibit a pronounced increase in short-circuit current and anomalous photovoltage (APV), confirming the dominance of the photovoltaic mechanism. Low-temperature (77 K) spectral analysis identifies deep energy levels (E_1–E_5) contributing to APV formation.

SEM observations demonstrate that thermal treatment promotes grain growth, structural densification, and improved surface uniformity. The reduction in grain boundary density enhances carrier mobility and suppresses recombination processes.

Overall, thermally treated polycrystalline CdTe:In thin films exhibit improved structural, electrical, and photoelectric properties, confirming their strong potential for high-efficiency photodetectors and photovoltaic applications.

ORCID

Iftikhorjon I. Yulchiev, https://orcid.org/0000-0001-9346-0441; **Dadakhon Sh. Khidirov,** https://orcid.org/0000-0003-1391-4250; **Jaxongir S. Raximjonov,** https://orcid.org/0009-0002-7513-6175; **Muminjon M. Madraximov,** https://orcid.org/0000-0001-5435-1242; **Sherzod Sh. Abdullaev,** https://orcid.org/0009-0007-9768-5008; **Valijon T. Mirzayev,** https://orcid.org/0000-0002-8382-6750

REFERENCES

[1] T.M. Razykov, C.S. Ferekides, D. Morel, E. Stefanakos, H.S. Ullal, and H.M. Upadhyaya, "Solar photovoltaic electricity: Current status and future prospects," Solar energy, **85**(8), 1580-1608 (2011). https://doi.org/10.1016/j.solener.2010.12.002

[2] D. Bonnet, and P. Meyers, "Cadmium-telluride—Material for thin film solar cells," Journal of Materials Research, **13**(10), 2740-2753 (1998). https://doi.org/10.1557/JMR.1998.0376

[3] V.T. Mirzaev, B.J. Akhmadaliyev, I.I. Yulchiev, M.M. Madraximov, and T.I. Rakhmonov, "Temperature and Infrared Quenching of Equilibrium Conductivity in $CdSe_xS_{1-x}$ Film," East European Journal of Physics, (2), 247-251 (2025). https://doi.org/10.26565/2312-4334-2025-2-29

[4] S.H. Wei, and S.B. Zhang, "Chemical trends of defect formation and doping limit in II-VI semiconductors: The case of CdTe," Physical Review B, **66**(15), 155211 (2002). https://doi.org/10.1103/PhysRevB.66.155211

[5] X. Wu, "High-efficiency polycrystalline CdTe thin-film solar cells," Solar energy, **77**(6), 803-814 (2004). https://doi.org/10.1016/j.solener.2004.06.006

[6] A. Romeo, and E. Artegiani, “CdTe-based thin film solar cells: past, present and future,” Energies, **14**(6), 1684 (2021). https://doi.org/10.3390/en14061684
[7] P.J.M.P. Scherrer, “Nachr Ges wiss goettingen,” Math. Phys. **2**, 98-100 (1918).
[8] J.A. Nelson, *The physics of solar cells*, (World Scientific Publishing Company, 2003).
[9] M. Ayibzhanov, O. Mamatov, V. Mirzaev, and B. Tuychibaev, “Luminescence spectrum of cadmium chalcogenide photovoltaic film structures and their power enhancement,” E3S Web of Conferences, **583**, 04003 (2024). https://doi.org/10.1051/e3sconf/202458304003
[10] H.R. Moutinho, M.M. Al-Jassim, D.H. Levi, P.C. Dippo, and L.L. Kazmerski, “Effects of $CdCl_2$ treatment on the recrystallization and electro-optical properties of CdTe thin films,” Journal of Vacuum Science and Technology A: Vacuum, Surfaces, and Films, **16**(3), 1251-1257 (1998). https://doi.org/10.1116/1.581269
[11] F.A. Giyasova, K.N. Bakhronov, M.A. Yuldoshev, I.B. Sapaev, R.G. Ikramov, F.A. Giyasov, *et al*., “Study of the Influence of Temperature on the Transitions of the CdS/Si/CdTe Heterosystem,” East European Journal of Physics, (4), 461-468 (2025). https://doi.org/10.26565/2312-4334-2025-4-47
[12] F.T. Yusupov, V.T. Mirzaev, T.I. Rakhmonov, O.R. Nurmatov, and D.S. Khidirov, “Enhanced optoelectronic properties of ZnO thin films through boron and fluorine Co-doping,” Journal of Ovonic Research, **21**(3), 285-296 (2025). https://doi.org/10.15251/JOR.2025.213.285
[13] I.M. Beker, F.B. Dejene, L.F. Koao, and J.J. Terblans, “Impact of deposition voltage on the physicochemical properties of electrodeposited Se-doped CdTe thin films for solar cell applications,” Ionics, **31**(7), 7453-7464 (2025). https://doi.org/10.1007/s11581-025-06401-2
[14] S.B. Utamuradova, F.A. Giyasova, K.N. Bakhronov, M.A. Yuldoshev, M.R. Bekchanova, and B. Ismatov, “Current Transfer Mechanism in a Thin-Based Heterosystem Based on A^2B^6 Compounds,” East European Journal of Physics, (3), 325-335 (2025). https://doi.org/10.26565/2312-4334-2025-3-31
[15] H. Bayhan, and A.S. Kavasoğlu, “Tunnelling enhanced recombination in polycrystalline CdS/CdTe and CdS/Cu (In, Ga) Se_2 heterojunction solar cells,” Solid-state electronics, **49**(6), 991-996 (2005). https://doi.org/10.1016/j.sse.2005.03.012
[16] M. Prabhu, M. Marikkannan, M.S. Pandian, P. Ramasamy, and K. Ramachandran, “Effect of zinc and indium doping in chalcogenide (CdS/Te) nanocomposites towards dye-sensitized solar cell applications,” Journal of Physics and Chemistry of Solids, **168**, 110802 (2022). https://doi.org/10.1016/j.jpcs.2022.110802
[17] R.S.Hall, D. Lamb, and S.J.C. Irvine, “Back contacts materials used in thin film CdTe solar cells—A review,” Energy Science and Engineering, **9**(5), 606-632 (2021). https://doi.org/10.1002/ese3.843
[18] F.A. Giyasova, A.Z. Rakhmatov, K.N. Bakhronov, M.A. Yuldoshev, F.A. Giyasov, A.N. Olimov, and N.A. Sattarov, “Physical Principles of Photocurrent Generation in a Silicon-Based Photodiode Structure with a Schottky Barrier,” East European Journal of Physics, (4), 397-406 (2025). https://doi.org/10.26565/2312-4334-2025-4-38
[19] T. Sinha, L. Verma, and A. Khare, “Variations in photovoltaic parameters of CdTe/CdS thin film solar cells by changing the substrate for the deposition of CdS window layer,” Appl. Phys. A, **126**, 867 (2020). https://doi.org/10.1007/s00339-020-04058-4

КОМПЛЕКСНИЙ АНАЛІЗ МОРФОЛОГІЇ, СТРУКТУРИ ТА ФОТОЕЛЕКТРИЧНИХ ВЛАСТИВОСТЕЙ ТОНКИХ ПЛІВОК CdTe та CdTe:In

Іфтіхоржон І. Юлчієв, Дадахон Ш. Хідіров, Жахонгір С. Рахімжонов, Мумінжон М. Мадрахімов, Шерзод Ш. Абдуллаєв, Валіжон Т. Мірзаєв
Ферганський державний технічний університет, Фергана, Узбекистан

У цій роботі було всебічно досліджено фотоелектричні властивості та спектри струму короткого замикання плівок CdTe, легованих індієм (In). Дослідження охоплює спектральну чутливість і характеристики поглинання світла нелегованих, свіжоотриманих і термічно оброблених плівок CdTe:In. Було проаналізовано вплив рівня легування та температури термічної обробки на параметри фотоелектричного ефекту. Отримані результати показали, що легування індієм і подальша термічна обробка суттєво підвищують фотоелектричну ефективність плівок CdTe. Використовуючи спектроскопічні методи та електронну мікроскопію, було визначено хімічний склад, морфологію поверхні та ширину забороненої зони плівок, а також встановлено їх взаємозв’язок з оптичними та електричними властивостями. Отримані результати свідчать про те, що плівки CdTe:In є перспективними для застосування в сонячній енергетиці.

Ключові слова: *тонкі плівки CdTe:In; фотоелектричний ефект; спектри струму короткого замикання; аномальна фотонапруга (APV); глибокі енергетичні рівні; термічна обробка; матеріали для сонячної енергетики*

EAST EUROPEAN JOURNAL OF PHYSICS. **2.** 419-426 (2026)
DOI:10.26565/2312-4334-2026-2-46 ISSN 2312-4334

THEORETICAL AND EXPERIMENTAL ANALYSIS OF MIXED EXCITON-POLARITON LUMINESCENCE IN *CdS* CRYSTALS IN THE REGIME OF STRONG EXCITON DAMPING

Bozorboy J. Akhmadaliev, Mekhriddin F. Akhmadjonov, Tokhirbek I. Rakhmonov*, Paxlovon I. Movlonov, Sherzod Sh. Abdullaev, Iftikhorjon I. Yulchiev
Fergana State Technical University, Fergana, Uzbekistan
**Corresponding Author e-mail: radiofizik2014@gmail.com*

Received March 2, 2026; revised April 23, 2026; accepted April 28, 2026

This work presents a combined theoretical and experimental study of mixed exciton-polariton luminescence in anisotropic CdS crystals in the regime of strong exciton damping near the A-exciton resonance. A spatially dispersive model of radiative mixed modes is used to analyze the transformation of the spectral contour, peak position, partial modal contributions, and angular dependence of the linewidth. Calculated spectra for emission angles from 10.4° to 85° are compared with photoluminescence measurements, and good agreement is obtained at $T \approx 77$ K for $\hbar\Gamma = 2.0$ meV and $L = 0.85$ μm. Unlike conventional approaches that relate the transition to a Lorentzian emission profile only to the condition $\Gamma \gg \Gamma_c$, we show that this regime additionally requires the transport-related constraint $2k_0L \cdot \operatorname{Im} n_{Mz} \ll 1$ Under these combined conditions, the mixed-mode emission contour approaches a quasiclassical Lorentzian profile with a half-width close to $\hbar\Gamma$. At the same time, spatial dispersion and intermode interference are not fully suppressed in anisotropic CdS crystals and become more pronounced at larger emission angles or smaller effective diffusion lengths. The results provide a refined criterion for identifying the quasiclassical emission regime and a practical framework for extracting exciton damping and effective diffusion depth from experimental spectra.

Keywords: *Mixed exciton-polariton luminescence; CdS crystal; Strong exciton damping; Spatial dispersion; Anisotropic semiconductor; Mixed modes; A-exciton resonance*
PACS: 71.36.+c, 71.35.Cc, 78.55.Et, 78.20.Bh, 78.20.Ci

INTRODUCTION

Exciton-polaritons arise from the strong coupling between resonant optical fields and excitonic excitations in crystals, and their spectral response near exciton resonances cannot be adequately described within a purely local dielectric framework [1-3]. In anisotropic semiconductors such as CdS, this light-matter interaction is further complicated by polarization-dependent mode mixing, boundary-transmission effects, and spatial dispersion, which together give rise to nonclassical optical phenomena in absorption, transmission, and emission spectra [2-6].

CdS has long been regarded as a model material for bulk exciton-polariton optics because of its pronounced optical anisotropy, relatively strong excitonic oscillator strength, and well-resolved A-exciton resonance at low temperatures [5-9]. Early transmission and luminescence studies showed that, in CdS single crystals, the spectral shape and angular behavior of excitonic emission are governed not by a simple local-exciton emission mechanism, but by the structure of the polariton branches [7-8]. Subsequent studies of damping dispersion demonstrated that the excitonic dephasing rate in CdS depends on both frequency and temperature, reflecting the influence of distinct impurity- and phonon-assisted relaxation channels [8-11]. These results make CdS particularly suitable for analyzing how dissipative decay modifies the observable manifestations of exciton-polariton coupling.

At the same time, the regime of strong exciton damping remains a theoretically and experimentally nontrivial problem. When the dissipative decay of excitons becomes comparable to or exceeds the characteristic polaritonic energy scales, the emission spectrum may approach a quasiclassical Lorentzian contour. However, in uniaxial crystals this transition is not complete, since spatial-dispersion effects, additional radiative waves, and interference between mixed modes may still remain observable, particularly at oblique emission angles. Recent studies on CdS-type crystals have shown that surface-radiative and longitudinal-exciton contributions are often smaller than the dominant bulk mixed-mode contribution; nevertheless, they are indispensable for achieving quantitative agreement with experiment and for explaining the appearance of additional spectral features near the longitudinal resonance frequency [12-13].

Despite these advances, the conditions under which mixed exciton-polariton luminescence acquires a quasiclassical Lorentzian profile remain insufficiently clarified. In most previous works, this transition is primarily associated with the condition $\Gamma \gg \Gamma_c$. However, such an interpretation does not fully account for the role of spatial dispersion, finite exciton transport, and boundary-induced mode conversion, which can significantly influence the spectral formation.

In this work, we demonstrate that the realization of the Lorentzian regime requires not only strong exciton damping but also an additional condition related to the effective diffusion length of polaritons. We show that the interplay between damping, spatial dispersion, and finite transport leads to a nontrivial angular evolution of the emission spectrum, which cannot be explained within conventional local approaches.

Therefore, a consistent description of mixed exciton-polariton luminescence in the strong-damping regime is important for both fundamental solid-state optics and the interpretation of experimental spectra. Such a description makes it possible to distinguish the roles of damping, interference, and spatial dispersion, and to extract physically meaningful parameters such as the exciton decay constant, effective diffusion depth, angular evolution of the linewidth, and the relative weights of partial radiative contributions [10-13]. This problem is especially relevant in anisotropic crystals, where the crystal boundary and mode conversion strongly influence which mixed states can radiate into the external medium [3-5].

Cite as: B.J. Akhmadaliev, M.F. Akhmadjonov, T.I. Rakhmonov, P.I. Movlonov, Sh.Sh. Abdullaev, I.I. Yulchiev, East Eur. J. Phys. 2, 419 (2026), https://doi.org/10.26565/2312-4334-2026-2-46

In this work, we present a theoretical and experimental analysis of mixed exciton-polariton luminescence in CdS crystals in the regime of strong exciton damping. The study is focused on the transformation of the spectral contour, linewidth, peak position, and partial modal contributions of the emitted radiation near the A-exciton resonance under different emission angles and damping conditions. By comparing calculated integral and partial spectra with experimental luminescence data, this work clarifies the conditions under which the spectrum approaches a classical Lorentzian form and those under which spatial-dispersion and interference effects continue to govern the observed emission, thereby providing a more rigorous physical basis for describing mixed-mode radiation in strongly dissipative excitonic systems.

METHODOLOGY

Mixed exciton-polariton luminescence in CdS crystals was analyzed within a combined theoretical, numerical, and experimental framework appropriate for the regime of strong exciton damping. The spectral behavior in the vicinity of the $A_{n=1}$ exciton resonance was described using the dispersion model of radiative mixed modes in a spatially dispersive crystal. Within this approach, the luminescence contour is determined by the coupled excitonic and electromagnetic response of the medium, while exciton damping, anomalous dispersion, modal interference, and boundary-related radiative effects are treated explicitly in the spectral formalism.

The theoretical analysis was performed for the limiting case of very strong exciton damping, where the contribution of spatial dispersion and light-exciton interaction is substantially weakened relative to dissipative broadening. Under these conditions, the total luminescence intensity was represented in a reduced form that makes it possible to separate the dominant radiative contribution from secondary terms and to trace the evolution of the emission contour toward a quasi-classical Lorentzian profile. Accordingly, the spectral half-width of the mixed-mode luminescence line was analyzed as a function of the damping parameter and the transport characteristics of the radiative states.

The numerical part of the study was based on calculations of both the integral luminescence spectra and their partial components in the spectral region of the $A_{n=1}$ exciton resonance. The spectra were calculated for radiation exit angles $\theta = 10.4°, 45°, 60°$, and $85°$. For the case $T \approx 77$ K, the calculations were performed with $\hbar\Gamma = 2.0$ meV using a common set of optical parameters. This procedure made it possible to evaluate the angular evolution of the spectral contour, including the position of the maximum, the degree of asymmetry, the role of interference terms, and the variation of the half-width with increasing observation angle.

Experimental verification was carried out by comparing the calculated spectra with photoluminescence data obtained for CdS crystals near the $A_{n=1}$ exciton resonance. The spectrum measured at $T = 77$ K and $\theta = 10.4°$ was fitted by the theoretical contour calculated from the model equations. In the fitting procedure, the damping parameter Γ was taken equal to the experimentally observed half-width of the A-line at the corresponding temperature, whereas the effective diffusion length L of the upper-branch polaritons was determined from the angular dependence of the A_L emission line by comparison with the calculated spectra. For the spectrum recorded at $T = 77$ K, the fitting was performed using $\hbar\Gamma = 2.0$ meV, $\ell = 70$ Å and $L = 0.85$ μm.

Since the emission spectrum in the exciton-resonance region contains a background contribution that is not directly related to the A_L-line formation mechanism, the background component was introduced separately in the comparison between theory and experiment. Therefore, the final theoretical contour was considered with the corresponding background-intensity correction. The remaining deviation between theory and experiment in the short-wavelength part of the spectrum was attributed to inelastic scattering processes of polaritons that were not included in the basic approximation.

The validity of the model was further tested by analyzing the angular dependence of the spectral half-width $\Delta(\theta)$ of the mixed-mode emission line at $T = 4.5,\ 15,\ 44$, and 77 K. The comparison between theoretical and experimental $\Delta(\theta)$ dependences was carried out using the parameter sets $L = 1.5,\ 1.7,\ 1.6,\ 0.85$ μm and $\Gamma = 0.1,\ 0.2,\ 0.5,\ 2.0$ meV, respectively. This procedure made it possible to determine the temperature and angular intervals in which mixed-mode luminescence approaches classical Lorentzian behavior and to evaluate the applicability of the line half-width as a practical indicator of exciton damping and crystal quality.

RESULTS AND DISCUSSION

Based on our theoretical calculations, we now analyze the partial contributions to the total luminescence intensity given by

$$I_p^{(0)}(\omega,\vec{\Omega}) = C \cdot \frac{4n_{ox}^2 n_{oz} L_{cr}}{|N_M|^2} \cdot \Gamma_f(\omega) \tag{1}$$

and examine several characteristic features of the spectrum $I_p^{(0)}(\omega,\theta)$ in the corresponding limiting case. Under these conditions, the effects of spatial dispersion (SD) and light-exciton interaction become substantially weaker than the exciton damping processes, and damping acquires the dominant role in the formation of mixed exciton-polariton luminescence (MEPL).

Thus, neglecting the contribution of the second branch, the spectral intensity of mixed exciton-polariton luminescence (MEPL) can be written in the form

$$I_p^{(0)}(\omega,\vec{\Omega}) \cong C \cdot \frac{4n_{ox}^2 n_{oz}}{|n_{M1}^2 - n_{M2}^2|^2} \left|\frac{n_{M1z}+n_{M2z}}{1+\bar{n}_p}\right|^2 \cdot \frac{\Gamma_f(\omega)}{2k_0 \operatorname{Im} n_{Mz} + L^{-1}}, \tag{2}$$

where n_{Mz} is the refractive index having the smallest absolute value among n_{M1z} and n_{M2z}.

$$n_{M\beta}^2(\omega,\theta) = \frac{1}{2}\left\{\left(1-\frac{M_\perp}{M_\parallel}\right)\sin^2\theta + \frac{\omega-\omega_L+i\Gamma/2}{\omega_{M\perp}} + \varepsilon_b - (-1)^\beta \left[\left(\left(1-\frac{M_\perp}{M_\parallel}\right)\sin^2\theta + \frac{\omega-\omega_L+i\Gamma/2}{\omega_{M\perp}} - \varepsilon_b\right)^2 + 4\frac{\omega_{LT}}{\omega_{M\perp}}\sin^2\theta\right]^{1/2}\right\}, \beta = 1,2. \tag{3}$$

Proceeding from this dispersion equation, it can be shown that in the case $\Gamma \gg \Gamma_c$, the following relation holds:

$$|n_{M1}^2 - n_{M2}^2|^2 = \frac{(\omega-\omega_c)^2 + \Gamma^2/4}{\omega_{M\perp}^2}. \tag{4}$$

Taking Eq. (4) into account, expression (2) can be reduced to the final form

$$I_p^{(0)}(\omega,\vec{\Omega}) \cong \frac{k_0^2}{(2\pi)^3}\hbar\omega \cdot \frac{2n_{ox}^2 n_{oz}\varepsilon_b\omega_{LT}}{(\omega-\omega_c)^2+\Gamma^2/4}\left|\frac{n_{M1z}+n_{M2z}}{1+\bar{n}_p}\right|^2 \cdot \frac{k_0 L\,\Gamma_f(\omega)}{2k_0 L\,\mathrm{Im}\,n_{Mz}+1}. \tag{5}$$

The calculations show that when $\Gamma \gg \Gamma_c$, the factor $\left|\frac{n_{M1z}+n_{M2z}}{1+\bar{n}_p}\right|^2$ is almost independent of frequency (with an accuracy better than 0.5%). Therefore, when the following condition is satisfied,

$$2k_0 L \cdot \mathrm{Im}\,n_{Mz} \ll 1, \tag{6}$$

Eq. (5) describes "classical" radiation, for which the effects of spatial dispersion (SD) and light-exciton interaction are very small. For this reason, the appearance of a Lorentz-type denominator in Eq. (5) is quite natural. When $\Gamma \gg \Gamma_c$ and condition (6) is fulfilled, this denominator predominantly determines the shape of the radiation spectrum. In this case, the spectral half-width Δ_A of the luminescence line of the mixed modes corresponds to $\hbar\Gamma$.

It should be emphasized here that, for the radiation of mixed modes to become fully "classical," the condition $\Gamma \gg \Gamma_c$ alone is not sufficient. As follows from Eq. (5), the inequality (6) must also be strictly satisfied. In the frequency range $\omega \geq \omega_c$, when $n_{Mz} = n_{M2z}$, the following relation holds: $\mathrm{Im}\,n_{Mz} \cong \frac{\Gamma_c^2/(\omega_{M\perp}\Gamma)}{16\sqrt{\varepsilon_b-\sin^2\theta}} \cdot \frac{\Gamma^2/4}{(\omega-\omega_c)^2+\Gamma^2/4}$.

Thus, when $\omega = \omega_c$, condition (6) takes the form of the following inequality:

$$\Gamma \gg \Gamma_c \frac{\Gamma_c k_0 L}{8\omega_{M_\perp}\sqrt{\varepsilon_b-\sin^2\theta}}, \qquad \text{i.e.,} \qquad L \gg \frac{8\omega_{M_\perp}\sqrt{\varepsilon_b-\sin^2\theta}}{\Gamma_c k_0}. \tag{7}$$

For the CdS crystal parameters, we take the following values into account:

$$\hbar\omega_{M_\perp} = 0.007\ \text{meV}, \qquad k_0 = 1.29 \cdot 10^5\ \text{cm}^{-1}, \qquad \varepsilon_{b\perp} = 9.4.$$

From this, it follows that $\hbar\Gamma_{c\,\max} = 4\hbar\sqrt{\omega_{LT}\omega_{M_\perp}} \approx 0.4753$ meV.

Accordingly, one obtains $\frac{8\omega_{M_\perp}\sqrt{\varepsilon_b-1}}{\Gamma_c k_0} \approx 0.02\ \mu$m.

Hence, for such crystals under the condition $\Gamma \gg \Gamma_c$, inequality (7) is well satisfied when the exciton diffusion length is $L \approx 1.0\ \mu$m.

However, when $L < 0.2\ \mu$m, this inequality is violated and the condition $\Gamma \gg \Gamma_c$ is no longer fulfilled. In this case, spatial dispersion (SD) affects the shape of the luminescence contour.

If the initial quantum states $T1$ and $M1$ are sufficiently well defined, then

$$I_p^{(0)}(\omega,\vec{\Omega}) = \textstyle\sum_{\beta=M1,M2} I_{p,\beta}^{(0)}(\omega,\vec{\Omega}) + I_{p,M12}^{(0)}(\omega,\vec{\Omega}) \tag{8}$$

$$I_{p,\beta}^{(0)}(\omega,\vec{\Omega}) = F(\omega,\vec{\Omega})\left|F_\beta(\omega,\vec{\Omega})\right|^2/\left(2k_0\,\mathrm{Im}\,n_{\beta z} + L^{-1}\right) \tag{9}$$

$$I_{p,M12}^{(0)}(\omega,\vec{\Omega}) = -F(\omega,\vec{\Omega}) \cdot 2\,\mathrm{Re}\left[\frac{F_{M1}(\omega,\vec{\Omega})F_{M2}^*(\omega,\vec{\Omega})}{-ik_0\left(n_{M1z}-n_{M2z}^*\right)+L^{-1}}\right] \tag{10}$$

$$F(\omega,\vec{\Omega}) = \frac{1}{(2\pi)^3}\frac{2M_\parallel^2 c\varepsilon_b\omega_{LT}\cos\theta}{\hbar\left|n_{M1}^2-n_{M2}^2\right|^2}\textstyle\sum_{\beta'=T1,M1}\sum_{\vec{k}_{\beta'}}\frac{f_{\beta'\vec{k}_{\beta'}}(\omega)}{\tau_{M,\beta'\vec{k}_{\beta'}}(\omega)} \tag{11}$$

$$F_\beta(\omega,\vec{\Omega}) = \frac{t_{0\beta}^{(p)}(\omega,\vec{\Omega})}{n_{\beta z}}\left[\frac{(n_\beta^2-\varepsilon_b)^2}{\varepsilon_b^2}\cdot\frac{n_{\beta z}^2}{n_\beta^2}+\frac{n_{ox}^2}{n_\beta^2}\right]^{1/2} \tag{12}$$

The above general theoretical relations obtained in our calculations, namely the equations describing mixed exciton-polariton luminescence (MEPL), remain valid in the case $\Gamma \gg \Gamma_c$ as well, since it is precisely under these conditions that scattering into the radiative $M1$ and $M2$ modes occurs.

Additional numerical calculations of the dispersion values of truncated normal waves for different values of Γ show that when $\Gamma \approx 2.0 \div 2.5$ meV ($T \approx 70 \div 80$ K), the kinetic approach remains applicable in the vicinity of the frequency ω_L and above it, provided that the quasiclassical Boltzmann approach is not treated as an excessively restrictive requirement. In this case, the upper dispersion branch $T1$ can also be described within the quasiclassical approximation, and under these conditions strong damping of the mixed $M1$ and $M2$ modes is ensured through elastic and inelastic scattering of $T1$ polaritons.

Indeed, as shown in Fig. 1, at $T = 77$ K and $\theta = 10.4°$, the experimental luminescence spectrum agrees well with the theoretical branch $I_p^{(0)}(\omega)$ calculated from Eqs. (8)-(12), where the values $\hbar\Gamma = 2.0$ meV, $\ell = 70$ Å, and $L = 0.85\ \mu$m were used. (The results presented here and below were obtained within the framework of experimental studies carried out by Prof. A.V. Sel'kin.)

In this case, the effective diffusion length L of the upper-branch polaritons at $T = 77$ K was determined for the A_L line by comparing with the theoretical calculation results based on the angular dependence $\Delta(\theta)$.

Likewise, the value of Γ was taken to be equal to the half-width Δ_A of the emission line at this temperature. The dotted straight line describes the contribution of the crystal background emission in the spectral region of the $A_{n=1}$ exciton resonance and is not related to the emission mechanisms of the A_L line. The theoretical solid curve is presented with a correction introduced to the background emission intensity. At the same time, in the short-wavelength part of the spectrum, a discrepancy of about 3-5% is observed between the theoretical and experimental results. This is associated with the fact that inelastic scattering in the $T1$ and $M1$ branches was not taken into account.

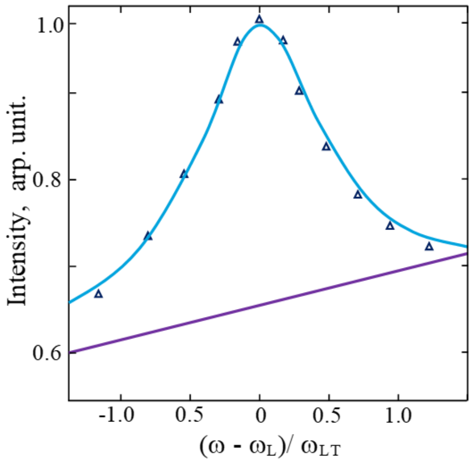

Figure 1. Experimental and theoretical comparison of the emission spectrum of mixed modes in a CdS crystal. The experimental data ($T = 77$ K, triangular symbols) and the theoretical curve (solid line), calculated for $\hbar\Gamma = 2.0$ meV, $\theta = 10.4°$, and $L = 0.85\ \mu$m, are shown. The dotted line represents the contribution of the crystal background emission in the spectral region of the $A_{n=1}$ exciton resonance.

In cases $a, b, c,$ and d of Fig. 2, the theoretical spectra of the total (integral) and partial contributions to mixed exciton-polariton luminescence (MEPL) in a CdS crystal are presented. The solid line denotes the total (integral) spectrum, the dotted line represents the I_{M1} contribution, the dashed line corresponds to the I_{M2} contribution, and the dash-dotted line shows the I_{M12} contribution. The calculations were performed for the emission angles $\theta = 10.4°$ (a), 45° (b), 60° (c), and 85° (d) at $\hbar\Gamma = 2.0$ meV ($T \approx 77$ K), using the same optical parameters as those employed for the theoretical spectrum in Fig. 1.

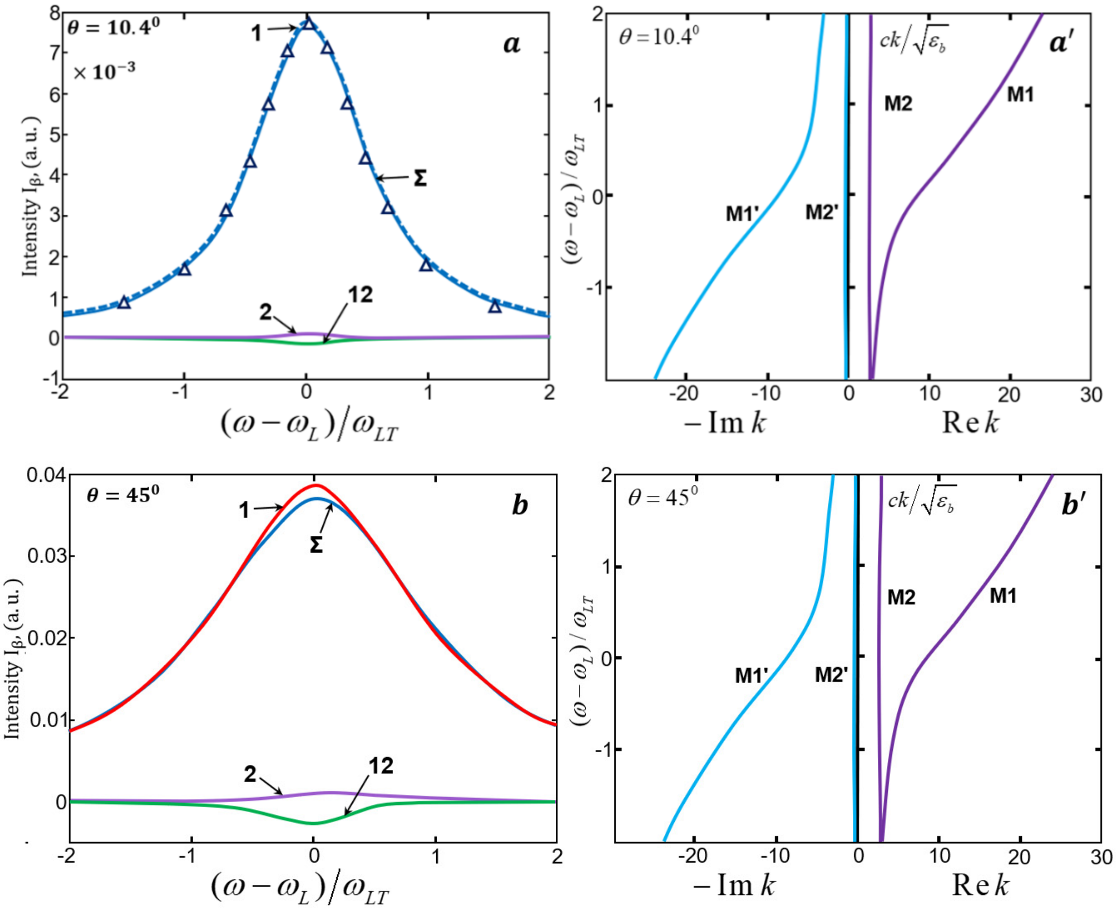

Figure 2. Theoretical photoluminescence spectra of mixed exciton-polariton modes in a CdS crystal (a-d) together with the corresponding dispersion curves (a′-d′), calculated for $\hbar\Gamma = 2.0$ meV ($T \approx 77$ K). The results are shown for emission angles into vacuum of $\theta = 10.4°$ (a, a′), 45° (b, b′), 60° (c, c′), and 85° (d, d′)

(continued on the next page)

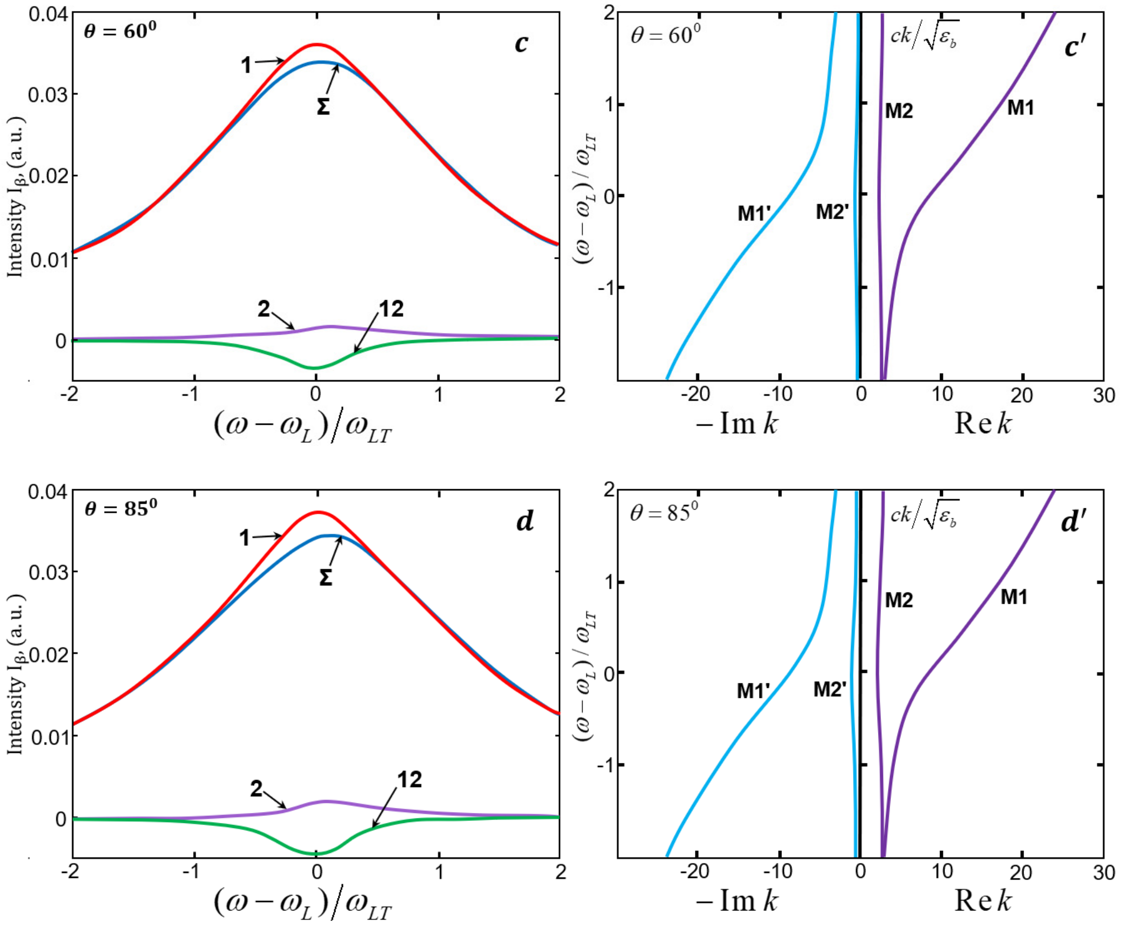

Figure 2. Theoretical photoluminescence spectra of mixed exciton-polariton modes in a CdS crystal (a-d) together with the corresponding dispersion curves (a′-d′), calculated for $\hbar\Gamma = 2.0$ meV ($T \approx 77$ K). The results are shown for emission angles into vacuum of $\theta = 10.4°$ (a, a′), 45° (b, b′), 60° (c, c′), and 85° (d, d′)

It is evident that, for the angle $\theta = 10.4°$, the total spectrum $I_p^{(0)}(\omega,\theta)$ and the partial spectrum $I_{M1}^{(0)}(\omega,\theta)$ coincide to within 98% accuracy and form a symmetric Lorentz contour with a maximum at the longitudinal frequency ω_L. The half-width of the line is $\Delta(10.4°) \approx 2.0$ meV. This agrees very well with the corresponding regime of MEPL formation under the condition $\Gamma \gg \Gamma_c$, with $\gamma_{SD} \approx 0.04$ and $\gamma_{LT} \approx 0.01$ [13].

In this case, the maximum combined contribution of $I_{M2}^{(0)}$ and $I_{M12}^{(0)}$ does not exceed 2%. However, at the angles 45°, 60°, and 85°, this contribution amounts to 7%, 10%, and 15%, respectively, which reflects the significant role of spatial dispersion (SD) ($\gamma_{SD} \approx 0.17, 0.20, 0.23$, and $\gamma_{LT} \approx 0.06, 0.08, 0.10$).

It should be emphasized that in this case ($\hbar\Gamma = 2$ meV and $\theta \geq 45°$), MEPL is actually formed when the following conditions are satisfied: $\Gamma \geq \Gamma_c$, $\Gamma \gg \widetilde{\omega}_{LT}$. Under these conditions, only the polariton effect is partially screened by damping, whereas anomalous dispersion and the interference contribution $I_{M\beta}^{(0)}$ continue to influence the shape of the spectral contour $I_p^{(0)}$. Thus, with increasing θ, the maximum of the A_L line shifts from ω_L toward the short-wavelength side (due to the inclusion of the $I_{M2}^{(0)}$ contribution). At the same time, the asymmetry and the half-width of the A_L line increase systematically (compare cases $a - d$ and $a' - d'$ in Fig. 2). Meanwhile, the minimum value of the spectral line $I_{M12}^{(0)}$ (at ω_L) and its half-width (≈ 2.0 meV) are almost independent of θ.

As the crystal temperature increases, the corresponding increase in Γ makes it possible to observe a transformation of the MEPL spectrum caused by dissipative exciton damping. In particular, characteristic features are manifested in the dependence of the half-width Δ_A of the mixed-mode emission line in a CdS crystal on temperature and on the emission angle θ.

As can be seen from Fig. 3, the theoretical and experimental $\Delta(\theta)$ curves corresponding to different temperatures ($T =$ 4.5 (1), 15 (2), 44 (3), 77 (4) K) differ significantly from one another. First of all, attention is drawn to the horizontal segments of these curves, whose length increases with increasing temperature. Comparing the measured values of Γ for CdS samples [14] with the values of $\Gamma_c(\theta)$, one finds that the above-mentioned horizontal segments of the $\Delta(\theta)$ curves correspond to the condition $\Gamma \gg \Gamma_c$, i.e., strong damping of mechanical excitons is observed.

For the "classical" radiation shown in panel (a) of Fig. 2 (a, b, c, d), i.e., radiation described by Lorentz oscillators, the corresponding θ values are in close agreement with the horizontal segments of the $\Delta(\theta)$ curves in Fig. 3, provided that $\Gamma \gg \Gamma_c$ and $\Delta \approx \Gamma$, that is, when the half-width does not depend on θ. This conclusion is of practical importance.

In the above Fig. 2, comparison plots of the dispersion curves of mixed modes $(a' - d')$ and the photoluminescence spectra $(a - d)$ are presented for $\Gamma = 2.0$ meV. For a CdS crystal at $\hbar\Gamma = 2.0$ meV ($T \approx 77$ K), with emission angles into vacuum $\theta = 10.4°$ (a), 45° (b), 60° (c), and 85° (d), the total (solid) and partial contributions to mixed exciton-polariton luminescence are shown in panels $(a-d)$: I_{M1} (red), I_{M2} (purple), and I_{M12} (green). The triangles represent the experimental points from Fig. 1 (with the background-emission contribution excluded, $T = 77$ K).

The measurement of the half-width of the A_L line in the emission of mixed exciton-polariton modes (MEPM) at small emission angles θ is the simplest method for determining the values of the parameter $\hbar\Gamma$ near the frequency ω_L over a wide temperature range. It should be taken into account, however, that any structural imperfections of the crystal also contribute to the value of Γ. Therefore, the half-width of the mixed-mode emission line can serve as a simple and reliable criterion for evaluating sample quality in the classical case. A detailed analysis carried out previously shows that, compared with methods for determining Γ from transmission and reflection spectra, the determination of Γ from the half-width of the A_L line in MEPL is a more reliable approach when the temperature of CdS samples exceeds 60 K.

Thus, the theoretical and experimental analysis performed in this work demonstrates that, in anisotropic CdS crystals, strong dissipative damping of mixed exciton–polariton modes leads to a substantial transformation of the MEPL spectra. In the regime $\Gamma \gg \Gamma_c$, the spectral contour approaches a quasiclassical Lorentzian form only if the additional condition expressed by Eq. (6) [Eq. (7)] is also satisfied. In this limit, dissipative broadening becomes dominant, whereas the influence of spatial dispersion and light–exciton interaction on the spectral contour is substantially reduced. However, when the additional condition is violated, for example at sufficiently small L, spatial-dispersion and intermode-interference effects may again become important and modify the line shape, even though strong damping is retained.

First, when $\Gamma \neq 0$, the transformation of the spectra of normal waves involves the transfer of energy through the crystal boundary into surface-radiative modes (including inhomogeneous ones). This determines the direct contribution of such modes to the total emission intensity at frequencies $\omega \leq \omega_L$.

Second, owing to the presence of spatial dispersion, interference interaction between mixed modes arises, which manifests itself in the formation of an additional interference energy flux at the crystal boundary.

The interference contribution to the luminescence intensity may become comparable, in absolute magnitude, with the individual contributions of the separate modes if the value of Γ and the emission angle θ of the radiation leaving the crystal satisfy the roots of the dispersion equation for radiative mixed modes. Third, at large values of Γ, when dissipative broadening becomes dominant and the additional condition for the quasiclassical regime is satisfied, the exciton luminescence spectrum of mixed modes approaches a Lorentzian form with a radiative-band half-width equal to Γ. In this case, the principal contribution to the total radiation from the two possible mixed modes is determined mainly by the exciton-like mixed mode for which the modulus of the wave vector (refractive index) has the minimum value.

The mechanism of formation of the considered MEPL spectra includes the elastic scattering of polaritons, initially in quantum states with sufficiently well-defined wave vectors, into the radiative states of mixed modes from relatively large $|\mathbf{k}|$ values. The distribution function of the scattered polaritons is characterized by an exponentially decaying spatial distribution described by the effective depth L. The value of L is determined unambiguously from the dependence of the position of the maximum luminescence spectral intensity on the emission angle θ. Here, L is in practice the only parameter of the theory that varies appreciably, since the values of all other parameters are determined from independent experimental data.

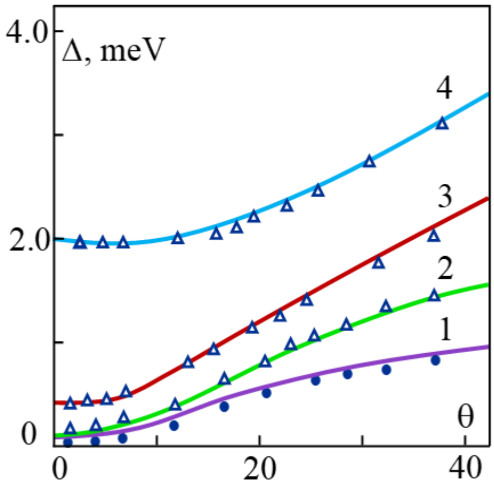

Figure 3. Dependence of the half-width Δ of the emission line of mixed modes in CdS crystals on the emission angle. The results are shown for temperatures $T = 4.5$ (1), 15 (2), 44 (3), and 77 (4) K. The points represent the experimental data, while the solid curves correspond to the theoretical calculations ($L = 1.5\,(1), 1.7\,(2), 1.6\,(3), 0.85\,(4)\ \mu$m; $\hbar\Gamma = 0.1\,(1), 0.2\,(2), 0.5\,(3), 2.0\,(4)$ meV).

CONCLUSIONS

In conclusion, the present work provides a comprehensive theoretical and experimental analysis of the formation mechanism of mixed exciton-polariton luminescence in CdS crystals under conditions of strong dissipative exciton damping. The obtained results make it possible to describe the dynamic behavior of excitons near the crystal surface, while fully accounting for the principal physical factors governing the radiation of mixed modes. The boundary conditions of the “crystal-external medium” interface employed in the theoretical model allow the emission process from the crystal surface to be explained at the microscopic level and are in good agreement with the available experimental data on specular and diffuse reflection of light for the CdS crystals under investigation [15-17].

The theoretical calculations made it possible to identify the principal features of mixed exciton-polariton luminescence spectra observed in the exciton-resonance region and to demonstrate their high degree of agreement with the experimental spectra. This approach enables one to determine a physically well-grounded set of exciton resonance parameters and also makes it possible to reproduce with high accuracy the experimental MEPL spectra observed in the $E \perp c$ and $k \perp c$ configurations. Here, ccc denotes the direction of the sixfold principal optical axis of the crystal.

The results of this study show that, under conditions of strong exciton damping, the spectral contour of mixed-mode luminescence approaches a quasiclassical Lorentzian profile. However, in anisotropic crystals, spatial dispersion and intermode interference effects continue to play an important role in spectral formation. In particular, it has been established that subtle spectral features may arise due to the mutual superposition of two mixed modes and the contribution of a single pure longitudinal mode.

Thus, the obtained results contribute to a deeper understanding of the physical nature of mixed exciton-polariton luminescence in anisotropic semiconductor crystals of the CdS type and provide an important theoretical basis for describing radiative processes in strongly dissipative excitonic systems. This approach can be used as an effective tool for determining such physical quantities as exciton damping parameters, diffusion depth, and the half-width of the emission line.

ORCID

Bozorboy J. Akhmadaliev, https://orcid.org/0000-0003-1930-8649;
Mekhriddin F.Akhmadjonov, https://orcid.org/0000-0002-1623-0404;
Tokhirbek I. Rakhmonov, https://orcid.org/0000-0002-6080-6159;
Paxlovon I. Movlonov, https://orcid.org/0009-0003-1380-9538;
Sherzod Sh. Abdullaev, https://orcid.org/0009-0007-9768-5008;
Iftikhorjon I. Yulchiev, https://orcid.org/0000-0001-9346-0441

REFERENCES

[1] S. Schumacher, G. Czycholl, and F. Jahnke, "Coherent propagation of polaritons in the nonlinear optical regime," Physical Review B – Condensed Matter and Materials Physics, **73**(3), 035318 (2006). https://doi.org/10.1103/PhysRevB.73.035318

[2] J.J. Hopfield, and D.G. Thomas, "Polariton absorption lines," Physical Review Letters, **15**(1), 22-25 (1965). https://doi.org/10.1103/PhysRevLett.15.22

[3] I. Carusotto, and C. Ciuti, "Quantum fluids of light," Reviews of Modern Physics, **85**(1), 299-366 (2013). https://doi.org/10.1103/RevModPhys.85.299

[4] J. Voigt, "Influence of spatial dispersion on the transmission spectra of CdS single crystals," Physica Status Solidi (b), **64**(2), 549-556 (1974). https://doi.org/10.1002/pssb.2220640216

[5] Y. Tian, S. Yao, Z. Zhou, H. Peng, B. Ke, W. Zhou, *et al.*, "Super-Broad-Wavelength-Range Polarization-Selective Exciton-Polariton in Sn-Doped CdS Nanowires," ACS Applied Optical Materials, **1**(1), 298-305 (2023). https://doi.org/10.1021/acsaom.2c00056

[6] V.V. Yatsyshen, and I.I. Borodina, "Reflection of circularly polarized light from a CdS semiconductor crystal near the exciton resonance taking into account spatial dispersion," Physics of Wave Processes and Radio Systems, **27**(4), 40-49 (2024). https://doi.org/10.18469/1810-3189.2024.27.4.40-49

[7] D. Sanvitto, and S. Kéna-Cohen, "The road towards polaritonic devices," Nature materials, **15**(10), 1061-1073 (2016). https://doi.org/10.1038/nmat4668

[8] M. Dagenais, and W.F. Sharfin, "Measurement of the damping dispersion of exciton polaritons in CdS," Physical Review Letters, **58**(17), 1776-1779 (1987). https://doi.org/10.1103/PhysRevLett.58.1776

[9] F. Dirnberger, J. Quan, R. Bushati, G.M. Diederich, M. Florian, J. Klein, "Magneto-optics in a van der Waals magnet tuned by self-hybridized polaritons," Nature, **620**(7974), 533-537 (2023). https://doi.org/10.1038/s41586-023-06275-2

[10] K.-H. Pantke, and I. Broser, "Damping dispersion of excitonic polaritons in CdS," Physical Review B, **48**(16), 11752-11758 (1993). https://doi.org/10.1103/PhysRevB.48.11752

[11] P. Ghosh, D. Kushavah, P.K. Mohapatra, P. Vasa, K.C. Rustagi, and B.P. Singh, "Investigations of temperature-dependent photoluminescence of uncoated and silver-coated CdS quantum dots," https://doi.org/10.48550/arXiv.1606.06711

[12] B.Zh. Akhmadaliev, N.Kh. Yuldashev, and I.I. Yulchiev, "Surface-radiative modes and longitudinal excitons in the spectra of exciton-polariton luminescence," Optics and Spectroscopy, **125**, 343-352 (2018). https://doi.org/10.1134/S0030400X18090023

[13] B.Z. Akhmadaliev, and N.K. Yuldashev, "Strong Interference Luminescence of Mixed Modes in the Neighborhood of the Critical Value of Exciton Decay," Optics and Spectroscopy, **129**(11), 1187-1192 (2021). https://doi.org/10.1134/S0030400X21090022

[14] N.N. Akhmediev, "Role of spatial dispersion in light absorption by excitons," Soviet Journal of Experimental and Theoretical Physics, **52**, 773 (1980). https://jetp.ras.ru/cgi-bin/dn/e_052_04_0773.pdf

[15] A.B. Pevtsov, and A.V. Selkin, "Diffuse reflection of light in the region of exciton resonance in a CdS crystal," Fizika Tverdogo Tela, **26**(9), 2875–2877 (1984). https://journals.ioffe.ru/articles/viewPDF/19256 (in Russian)

[16] R.D.Delgado, V.A. Kosobukin, and A.V. Selkin, "Correlation effects of a rough crystal surface in exciton spectra of diffuse reflection," Optics and Spectroscopy, **63**(1), 6–8 (1987). https://link.springer.com/article/10.1007/BF00654344

[17] N.R. Grigorieva, and A.V. Sel'kin, "Emission of Light from Compositionally Graded CdSSe/CdS Heterostructure with Smooth Near-surface Excitonic Potential," Semiconductors, **53**(16), 2052-2054 (2019). https://doi.org/10.1134/S1063782619120108

ТЕОРЕТИЧНИЙ ТА ЕКСПЕРИМЕНТАЛЬНИЙ АНАЛІЗ ЛЮМІНЕСЦЕНЦІЇ ЗМІШАНИХ ЕКСИТОН-ПОЛЯРИТОНІВ У КРИСТАЛАХ *CdS* В УМОВАХ СИЛЬНОГО ЗАТУХАННЯ ЕКСИТОНІВ

Базарбой Дж. Ахмадалієв, Мехріддін Ф. Ахмаджонов, Тохірбек І. Рахмонов, Пахловон І. Мовлонов, Шерзод Ш. Абдуллаєв, Іфтіхорджон І. Юльчієв
Ферганський державний технічний університет, Фергана, Узбекистан

У даній роботі представлено комбіноване теоретичне та експериментальне дослідження люмінесценції змішаних екситон-поляритонів в анізотропних кристалах *CdS* у режимі сильного затухання екситонів поблизу резонансу A-екситона. Просторово-дисперсійна модель радіаційних змішаних мод використовується для аналізу трансформації спектрального контуру, положення максимуму, часткових модових внесків та кутової залежності ширини лінії. Розраховані спектри для кутів випромінювання від $10.4°$ до $85°$ порівнюються з вимірюваннями фотолюмінесценції, і отримано хорошу відповідність при температурі $T \approx 77$ K для $\hbar\Gamma = 2.0$ меВ та $L = 0.85$ мкм. На відміну від традиційних підходів, які пов'язують перехід до лоренцівського профілю випромінювання лише з умовою $\Gamma \gg \Gamma_c$, показано, що цей режим додатково вимагає виконання умови, пов'язаної з транспортом екситонів, а саме $2k_0L \cdot \mathrm{Im}(n_{Mz}) \ll 1$. За виконання цих умов контур випромінювання змішаних мод наближається до квазікласичного лоренцівського профілю з напівшириною, близькою до $\hbar\Gamma$. Водночас у анізотропних кристалах *CdS* ефекти просторової дисперсії та міжмодової інтерференції не повністю пригнічуються і стають більш вираженими при більших кутах випромінювання або менших ефективних дифузійних довжинах. Отримані результати пропонують уточнений критерій ідентифікації квазікласичного режиму випромінювання та практичну основу для визначення параметра затухання екситонів і ефективної глибини дифузії з експериментальних спектрів.

Ключові слова: *люмінесценція змішаних екситон-поляритонів; кристал CdS; сильне затухання екситонів; просторова дисперсія; анізотропний напівпровідник; змішані моди; резонанс A-екситона*

EAST EUROPEAN JOURNAL OF PHYSICS. **2.** 427-430 (2026)
DOI:10.26565/2312-4334-2026-2-47 ISSN 2312-4334

SYNTHESIS AND THERMOELECTRIC PROPERTIES of TuSnSe$_2$ COMPOUND

Razim Bayramli, Ulkar Abdurahmanova*
Department of Physics, Baku Engineering University, Baku, Azerbaijan
**Corresponding Author email: uabdurahmanova@beu.edu.az*

Received January 14, 2026; revised May 12, 2026; accepted May 22, 2026

In this research work, the interaction of the SnSe-TuSe system was studied, and as a result of complex physicochemical analyses, the solubility region of TuSe in SnSe (75-100%) was determined. It was also determined that the TuSnSe$_2$ compound was obtained in a 1:1 ratio of its components, and a phase diagram of the system was constructed. X-ray structure and differential thermal analysis of the sample showed that this compound crystallizes in a hexagonal syngony. Some kinetic parameters of the triple compound TuSnSe$_2$ were determined at room temperature. Electrical conductivity (σ), thermo electromotive force (e.m.f.) (α) and thermal conductivity (χ) were studied in the temperature range T=300÷800K. In order to determine the variation in the charge carrier scattering mechanism the temperature dependences of the Hall mobility and electrical conductivity of this compound were also investigated. Based on the sign of the thermo-electromotive force and the Hall coefficient, it was determined that the conductivity in this compound is n- type. Based on the obtained results, it was determined how the concentration of charge carriers and the Hall mobility changed. Anomaly changes are observed in the temperature dependence of the electrical conductivity, thermoelectric potential and total thermal conductivity in the temperature interval T=460÷500K.

Keywords: *Electrical conductivity; Triple compound; Hexagonal syngony; Hall mobility*
PACS: 71.20.Nr,

1. INTRODUCTION

Interest in the study of semiconductor compounds of $A^{IV}B^{VI}$-type is driven by prospects for their use in semiconductor devices. For example, SnS and SnSe are used as the main materials for obtaining active elements operating in the infrared region of the optical spectrum in thermodynamic converters [1,2]. They are also used as absorber layers in thin-film solar energy converters [3,4], as photoconductors [5], as semiconductor sensors [6], and as microbatteries [7].

Thus, the fundamental properties of these compounds - small band gap, high conductivity, relatively high radiation resistance, and the predominance of ionic bonding expand their application possibilities [8]. In recent years, significant efforts have been devoted to developing photovoltaic devices using low-cost materials and simpler, more cost-effective fabrication technologies. SnSe, which has complex ionic-covalent chemical bonds, crystallizes in a deformed NaCl-type structure and has a high degree of defects and vacancies in both sublattices [9].

The high concentration of these defects, especially tin vacancies (~10^{17} cm^{-3}), results in the formation of positive-type conductivity in SnSe. On the other hand, rare earth metals are distinguished by their unique specific properties [10, 11]. It is known that the physical properties of compounds formed from defect-structured substances and lanthanide atoms vary depending on the nature of their constituent atoms.

This is due to the fact that the 4*f* level in the electronic structure of lanthanoid element atoms is not completely filled, the 4*f*- 5*d*- 6*s* transition easily occurs, and the formation of variable valence due to mobile electrons at the 4*f* level of atoms makes materials obtained with their participation an interesting object of research. For this reason, the study of the complex TuSnSe$_2$ compound with the participation of lanthanide elements, including the Tu element, is of particular interest.

Due to the presence of mobile electrons in the internal 4*f* levels in the electronic structure $f \rightarrow d \rightarrow s$ transitions easily occur, which leads to the formation of variable valence in them. Although rare earth metals are trivalent, intermediate valence arises due to transitions between electronic energy levels. This significantly affects the kinetic properties of materials obtained with their participation. The partial replacement of tin with rare-earth metals in SnSe leads to the emergence of certain physical properties. In this regard, the synthesis of new materials based on alloys and compounds involving rare earth metals demonstrates the importance of their investigation. The special importance of this research is the possibility of obtaining new promising materials with the required physical properties based on alloys and compounds with the participation of rare earth elements. [12, 13].

2. EXPERIMENTAL PROCEDURE

In this work, the SnSe-TuSe system was studied in the entire concentration range. However, since the melting temperature of the TuSe compound is very high, it was not possible to synthesize samples containing 75-100% TuSe.

A physicochemical analysis of the SnSe-TuSe system was conducted and a phase diagram of the system was constructed. At 10 mol% TuSe, a eutectic point is obtained and its melting point is 1053.2 K (780°C). The triple

---

Cite as: R. Bayramli, U. Abdurahmanova, East Eur. J. Phys. 2, 427 (2026), https://doi.org/10.26565/2312-4334-2026-2-47

compound $TuSnSe_2$ decomposes at 1053.2 K before reaching its melting point 1093.2 K. Therefore, it cannot be synthesized by direct melting of its components and it is obtained by pressing [14].

The process is carried out in the following sequence: To ensure the homogeneity and mechanical strength of the material, the components are ground into a fine powder, mixed by mechanical vibration, and then pressed. Pressing was carried out in two sequential processes: cold and hot pressing. In cold pressing, the sample was kept under a pressure of $P = 7.4$ ton/cm^2 for 5 minutes. In hot pressing, the press mold was heated to $t = 663.15$ K and kept under pressure $P = 5$ ton/cm^2 for 5 minutes.

To create homogeneity in the obtained substance, the ampoule was placed horizontally in a heater at a temperature of 953.15 K and kept for 336 hours, during which the infusion was carried out.

To determine the stoichiometric composition and crystal structure of the compound, a physicochemical analysis was carried out. The results of the complex physicochemical analyses are given in Table 1.

Table 1. Physicochemical parameters of the $TuSnSe_2$ compound

Thermal heating efficiency	Density×10^3 g/m^3		Microhardness, *MPa*	Lattice parameters, Å		
	ρ_{pikno}	ρ_{rent}		*a*	*b*	*c*
716.86	7.22	7.34	263	4.77	-	11.58

The table notes show that the obtained $TuSnSe_2$ compound is a crystal with a stoichiometric composition, a defective and partially deformed hexagonal structure.

3. RESULTS AND DISCUSSION

The main kinetic parameters of the obtained $TuSnSe_2$ triple compound were determined at room temperature, the Hall coefficient (R), electrical conductivity (σ), thermo electromotive force (α) and thermal conductivity (λ) were studied in the temperature range T = 300÷800 K. The concentration of charge carriers (n) and the Hall mobility (μ) of the sample were calculated. The results obtained for the main kinetic parameters of the $TuSnSe_2$ triple compound at a temperature of 300 K are given in Table 2.

Table 2. Some kinetic parameters of the $TuSnSe_2$ compound (300 K)

Compound	R, cm^2/C	P(n)·10^{19}, cm^{-3}	σ, Ω^{-1}·cm^{-1}	μ, cm^2/V·sec	α, μV/K	λ, W/cmK
$TuSnSe_2$	-0.22	2.8	16.2	4	-155	14.67

Figure 1 shows a graph of the temperature dependence of the electrical conductivity in the $ln\,\sigma = f(10^3/T)$ coordinates of the triple compound $TuSnSe_2$ in the temperature range T=300÷750 K

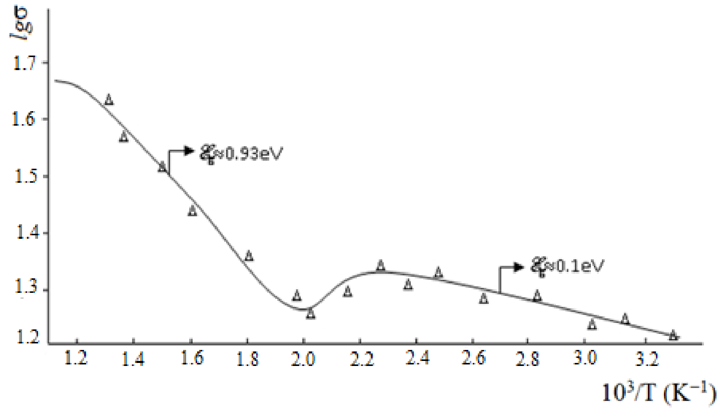

Figure 1. Temperature dependence of the electrical conductivity of the triple compound $TuSnSe_2$

The temperature dependence of the electrical conductivity can be analyzed as follows:

1. In the temperature range T=300÷440 K, the change in electrical conductivity varies according to the law $\sigma \sim T^{1.2}$, and the activation energy of charge carriers is $\Delta E_g \approx 0.1$eV.
2. In the temperature range T>510 K, this variation is according to the law of $\sigma \sim T^{1.7}$, and the width of the bandgap is $\Delta E_g \approx 0.93$eV [15].
3. In the temperature range T=440÷520 K, an anomalous change is observed. This change is most likely due to a sharp decrease in the mobility of charge carriers.

It should be noted that the main reason for the observed anomalous change is the region where the concentration of charge carriers does not change (n=const) and the region where the specific conductivity corresponds to a decrease. Thus, the concentration of charge carriers does not change with increasing temperature (n = const), that is, all free electrons in the conduction band participate in conduction.

To excite the donor (acceptor) levels, a certain amount of energy is required (the temperature should be increased). Analyses show that the decrease in σ due to the decrease in the Hall mobility of charge carriers is approximately 0.06%. The remaining part of the decrease in the value of σ is due to the anomalous change as shown above. This anomalous change is also confirmed by the properties observed in the temperature dependence of thermo-electromotive force (e.m.f.) and electrical conductivity (Fig. 2)

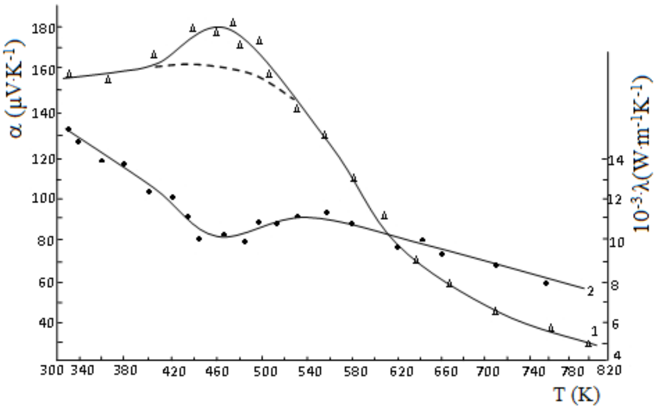

Figure 2. Temperature dependence of the thermo e.m.f. (1) and thermal conductivity (2) of the $TuSnSe_2$ compound

As can be seen from the figure, a gradual increase in the thermo e.m.f. is observed in the temperature range T = 300÷420 K. In the temperature range T = 440÷500 K α(T) changes anomalously; at temperatures T ≥ 500 K the magnitude of α(T) decreases monotonically with increasing temperature, and this rate of decrease follows the law $\alpha \sim T^{-1.38}$. The anomalous change in the temperature range T = 440÷500 K is likely to be due to a structural transformation, as in SnSe [3,4]. The anomaly in the SnSe crystal is explained by the transition of the orthorhombic structure to the cubic structure [5]. The physicochemical analysis of the obtained triple compound $TuSnSe_2$ shows that it crystallizes in a hexagonal syngony.

It is likely that a structural transformation occurs at T = 440÷500K. In order to determine the type of this structural transformation, its mechanism, and at the same time how the scattering mechanism of charge carriers changes, and to identify a general pattern, the temperature dependences of the Hall coefficient and electrical conductivity of this compound were also studied. The variations in the charge carrier concentration and Hall mobility were determined based on the obtained values.

4. CONCLUSIONS

Physicochemical analyses indicate that a eutectic is formed at the 10 mol% TuSe compound and its melting temperature is 1053.15 K. X-ray structure and differential thermal analysis showed that this compound crystallizes in a hexagonal syngony. Based on the sign of the thermo e.m.f. and the Hall coefficient, it was determined that this compound has n-type conductivity. In the temperature dependence of the electrical conductivity, thermo e.m.f., and coefficient of thermal conductivity anomaly changes are observed in the T = 460÷500 K temperature interval. Based on the values of electrical conductivity, carrier concentration and Hall conductivity, it was determined that this compound is a partially compensated semiconductor. From the temperature dependence of electrical conductivity, the activation energy of charge carriers ($E_g \approx 0.1$ eV) and the energies of the bandgap ($E_g \approx 0.93$ eV) were calculated.

Since the localized energy levels in the ground and excited states are close to the chemical potential, the effective potential created by the 4*f* scattering of Tu^{3+} ions affects the change in kinetic parameters. These energy levels are close to the Fermi energy level and affect the electronic spectrum and valence of the material. This causes changes in the values of physical parameters.

ORCID

Razim Bayramli, https://orcid.org/0009-0005-3272-2395; **Ulkar Abdurahmanova,** https://orcid.org/0000-0003-3481-0143

REFERENCES

[1] W. Shi, M. Gao, J. Wei, J. Gao, C. Fan, E. Ashalley, H. Li, and Z. Wang, "Tin selenide (SnSe): growth, properties, and applications," Advanced Sci. **5**(4), 1700602 (2018). https://doi.org/10.1002/advs.201700602

[2] Y. Zhou, W. Li, M. Wu, L.D. Zhao, J. He, S.H. Wei, and L. Huang, "Influence of defects on the thermoelectricity in SnSe: A comprehensive theoretical study," Phys. Rev. B, **97**, 245202 (2018). https://doi.org/10.1103/PhysRevB.97.245202

[3] M.A. Dar, D. Govindarajan, K.M. Batoo, M. Hadi, and G.N. Dar, "Photovoltaic and Supercapacitor performance of SnSe nanoparticles prepared through co-precipitation method," Mater. Technol. **37**(10), 1396-1409 (2022). https://doi.org/10.1080/10667857.2021.1950887

[4] G. Kaur, A. Vij, and A. Kumar, "Recent Advances in Earth Abundant and Environmentally Green Semiconducting Chalcogenide Nanomaterials for Photovoltaics Applications," Advanced Nanomaterials, 21-50 (2022). https://doi.org/10.1007/978-3-031-11996-5_2

[5] Z. Li, Y. Guo, F. Zhao, C. Nie, H. Li, J. Shi, X. Liu, *et al.*, "Effect of film thickness and evaporation rate on co-evaporated SnSe thin films for photovoltaic applications," RSC Adv. **10**(28), 16749-16755 (2020). https://doi.org/10.1039/D0RA01749C

[6] K. Assili, O. Gonzalez, K. Alouani, and X. Vilanova, "Structural, morphological, optical and sensing properties of SnSe and $SnSe_2$ thin films as a gas sensing material," Arab. J. Chem. **13**(1), 1229-1246 (2020). https://doi.org/10.1016/j.arabjc.2017.10.004

[7] Z. Li, J. Ding, and D. Mitlin, "Tin and tin compounds for sodium ion battery anodes: phase transformations and performance," Acc. Chem. Res. **48**(6), 1657-1665 (2015). https://doi.org/10.1021/acs.accounts.5b00114

[8] H.S. Jagani, V. Dixit, A. Patel, J. Gohil, and V.M. Pathak, "Stability & durability of self-driven photo-detective parameters based on $Sn_{1-\beta}Sb_{\beta}Se$ (β = 0, 0.05, 0.10, 0.15, 0.20) ternary alloy single crystals," RSC Adv. **12**(44), 28693-28706 (2022). https://doi.org/10.1039/D2RA05492B

[9] M.R. Burton, C.A. Boyle, T. Liu, J. McGettrick, I. Nandhakumar, O. Fenwick, and M.J. Carnie, "Full Thermoelectric Characterization of Stoichiometric Electrodeposited Thin Film Tin Selenide (SnSe)," ACS Appl Mater Interfaces, **12**(25), 28232-28238 (2020). https://doi.org/10.1021/acsami.0c06026

[10] W. Shi, M. Gao, J. Wei, and J. Gao, "Tin Selenide (SnSe): Growth, Properties, and Applications," Advanced Science, **5**(4), 1700602 (2018). http://dx.doi.org/10.1002/advs.201700602

[11] M. Kumar, S. Rani, Y. Singh, and K.S. Gour, "Tin-selenide as a futuristic material: properties and applications," **11**(12), 6477-6503 (2021). http://dx.doi.org/10.1039/d0ra09807h

[12] J.I. Huseynov, M.I. Murguzov, and S.S. Ismayilov, "Specific features of self-compensation in $Er_xSn_{1-x}Se$ solid solutions," Semiconductors, **47**, 323–326 (2013). https://doi.org/10.1134/S106378261303010X

[13] D.I. Huseynov, M.I. Murguzov, and S.S. Ismailov, "Thermal conductivity of $Er_xSn_{1-x}Se$ ($x \leq 0.025$) solid solutions," Inorg. Mater. **44**, 467–469 (2008). https://doi.org/10.1134/S0020168508050063

[14] J.I. Huseynov, R.B. Bayramov, and A.M. Mammadov, "Physical-chemical properties of SnSe-DySe system alloys," Chemical Problems, (1), 110-113 (2009). https://chemprob.org/?page_id=161

[15] I. Abbasov, M. Musayev, J. Huseynov, E. Gavrishuk, S. Asadullayeva, A. Rajabli, and D. Askerov, "Temperature behavior of X-Ray luminescence spectra of ZnSe," International Journal of Modern Physics B, **36**(2), 2250018 (2022). https://doi.org/10.1142/S0217979222500187

СИНТЕЗ ТА ТЕРМОЕЛЕКТРИЧНІ ВЛАСТИВОСТІ СПОЛУКИ $TuSnSe_2$

Разім Байрамлі, Улькар Абдурахманова
Кафедра фізики, Бакинський інженерний університет, Баку, Азербайджан

У цій дослідницькій роботі було вивчено взаємодію системи SnSe-TuSe, і в результаті комплексних фізико-хімічних аналізів було визначено область розчинності TuSe в SnSe (75-100%). Також було встановлено, що сполуку $TuSnSe_2$ отримано у співвідношенні її компонентів 1:1, і побудовано фазову діаграму системи. Рентгеноструктурний та диференціально-термічний аналіз зразка показали, що ця сполука кристалізується в гексагональній сингонії. Деякі кінетичні параметри потрійної сполуки $TuSnSe_2$ були визначені за кімнатної температури. Електропровідність (σ), термоелектрорушійна сила (ЕРС) (σ) та теплопровідність (σ) були досліджені в діапазоні температур T = 300÷800 K. Для визначення зміни механізму розсіювання носіїв заряду також було досліджено температурні залежності рухливості Холла та електропровідності цієї сполуки. На основі знака термоелектрорушійної сили та коефіцієнта Холла було встановлено, що провідність у цій сполуці є n-типу. На основі отриманих результатів було визначено, як змінювалися концентрація носіїв заряду та рухливість Холла. Спостерігаються аномальні зміни в температурній залежності електропровідності, термоелектричного потенціалу та загальної теплопровідності в інтервалі температур T=460÷500K.

Ключові слова: *електропровідність; потрійна сполука; гексагональна сингонія; рухливість Холла*

EAST EUROPEAN JOURNAL OF PHYSICS. **2.** 431-435 (2026)
DOI:10.26565/2312-4334-2026-2-48 ISSN 2312-4334

TEMPERATURE DEPENDENCE OF THE MAIN PARAMETERS DETERMINING THE INTERBAND ABSORPTION SPECTRUM OF a-Si:H

Rustamjon G. Ikramov[1], **Khurshidbek A. Muminov**[1]*, **Mashkhura A. Nuritdinova**[1],
Bobur Q. Sultanov[1], **Sarvar S. Umarov**[1], **Nosirbek A. Sattarov**[2]
[1]*Namangan State Technical University, 12, Yangi Namangan, Namangan 160115, Uzbekistan*
[2]*Kimyo International University in Tashkent, Uzbekistan*
**Corresponding Author e-mail: mxadhamjon@gmail.com*

Received March 2, 2026; revised May 18, 2026; accepted May 19, 2026

In this work, the temperature dependence of the interband optical absorption coefficient of hydrogenated amorphous silicon (a-Si:H) has been investigated both experimentally and theoretically. By fitting the values obtained from the optical absorption coefficient formula, the temperature dependence of the characteristic vibration energy of a-Si:H was studied using the Bose-Einstein and Varshni formulas.

Keywords: *Hydrogenated amorphous silicon; Interband optical absorption coefficient; Temperature; Characteristic vibration energy; Bose-Einstein formula; Varshni formula*
PACS: 61.43Dq, 68.43 Mn

INTRODUCTION

Currently, semiconductor materials, especially semiconductor-ferroelectric and amorphous semiconductor structures, are of great interest to researchers [1-3]. Based on theoretical and practical research on these structures, it has been possible to increase the thermal, optical, and energy efficiency of several diode structures [4-8].

Amorphous hydrogenated silicon *(a-Si:H)* has remained one of the most popular semiconductor electronics materials for many years due to its combination of low production costs, the ability to fabricate large-area devices, and a high optical absorption coefficient [9]. It is widely used in the production of thin-film solar cells, photosensitive sensors, and active matrices of liquid crystal displays [10-12]. One of the key characteristics determining the efficiency of optoelectronic devices based on *a-Si:H* is the mobility gap. The energy spectrum of amorphous materials is characterized by density-of-states "tails," making the optical properties of *a-Si:H* extremely sensitive to external influences, particularly temperature [13]. Analysis of the temperature dependence of interband absorption is crucial for predicting the performance of photovoltaic converters under real-world operating conditions, where temperature fluctuations are inevitable.

Typically, the empirical Varshni equation and the semi-empirical Bose–Einstein model, which takes into account the interaction of electrons with phonons, are used to describe the temperature dependence of the energy gap in semiconductors [14, 15]. However, the applicability of these models to amorphous structures requires a detailed comparison of theoretical calculations with experimental data over a wide temperature range. Furthermore, the proportionality coefficient in the interband absorption formula, which reflects the degree of disorder in the structure, can also be temperature-dependent, as is often observed in simplified models [16].

The aim of this work is to investigate the temperature dependence of the mobility gap width and proportionality coefficient in *a-Si:H* by fitting experimental absorption spectra to theoretical dependences. A comparative analysis of parameters obtained using the Bose-Einstein and Varshni models is also provided, clarifying the mechanisms by which thermal disorder influences the material's electronic structure.

In [13], experimentally determined values of the temperature dependence of the spectra of the interband absorption coefficient of amorphous hydrogenated silicon *a-Si:H* are presented (Fig. 1).

In the work [17] for the analytical form of the interband absorption spectrum, according to the Kubo-Greenwood formula and the Davis-Mott approximation method, the expression was obtained:

$$\alpha_2(\hbar\omega)=\frac{B}{4\hbar\omega E_g}\left[2(\hbar\omega-E_g)\sqrt{E_g\hbar\omega}-(E_g-\hbar\omega)^2\,arctg\left(\frac{E_g-\hbar\omega}{2\sqrt{E_g\hbar\omega}}\right)\right] \qquad (1)$$

where $B=N(\varepsilon_V)N(\varepsilon_C)\dfrac{8\pi^4e^2\hbar^2a}{nc(m^*)^2}\lim\limits_{\delta x\to 0}$, a is the average distance between semiconductor atoms, m^* is the effective mass of electrons in the allowed bands of *a-Si:H*, and E_g is the energy width of the mobility gap of *a-Si:H*. $N(\varepsilon_V)$ and

---

Cite as: R.G. Ikramov, Kh.A. Muminov, M.A. Nuritdinova, B.Q. Sultanov, S.S. Umarov, N.A. Sattarov, East Eur. J. Phys. 2, 431 (2026), https://doi.org/10.26565/2312-4334-2026-2-48

$N(\varepsilon_C)$ are the effective values of the density of electron states at the boundaries of the valence band and conduction band, respectively.

RESEARCH METHODS AND RESULTS

From expression (1), it is evident that in order to calculate the interband absorption spectrum, it is necessary to determine the values of B and E_g included in it. According to the Tauc rule [15], the mobility gap energy could not be determined due to the limited number of experimental points. But these calculations showed that as the temperature increases, the mobility gap decreases. Therefore, considering B and Eg as fitting parameters, we use trial and error to fit the calculation results obtained by formula (1) to the experimental results shown in Fig. 1. To ensure consistency between the experimental and calculated results (curves in Fig. 1), the obtained values of the parameters B and E_g are presented in Table 1. The error of the experimental points and the calculation results does not exceed the permissible error of the experiment.

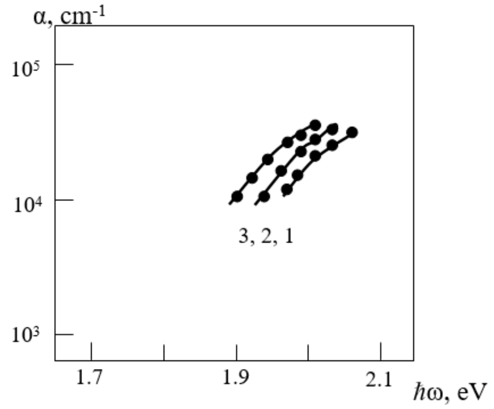

Figure 1. Experimental data from work [9]: 1 - T=12.7 K, 2 - T=151 K, 3 - T=293 K, and the results of calculations using formula (1) (solid curves). Points – experiment.

Table 1. Temperature dependence of the mobility gap width of unannealed a-Si:H and the proportionality coefficient (B) of formula (1).

No.	T	E_g, eV	B, cm^{-1}
1	12.7 K	1.861	$3.647{*}10^5$
2	151 K	1.841	$3.745{*}10^5$
3	293 K	1.793	$3.861{*}10^5$

In work [14], the Varshni empirical formula, which determines the dependence of the band gap of semiconductors (for amorphous semiconductors, the energy width of the mobility gap) on temperature, is presented in the following form: (Varshni's formula):

$$E_g = E_{g0} - \alpha T^2 / (T + \beta) \tag{2}$$

Here, E_{g0} is the width of the forbidden band at temperature T = 0 K, the empirical Varshni coefficients α are the temperature coefficient of the width of the mobility gap, β is a constant value.

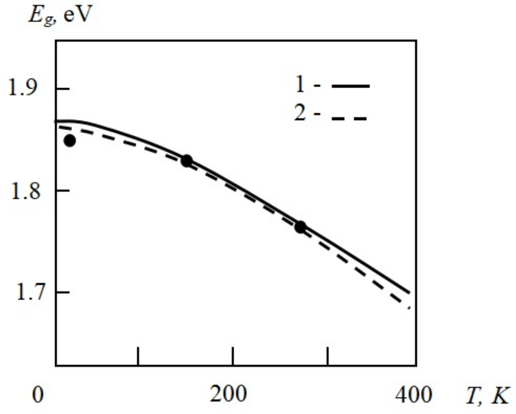

Figure 2. Dependence of the width of the mobility gap of amorphous hydrogenated silicon on temperature. Results obtained: 1 - according to the Varshni formula and 2 - according to the Bose-Einstein formula. Points - experimental data.

In work [18], the expression that determines the dependence of the band gap width of a semiconductor on temperature is presented in the following form (Bose-Einstein formula):

$$\Delta E_g(T) = 2\alpha_B / (\exp(\Theta./T) - 1) \tag{3}$$

Here, $\Delta E_g = E_{g0} - E_g$ is the change in the mobility gap width depending on temperature, $\boldsymbol{\alpha_B}$ is the temperature coefficient of the mobility band gap width, and Θ is the average phonon temperature.

In the work [19] for theoretical studies of the temperature dependence of the energy width of the mobility band of semiconductors *(MoS_2, $MjSe_2$, $MoTe_2$, WSe_2)* in the temperature range from 20 to 300 K using the Varshni (2) and Bose-Einstein (3) formulas. By fitting the experimental data to formula (2) for α and β, the average values obtained were $\alpha \approx (5.9 \cdot 10^{-4} - 4.4 \cdot 10^{-4})$ eV/K and for $\beta \approx (250 - 190)$ K.

Precisely, thus from formula (3) for α_B and Θ the values $\alpha_B \approx (6.8 \cdot 10^{-2} - 2.5 \cdot 10^{-2})$ eV and for $\Theta \approx (220\text{-}150)$ K were obtained.

In the work [20], the temperature dependence of the energy width of the mobility band of crystalline semiconductors such as (*GaAs, InP, ZnSe, Si*) was investigated using the present method. For the higher than the specified parameters, the following results were obtained for $\alpha \approx (1.02 \cdot 10^{-3} - 5.5 \cdot 10^{-4})$ eV/K and, for $\beta \approx (823\text{-}225)$ K and for $\alpha_B \approx (7.3 \cdot 10^{-2} - 5.7 \cdot 10^{-2})$ eV and for $\Theta \approx (260\text{-}240)$ K. Also, in the work [21] for InSe for these parameters, the values $\alpha \approx 4.6 \cdot 10^{-4}$ eV/K, $\beta \approx 279$ K, and for $\alpha_B \approx 2.06 \cdot 10^{-2}$ eV, $\Theta \approx 205$ K were obtained.

Calculations performed by substituting the energy mobility gap values for a-Si:H from Table 1 into formula (2) showed that at $\alpha = 4.95 \cdot 10^{-4}$ eV/K and $\beta = 438$ K, these values are in good agreement with formula (2). These results are presented in Fig. 2 (solid curve).

Calculations performed by substituting the mobility gap values from Table 1 into formula (3) showed that at $\boldsymbol{\alpha_B} = 3.61 \cdot 10^{-2}$ eV and $\Theta = 236$ K, these values are in good agreement with formula (3) (Fig. 2, dashed curve). From the above values, it is evident that the coefficients in formulas (2) and (3) do not differ significantly for crystalline and amorphous semiconductors.

Figure 3 shows the dependence of the value of the proportionality coefficient B from formula (1) on temperature. It is clear from the figure that as the temperature increases, the proportionality coefficient also increases.

Figure 4 shows the experimentally determined values of the spectra of the interband optical absorption coefficient of samples prepared using the same technology as amorphous hydrogenated silicon, with similar electrophysical properties, annealed for 30 minutes in the temperature range of 400–600 K, with a step of Δ25 K from 773 K to 898 K [9].

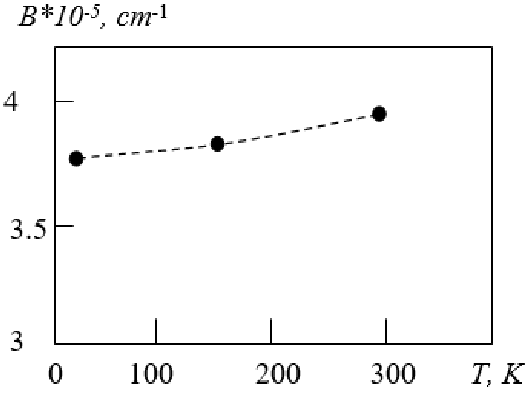

Figure 3. Dependence of the proportionality coefficient (B) in formula (1), written for the spectrum of the interband optical absorption coefficient of amorphous hydrogenated silicon, on temperature

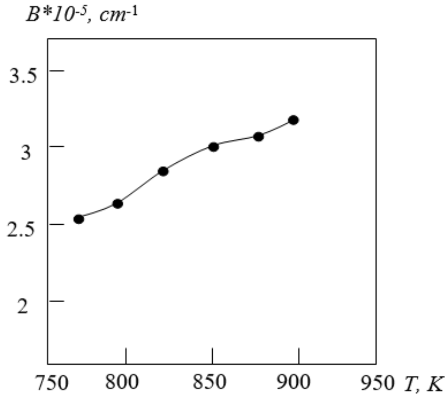

Figure 6. Dependence of the proportionality coefficient B from formula (1) on the temperature for annealed amorphous hydrogenated silicon

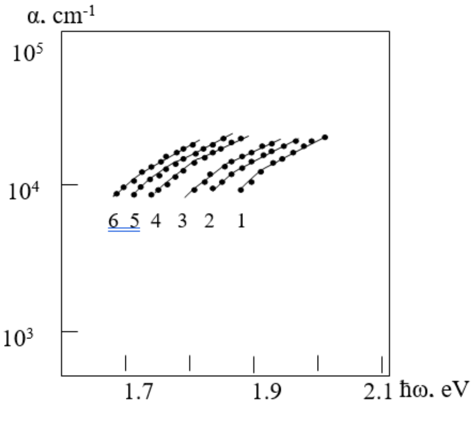

Figure 4. Experimental data from work [9]: 1 - T=773 K, 2 - T=798 K, 3 - T=823 K, 4 - T=848 K, 5 - T=873 K, 6 - T=898 K, and the results of calculations using formula (1) (solid curves). Points - experiment

The same figure also presents the results (curves) of calculations obtained using formula (1) by approximating the experimental data. Table 2 presents the values of $\boldsymbol{E_g}$ and $\boldsymbol{B}$ from formula (1), obtained as a result of these approximations, and shows their dependence on temperature. Figure 5 shows the results obtained using the Varshni and Bose-Einstein formulas for the dependence of $\boldsymbol{E_g}$ on temperature from Table 2.

The error in Fig. 5 and the other figures of experimental and calculated data does not exceed 8%. It was found that to calculate the mobility gap width of amorphous hydrogenated silicon using formula (2), the parameters of this formula should be equal to $\alpha=3.29\times10^{-4}$ eV/K and $\beta=135$ K. It was determined that to calculate the mobility gap width of a-Si:H using formula (3), the parameters should be equal to $\alpha_B=5.63\times10^{-2}$ eV and $\Theta=344$ K.

Table 2. Temperature dependence of the mobility gap width of annealed a-Si:H samples and the proportionality coefficient (B) of formula (1)

T, K	773	798	823	848	873	898
E_g, eV	1.673	1.659	1.651	1.642	1.634	1.626
$B*10^{-5}$, cm^{-1}	2.568	2.652	2.875	2.988	3.022	3.324

Figure 6 shows the dependence of the proportionality coefficient from Eq. (1) on temperature. For amorphous semiconductors, the value of B is equal to $B = N(\varepsilon_V)N(\varepsilon_C)\dfrac{8\pi^4 e^2\hbar^2 a}{nc(m^*)^2}$.

Here, it is known that the only free variable is the average distance a between the atoms of amorphous hydrogenated silicon. Figures 3 and 6 show that B increases with increasing temperature, which is associated with an increase in the vibrational frequency and amplitude of the atoms with increasing temperature, as a result of which the average distance between them also increases.

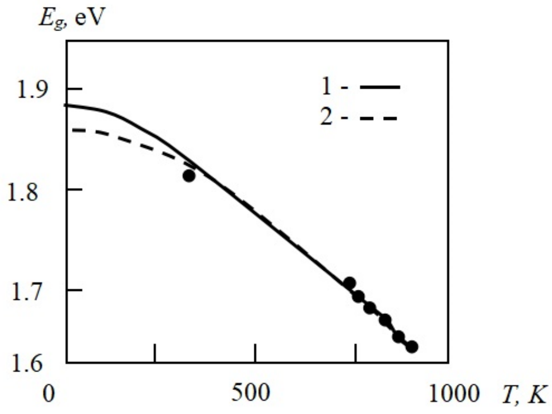

Figure 5. The mobility gap width of annealed amorphous hydrogenated silicon as a function of temperature. Results obtained using: 1 - the Varshni formula and 2 - the Bose-Einstein formula Points-experimental data

CONCLUSIONS

Thus, in this study, the temperature dependence of the interband absorption coefficient spectra of amorphous hydrogenated silicon was theoretically investigated. By comparing the experimentally determined interband absorption spectrum with the results obtained using the derived interband absorption formula, the mobility gap widths and proportionality coefficients in the formula were determined. It was shown that the determined temperature dependence of the mobility gap width is consistent with the Varshni and Bose-Einstein distributions. From the temperature dependence of the proportionality coefficient, it was established that the average distance between atoms in amorphous semiconductors increases with increasing temperature.

ORCID

Rustamjon G. Ikramov, https://orcid.org/0000-0003-1629-1300; **Khurshidbek A. Muminov**, https://orcid.org/0000-0001-6547-2592
Nosirbek A. Sattarov, https://orcid.org/0009-0005-0506-0269

REFERENCES

[1] Z.T. Azamatov, Sh.B. Utamuradova, M.A. Yuldoshev, and N.N. Bazarbaev. “Some properties of semiconductor-ferroelectric structures,” East Eur. J. Phys. (2), 187-190. (2023). https://doi.org/10.26565/2312-4334-2023-2-19

[2] B.M. Ali, A.A. Abdulazez, G.P. Priya, S. Ray, A. Pal, R. Sharma, S. Usanov, *et al.*, “Modification of graphenylene nanostructure as a promising material for adsorption and sensing of 5-fluorouracil,” First-principles investigations. Journal of Molecular Graphics and Modelling, **142**, 109210 (2026). https://doi.org/10.1016/j.jmgm.2025.109210

[3] S.F. Samadov, N.V.M. Trung, A.A. Sidorin, S.I. Ibragimova, S.H. Jabarov, M.A. Yuldoshev, O.S. Orlov, *et al.*, “Effect of Zn and Fe doping on vacancy cluster formation in Cu–In–Se system,” Micro and Nanostructures, **209**, 208451 (2026). https://doi.org/10.1016/j.micrna.2025.208451

[4] J.R. Yusupov, M. Ehrhardt, Kh.Sh. Matyokubov, and D.U. Matrasulov, “Driven transparent quantum graphs,” Physica Scripta, **100**(7), (2025). https://doi.org/10.1088/1402-4896/ade014

[5] F.A. Giyasova, A.Z. Rakhmatov, Kh.N. Bakhronov, M.A. Yuldoshev, F.A. Giyasov, A.N. Olimov, and N.A. Sattarov, “Physical Principles of Photocurrent Generation in a Silicon-Based Photodiode Structure with a Schottky Barrier,” East Eur. J. Phys. (4), 397 (2025). https://doi.org/10.26565/2312-4334-2025-4-38

[6] F.A. Giyasova, Kh.N. Bakhronov, M.A. Yuldoshev, I.B. Sapaev, R.G. Ikramov, F.A. Giyasov, M.R. Bekchanova, *et al*., “Study of the Influence of Temperature on the Transitions of the CdS/Si/CdTe Heterosystem,” East Eur. J. Phys. (4), 461 (2025). https://doi.org/10.26565/2312-4334-2025-4-47

[7] F.A. Giyasova, and M.A. Yuldoshev, “Investigation of temporal characteristics of photosensitive heterostructures based on gallium arsenide and silicon,” Chalcogenide Letters, 22(2), 123–129 (2025). https://doi.org/10.15251/CL.2025.222.123

[8] M.S. Payzullakhanov, F.A. Giyasova, M.A. Yuldoshev, Ch.X. Toshpulatov, R.U. Ernazarov, F.A. Giyasov, A. Urishev, A.D. Paluanova, East Eur. J. Phys. (1), 233 (2026). https://doi.org/10.26565/2312-4334-2026-1-25

[9] R.A. Street, *Hydrogenated Amorphous Silicon*, (Cambridge University Press, 1991).

[10] A.V. Shah, J. Meier, E. Vallat-Sauvain, N. Wyrsch, U. Kroll, C. Droz, and U. Graf, “Thin-film silicon solar cell technology,” Solar Energy Materials and Solar Cells, **78**, 469–491 (2003). https://doi.org/10.1016/s0927-0248(02)00448-8

[11] M.S. Paizullakhanov, F.A. Giyasova, Kh.N. Bakhronov, M.A. Yuldoshev, A.A. Mamadaliev, F.A. Giyasov, F.T. Akbarova, B. Ismatov, M.R. Bekchanova. Investigation of the Processes Involved in the Formation of Pyroxene Materials during Solar Melting in a Large Solar Furnace. Journal of Ovonic Research. Vol. 22, No. 1, (2026). https://doi.org/10.15251/JOR.2026.221.51

[12] N.Yu. Sharibaev, A.Q. Ergashov, S.B. Fazliddinov, R.G. Ikramov, M.A. Yuldoshev, A.A. Abdulxayev, Journal of Ovonic Research. Vol.21, No.6, (2025). https://doi.org/10.15251/JOR.2025.216.859

[13] G.D. Cody, T. Tiedje, B. Abeles, B. Brooks, and Y. Goldestein, “Disorder and the Optical-Absorption Edge of Hydrogenated Amorphous Silicon,” Physical Review Letters, **47**(20), 1480-1483 (1981). https://doi.org/10.1051/jphyscol:1981463

[14] Y.P. Varshni, “Temperature Dependence of the Energy Gap in Semiconductors,” Physica, **34**, 149-154 (1967). https://doi.org/10.1016/0031-8914(67)90062-6

[15] K.P. O’Donnell, and X. Chen, “Temperature dependence of semiconductor band gaps,” Applied Physics Letters, **58**(25), 2924-2926 (1991). https://doi.org/10.1063/1.104723

[16] G. Weiser, and H. Mell, “The temperature dependence of the optical absorption edge of a-Si:H,” Journal of Non-Crystalline Solids, **299**, 313–317 (2002). https://doi.org/10.1016/0022-3093(89)90143-9

[17] R.G. Ikramov, Kh.A. Muminov, M.A. Nuritdinova, B.Q. Sutonov, and O.T. Kholmirzayev, “Calculation of the density of the distribution of electronic states in the conduction band from the fundamental absorption spectra of amorphous semiconductors, ” East European Journal of Physics, (4), 153-2158 (2023). https://10.26565/2312-4334-2023-4-16

[18] Q. Guo, and A. Yoshida, “Temperature Dependence of Band Gap Chang in InN and AlN,” Pn. J. Appl. Phys. **33**, 2453-2456 (1994). https://doi.org/10.1143/JJAP.33.2453

[19] J. Kopaczek, S. Zelewski, K. Yumigeta, R. Sailus, S. Tongay, and R. Kudrawiec, “Temperature Dependence of the indirect Gap and the Direct Optical Transitions at the High-Symmetry Point of the Brillouin Zone and Band Nesting in MoS_2, $MoSe_2$, WS_2, and WSe_2 Crystals,” J. Phys. Chem. C, **126**, 5665-5674 (2022). https://pubs.acs.org/doi/pdf/10.1021/acs.jpcc.2c01044

[20] D.-Y. Lin, H.-P. Hsu, C.-W. Wang, S.-W. Chen, Y.-T. Shih, S.-B. Hwang, and P. Sitarek, “Temperature-Dependent Absorption of Ternary $HfS_{2-x}Se_x$ 2D Layered Semiconductors,” Materials, **15**, 6304 (2022). https://doi.org/10.3390/ma15186304

[21] W.-T. Wu, K.-K. Tiong, S.-Y. Hu, Y.-C. Lee, R.-S. Chen, and C.-T. Wu, “Optical Study on Temperature-Dependent Absorption Edge of γ-InSe-Layered Semiconductor,” Appl. Sci. **14**, 6676 (2024). https://doi.org/10.3390/app14156676

ТЕМПЕРАТУРНА ЗАЛЕЖНІСТЬ ОСНОВНИХ ПАРАМЕТРІВ, ЩО ВИЗНАЧАЮТЬ СПЕКТР МІЖЗОННОГО ПОГЛИНАННЯ a-Si:H

Рустамджон Г. Ікрамов[1], Хуршидбек А. Мумінов[1], Машхура А. Нурітдінова[1], Бобур Q. Султанов[1], Сарвар С. Умаров[1], Носірбек А. Саттаров[2]

[1]Наманганський державний технічний університет, 12, Янгі Наманган, Наманган 160115, Узбекистан
[2]Міжнародний університет Кіміо в Ташкенті, Узбекистан

У даній роботі експериментально та теоретично досліджено температурну залежність коефіцієнта міжзонного оптичного поглинання гідрогенізованого аморфного кремнію (a-Si:H). Шляхом апроксимації значень, отриманих з формули коефіцієнта оптичного поглинання, температурну залежність характеристичної енергії коливань a-Si:H було досліджено за формулами Бозе-Ейнштейна та Варшні.

Ключові слова: *гідрогенізований аморфний кремній; коефіцієнт міжзонного оптичного поглинання; температура; характеристична енергія коливань; формула Бозе-Ейнштейна; формула Варшні*

East European Journal of Physics. 2. 436–444 (2026)

DOI: 10.26565/2312-4334-2026-2-49 ISSN 2312-4334

ELECTROMAGNETIC PROPERTIES OF A HYBRID SOLID-STATE STRUCTURE INCORPORATING A PLASMA-LIKE MEDIUM AND A METASURFACE

N.N. Beletskii, **O.Yu. Averkov**, **Yu.O. Averkov**[*]
O. Ya. Usikov Institute for Radiophysics and Electronics of the National Academy of Sciences of Ukraine,
12, Acad. Proskura Str., Kharkiv, 61085, Ukraine
[*]*Corresponding Author e-mail: yuriyaverkov@gmail.com*

Received February 24, 2026; revised April 5, 2026; accepted May 6, 2026

In this paper, we theoretically investigate the dispersion properties of surface and bulk-surface electromagnetic waves propagating in a hybrid layered solid-state structure containing an isotropic plasmonic metasurface. This structure consists of a semi-infinite dielectric 1, an isotropic metasurface, a dielectric layer 2, and a semi-infinite plasma-like medium. We derive an exact analytical dispersion relation for the coupled electromagnetic modes and perform a comprehensive numerical analysis of it. Our analysis demonstrates how the metasurface conductivity, the dielectric layer thickness, and the semiconductor plasma frequency significantly influence the resonant interaction of the surface waves. It has been revealed that adding a plasma-like medium as a substrate leads to the emergence of hybrid surface waves and the possibility of bulk-surface waves. In fact, we found a significant difference between metal and semiconductor substrates. Indeed, to obtain exactly the same splitting value in a system with a metal substrate, a dielectric spacer approximately seven times thicker is required. This geometry difference makes semiconductors a much more practical choice for deep subwavelength miniaturization. The results provide a theoretical basis for the development and optimization of novel tunable waveguides, sensors, and slow-wave devices operating in the microwave and terahertz frequency ranges.

Keywords: *Plasmonic metasurface; Dielectric layer; Semiconductor; Plasma-like medium; Surface electromagnetic wave; Bulk-surface electromagnetic wave; Dispersion relation*

PACS: 78.67.Pt, 73.20.Mf, 72.30.+q

1. INTRODUCTION

Nanophotonics and optoelectronics today depend heavily on finding new ways to manipulate electromagnetic waves at the subwavelength level. In this context, two-dimensional metamaterials, or metasurfaces, have become the subject of intense research interest because they exhibit electrodynamic properties that simply do not exist in natural media [1]. Plasmonic metasurfaces are of particular interest. Such structures are powerful tools for light control, enabling tight field confinement, individual routing of surface waves, and precise control of photon density states. Fundamental theory of plasmonic metasurfaces has already clarified many of their unusual dispersion characteristics. For example, previous studies have shown that these metasurfaces support highly localized hybrid electromagnetic waves. Their spectrum is usually divided into two separate branches associated with hybrid transverse electric (TE) and transverse magnetic (TM) modes [2, 3]. A distinctive feature of these systems is that their isofrequency contours can transform from closed elliptical shapes to open hyperbolas as the frequency changes—a phenomenon known as an optical topological transition [4]. To

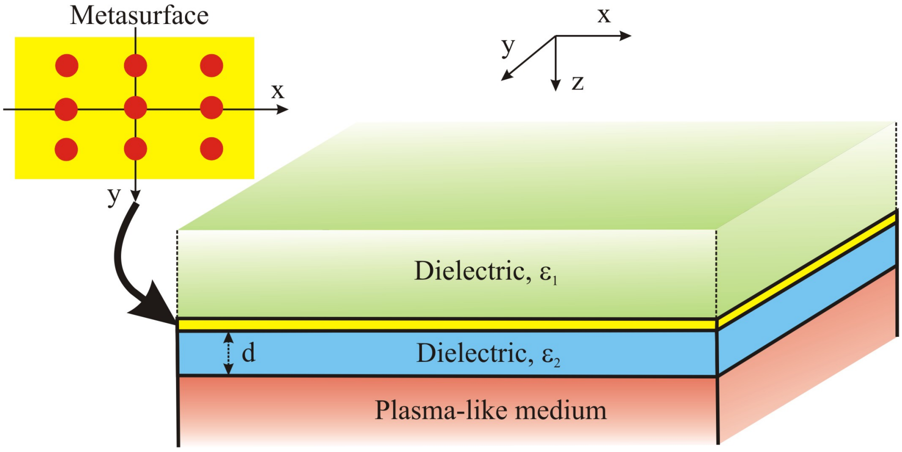

Figure 1. Geometry of the structure.

Cite as: N.N. Beletskii, O.Yu. Averkov, Yu.O. Averkov, East Eur. J. Phys. 2, 436 (2026), https://doi.org/10.26565/2312-4334-2026-2-49

accurately model these effects, it is necessary to carefully determine the effective surface conductivity, a parameter that can be successfully extracted using a combination of far-field and near-field measurements [5].

Applying anisotropic metasurface concepts to natural two-dimensional materials such as black phosphorus or graphene, as well as to complex multilayer heterostructures, provides even greater flexibility for wave control. Doped 2D materials naturally support strongly directional hyperbolic plasmons, and their routing can be dynamically tuned using an electric gate [6]. Interestingly, strong field localization can also occur at the physically tilted edges of these anisotropic sheets [7]. When multiple metasurfaces are stacked on top of each other, the interactions of their eigenmodes become quite complex. Some studies even draw a parallel between these coupled optical states and Feynman paths in electron transport [8]. From a theoretical point of view, the analysis of such stratified systems is most conveniently and rigorously performed using the transfer matrix formalism [9].

Recent work has considerably broadened the known classes of guided modes and dispersion regimes supported by engineered metasurfaces. In particular, analytical models for metasurfaces with anisotropic polarizabilities and arbitrary incident angles have been developed [10], engineered equifrequency contours have been used to realize self-collimated surface-wave steering [11], and twisted anisotropic heterometasurfaces have been shown to support hybrid surface waves [12]. In parallel, hyperbolic shear metasurfaces [13] and antihyperbolic surface waves on hyperbolic metasurfaces [14] have revealed additional possibilities for tailoring axial dispersion, confinement, and modal topology in artificial anisotropic platforms.

Recent studies have also demonstrated the possibility of realizing a scattering-free plasmonic Brewster effect via isotropic metasurfaces, including the all-angle regime for p-polarized surface waves [15].

Due to their strong anisotropy and tunability, these structures enable a wide range of specialized electromagnetic effects. Recent publications highlight their use to achieve nearly perfect spin selectivity of photons [16] and highly sensitive chiral probing [17]. They also serve as an excellent means for generating quantum photon-plasmon states under nonlinear conditions [18]. Because surface plasmons are so strongly confined near these structures, they can exert enormous transverse optical forces on neighboring nanoparticles [19] or contribute to highly directional radiative heat transfer [20]. Other practical applications include multi-band polarization converters [21] and fast helicity switches, often implemented using reversible Babinet checkerboard patterns [22, 23] or periodic arrangements of polariton cylinders [24].

Despite rapid developments in this field, some complex hybrid configurations still lack a detailed electrodynamic description. One such system is an asymmetric solid-state structure in which a dielectric layer is located between a plasmonic metasurface and a semi-infinite plasma-like medium (e.g., a semiconductor or metal). In this article, we theoretically and numerically investigate the dispersion characteristics of electromagnetic waves propagating through this geometry. Our main goal is to establish the exact conditions that lead to strong localization of electromagnetic waves and to investigate the frequency splitting effect of coupled surface modes guided at different interfaces of the solid-state structure with an isotropic plasmonic metasurface.

2. PROBLEM STATEMENT

2.1. Main equations and boundary conditions

Consider a flat-layered solid-state structure consisting of a semi-infinite dielectric with dielectric permittivity ε_1, a plasmonic metasurface, a dielectric layer with thickness d and dielectric permittivity ε_2, bordering on a semi-infinite plasma-like solid medium (a semiconductor or metal, see Fig. 1). The axis Oz is perpendicular to the boundary between the media and points deep into the plasma-like medium. The plane $z = 0$ coincides with the plane of the metasurface. The physical implementation of a metasurface is a periodic array of conductive thin discs, whose thickness, like the period, is much smaller than the wavelength. In this case, the electrodynamic response of such a structure can be described by macroscopic isotropic effective surface conductivity σ without taking into account spatial dispersion normal to the interface. The expression for σ will be given below. Electromagnetic fields in the structure under consideration are described by Maxwell's equations:

$$\nabla \times \mathbf{H}(\mathbf{r},t) = \frac{1}{c}\frac{\partial \mathbf{D}(\mathbf{r},t)}{\partial t} + \frac{4\pi}{c}\mathbf{j}(\mathbf{r},t), \tag{1}$$

$$\nabla \times \mathbf{E}(\mathbf{r},t) = -\frac{1}{c}\frac{\partial \mathbf{B}(\mathbf{r},t)}{\partial t}, \tag{2}$$

$$\nabla \cdot \mathbf{D}(\mathbf{r},t) = 0, \tag{3}$$

$$\nabla \cdot \mathbf{B}(\mathbf{r},t) = 0. \tag{4}$$

where e is the electron charge, $\mathbf{E}(\mathbf{r},t)$ is the electric field vector, $\mathbf{B}(\mathbf{r},t)$ is the magnetic induction vector, and $\mathbf{H}(\mathbf{r},t)$ is the magnetic field vector; for all media considered below, $\mu = 1$, hence, in Gaussian units, $\mathbf{B}(\mathbf{r},t) = \mathbf{H}(\mathbf{r},t)$. Here $\mathbf{D}(\mathbf{r},t)$ is the electric displacement vector, $\mathbf{j}(\mathbf{r},t) = (\mathbf{j}_\tau(\mathbf{r},t), 0)$ and $\mathbf{j}_\tau(\mathbf{r},t) = \mathbf{j}_\tau(\rho,t)\delta(z)$ is the surface current in the metasurface plane, $\boldsymbol{\rho} = (x,y,0)$ is the radius-vector in the $z = 0$-plane, $\delta(z)$ is the Dirac delta function.

Let us represent electromagnetic fields using Fourier integrals of the following form [25]:

$$\mathbf{E}(\mathbf{r},t)=\int\limits_{-\infty}^{\infty}\int\limits_{-\infty}^{\infty}\mathbf{E}(\boldsymbol{k},\omega)\exp\left[i(k_z z+\boldsymbol{\kappa\rho}-\omega t)\right]d\boldsymbol{k}d\omega, \tag{5}$$

where ω denotes the angular frequency, $\boldsymbol{k}=(\boldsymbol{\kappa},k_z)$ is the wave vector, $\boldsymbol{\kappa}=(k_x,k_y,0)$ is the wave vector in the $z=0$-plane, k_z is the normal component of the wave vector.

The material equations linking the electric displacement vector to the electric field intensity vector are described, in general, by the following non-local relationship:

$$D_j(\mathbf{r},t)=\int_{-\infty}^{t}\hat{\varepsilon}_{jg}(t-t')E_g(\mathbf{r},t')dt', \tag{6}$$

where indices j and g take values x,y,z, and summation is performed over index g. The kernel $\hat{\varepsilon}_{jg}(t-t')$ represents the dielectric response tensor of the medium. The dependence of the type $t-t'$ means the homogeneity of the structure's electrodynamic properties over time. For the Fourier components of fields, this material ratio takes the form:

$$D_j(\boldsymbol{k},\omega)=\varepsilon_{jg}(\omega)E_g(\boldsymbol{k},\omega). \tag{7}$$

Here, $\varepsilon_{jg}(\omega)$ is the frequency-dependent dielectric permittivity tensor, defined as the Fourier transform of the temporal response function $\hat{\varepsilon}_{jg}(\tau)$:

$$\varepsilon_{jg}(\omega)=\int_{0}^{\infty}\hat{\varepsilon}_{jg}(\tau)\exp(i\omega\tau)d\tau. \tag{8}$$

In the dielectric regions ($z<0$ and $0<z<d$), we have $\hat{\varepsilon}_{ij}(\tau)=\varepsilon_d\delta_{ij}\delta(\tau)$, where δ_{ij} is the Kronecker delta symbol. Then the constitutive relation (7) takes the form $\mathbf{D}_{1,2}(\boldsymbol{k},\omega)=\varepsilon_{1,2}\mathbf{E}(\boldsymbol{k},\omega)$. For plasma-like region ($z>d$) we have $\mathbf{D}_p(\boldsymbol{k},\omega)=\varepsilon_p(\omega)\mathbf{E}(\boldsymbol{k},\omega)$, where

$$\varepsilon_p(\omega)=\varepsilon_0-\frac{\omega_p^2}{\omega(\omega+i\nu)}, \tag{9}$$

ε_0 is the high-frequency permittivity, ω_p is the plasma frequency of charge carriers in the plasma-like medium, and ν is the effective collision frequency accounting for dissipative losses.

We represent the surface current $\mathbf{j}_\tau(\boldsymbol{\rho},t)\delta(z)$ as

$$\mathbf{j}_\tau(\boldsymbol{\rho},t)=\int\limits_{-\infty}^{\infty}\int\limits_{-\infty}^{\infty}\mathbf{j}_\tau(\boldsymbol{\kappa},\omega)\exp\big[i(\boldsymbol{\kappa\rho}-\omega t)\big]d\boldsymbol{\kappa}d\omega, \tag{10}$$

where

$$\mathbf{j}_\tau(\boldsymbol{\kappa},\omega)=\sigma\left(\omega\right)E\left(\boldsymbol{\kappa},\omega\right), \tag{11}$$

$\sigma(\omega)$ is the Fourier transform of the effective conductivity of a metasurface,

$$\sigma(\omega)=\frac{c}{4\pi}\left(\sigma_\infty+\frac{iA\omega}{\omega^2-\Omega^2+i\gamma\omega}\right), \tag{12}$$

where σ_∞ is the background conductivity accounting for the lower electronic bands contributions ($\mathrm{Re}\sigma_\infty=0$), A is defined by the metasurface design (ImA $=0$), Ω is the metasurface resonant frequency, γ is the bandwidth of the resonance, defined by ohmic and radiation losses. In the future, we will not take into account dissipative losses in the metasurface as well as in plasma-like medium and will assume $\gamma=0$ and $\nu=0$.

The boundary conditions in the metasurface plane $z=0$ are the conditions of continuity of the tangential components of the electric field intensity vectors and the jumps of the tangential components of the magnetic field intensity vectors associated with the presence of surface current:

$$\mathbf{n}_{1,2}\times\Big(\mathbf{E}_2(\boldsymbol{r},t)-\mathbf{E}_1(\boldsymbol{r},t)\Big)=0, \tag{13}$$

$$\mathbf{n}_{1,2}\times\Big(\mathbf{H}_2(\boldsymbol{r},t)-\mathbf{H}_1(\boldsymbol{r},t)\Big)=\frac{4\pi}{c}\boldsymbol{j_\tau(\rho,t)}, \tag{14}$$

where $\mathbf{n}_{1,2}=(0,0,1)$ is a unit normal vector pointing from medium 1 to medium 2. The boundary conditions at the interface between dielectric 2 and the plasma-like medium ($z=d$) are the continuity conditions of the tangential components of the electric and magnetic fields:

$$\mathbf{n}_{1,2}\times\Big(\mathbf{E}_2(\boldsymbol{r},t)-\mathbf{E}_1(\boldsymbol{r},t)\Big)=0,\ \mathbf{n}_{1,2}\times\Big(\mathbf{H}_2(\boldsymbol{r},t)-\mathbf{H}_1(\boldsymbol{r},t)\Big)=0. \tag{15}$$

2.2. Dispersion relations of structure eigenwaves

Let us obtain the dispersion relation for p-polarized eigenwaves of the structure under study with field components $\mathbf{E}(\boldsymbol{r},t) = (E_x(\boldsymbol{r},t), 0, E_z(\boldsymbol{r},t))$, $\mathbf{H}(\boldsymbol{r},t) = (0, H_y(\boldsymbol{r},t), 0)$ and assume that waves propagate along the x-axis, i.e. $\boldsymbol{k} = (k_x, 0, k_z)$. For the selected polarization, the boundary conditions (13)-(15) take the form:

$$E_{x2}(x,t)\Big|_{z=0} = E_{x1}(x,t)\Big|_{z=0}, \tag{16}$$

$$H_{y2}(x,t)\Big|_{z=0} - H_{y1}(x,t))\Big|_{z=0} = -\frac{4\pi}{c} j_x(\boldsymbol{\rho},t)\Big|_{z=0}, \tag{17}$$

$$E_{x2}(x,t)\Big|_{z=d} = E_{x1}(x,t)\Big|_{z=d},\ H_{y2}(x,t)\Big|_{z=d} = H_{y1}(x,t))\Big|_{z=d}. \tag{18}$$

First, we obtain the dispersion relation for the *surface waves* of the structure under investigation. Hereafter, we will use the following dimensionless variables and structure parameters:

$$\xi = \frac{\omega}{\Omega},\ q = \frac{ck_x}{\Omega},\ \eta_{1,2} = i\frac{ck_{z1,2}}{\Omega}\sqrt{q^2 - \xi^2\varepsilon_{1,2}},\ \eta_p = i\frac{ck_{zp}}{\Omega}\sqrt{q^2 - \xi^2\varepsilon_p(\xi)} \tag{19}$$

$$\bar{A} = \frac{A}{\Omega},\ \bar{\omega}_p = \frac{\omega_p}{\Omega},\ \bar{\sigma}_\infty = -\frac{4\pi i}{c}\sigma_\infty,\ \delta = \frac{d\Omega}{c}. \tag{20}$$

Expressions (9) and (12) for the Fourier transforms of dielectric permittivity of the plasma-like medium and conductivity in dimensionless forms are written as follows:

$$\varepsilon_p(\xi) = \varepsilon_0 - \frac{\bar{\omega}_p^2}{\xi^2},\ \bar{\sigma}(\xi) = -\frac{4\pi i}{c}\sigma(\omega) = \bar{\sigma}_\infty + \frac{\bar{A}\xi}{\xi^2 - 1}. \tag{21}$$

Using the representation of fields (5) and surface current (10) from boundary conditions (16)-(18), we obtain the following dispersion relation for the surface eigenwaves:

$$\left[\xi\left(\frac{\varepsilon_1}{\eta_1} + \frac{\varepsilon_2}{\eta_2}\right) - \bar{\sigma}(\xi)\right]\left(\frac{\varepsilon_p(\xi)}{\eta_p} + \frac{\varepsilon_2}{\eta_2}\right) - \left[\xi\left(\frac{\varepsilon_1}{\eta_1} - \frac{\varepsilon_2}{\eta_2}\right) - \bar{\sigma}(\xi)\right]\left(\frac{\varepsilon_p(\xi)}{\eta_p} - \frac{\varepsilon_2}{\eta_2}\right)\exp(-2\eta_2\delta) = 0. \tag{22}$$

In the limit $\delta \longrightarrow \infty$, the dispersion relation (22) decouples into two independent relations describing the eigenwaves of the isolated subsystems: dielectric 2 / plasma-like medium and dielectric 1 / metasurface / dielectric 2:

$$\xi\left(\frac{\varepsilon_1}{\eta_1} + \frac{\varepsilon_2}{\eta_2}\right) - \bar{\sigma}(\xi) = 0. \tag{23}$$

Let us consider *bulk-surface* eigenwaves whose fields decrease exponentially in dielectric 1 and plasma-like medium, but have an oscillatory character in dielectric 2. For these waves, the condition $\xi^2\varepsilon_1 < q^2 < \xi^2\varepsilon_2$ is satisfied. We introduce the following notation for the normal component of the wave vector in dielectric 2:

$$\zeta_2 = \frac{ck_{z2}}{\Omega} = \sqrt{\xi^2\varepsilon_2 - q^2}. \tag{24}$$

Satisfying the boundary conditions (16)-(18), we obtain the desired dispersion relation:

$$\left[\zeta_2^2\frac{\varepsilon_p(\xi)}{\eta_p}\left(\xi\frac{\varepsilon_1}{\eta_1} - \bar{\sigma}(\xi)\right) - \xi\varepsilon_2^2\right]\tan(\zeta_2\delta) - \varepsilon_2\zeta_2\left[\xi\left(\frac{\varepsilon_1}{\eta_1} + \frac{\varepsilon_p(\xi)}{\eta_p}\right) - \bar{\sigma}(\xi)\right] = 0. \tag{25}$$

Below, we will perform a numerical analysis of dispersion relations (22) and (25).

3. NUMERICAL ANALYSIS OF DISPERSION RELATIONS

For the numerical calculation of dispersion curves, we will select the following structure parameters: $\varepsilon_1 = 1$ (vacuum), $\varepsilon_2 = 2.1$ (teflon dielectric), $\varepsilon_0 = 15.68$ (InSb semiconductor) or $\varepsilon_0 = 1$ (metal), $\bar{\sigma}_\infty = 0.2$, $\bar{A} = 0.2$. We will only change the dimensionless quantities $\bar{\omega}_p$ and δ. Let us first consider the eigenspectrum of surface electromagnetic waves in the structure dielectric 1 - metasurface - dielectric 2, shown in Fig. 2. We see that only surface waves are present in the spectrum. Indeed, as follows from dispersion relation (23), for purely imaginary values of η_1 or η_2 (in the absence of dissipative losses), there are no real solutions to this relation. It can also be seen that the low-frequency branch ($\xi < 1$) of the spectrum (curve 4) originates at the beginning of the coordinates, while the high-frequency branch ($\xi > 1$, curve 5)

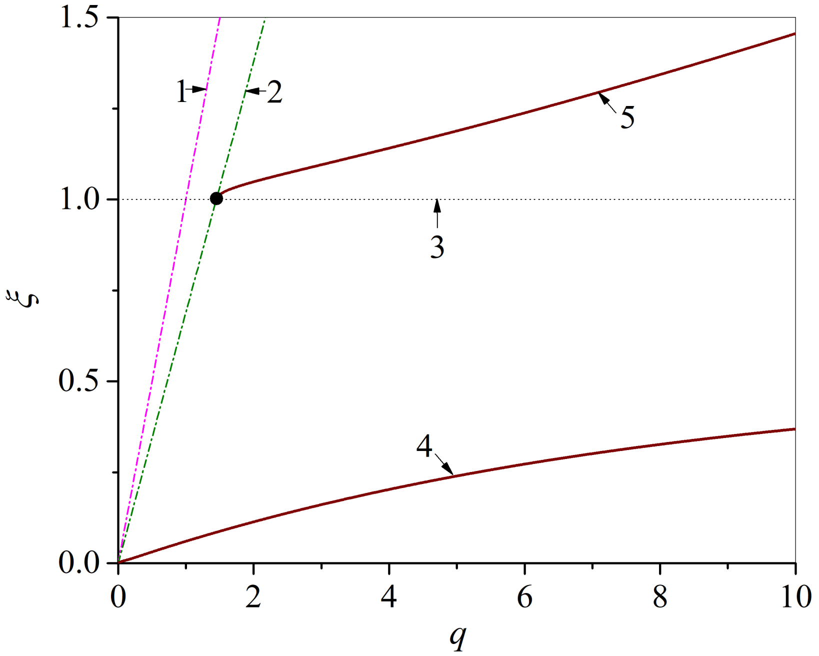

Figure 2. Eigenspectrum of surface electromagnetic waves in the structure dielectric 1 - metasurface - dielectric 2, calculated for the above-mentioned parameter values. Curves 1 and 2 correspond to the light lines in dielectrics 1 and 2, respectively. Curve 3 is for the dimensionless metasurface resonant frequency $\xi = 1$, curves 4 and 5 are for the low- and high frequency modes, respectively. The black circle corresponds to the starting point of the dispersion curve spectrum 5.

has its starting point on the light line 2. Note also that the low-frequency branch appears in the spectrum only when $\bar{\sigma}_\infty > 0$.

In Fig. 3 - Fig. 6, we analyze the effect of hybridization of surface eigenwaves in the structure dielectric 1 - metasurface - dielectric 2 - plasma-like medium, arising from the interaction of the high-frequency intrinsic surface wave of the "metasurface" with the eigenwave of the plasma-like medium as a substrate. We consider the influence of such structural parameters as the high-frequency dielectric permittivity of the plasma-like medium, its plasma frequency, and the thickness of the dielectric layer 2 on this effect. Fig. 3 shows the intrinsic spectrum of such a structure for a semiconductor substrate for $\bar{\omega}_p = 5$ and $\delta = 0.45$. Fig. 3 shows that taking into account the plasma-like medium leads to the appearance of an additional branch of the spectrum (curve 6), which, with an increase in the longitudinal wave number q, asymptotically tends towards the surface plasmon frequency ξ_{sp} and has a spectrum starting point at the light line 2. The region of interaction between the high-frequency mode of the metasurface (curve 7) and the mode of the plasma-like medium (curve 6) is also visible – region A, where dispersion curves 6 and 7 are closest to each other. The frequency gap in region A is $\Delta\xi \approx 0.0521$. Unlike the spectrum shown in Fig. 2, the presence of a plasma-like substrate leads to the appearance of so-called bulk-surface (or waveguide) modes, shown in Fig. 3 by dotted lines. The dispersion curves of these modes are located in the region between light lines 1 and 2 and transition into the dispersion curves of the corresponding surface modes. The amplitudes of the fields of the bulk-surface modes under consideration oscillate in the region of dielectric 2 and decrease monotonically along the normal in the regions of dielectric 1 and the plasma-like medium as they move deeper into these media. The bulk-surface mode corresponding to the high-frequency branch 7 has a spectrum starting point on the light line 1. Taking into account dissipative losses in the structure to the left of this point, there is a section of the dispersion curve corresponding to the so-called leaky mode [26]. Note that the region of greatest interaction (resonant interaction) of surface modes corresponding to dispersion curves 6 and 7 (region A) is located near the surface plasmon frequency ξ_{sp}, where the following relations hold: $\varepsilon_p(\xi) < 0$ and $\bar{\sigma}(\xi) > 0$.

Fig. 4 demonstrates the influence of the plasma frequency value on the position and magnitude of the frequency gap in the region of maximum interaction of surface modes. The dispersion curves in Fig. 4 are calculated for the same structure and with the same parameters as in Fig. 3, except for the plasma frequency value, $\bar{\omega}_p = 5.3$. Comparing Fig. 3 and Fig. 4 reveals that increasing the plasma frequency $\bar{\omega}_p$ at a fixed dielectric thickness δ shifts the resonant interaction zone (region A) toward higher frequencies and larger longitudinal wavenumbers q. Concurrently, the magnitude of the frequency splitting narrows down to $\Delta\xi \approx 0.0333$.

The influence of the thickness of the dielectric layer 2 on the structure of the dispersion curves 6 and 7 in the structure under consideration with a semiconductor substrate is shown in Fig. 5. The dispersion curves in Fig. 5 were constructed using the same structure parameters as in Fig. 3, except for the thickness of the dielectric 2, $\delta = 0.6$. As evident from comparing Figs. 3 and 5, expanding the dielectric layer thickness δ under a constant plasma frequency $\bar{\omega}_p$ reduces the frequency splitting to $\Delta\xi \approx 0.0171$. Numerical calculations confirm that the resonant interaction zone shifts toward

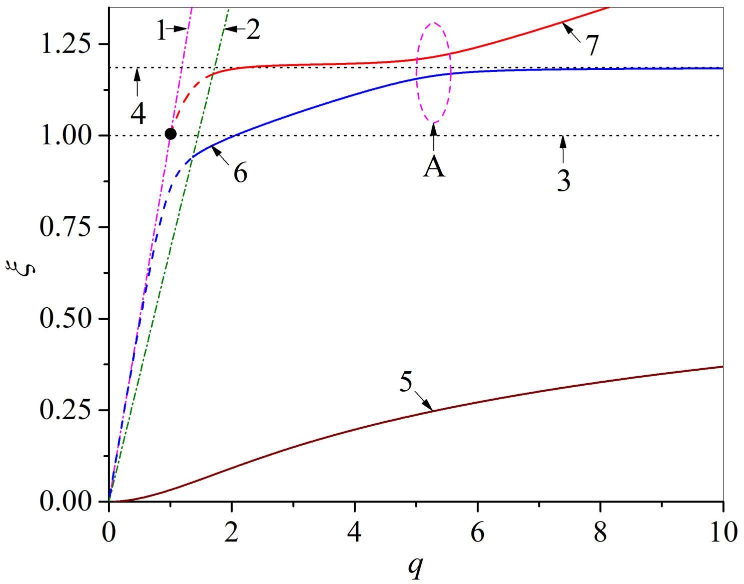

Figure 3. Eigenspectrum of the surface waves of the structure dielectric 1 - metasurface - dielectric 2 - InSb semiconductor, calculated for the above-mentioned dielectric and metasurface parameters and $\bar{\omega}_p = 5$, $\delta = 0.45$. Curves 1 and 2 correspond to the light lines in dielectrics 1 and 2, respectively. Curve 3 is for the dimensionless metasurface resonant frequency $\xi = 1$, curve 4 is for surface plasmon frequency $\xi_{sp} = \bar{\omega}_p/\sqrt{\varepsilon_0 + \varepsilon_2} \approx 1.2$, curve 5 is for the low frequency mode, curve 6 and 7 are hybridized high-frequency modes. The solid sections of curves 6 and 7 correspond to surface modes, while the dashed sections correspond to bulk-surface modes. Area A shows the area of resonant interaction between modes 6 and 7. The black circle corresponds to the starting point of the dispersion curve of bulk-surface mode.

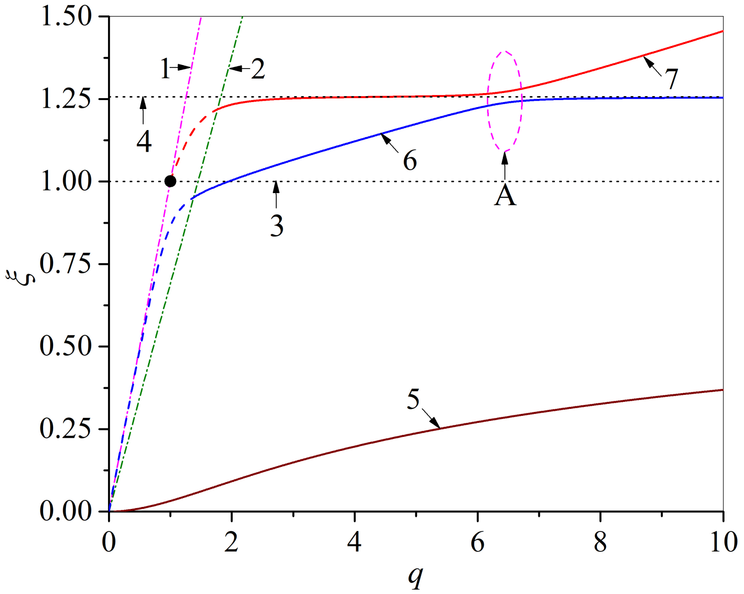

Figure 4. Eigenspectrum of the surface waves of the structure dielectric 1 - metasurface - dielectric 2 - InSb semiconductor, calculated for the above-mentioned dielectric and metasurface parameters and $\bar{\omega}_p = 5.3$, $\delta = 0.45$. Curves 1 and 2 correspond to the light lines in dielectrics 1 and 2, respectively. Curve 3 is for the dimensionless metasurface resonant frequency $\xi = 1$, curve 4 is for surface plasmon frequency $\xi_{sp} \approx 1.26$, curve 5 is for the low frequency mode, curve 6 and 7 are hybridized high-frequency modes. The solid sections of curves 6 and 7 correspond to surface modes, while the dashed sections correspond to bulk-surface modes. Area A shows the area of resonant interaction between modes 6 and 7. The black circle corresponds to the starting point of the dispersion curve of bulk-surface mode.

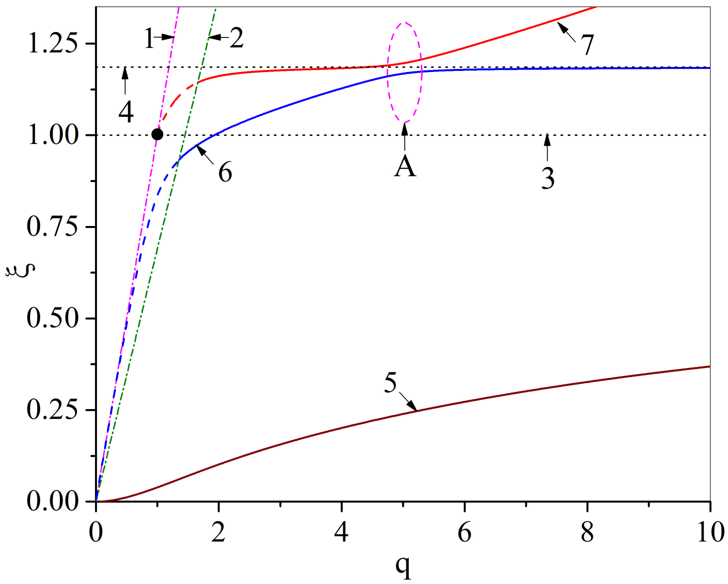

Figure 5. Eigenspectrum of the surface waves of the structure dielectric 1 - metasurface - dielectric 2 - InSb semiconductor, calculated for the above-mentioned dielectric and metasurface parameters and $\bar{\omega}_p = 5, \delta = 0.6$. Curves 1 and 2 correspond to the light lines in dielectrics 1 and 2, respectively. Curve 3 is for the dimensionless metasurface resonant frequency $\xi = 1$, curve 4 is for surface plasmon frequency $\xi_{sp} \approx 1.2$, curve 5 is for the low frequency mode, curve 6 and 7 are hybridized high-frequency modes. The solid sections of curves 6 and 7 correspond to surface modes, while the dashed sections correspond to bulk-surface modes. Area A shows the area of resonant interaction between modes 6 and 7. The black circle corresponds to the starting point of the dispersion curve of bulk-surface mode.

smaller q values in this geometry.

Dispersion curves for the structure under investigation, where metal is selected as the plasma-like medium, are shown in Fig. 6. Comparing the semiconductor and metallic substrates (Figs. 3 and 6) demonstrates a striking contrast. For the same plasma frequency $\bar{\omega}_p$ and comparable mode splitting ($\Delta\xi \approx 0.052$), the high-frequency mode interaction in the metal-backed structure occurs at notably smaller wave vectors q. Achieving this exact splitting in the metallic case requires a dielectric spacer approximately seven times thicker than its semiconductor counterpart. It should also be noted that for all structures considered in the field of resonant interaction, the conditions $\varepsilon_p(\xi) < 0$ and $\bar{\sigma}(\xi) > 0$ are satisfied.

4. DISCUSSION AND CONCLUSION

We have developed a rigorous electrodynamic model to study the dispersion features of localized electromagnetic waves in a hybrid solid-state structure, combining a plasmonic metasurface with a plasma-like substrate. We obtained an analytical expression for the eigenmodes of the studied structure, which are coupled modes of the metasurface and the plasma-like medium. The numerical analysis shows that the presence of a plasma-like medium significantly changes the spectrum of electromagnetic waves compared to isolated metasurfaces. In particular, it allows bulk-surface waves to propagate and causes strong hybridization between the eigenmodes of metasurface and surface plasmons of the substrate.

The degree of this mode coupling is highly sensitive to the geometry and material properties. Our calculations show that the frequency splitting $\Delta\xi$ (the gap between the interacting branches) is governed primarily by the dimensionless dielectric spacer thickness δ. It has been demonstrated that widening this gap weakens the field overlap, predictably narrowing the splitting. Furthermore, tuning the plasma frequency $\bar{\omega}_p$ of the substrate allows one to shift the resonant interaction zone across the frequency-wave vector plane. In practice, this could be achieved through optical pumping, thermal heating, or electrical gating of the semiconductor. We also determined the frequency and wave vector range in which bulk-surface waves transition into leaky waves, which is an important factor in estimating radiation losses in practical devices. A comparison of the semiconductor (InSb) and metal substrates shows the profound influence of dielectric contrast.

We found that to achieve a similar degree of mode separation in a structure with a metal substrate, a dielectric layer approximately seven times thicker than that required for a semiconductor is needed. This significant geometric difference highlights the clear advantage of using semiconductor substrates for applications focused on deep miniaturization with sub-wavelength dimensions. Ultimately, the ability to selectively control the phase velocity, field localization, and spectral gaps of these hybrid waves provides a robust physical foundation for creating advanced microwave and terahertz components, from compact delay lines and sensors to dynamic cloaking coatings.

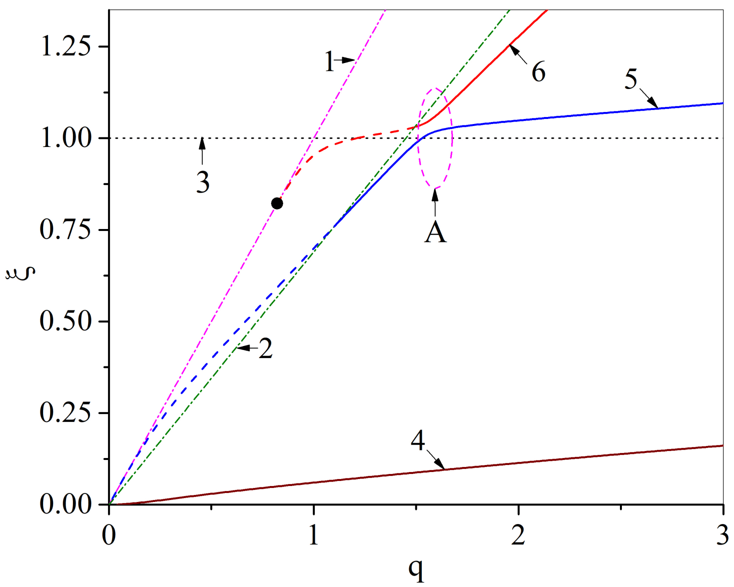

Figure 6. Eigenspectrum of the surface waves of the structure dielectric 1 - metasurface - dielectric 2 - metal, calculated for the above-mentioned dielectric and metasurface parameters and $\bar{\omega}_p = 5$, $\delta = 3.3$. Curves 1 and 2 correspond to the light lines in dielectrics 1 and 2, respectively. Curve 3 is for the dimensionless metasurface resonant frequency $\xi = 1$, curve 4 is for the low frequency mode, curve 5 and 6 are hybridized high-frequency modes. The solid sections of curves 5 and 6 correspond to surface modes, while the dashed sections correspond to bulk-surface modes. Area A shows the area of resonant interaction between modes 5 and 6. The black circle corresponds to the starting point of the dispersion curve of bulk-surface mode.

ORCID

N.N. Beletskii, https://orcid.org/0000-0002-3194-7251; **O.Yu. Averkov**, https://orcid.org/0000-0002-1169-9393; **Yu.O. Averkov**, https://orcid.org/0000-0001-6055-015X

REFERENCES

[1] A. Ranjbar and A. Grbic, ”Broadband, Multiband, and Multifunctional All-Dielectric Metasurfaces,” Phys. Rev. Applied, **11**, 054066 (2019). https://doi.org/10.1103/PhysRevApplied.11.054066

[2] D. Correas-Serrano, J. S. Gomez-Diaz, A. Alvarez-Melcon, and A. Alù, ”Black phosphorus plasmonics: anisotropic elliptical propagation and nonlocality-induced canalization,” J. Opt., 18, 104006 (2016). https://doi.org/10.1088/2040-8978/18/10/104006

[3] J. S. Gomez-Diaz, M. Tymchenko, and A. Alù, ”Hyperbolic Plasmons and Topological Transitions Over Uniaxial Metasurfaces,” Phys. Rev. Lett., 114, 233901 (2015). https://doi.org/10.1103/PhysRevLett.114.233901

[4] A. A. High, R. C. Devlin, A. Dibos, M. Polking, D. S. Wild, J. Perczel, N. P. de Leon, M. D. Lukin, and H. Park, ”Visible-frequency hyperbolic metasurface,” Nature, **522**, 192–196 (2015). https://doi.org/10.1038/nature14477

[5] C. L. Holloway, E. F. Kuester, J. A. Gordon, J. O’Hara, J. Booth, and D. R. Smith, ”An overview of the theory and applications of metasurfaces: The two-dimensional equivalents of metamaterials,” IEEE Antennas Propag. Mag., **54**, 10–35 (2012). https://doi.org/10.1109/MAP.2012.6230714

[6] A. Nemilentsau, T. Low, and G. Hanson, ”Anisotropic 2D Materials for Tunable Hyperbolic Plasmonics,” Phys. Rev. Lett., **116**, 066804 (2016). https://doi.org/10.1103/PhysRevLett.116.066804

[7] P. A. D. Gonçalves, L. P. Bertelsen, S. Xiao, and N. A. Mortensen, ”Hybridized Plasmons in 2D Nanoslits: From Graphene to Anisotropic 2D Materials,” ACS Photonics, 4, 2645–2652 (2017). https://doi.org/10.1021/acsphotonics.7b00558

[8] J. Sperrhake, M. Falkner, S. Fasold, T. Kaiser, and T. Pertsch, ”Equivalence of reflection paths of light and Feynman paths in stacked metasurfaces,” Phys. Rev. B, **102**, 245108 (2020). https://doi.org/10.1103/PhysRevB.102.245108

[9] T. Zhan, X. Shi, Y. Dai, X. Liu, and J. Zi, ”Transfer matrix method for optics in graphene layers,” J. Phys.: Condens. Matter, **25**, 215301 (2013). https://doi.org/10.1088/0953-8984/25/21/215301

[10] I. Allayarov, V. R. Tuz, A. Cala Lesina, and A. B. Evlyukhin, ”Analytical model of metasurfaces comprising meta-atoms with anisotropic polarizabilities and for arbitrary incident angles,” Phys. Rev. B, **111**, 155438 (2025). https://doi.org/10.1103/PhysRevB.111.155438

[11] S. M. Kandil, D. J. Bisharat, and D. F. Sievenpiper, ”Engineering equifrequency contours of metasurfaces for self-collimated surface-wave steering,” Phys. Rev. Applied, **21**, 044006 (2024). https://doi.org/10.1103/PhysRevApplied.21.044006

[12] X. Zhang, C. Bian, Z. Gong, R. Chen, T. Low, H. Chen, and X. Lin, "Hybrid surface waves in twisted anisotropic heterometasurfaces," Phys. Rev. Applied, **21**, 064034 (2024). https://doi.org/10.1103/PhysRevApplied.21.064034

[13] E. M. Renzi, E. Galiffi, X. Ni, and A. Alù, "Hyperbolic Shear Metasurfaces," Phys. Rev. Lett., 132, 263803 (2024). https://doi.org/10.1103/PhysRevLett.132.263803

[14] C. Bian, X. Zhang, W. Ma, X. Chen, H. Chen, T. Low, and X. Lin, "Antihyperbolic surface waves on hyperbolic metasurfaces," Phys. Rev. A, **111**, 033522 (2025). https://doi.org/10.1103/PhysRevA.111.033522

[15] X. Zhang, X. Cui, T. Cai, W. Cai, T. Low, H. Chen, and X. Lin, "Scattering-free Plasmonic Brewster Effect via Metasurfaces," ACS Photonics, **12**(4), 1865–1872 (2025). https://doi.org/10.1021/acsphotonics.4c02263

[16] R. Ogier, Y. Fang, M. Käll, and M. Svedendahl, "Near-Complete Photon Spin Selectivity in a Metasurface of Anisotropic Plasmonic Antennas," Phys. Rev. X, **5**, 041019 (2015). https://doi.org/10.1103/PhysRevX.5.041019

[17] S. Droulias and L. Bougas, "Chiral sensing with achiral anisotropic metasurfaces," Phys. Rev. B, **104**, 075412 (2021). https://doi.org/10.1103/PhysRevB.104.075412

[18] C. L. Cortes, W. Newman, S. Molesky, and Z. Jacob, "Quantum nanophotonics using hyperbolic metamaterials," J. Opt., **14**, 063001 (2012). https://doi.org/10.1088/2040-8978/14/6/063001

[19] N. K. Paul, D. Correas-Serrano, and J. S. Gomez-Diaz, "Giant lateral optical forces on Rayleigh particles near hyperbolic and extremely anisotropic metasurfaces," Phys. Rev. B, 99, 121408(R) (2019). https://doi.org/10.1103/PhysRevB.99.121408

[20] Y. Zhang, M. Antezza, H.-L. Yi, and H.-P. Tan, "Metasurface-mediated anisotropic radiative heat transfer between nanoparticles," Phys. Rev. B, **100**, 085426 (2019). https://doi.org/10.1103/PhysRevB.100.085426

[21] B.-Q. Lin, J.-X. Guo, P. Chu, W.-J. Huo, Z. Xing, B.-G. Huang, and L. Wu, "Multiple-Band Linear-Polarization Conversion and Circular Polarization in Reflection Mode Using a Symmetric Anisotropic Metasurface," Phys. Rev. Applied, **9**, 024038 (2018). https://doi.org/10.1103/PhysRevApplied.9.024038

[22] Y. Nakata, Y. Urade, K. Okimura, T. Nakanishi, F. Miyamaru, M.W. Takeda, and M. Kitano, "Anisotropic Babinet-Invertible Metasurfaces to Realize Transmission-Reflection Switching for Orthogonal Polarizations of Light," Phys. Rev. Applied, **6**, 044022 (2016). https://doi.org/10.1103/PhysRevApplied.6.044022

[23] Y. Nakata, K. Fukawa, T. Nakanishi, Y. Urade, K. Okimura, and F. Miyamaru, "Reconfigurable Terahertz Quarter-Wave Plate for Helicity Switching Based on Babinet Inversion of an Anisotropic Checkerboard Metasurface," Phys. Rev. Applied, **11**, 044008 (2019). https://doi.org/10.1103/PhysRevApplied.11.044008

[24] C.P. Mavidis, A.C. Tasolamprou, E.N. Economou, C.M. Soukoulis, and M. Kafesaki, "Polaritonic cylinders as multifunctional metamaterials: Single scattering and effective medium description," Phys. Rev. B, **102**, 155310 (2020). https://doi.org/10.1103/PhysRevB.102.155310

[25] J. D. Jackson, *Classical Electrodynamics*, 3rd ed. (John Wiley & Sons, New York, 1999).

[26] R.S. Brazis, "Active and nonlinear interactions under excitation of plasma-type polaritons in semiconductors," Litov. Fiz. Sb., **21**(4), 73-117 (1981). (in Russian)

ЕЛЕКТРОМАГНІТНІ ВЛАСТИВОСТІ ГІБРИДНОЇ ТВЕРДОТІЛЬНОЇ СТРУКТУРИ, ЩО ВКЛЮЧАЄ ПЛАЗМОПОДІБНЕ СЕРЕДОВИЩЕ ТА МЕТАПОВЕРХНЮ

М.М. Білецький, О.Ю. Аверков, Ю.О. Аверков

Інститут радіофізики та електроніки ім. О. Я. Усикова НАН України, вул. Акад. Проскури, 12, Харків, 61085, Україна

У цій статті ми теоретично досліджуємо дисперсійні властивості поверхневих і об'ємно-поверхневих електромагнітних хвиль, що поширюються в гібридній шаруватій твердотільній структурі, яка містить ізотропну плазмонну метаповерхню. Ця структура складається з напівнескінченного діелектрика 1, ізотропної метаповерхні, діелектричного шару 2 і напівнескінченного плазмоподібного середовища (напівпровідника або металу). Ми виводимо точне аналітичне дисперсійне співвідношення для зв'язаних електромагнітних мод і проводимо його детальний чисельний аналіз. Наш аналіз демонструє, що провідність метаповерхні, товщина діелектричного шару та плазмова частота напівпровідника значно впливають на резонансну взаємодію поверхневих хвиль. Було виявлено, що додавання плазмоподібного середовища як підкладки призводить до появи гібридних поверхневих хвиль та можливості виникнення об'ємно-поверхневих хвиль. Фактично, ми виявили значну різницю між металевими та напівпровідниковими підкладками. Дійсно, щоб отримати точно таке саме значення розщеплення в системі з металевою підкладкою, необхідний діелектричний прошарок, товщина якого приблизно в сім разів більша. Ця геометрична різниця робить напівпровідники набагато більш практичним вибором для глибокої субхвильової мініатюризації. Результати надають теоретичну основу для розробки та оптимізації нових перебудовних хвилеводів, датчиків та пристроїв на повільних хвилях, що працюють у діапазонах мікрохвильових та терагерцових частот.

Ключові слова: *плазмонна метаповерхня; діелектричний шар; напівпровідник; плазмоподібне середовище; поверхнева електромагнітна хвиля; об'ємно-поверхнева електромагнітна хвиля; дисперсійне співвідношення*